

**Experimental investigation of calcium carbonate mineralogy in past
and future oceans**

Pieter Bots

Submitted in accordance with the requirements for the degree of
Doctor of Philosophy

The University of Leeds
School of Earth and Environment

November, 2011

The candidate confirms that the work submitted is his own, except where work, which has formed part of jointly-authored publications, has been included. The contributions of the candidate and the other authors to this work have been explicitly indicated overleaf. The candidate confirms that appropriate credit has been given where reference has been made to the work of others.

This copy has been supplied on the understanding that it is copyright material and that no quotation from the thesis may be published without proper acknowledgement.

Declaration

Section 3.5 summarizes method development and the final methodologies for two analytical methods.

The analyses described in section 3.5.2 were performed by the candidate, initially with the help of David Ashley.

Chapter 4 is a reproduction of a peer-reviewed publication in *Geology*.

Bots, P., Benning, L. G., Rickaby, R. E. M., and Shaw, S., 2011. The role of SO₄ in the switch from calcite to aragonite seas. *Geology* **39**, 331-334.

All the experimental and modelling work for chapter 4 has been conducted by the candidate and the interpretation was performed by, and the manuscript was prepared by the candidate with the help of his supervisors: Liane G. Benning, Sam Shaw and Ros Rickaby.

Chapter 5 is a reproduction of a final draft of a manuscript for publication, to be submitted to the *Journal of the American Chemical Society*.

Bots, P., Benning, L.G., Rodriguez-Blanco, J.D., Roncal-Herrero, T., and Shaw, S., in prep. Mechanistic Insights into the Crystallization of Amorphous Calcium Carbonate (ACC).

The experimental, analytical and modelling work for chapter 5 has been conducted by the candidate. During synchrotron beamtime at Diamond Light Source, the experimental work for chapter 5 was assisted by Juan-Diego Rodriguez-Blanco and Teresa Roncal-Herrero. The interpretation of the experimental and modelling data was performed by, and the manuscript was prepared by the candidate with the help of his supervisors: Liane G. Benning and Sam Shaw.

Chapter 6 is a reproduction of a manuscript in preparation for publication.

Bots, P., Benning, L.G., Rodriguez-Blanco, J.D., Roncal-Herrero, T., and Shaw, S., in prep. Using WAXS to study intricate crystallization pathways – gypsum and vaterite crystallization via rapidcreekite

The experimental work for chapter 6 has been conducted by the candidate. During synchrotron beamtime at Diamond Light Source, the experimental work for

chapter 6 was assisted by Juan-Diego Rodriguez-Blanco and Teresa Roncal-Herrero. The interpretation of the experimental and modelling data was performed by, and the manuscript was prepared by the candidate with the help of his supervisors: Liane G. Benning and Sam Shaw.

Chapter 7 is a reproduction of a manuscript in preparation for publication.

Bots, P., Benning, L.G., Brinza, L., Lennie, A., and Shaw, S., in prep. Vaterite, formation and the effect of sulfate.

All experiments, analyses and data processing described in chapter 7 were carried out by the candidate, except the analyses and interpretation of the vaterite XANES (by Loredana Brinza, Diamond Light Source) and the high-resolution XRD pattern by (Alistair Lennie, Diamond Light Source). These analyses were provided via a collaborative agreement with my supervisors.

Collaborative publications

Roncal-Herrero, T., Blanco, J. D. R., Bots, P., Shaw, S., and Benning, L. G., 2011. The role of Zn, Sr, Mg and PO₄ in the interaction of carbonate-rich waters with sulphate minerals. *Macla* **15**, 181-182.

The candidate helped with the interpretations of the data and with the preparation of the draft.

Rodriguez-Blanco, J. D., Bots, P., Roncal-Herrero, T., Shaw, S., and Benning, L. G., in press. The role of pH and Mg on the stability and crystallization of amorphous calcium carbonate. *Journal of Alloys and Compounds*.

The candidate helped with the experimental part and the data analyses and with the preparation of the draft.

Van Driessche, A. E. S., Benning, L. G., Rodriguez-Blanco, J. D., Ossorio, M., Bots, P., and García-Ruiz, J. M., in review. The role, and implications, of bassanite as a precursor phase to gypsum precipitation. *Science*

The candidate helped with the experimental part and data analyses and with the preparation of the draft.

Acknowledgements

Even though it is my name on this thesis, I could not have done this work without the guidance and help of several people to whom I would like to express my eternal gratitude.

My supervisors: *Liane Benning* and *Sam Shaw* for their brilliant guidance and trusting me with the science, for allowing me to come along to Diamond and sending me to several major conferences and making me aware of all the Pieterisms and Pieterites I use when writing, and *Ros Rickaby* for her guidance and ideas during the preparation of my Geology paper.

Rob Newton for being part of my research support group and the discussions about the applications of my work for the paleoceanography world.

Juan Diego Rodriguez-Blanco and *Teresa Roncal-Herrero* for the countless discussions on the work we have done and for their assistance with my experiments at Diamond.

David Ashley for his enthusiastic assistance during the method development and for the training on Ion Chromatography, *Lesley Neve* for training me on XRD and *Eric Condliffe* for training me on SEM.

The Marie Curie Research Training Network: *Min-Gro* for the funding for my PhD and all the fancy network meetings I was allowed to go to, *the School of Earth and Environment* at the University of Leeds for their travel bursary and their students' publication prize 2010-2011, *the Mineralogical Society of Great Britain and Ireland* for their travel bursary to attend Goldschmidt 2009 and *Diamond Light Source* for beamtime at station I22 (SAXS/WAXS).

All the people from the Cohen group and the other parts of the School of Earth and Environment for discussions and drinks after work.

I would also like to thank my friends for making my time in Leeds very enjoyable and the *LGBT society* at Leeds University Union for all the friends I made and the experience I had during my time on the committee.

Finally, I would like to thank my family for supporting me all the way.

Abstract

Inorganic marine calcium carbonate formation and mineralogy varies significantly concurrent with the solution composition. During the Phanerozoic, due to oscillations in the seawater composition, this resulted in the formation of either dominantly calcite or aragonite. Variations in seawater composition also appear to have influenced the evolution of biomineralizing organisms. Additionally, many organisms utilize amorphous calcium carbonate (ACC) during biomineralization.

The occurrence of calcite and aragonite throughout the Phanerozoic and calcium carbonate biomineralization were investigated. This was done by determining the influence of solution chemistry (SO_4 and Mg) on calcium carbonate formation, mineralogy and stability via a variety of laboratory and synchrotron based synthesis experiments.

During the formation of aragonite and calcite, aqueous SO_4 and the Mg/Ca ratio both affect the formation of calcite and aragonite. An increase in aqueous SO_4 decreases the Mg/Ca ratio at which calcite is destabilized and aragonite becomes dominant. These results suggest that the models relating seawater chemistry to calcium carbonate formation needs re-evaluation.

Abiotic ACC crystallization to vaterite occurs in three stages. In the first stage, ACC crystallizes to vaterite via a spherulitic growth mechanism. The second stage is characterized by surface particle growth at the expense of ACC. Finally, particle growth via Ostwald ripening is the only remaining process. This process can be described as the inorganic analogue to biological ACC crystallization, which is adjusted by organisms to produce their preferred calcium carbonate polymorph and morphology. An increase in SO_4 concentration only decreases the spherulitic growth rate and Ostwald ripening, even when rapidcreekite (as an intermediate) and gypsum crystallizes.

Finally, SO_4 promotes the formation of vaterite. Depending on the formation process this is caused by either the stabilization of vaterite and destabilization of calcite (slow heterogeneous formation), or by the destabilization and inhibition of calcite formation (spherulitic growth).

Contents

Declaration	II
Acknowledgements	IV
Abstract	V
Contents	VI
Figures	X
Tables	XVII
Chapter 1 Introduction	1
1.1 Background information	1
1.2 Research objectives	3
1.3 Experimental approaches	4
1.4 Thesis outline	5
Chapter 2 Literature review	6
2.1 CaCO ₃ mineralogy	6
2.2 ACC crystallization.....	10
2.3 Chemical factors influencing the precipitation and stability of CaCO ₃	12
2.3.1 Magnesium.....	15
2.3.2 Sulfate	18
2.3.3 pH, alkalinity and pCO ₂	21
2.3.4 Temperature	23
2.4 The chemical evolution of Phanerozoic seawater.....	24
2.4.1 Calcite vs. Aragonite seas	29
2.5 Biomineralization.....	31
2.5.1 Biomineralization throughout the Phanerozoic.....	32
Chapter 3 Methods	34
3.1 Laboratory based experimental methods	35
3.1.1 Constant addition experiments.....	35
3.1.2 Vaterite formation and ageing.....	37
3.2 Laboratory based analytical methods.....	38
3.2.1 A spectrophotometric method to analyse Ca and Mg.....	38
3.2.2 Ion Chromatography	39
3.2.3 Field Emission Gun-Scanning Electron Microscopy.....	40

3.2.4 X-ray diffraction.....	40
3.2.4.1 Relative mass of a phase in a sample	43
3.2.4.2 Crystallite size and strain on the crystalline phase	44
3.2.4.3 Changes in the unit cell dimensions.....	44
3.3 Small and Wide Angle X-ray Scattering (SAXS/WAXS) and synchrotron based experimental methods	45
3.3.1 Synchrotron light.....	45
3.3.2 WAXS	47
3.3.3 SAXS	49
3.3.4 Experimental methods and data collection	53
3.4 PHREEQC modelling	55
3.4.1 Evaporation simulations.....	55
3.4.2 Modelling the chemical evolution of the SAXS/WAXS experiments	56
3.5 Method development.....	57
3.5.1 A photospectrometric method to analyse Ca and Mg.....	58
3.5.1.1 Basic principles	58
3.5.1.2 Tests	59
3.5.1.3 Final method	62
3.5.2 Measuring solid composition of CaCO ₃ using Ion Chromatography.....	64
3.5.2.1 Cations	65
3.5.2.2 Anions	69
Chapter 4 The role of SO₄ in the switch from calcite to aragonite seas.....	75
4.1 Abstract	75
4.2 Introduction	75
4.3 Methods.....	77
4.4 Results and discussion	79
4.5 Implications for Phanerozoic seawater chemistry.....	81
4.6 GSA data repository	84
4.6.1 PHREEQC evaporation simulations	84
4.6.2 Validation of the experimental method.....	85
Chapter 5 Mechanistic Insights into the Crystallization of Amorphous Calcium Carbonate (ACC).....	87
5.1 Introduction	87
5.2 Methods.....	90
2.3 Results	92

5.4 Discussion	97
5.4.1 Stage one: ACC formation and vaterite spherulitic growth	97
5.4.1.1 The effect of sulfate on vaterite spherulitic growth	101
5.4.2 Stages two and three: vaterite growth and ripening	102
5.4.2.1 The effect of sulfate on vaterite growth and ripening	103
5.5 Summary and conclusions	104
Chapter 6 Using WAXS to study intricate crystallization pathways – gypsum and vaterite crystallization via rapidcreekite.....	107
6.1 Introduction	107
6.2 Methods.....	108
6.3 Results and discussion	110
6.3.1 ‘Replacement’ experiment	112
6.3.2 ‘Additive’ and ‘additive-Mg’ experiments	116
6.3.3 Vaterite formation mechanisms and kinetics	120
6.4 Concluding remarks	123
Chapter 7 Vaterite, formation and the effect of sulfate.....	124
7.1 Introduction	124
7.2 Methods.....	126
7.2.1 Synthesis experiments.....	126
7.2.2 Ageing experiments	127
7.3 Results and discussion	128
7.3.1 Synthesis experiments.....	128
7.3.2 Structural analyses of vaterite	131
7.3.3 Vaterite ageing	134
7.3.4 The effects on vaterite stability.....	136
7.4 Concluding remarks	137
Chapter 8 Summary and concluding remarks	139
8.1 Effects of solution composition (sulfate and magnesium) on the precipitated calcium carbonate polymorph	139
8.2 Amorphous calcium carbonate crystallization and the effect of the sulfate concentration	140
8.3 Relating the experimental results to natural calcium carbonate formation.....	142
8.4 Outlook.....	144

References	147
Appendix A Supplementary information to chapter 4	175
Appendix B Supplementary information to chapter 5	194

Figures

- Figure 2.1** Proposed phase diagram of calcite, aragonite and vaterite at different pressures and temperatures (ALBRIGHT, 1971)..... 8
- Figure 2.2** The crystal structure of (A) calcite and (B) aragonite using the crystal systems described in Table 2.1; the green, grey and red spheres represent calcium, carbon and oxygen respectively, and the thin lines represent the unit cell edges 8
- Figure 2.3** Two proposed crystal structures of vaterite (A) orthorhombic (MEYER, 1960) and (B) hexagonal (Table 2.1; KAMHI, 1963); the black, grey and light grey spheres represent calcium, carbon and oxygen respectively, and the dashed boxes represent the unit cell edges 9
- Figure 2.4** Stereographic representation of the structure of ACC (GOODWIN et al., 2010), the calcium rich regions are represented with the red sticks and the carbonate rich regions are represented with the blue surfaces 10
- Figure 2.5** Computed Lippmann diagram from the calcite dolomite solid solution series (KULIK, 2006); χ_2 is the solid fraction and $\chi_{2,aq}$ is the aqueous fraction of dolomite and $\log\Sigma II$ is the total solubility/ion activity product of the corresponding calcite-dolomite solid solution/aqueous solution ($\Sigma II = aCO_3^{2-} \cdot [aCa^{2+} + (aCa^{2+})^{0.5} \cdot (aMg^{2+})^{0.5}]$), the lower solid curve represents the aqueous fraction of dolomite in equilibrium with a solid solution with a composition represented by the upper curve (e.g. the solid solutions in equilibrium with a solution with the chemical composition ($\chi_{2,aq}$) represented by the eutectic point (*E*) are represented by solids with a composition (χ_2) represented by *B1* and *B2*) the squares represent experimentally obtained solubility products, determined via stoichiometry dissolution (BISCHOFF et al., 1987) 15
- Figure 2.6** The effect of the incorporation of magnesium on the solubility product of calcite (BUSENBERG and PLUMMER, 1989), the figure includes data described by BISCHOFF et al. (1987) and MUCCI and MORSE (1984)..... 16
- Figure 2.7** Schematics of the exchange of carbonate (a) and sulfate (b) in the calcite structure highlighting the increase in the length of the c axis (*00l*) caused by this exchange (KONTREC et al., 2004)..... 18
- Figure 2.8** The effect of the incorporation of sulfate on the solubility product (*K*) of calcite (BUSENBERG and PLUMMER, 1989) 19

Figure 2.9 The effect of sulfate and the magnesium to calcium ratio in solution on the precipitation of calcite and aragonite as determined from seeded kinetic experiments; the curved lines represent the activities where calcite and aragonite formation kinetics are equal and the numbers along these lines represent the supersaturation (BURTON, 1993)	20
Figure 2.10 The effects of the concentration of bicarbonate on the magnesium incorporation into calcite (BURTON and WALTER, 1991)	22
Figure 2.11 Temperature versus calcium carbonate mineralogy; the black squares represent the situation when only calcite precipitates, the white squares represent the situation when only aragonite precipitates and the split squares show when calcite precipitates and due to a change in the magnesium to calcium ratio in solution, caused by the experimental set-up, the calcite is overgrown by aragonite (MORSE et al., 1997)	24
Figure 2.12 Evolution of seawater chemistry for major ions as predicted by HARDIE (1996).....	25
Figure 2.13 Chemical evolution of the magnesium (A) and calcium (B) concentration during the Phanerozoic as determined from halite fluid inclusions from: HORITA et al. (2002, dashed lines); the solid lines represent models from HARDIE (1996), STANLEY and HARDIE (1998), WALLMANN (2001) and WILKINSON and ALGEO (1989); figure reprinted from HORITA et al. (2002)	27
Figure 2.14 Chemical evolution of the sulfate concentration during the Phanerozoic as determined from halite fluid inclusions from: HORITA et al. (2002, dashed line); the solid line represents the model from HARDIE (1996); figure reprinted from HORITA et al. (2002).....	28
Figure 2.15 The distribution of the calcite and aragonite seas as determined by SANDBERG (1983)	30
Figure 3.1 Schematic representation of the constant addition experiments.....	36
Figure 3.2 Scanning Electron Microscope image of the glass beads used during the constant addition experiments	37
Figure 3.3 Schematic representation of a standard IC set-up	39
Figure 3.4 Graphic representation of the interactions of waves; 1) constructive interference and 2) destructive interference	41
Figure 3.5 Bragg diffraction represented by a schematic representation of two parallel incident beams diffracted by two planes; $\sin\theta = \frac{abd}{cad}$, so: $d\sin\theta = ab = ca$	41

Figure 3.6 Calcite example on Bragg diffraction, the calcite unit cell is shown from two different angles, with the dotted lines representing the edges of the unit cell, the green spheres represent calcium, the grey spheres represent carbon and the red spheres represent oxygen, the carbonate ions only partly in the unit cells have been completed for ease, the structural information by MARKGRAF AND REEDER (1985) is used to construct the figure; A) 3D representation of a calcite unit cell, the black parallelograms show where the (1 0 4) planes are in the unit cell (these planes have the highest diffraction intensity); B) a view of two unit cells along the b axis, the tilted black lines show where the (1 0 4) planes are in this view, the red arrows represent the diffracted (X-ray) beams and at the bottom a typical diffraction pattern of calcite (with 7 weight% Si standard) is shown ($2\theta < 2\theta < 50$)	43
Figure 3.7 Schematic representation of Diamond Light Source (www.diamond.ac.uk/Home/Technology.html)	46
Figure 3.8 Schematic representation of the <i>in situ</i> experimental set-up at the SAXS/WAXS beamline at station I22	47
Figure 3.9 Examples of idealized SAXS patterns of a system with spherical particles with a radius (<i>R</i>) (modified from: http://www.ansto.gov.au)	50
Figure 3.10 Graphical summary of all experimental conditions used in experiments performed at station I22 at Diamond Light Source	54
Figure 3.11 The chemical structure of Calmagite	58
Figure 3.12 The calibration curves for the first set of standard solutions tested.....	60
Figure 3.13 The calibration curves for the second set of standard solutions tested.....	62
Figure 3.14 The final calibration curves	63
Figure 3.15 Magnesium and calcium concentrations from a selection of constant addition experiments (chapter 4) measured with the photospectrometric method; the legend states the chemistry of the solution as added before starting the experiments.....	64
Figure 3.16 Chromatographs of the first test of the method to measure cations (A) a standard with: 2.5 ppm Na, 1 ppm Mg and 25 ppm Ca (B) a standard with: 10 ppm Na, 7.5 ppm Mg and 100 ppm Ca (C) a test sample from the constant addition experiments (chapter 4).....	65
Figure 3.17 Chromatographs of the second test of the method to measure cations (A) a standard with: 2.5 ppm Na, 1 ppm Mg and 25 ppm Ca (B) a standard with: 10 ppm Na, 7.5 ppm Mg and 100 ppm Ca (C) a test sample from the constant addition experiments (chapter 4).....	66

Figure 3.18 Chromatographs of the final method to measure the cation contents of dissolved calcium carbonate samples (A) a standard with: 2 ppm Na, 2 ppm Mg and 50 ppm Ca, (B) a standard with: 15 ppm Na, 15 ppm Mg and 200 ppm Ca (C) and (D) samples from the constant addition experiments (Table 4.1).....	67
Figure 3.19 Calibration curves from the final method to measure cation content of dissolved carbonate samples	68
Figure 3.20 Test on the analyses of cations in an unwashed foraminifera sample as a function of the mass of material weighed, the symbols represent the averages of three analyses on the same dissolution and the error bars represent the respective standard deviations	69
Figure 3.21 Column switching ion chromatography set-up used for the method to analyse anions in dissolved calcium carbonates, based on the method described by BRUNO et al. (2003).....	70
Figure 3.22 Test chromatographs of a standard with 50 ppm SO ₄ to determine the timing of the column switch (A) chromatograph of the 50 ppm standard using only the guard columns in the set-up (B) chromatograph of the 50 ppm standard using the guard columns and the switching valve (at 1 min) without the analytical column	71
Figure 3.23 Chromatographs of the test with the analytical column in line and with the column switch at 1 min. (A) a standard with 20 ppm SO ₄ (B) a standard with 50 ppm SO ₄ (C) a CaCO ₃ sample described in chapter 7	72
Figure 3.24 Two calibrations of the method to measure anions in dissolved calcium carbonate samples with the column switch at (A) 1 min. (Figure 3.23) (B) 0.85 min. (Figure 3.25); the red lines are the best fit for the calibration with the column switch at 0.85 min	72
Figure 3.25 Chromatographs of the final method with the analytical column in line and with the column switch at 0.85 min. (A) a standard with 20 ppm SO ₄ (B) a standard with 50 ppm SO ₄ (C) a CaCO ₃ sample described in chapter 7.....	73
Figure 3.26 Measurements on the amount of CAS in foraminiferal calcite, the black squares represent the average of 4 separate analyses on the amount of CAS using IC and the error bars represent the respective standard deviation, the red circles represent the amount of CAS determined using the gravimetric method (CLERC, 2007); multiple analyses with the same age were performed on different size fractions of the same sample	74

Figure 4.1 Polymorph distribution as a function of solution chemistry; closed symbols represent dominant CaCO₃ polymorph as measured in current study; open symbols represent previous research (DONER and PRATT, 1969, 26 °C; LEE and MORSE, 2010, 23 °C; MORSE et al., 1997, 20 °C; SIMKISS, 1964, 22 °C with an increase to 28 °C); diagonally shaded area highlights Mg/Ca and SO₄ field where calcite was present in solid phase after 48 h between 0% and 50%; horizontally shaded area represents proposed calcite sea concentrations (HORITA et al., 2002); and dashed horizontal line represents switch from KCl to MgSO₄ evaporites (LOWENSTEIN et al., 2003) as determined from PHREEQC evaporite simulations..... 80

Figure 4.2 Mg/Ca thresholds for 100% calcite, calcite dominance, and presence; error bars are estimated from Figure 1, and horizontally shaded area represents proposed calcite sea chemistry (HORITA et al., 2002). 83

Figure 4.3 FEG-SEM images of aragonite (a-c) and calcite (d-e) precipitated on glass spheres..... 86

Figure 5.1 (A) 3D representations of the time resolved WAXS patterns from the ‘no additive’ experiment (time is plotted on a base 2 log scale for clarity); (B) stacked time series of selected SAXS patterns from the ‘no additive’ experiment, with the legend showing time in minutes and the arrows illustrating the position of the peaks caused by the scattering from the growing vaterite crystallites 92

Figure 5.2 (A) α_{vaterite} and α_{ACC} vs. time (base 2 log scale) plot including a pH vs. time profile for the ACC to vaterite transformation for the ‘no additive’ experiment; (B) α_{vaterite} vs. time plots for the 1st stage of the crystallization of vaterite for all experiments with the best fit lines (see below) in green; (C) ACC nanoparticle and vaterite crystallite sizes derived from the SAXS data vs. time (on a time^{1/2} scale) for the ‘no additive’ and ‘replacement’ experiments; (D) detail of (C), showing ACC nanoparticle size vs. time (E) comparison of α_{vaterite} vs. time (base 2 log scale) of all three stages of all experiments; vertical lines and numbers in the figures (A) (C) and (E) represent the three different reaction stages..... 94

Figure 5.3 FEG-SEM images of solids quenched throughout the ‘no additive’ experiment; (A) 1 minute (B) 2 minutes (C) 35 minutes; the scale bar is 1 μm in the main images; the insets are enlargements of the dominant phase ((A) ACC and (B) and (C) vaterite) in the respective main image and the scale bar in the insets is 100 nm. 95

Figure 5.4 The slope of the Porod region ($I(q) \propto q^{-p}$) calculated from the SAXS patterns for the ‘no additive’ and ‘replacement’ experiments as a function of time (on a base 2 log scale) 96

Figure 5.5 Evolution of the solution composition with time (base 2 log scale); (A) calcium and (B) sulfate; the black vertical lines and numbers in both figures indicate the different reaction stages and the errors bars represent the standard deviation of three measurements 97

- Figure 5.6** The evolution of the saturation indices vs. time (base 2 log scale) for the “no additive” system (based on PHREEQC calculations, further summarized in Appendix B); the vertical lines separate the three stages of the transformation reaction; not plotted is the *SI* for the initial solution (prior to ACC precipitation), which was ~4.2 (Table S1), calculated based on $K_{sp,vaterite} = 10^{-7.74}$ (PLUMMER and BUSENBERG, 1982), the horizontal line represents the relative supersaturation (σ) of 5 ($\sigma = \sqrt{(Ca^{2+}CO_3^{2-})/K_{sp,vaterite}}$) (ANDREASSEN, 2005) 100
- Figure 5.7** Schematic representation of the proposed multi stage ACC → Vaterite → Calcite crystallization pathway (top) with the underlying combined reaction progress, α_{ACC} , $\alpha_{vaterite}$ and $\alpha_{calcite}$ for the full crystallization reaction in the ‘no additive’ system (the green triangles and full black squares represent the ACC and vaterite from this study and the open squares and red triangles represent the vaterite and calcite from RODRIGUEZ-BLANCO et al. (2011)) , stages 1, 2 and 3 of the reaction mechanism are labeled on the figure..... 105
- Figure 6.1** (A) 3D plot of the time resolved WAXS patterns with time on a base 2 log scale and (B) averaged WAXS patterns over 4 time intervals from the ‘replacement’ experiment; the position of the main peaks for gypsum, rapidcreekite and vaterite are labelled with G, Rc and V, respectively 112
- Figure 6.2** $\alpha(t)$ plots for vaterite, gypsum and rapidcreekite from the ‘replacement’ experiment (A) $\alpha(t)$ calculated using Eq. 6.1 and 6.2; (B) and (C): $\alpha(t)$ recalculated to the mole % of crystalline phases in the system using Eq. 6.3, including the sum of mole % of (B) gypsum and rapidcreekite and (C) vaterite and rapidcreekite 113
- Figure 6.3** The pH and $\alpha(t)$ for gypsum (Figure 6.2A) during the ‘replacement’ experiment..... 114
- Figure 6.4** $\alpha(t)$ plots for vaterite, gypsum and rapidcreekite from the ‘additive’ experiment (A) $\alpha(t)$ calculated using Eq. 6.1 and 6.2; (B) and (C): $\alpha(t)$ recalculated to the mole % of crystalline phases in the system using Eq. 6.3, including the sum of mole % of (B) gypsum and rapidcreekite and (C) vaterite and rapidcreekite 117
- Figure 6.5** $\alpha(t)$ plots for vaterite, calcite, gypsum and rapidcreekite from the ‘additive-Mg’ experiment (A) $\alpha(t)$ calculated using Eq. 6.1 and 6.2; (B) and (C): $\alpha(t)$ recalculated to the mole % of crystalline phases in the system using Eq. 6.3, including the sum of mole % of (B) gypsum and rapidcreekite and (C) vaterite and rapidcreekite..... 118
- Figure 6.6** $\alpha(t)$ for the initial stage of vaterite formation in the ‘replacement’, ‘additive’ and ‘additive-Mg’ experiments with the JMAK fits superimposed 121
- Figure 7.1** Stacked XRD patterns showing the effect of SO_4/CO_3 on the formation of calcium carbonate; the legend represents the initial SO_4/CO_3 ratio and the calculated weight percentage of calcite 129

Figure 7.2 Stacked XRD patterns from five repeats of experiment 5 ($\text{SO}_4/\text{CO}_3 = 25$); the legend represents the time after mixing that the solid sample was separated from solution and the patterns show the development of only vaterite Bragg peaks	130
Figure 7.3 pH evolution during experiment 5 ($\text{SO}_4/\text{CO}_3 = 25$, Table 7.1), including the saturation index with respect to vaterite (SI_{vaterite}) as calculated using PHREEQC, assuming no CO_2 exchange with the atmosphere (PARKHURST and APPELO, 1999), the arrow represents the inflection point (OGINO et al., 1987), the dotted horizontal line represents the SI_{vaterite} required for spherulitic growth and the solid horizontal line represents the ‘solubility’ of vaterite if no CO_2 exchange with the atmosphere occurred.....	130
Figure 7.4 HR-XRD pattern of the ‘4% SO_4 vaterite’ in blue (measured with a $\lambda = 0.826404 \text{ \AA}$), fitted vaterite pattern using the structural model by KAMHI et al. (1963) in red and the difference plot in grey; a selection of the Miller indices are shown above the corresponding Bragg peaks	132
Figure 7.5 XANES spectrum at the Ca K-edge from the vaterite from experiment ‘4% SO_4 vaterite’, including a calcite and aragonite standard	134
Figure 7.6 Polymorph distribution vs. time during all vaterite ripening experiments; the legend represents the SO_4 and Mg concentration in solution as described in Table 7.2	135
Figure 7.7 The Ca (A) and SO_4 (B) concentration in the ageing experiments without SO_4 present in the initial solutions; the legend represents the Mg concentration in solution as described in Table 7.2, the numbering in (B) represents the experiment number as listed in Table 7.2 and the error bars represent the standard deviation from triplicate measurements	135

Tables

Table 2.1 Mineralogical and solubility information for known calcium carbonate phases; *the hexagonal crystal system described by KAMHI (1963) is listed in this table because this crystal system is most widely used in the literature (TANG et al., 2009)	7
Table 3.1 Table listing the fractal properties of scatterers (SCHMIDT, 1991) and relating these to the Porod slope, D is the fractal dimension, D_m is the mass fractal dimension, D_s is the surface fractal dimension and p is the Porod slope (Figure 3.9).....	53
Table 3.2 The first 29 lines of the input file for the PHREEQC simulations to model the chemical evolution during the SAXS/WAXS experiments, the example here is for the ‘replacement’ experiment described in chapter 5.....	57
Table 3.3 Concentrations of the first set of standard solutions tested including the respective absorbance measurements; the measured absorbance is for the solution with calmagite and EDTA (1), calmagite and EGTA (2) and only calmagite (3)	59
Table 3.4 Concentrations in second set of standard solutions tested including the respective adsorbance measurements; the measured absorbance is for the solution with calmagite and EDTA (1), calmagite and EGTA (2) and only calmagite (3)	61
Table 3.5 Concentrations in final set of standard solutions tested tested including the respective adsorbance measurements; the measured absorbance is for the solution with calmagite and EDTA (1), calmagite and EGTA (2) and only calmagite (3)	63
Table 4.1 Summary of the CaCO₃ mineralogy and composition from the constant addition experiments	79
Table 5.1 Summary of the experimental conditions for all experiments	90
Table 5.2 The kinetic constant (k) and the induction time (t_0) derived from the α data for vaterite to the JMAK model using an Avrami exponent (n) of 4 (Eq. 5.1)	100
Table 6.1 Summary of the experimental conditions for all experiments	109
Table 6.2 Extract from Table D.1 on the solution chemistry prior to the formation of vaterite, from the results of experiments described in chapter 5 with no additive or 10% SO₄ in the initial carbonate solution instead of 30% (‘no additive’, ‘replacement (10%)’ and ‘additive (10%)’)	115
Table 6.3 JMAK fitted parameters (with $n = 4$) for the spherulitic growth of vaterite; including a reproduction of the fitted parameters from the experiments described in chapter 5 and Table 5.2 (‘no additive’, ‘replacement (10%)’ and ‘additive (10%)’) for comparison	122

Table 7.1 Summary of the solutions used for the formation experiments	127
Table 7.2 Solution chemistry of the ageing experiments	128
Table 7.3 Summary of the Rietveld refinement on the HR-XRD pattern of the '4%SO₄ vaterite'; *the Rietveld refinement using the structural model from MEYER (1969) did not result in a fit, hence this structural model was fitted with performing a Le Bail refinement resulting in a low R_{Bragg}.....	133

Chapter 1

Introduction

1.1 Background information

Calcium carbonate minerals (calcite, aragonite and vaterite) have been observed in many environments throughout geological history (MORSE and MACKENZIE, 1990). They can form inorganically in many marine and alkaline fresh water environments and are also the most abundant biologically formed minerals (biominerals) (CUSACK and FREER, 2008; LOWENSTAM, 1981; MELDRUM and CÖLFEN, 2008; WEINER and DOVE, 2003). Due to their inorganic and biological abundance, calcium carbonate minerals play an important role in the global calcium and carbon biogeochemical cycles (MORSE and MACKENZIE, 1990). Additionally, calcium carbonate phases with specific properties are also important products in many industrial processes (MELDRUM and CÖLFEN, 2008).

The formation and mineralogy of calcium carbonate phases has been shown to vary concurrently with changing solution chemistry (e.g. composition and pH) (e.g. BUSENBERG and PLUMMER, 1985; BUSENBERG and PLUMMER, 1989; GEBAUER et al., 2010; LAM et al., 2007; MORSE et al., 1997) and physical properties (e.g. temperature) (e.g. BURTON and WALTER, 1987; MORSE et al., 1997). During the formation of calcium carbonate minerals, organic and inorganic ions present in solution (in addition to calcium and carbonate) may adsorb onto surfaces and incorporate into the structure (e.g. DAVIS et al., 2000; MUCCI and MORSE, 1985). The adsorption and incorporation of such ions varies with concentration, pH and temperature, causing changes in the crystallinity, composition, morphology and the dominant calcium carbonate polymorph (e.g. BURTON and WALTER, 1987; LEE and MORSE, 2010; MORSE et al., 1997). Due to these processes, calcium carbonate minerals record the chemical and physical condition of the formation environments and are thus widely used as paleoproxies to reconstruct past ocean conditions (e.g. Phanerozoic seawater composition and temperature; the last ~550 million years) (CUSACK and FREER, 2008). Two main paleoproxies often used to reconstruct the

past seawater chemistry and the temperature are trace element composition (e.g. Mg/Ca, Sr etc.) (CUSACK and FREER, 2008; OKAFOR et al., 2009; de VILLIERS et al., 2002; Yu et al., 2005) and isotopic composition (C, O, S) (GILL et al., 2007; GILL et al., 2011; KAH et al., 2004; NEWTON et al., 2011; PAYTAN et al., 1998; PAYTAN et al., 2004; WORTMANN and CHERNYAVSKY, 2007).

The use of paleoproxy data in combination with information on the composition of evaporite fluid inclusions has helped to understand the chemical evolution of the Phanerozoic seawater (HORITA et al., 2002; KOVALEVICH et al., 1998; LOWENSTEIN et al., 2003; LOWENSTEIN et al., 2001; TIMOFEEFF et al., 2006; ZIMMERMANN, 2000). This revealed that the chemical composition of Phanerozoic seawater oscillated between calcium chloride rich and magnesium sulfate rich (HORITA et al., 2002). However, the exact magnitudes of the seawater compositional oscillations are still debated due to the lack of any unaltered ancient seawater samples. It is however known that during the Phanerozoic, the seawater composition caused the dominant primary (abiotic) calcium carbonate phase to oscillate between calcite and aragonite (HARDIE, 1996; LOWENSTEIN et al., 2003; SANDBERG, 1983). These calcite and aragonite dominant periods are now known as calcite and aragonite seas (SANDBERG, 1983). The main control on the oscillation between calcite and aragonite seas is believed to be the seawater magnesium to calcium ratio (MORSE et al., 1997; STANLEY, 2006). At low magnesium to calcium ratios (< 1~2), calcite formation is dominant, while at higher magnesium to calcium ratios and aragonite formation becomes dominant. However, the sulfate concentration also oscillated concurrent to oscillations of the magnesium to calcium ratio in seawater during the Phanerozoic (HORITA et al., 2002). This suggests that the sulfate concentration in addition to the magnesium to calcium ratio might be an important factor influencing the formation of calcite and aragonite (RAILSBACK and ANDERSON, 1987). However, the control of sulfate on the oscillations between the calcite and aragonite seas has so far largely been overlooked (LEE and MORSE, 2010).

In addition to affecting the primary calcium carbonate mineralogy, oscillations in the seawater composition have also influenced the dominant calcium carbonate minerals formed by organisms (KNOLL, 2003; MARTIN, 1995; PORTER, 2007; PORTER, 2010). Organisms usually form the calcium carbonate phase most thermodynamically stable at the time of origin; they rarely deviate from this,

following changes in seawater composition (PORTER, 2007; PORTER, 2010). This is further complicated by the recognition that many organisms utilize amorphous calcium carbonate (ACC) to control the morphology, mineralogy and physical properties of their final crystalline products (MELDRUM and CÖLFEN, 2008; WEINER and DOVE, 2003). Organisms can exert control on ACC crystallization (e.g. to calcite or aragonite) through, for example, directing the crystallization process by using proteins or other organic molecules to act as a crystallization template (e.g. POUGET et al., 2009). ACC crystallization processes that occur during biomineralization have also informed many (industrial) biomimetic processes, for example, in dyestuff pigment synthesis (GOWER, 2008; MELDRUM and CÖLFEN, 2008). ACC is unstable and rapidly crystallizes to calcite, aragonite or vaterite (NJEJIC-DZAKULA et al., 2010; GEBAUER et al., 2010; OGINO et al., 1987; RODRIGUEZ-BLANCO et al., 2011). Several mechanisms have been proposed for abiotic ACC crystallization. It is thought to occur via initial dehydration of ACC (RODRIGUEZ-BLANCO et al., 2011), which is followed by either a solid state (POUGET et al., 2010) or a solution mediated crystallization mechanism (ANDREASSEN, 2005; SHEN et al., 2006; STÁVEK et al., 1992; VACASSY et al., 2000). The exact mechanisms of inorganic ACC crystallization are not yet clear due to the inherent instability of ACC and the rapid kinetics of crystallization.

Even though various effects of changes in solution chemistry (e.g. pH and composition) on the formation, transformation and structure of calcium carbonate phases, have been studied widely, the effect of aqueous sulfate (in combination with that of magnesium) on these processes have so far not been quantified. Additionally, studies have proposed several mechanisms of ACC crystallization, but a clear picture of the fundamental processes (and their relation to biomineralization and biomimetic processes) is still lacking.

1.2 Research objectives

Hence, the research objectives of this project were to determine the effects of sulfate (in combination with magnesium) on the formation, transformation and mineralogy of calcium carbonate phases and additionally to relate these processes to

the formation of calcium carbonate phases in natural environments and during biomineralization. The research objectives can be divided into three main areas:

- (1) To determine the chemical controls on the occurrence of calcite and aragonite seas during the Phanerozoic by examining how the solution composition (i.e. sulfate and magnesium) affects the formation and stability of calcium carbonate polymorphs.
- (2) To determine the abiotic mechanism of ACC crystallization and how sulfate affects this process.
- (3) To determine how and why the thermodynamically metastable calcium carbonate phase, vaterite, can be synthesized and stabilized using sulfate.

1.3 Experimental approaches

All research approaches are described in detail in chapter 3. A brief overview is given in this section to highlight the novelty of the approaches used in this thesis.

Solution based constant addition crystallization experiments were performed to determine the effects of variations in solution composition (i.e. magnesium and sulfate) on the calcium carbonate polymorph that precipitated. This was done by performing controlled, constant addition batch experiments, where heterogeneous nucleation of calcium carbonate was induced on glass spheres (to mimic oöid formation) and only the magnesium and sulfate concentrations were varied. Both, the variations in solution composition and the variations in the calcium carbonate solids that precipitated were analysed for their chemical composition and mineralogy to quantify the role and effects of the solution composition.

In a second set of experiments, the crystallization of ACC was followed by homogeneous precipitation experiments. These experiments were performed at high initial supersaturation to be able to follow the crystallization reaction *in situ* using synchrotron based scattering techniques. The results from these *in situ* experiments were combined with off-line characterization of the solid phases and solution composition to derive the crystallization kinetics and mechanisms. Additionally, the

sulfate concentration was varied to quantify the influence of sulfate on the crystallization kinetics and mechanisms.

Finally, in a second set of homogeneous precipitation experiments, the effect of sulfate on the nucleation and growth of vaterite was investigated using varying sulfate concentrations during the experiments. Furthermore, room temperature aging in solution was used to quantify the conditions under which vaterite can be stabilized. To determine the effect of sulfate on the structure and stability of vaterite, a variety of structural and chemical analytical tools were used.

1.4 Thesis outline

This thesis consists of eight chapters. This introductory chapter 1 is followed by chapter 2, which provides an overview of the literature on the effects of solution chemistry on calcium carbonate formation, transformation and mineralogy and summarizes the known occurrence of calcium carbonate minerals throughout the geological history. Chapter 3 contains a detailed description of all experimental and analytical methods (including the development of two analytical methods) used during this PhD project. This is followed by four results chapters. Chapter 4 describes the influence of aqueous sulfate and magnesium on calcium carbonate formation and mineralogy, and the relation to Phanerozoic seawater composition. Chapter 5 and 6 describe the mechanisms of ACC crystallization in the absence and presence, respectively, of increasing sulfate concentrations. Chapter 7 describes the formation, stability and structure of vaterite formed in the presence of aqueous sulfate. Finally, the results from chapter 4 to 7 are summarized and discussed in chapter 8.

Chapter 2

Literature review

This chapter summarizes the literature on the influences of the solution composition on calcium carbonate formation and mineralogy. Additionally, the literature on the Phanerozoic seawater chemistry and biomineralization are summarized. This chapter is divided into 5 sections:

- (1) Calcium carbonate mineralogy
- (2) Amorphous Calcium Carbonate (ACC) crystallization
- (3) The influences of solution chemistry on the formation of calcium carbonate phases
- (4) The Phanerozoic seawater composition and the dominant calcium carbonate mineralogy formed during the Phanerozoic
- (5) Biomineralization

2.1 CaCO₃ mineralogy

The two most dominant anhydrous CaCO₃ minerals that occur in nature are calcite and aragonite, which have a rhombohedral and orthorhombic crystal system, respectively (Table 2.1, DE VILLIERS, 1971; MARKGRAF and REEDER, 1985). A third, rare, anhydrous CaCO₃ mineral that can occur in nature is vaterite. Several refinements have determined that vaterite has either a hexagonal or orthorhombic crystal system (KAMHI, 1963; LE BAIL et al., 2011; MEDEIROS et al., 2007; MEYER, 1960; MEYER, 1969; WANG and BECKER, 2009). From the three anhydrous minerals, calcite is most stable under ambient conditions and vaterite is least stable (PLUMMER and BUSENBERG, 1982). Aragonite is most stable at high pressure and low temperature while vaterite is thought to be stable at low temperature and pressure (Figure 2.1, ALBRIGHT, 1971). The structure of calcite is characterized by layers of alternating 6-fold coordinated calcium ions with layers of carbonate ions (Figure 2.2A, GRAF, 1961; MARKGRAF and REEDER, 1985). In comparison, dolomite (Ca_{0.5}Mg_{0.5}CO₃) has the same crystal system as calcite and alternating layers of calcium (and magnesium) and carbonate ions. However, in dolomite every second

calcium layer is exchanged for a magnesium layer (ALTHOFF, 1977). The structure of aragonite resembles a hexagonal close packed structure, where the calcium ions are 9-fold coordinated (Figure 2.2B, DE VILLIERS, 1971). Hence, the aragonite structure is more dense compared to the calcite structure (APPELO and POSTMA, 2005). In contrast, vaterite has a less dense structure compared to calcite and aragonite. However, the exact nature to the vaterite crystal system is still debated. The calcium ions in the vaterite structure have been determined to be either 6 or 8-fold coordinated in a hexagonal sub-lattice (Figure 2.3, KAMHI, 1963; LE BAIL et al., 2011; MEYER, 1960; MEYER, 1969) with carbonate planes aligned roughly parallel to the c-axis (Figure 2.3, KAMHI, 1963; MEYER, 1960; MEYER, 1969). However, the carbonate ions in the vaterite structure have a high degree of disorder (LE BAIL et al., 2011; MEDEIROS et al., 2007; MEYER, 1969; WANG and BECKER, 2009).

Table 2.1 Mineralogical and solubility information for known calcium carbonate phases; *the hexagonal crystal system described by KAMHI (1963) is listed in this table because this crystal system is most widely used in the literature (TANG et al., 2009)

Mineral name	Chemical formula	Crystal system	Crystal system (Å)	Reference	-log K_{sp} (at 25°C)	Reference
Dolomite	$\text{Ca}_{0.5}\text{Mg}_{0.5}\text{CO}_3$	Rhombohedral	a = 4.8079 c = 16.010	(GRAF, 1961)	8.55	(APPELO and POSTMA, 2005)
Calcite	CaCO_3	Rhombohedral	a = 4.9900 c = 17.061	(GRAF, 1961)	8.48	(PLUMMER and BUSENBERG, 1982)
Aragonite	CaCO_3	Orthorhombic	a = 4.9614 b = 7.9671 c = 5.7404	(DE VILLIERS, 1971)	8.34	(PLUMMER and BUSENBERG, 1982)
Vaterite*	CaCO_3	Hexagonal	a = 4.13 c = 8.49	(KAMHI, 1963)	7.73	(PLUMMER and BUSENBERG, 1982)
Monohydrocalcite	$\text{CaCO}_3 \cdot \text{H}_2\text{O}$	Hexagonal	a = 10.5547 c = 7.5644	(SWAINSON, 2008)	7.6	(HULL and TURNBULL, 1973)
Ikaite	$\text{CaCO}_3 \cdot 6\text{H}_2\text{O}$	Monoclinic	a = 8.8053 b = 8.3138 c = 11.0328 $\beta = 110.598$	(LENNIE et al., 2004)	6.59	(BISCHOFF et al., 1993)
ACC	$\text{CaCO}_3 \cdot 0-1.6\text{H}_2\text{O}$	Amorphous	-	(RADHA et al., 2010)	6.40	(BREČEVIĆ and NIELSEN, 1989)

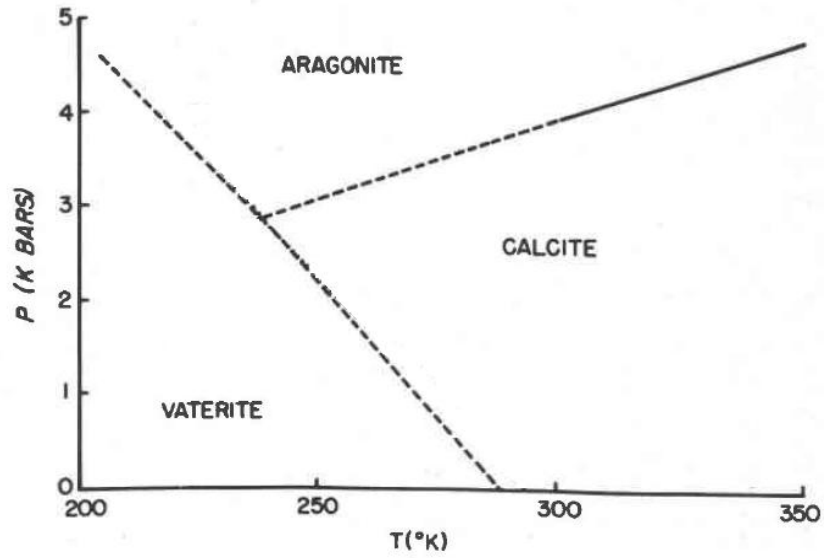


Figure 2.1 Proposed phase diagram of calcite, aragonite and vaterite at different pressures and temperatures (ALBRIGHT, 1971)

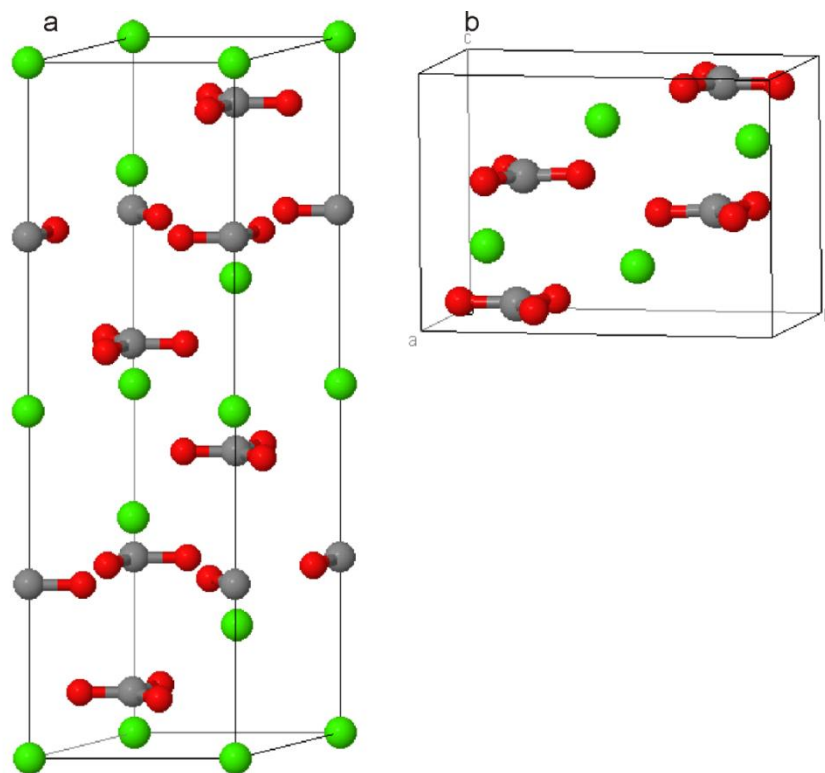


Figure 2.2 The crystal structure of (A) calcite and (B) aragonite using the crystal systems described in Table 2.1; the green, grey and red spheres represent calcium, carbon and oxygen respectively, and the thin lines represent the unit cell edges

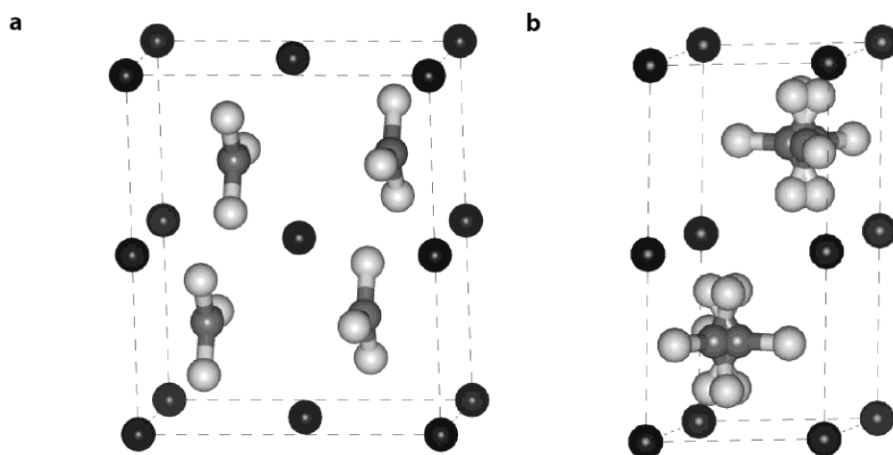


Figure 2.3 Two proposed crystal structures of vaterite (A) orthorhombic (MEYER, 1960) and (B) hexagonal (Table 2.1; KAMHI, 1963); the black, grey and light grey spheres represent calcium, carbon and oxygen respectively, and the dashed boxes represent the unit cell edges

In addition to the three anhydrous minerals, two less stable hydrated calcium carbonate minerals can form in nature. These are monohydrocalcite (hexagonal $\text{CaCO}_3 \cdot \text{H}_2\text{O}$) and ikaite (monoclinic $\text{CaCO}_3 \cdot 6\text{H}_2\text{O}$). The monohydrocalcite structure is characterized by screw axes (parallel to the c-axis) of carbonate and 8-fold coordinated calcium ions. Additionally, structural water is situated in between the screw axes and bound to the carbonate ions via hydrogen bridges (SWAINSON, 2008). Monohydrocalcite is thought to be metastable under all conditions (HULL and TURNBULL, 1973). However, monohydrocalcite does form in some (predominantly freshwater) environments (DAHL and BUCHARDT, 2006). The structure of ikaite is characterized by hydrated calcium carbonate chains, which are aligned along the a-axis. The hydrated calcium carbonate chains are linked together by hydrogen bonds and the calcium ions are 8-fold coordinated (LENNIE et al., 2004). Ikaite has been determined to be stable at high pressure and low temperatures in an alkaline aqueous environment (BISCHOFF et al., 1993; MARLAND, 1975; SHAHAR et al., 2005) and has been observed in bottom waters in fjords and on deep sea floors (JANSEN et al., 1987).

Finally, the least stable calcium carbonate phase that has been identified is amorphous calcium carbonate (ACC). Research suggested that nanoparticulate ACC preferentially forms over nanoparticulate crystalline calcium carbonate phases due to a low energetic barrier for ACC nucleation and growth (RAITERI and GALE, 2010;

TRIBELLO et al., 2009). However, in nature, ACC has so far predominantly been identified as an intermediate phase during biomineralization (ADDADI et al., 2003; CUSACK and FREER, 2008; MELDRUM and CÖLFEN, 2008; WEINER and DOVE, 2003, see also Section 2.5). Structural characterization of ACC indicates that this phase has no long range (>15 Å) order (GOODWIN et al., 2010; MICHEL et al., 2008; QUIGLEY and RODGER, 2008) and is characterized by calcium rich and carbonate rich regions (Figure 2.4, GOODWIN et al., 2010). The short range order (<15 Å) resembles the short range order of either one or multiple crystalline calcium carbonate phases (GEBAUER et al., 2010; LAM et al., 2007; TRIBELLO et al., 2009). Finally, the short range order and stability depend on the synthesis method (e.g.: pH and Mg, GEBAUER et al., 2010; LAM et al., 2007), the organic versus inorganic origin (RADHA et al., 2010) and the hydration of the ACC phase (RADHA et al., 2010).

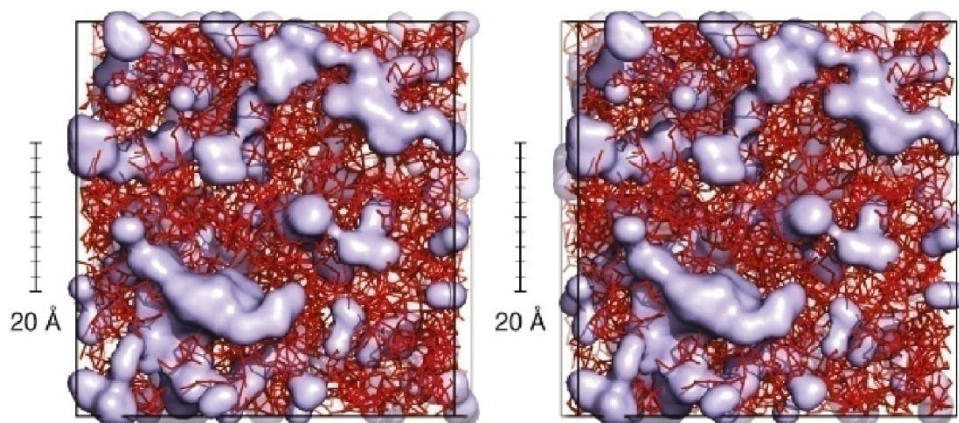


Figure 2.4 Stereographic representation of the structure of ACC (GOODWIN et al., 2010), the calcium rich regions are represented with the red sticks and the carbonate rich regions are represented with the blue surfaces

2.2 ACC crystallization

In general, in solutions highly supersaturated with respect to the crystalline calcium carbonate phases, the first phase that forms is ACC (NJEGIC-DZAKULA et al., 2010; OGINO et al., 1987; RODRIGUEZ-BLANCO et al., 2011). Furthermore, RADHA et al. (2010) calculated the formation enthalpy of several different ACC phases (with different origins and different amounts of structural water) in relation

to the crystalline calcium carbonates. They showed that energetically the sequence of increasing stability and therefore the crystallization pathway (according to the Ostwald step rule, VAN SANTEN, 1984) should be as follows: disordered, hydrated ACC → less disordered, less hydrated ACC → anhydrous ACC → vaterite → aragonite → calcite (RADHA et al., 2010). This sequence shows that ACC can act as a precursor to any of the anhydrous crystalline phases.

ACC crystallization is thought to be initiated by destabilizing ACC due to particle growth (RAITERI and GALE, 2010). Depending on the mode of ACC formation (e.g. pH, additive and T), ACC can initially transform to all three anhydrous calcium carbonate polymorphs (calcite, aragonite and vaterite, GEBAUER et al., 2010; OGINO et al., 1987; RODRIGUEZ-BLANCO et al., in press). In inorganic systems, ACC crystallization often proceeds via the formation of transient vaterite (ANDREASSEN, 2005; POUGET et al., 2010; RODRIGUEZ-BLANCO et al., 2011). The crystallization of ACC to vaterite generally occurs in seconds to minutes (RODRIGUEZ-BLANCO et al., 2011). To date, several different mechanisms for the ACC crystallization to vaterite transformation have been proposed. Many studies suggested that ACC dissolves and vaterite spheres form via homogeneous nucleation of nanocrystalline vaterite particles, followed by fast aggregation to form μm sized polycrystalline spheres (SHEN et al., 2006; STÁVEK et al., 1992; VACASSY et al., 2000). A solid state mechanism for the ACC to vaterite crystallization has also been proposed, with the ACC particles dehydrating and recrystallizing to form vaterite (POUGET et al., 2010). Finally, a study based on imaging of inorganically precipitated vaterite, suggested that vaterite forms via ACC dissolution coupled to spherulitic growth (ANDREASSEN, 2005). After vaterite is fully formed, vaterite generally transforms to the most stable calcium carbonate polymorph, calcite. The mechanism of this latter crystallization stage (to stable calcite) has been shown to proceed via the dissolution of vaterite and precipitation of calcite, with the rate of transformation controlled by the surface area of calcite (OGINO et al., 1990; RODRIGUEZ-BLANCO et al., 2011).

2.3 Chemical factors influencing the precipitation and stability of CaCO_3

In order to understand the influence of the chemical composition on the formation and stability of CaCO_3 phases, the basic precipitation and dissolution reactions of these phases need to be understood. Eq. 2.1 shows the most common and elemental dissolution/precipitation reaction. The chemical solubility product (K_{sp}) is derived from this reaction equation (Eq 2.2, APPELO and POSTMA, 2005; DREVER, 1997).

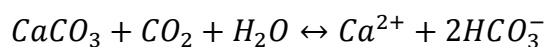


(Eq. 2.1)

$$K_{sp} = a_{\text{Ca}^{2+}} a_{\text{CO}_3^{2-}}$$

(Eq. 2.2)

In Eq. 2.2, a represents the aqueous activity of the chemical species in the subscript. When CaCO_3 dissolves in environments with a pH less than ~ 10.3 (i.e. $a_{\text{CO}_3^{2-}} < a_{\text{HCO}_3^-}$), the released carbonate (Eq. 2.1) will react with H^+ to form bicarbonate (APPELO and POSTMA, 2005). This increases the pH of the system and decrease the amount of aqueous CO_2 , resulting in an average dissolution/precipitation reaction as shown in Eq. 2.3.

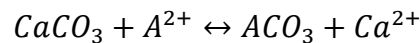


(Eq. 2.3)

Eq. 2.3 represents the average stoichiometry better as most natural systems have a

pH less than 9. Eq. 2.3 indicates that when CO₂ levels increase, calcium carbonate will dissolve. Dissolution and precipitation is thus able to (partly) buffer the CO₂ concentration (Eq. 2.3, ARVIDSON et al., 2006a). In addition to the calcium and carbonate chemistry (Eq. 2.1 and 2.3), the presence of other ions can alter calcium carbonate formation (and dissolution) processes (BISCHOFF, 1968; BISCHOFF and FYFE, 1968; BURTON and WALTER, 1987; DAVIS et al., 2000; RUIZ-AGUDO et al., 2009; WALTER, 1986). This is thought to occur via the adsorption of these ions onto growth sites (DAVIS et al., 2000; MEYER, 1984) and by changing the stability of the phase due to incorporation (DAVIS et al., 2000; SHTUKENBERG et al., 2006).

Incorporation of ions besides calcium and carbonate causes the formation of a solid solution. In general, the chemical composition of a solid solution reflects the solution chemistry (DOERNER and HOSKINS, 1925; HENDERSON and KRACEK, 1927; MORSE and BENDER, 1990). The chemical reaction described in Eq. 2.4 was used to describe the solid solution: (Ca,A)CO₃ (where A represents a second divalent cation) in equilibrium with a specific solution chemistry. From Eq. 2.4, the distribution coefficient ($D_{A/Ca}$), for the incorporation of cations into calcium carbonate, can be calculated (Eq. 2.5).



(Eq. 2.4)

$$D_{A/Ca} = \frac{X_{ACO_3} / X_{CaCO_3}}{m_{A^{2+}} / m_{Ca^{2+}}}$$

(Eq. 2.5)

In Eq. 2.5, X denotes the fraction of the solid species in the subscript and m denotes the molarity of the aqueous species in the subscript. The distribution coefficient describes the relation between a solid solution and an aqueous solution (DOERNER and HOSKINS, 1925; HENDERSON and KRACEK, 1927; MORSE and BENDER, 1990).

Although the distribution coefficient was initially thought to be constant, it is now clear that many thermodynamic and kinetic factors influence the distribution

coefficient (BUSENBERG and PLUMMER, 1985; BUSENBERG and PLUMMER, 1989; KULIK et al., 2010; MUCCI, 1986; MUCCI and MORSE, 1983; PRIETO et al., 2000; TESORIERO and PANKOW, 1996). At thermodynamic equilibrium, the distribution coefficient is governed by the activity of the solid species (GLYNN, 2000; GLYNN and REARDON, 1990; PRIETO, 2009) and the stability of the solid solution with respect to the chemical composition of the aqueous solution (GAMSJÄGER et al., 2000; KORNIKER et al., 1991; KULIK, 2006; KULIK et al., 2010). The thermodynamic equilibrium between a solid solution and aqueous solution can be represented with a Lippmann diagram (GAMSJÄGER et al., 2000; GLYNN, 2000; KULIK, 2006; KULIK et al., 2010; PRIETO, 2009; SHTUKENBERG et al., 2006). Figure 2.5 shows an example of a Lippmann diagram, representing the solid solution – aqueous solution series between calcite and dolomite (KULIK, 2006). The horizontal axis represents the solid (χ_2) and solution ($\chi_{2, \text{aq}}$) fraction of dolomite (Figure 2.5). The vertical axis represents the total solubility of the solid solution and the ion activity product of the solution chemistry in equilibrium with the respective solid solution (Figure 2.5). However, thermodynamic equilibrium is rarely reached in natural systems (DE YOREO et al., 2009; SHTUKENBERG et al., 2006).

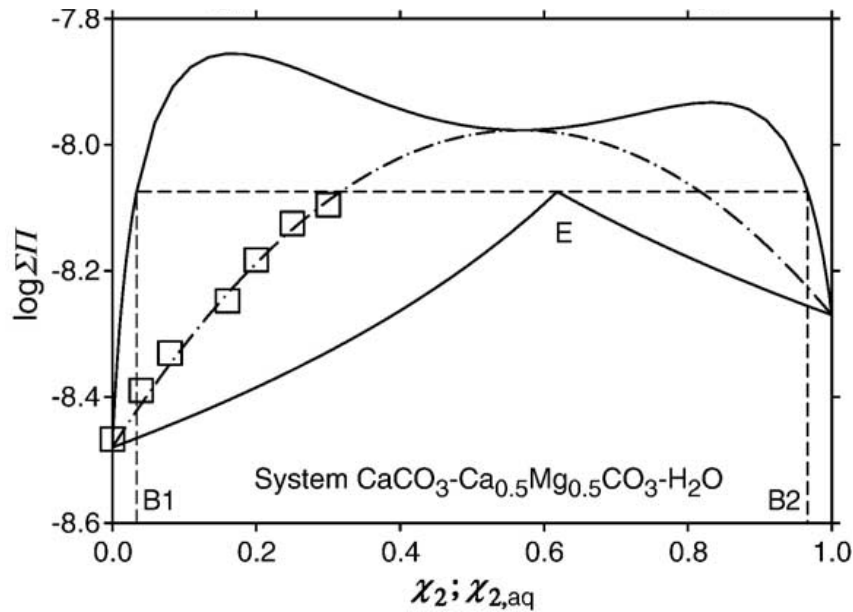


Figure 2.5 Computed Lippmann diagram from the calcite dolomite solid solution series (KULIK, 2006); χ_2 is the solid fraction and $\chi_{2,aq}$ is the aqueous fraction of dolomite and $\log \Sigma II$ is the total solubility/ion activity product of the corresponding calcite-dolomite solid solution/aqueous solution ($\Sigma \Pi = a_{\text{CO}_3^{2-}} \cdot [a_{\text{Ca}^{2+}} + (a_{\text{Ca}^{2+}})^{0.5} \cdot (a_{\text{Mg}^{2+}})^{0.5}]$), the lower solid curve represents the aqueous fraction of dolomite in equilibrium with a solid solution with a composition represented by the upper curve (e.g. the solid solutions in equilibrium with a solution with the chemical composition ($\chi_{2,aq}$) represented by the eutectic point (E) are represented by solids with a composition (χ_2) represented by $B1$ and $B2$) the squares represent experimentally obtained solubility products, determined via stoichiometry dissolution (BISCHOFF et al., 1987)

2.3.1 Magnesium

In the presence of magnesium in solution, calcium in the calcite structure can be exchanged for magnesium (Figure 2.5). The incorporation of magnesium into calcite can be expressed as a function of the aqueous magnesium to calcium ratio as described in Eq. 2.4. Calcite with magnesium incorporated is also called magnesian calcite (APPELO and POSTMA, 2005; MORSE and MACKENZIE, 1990; PAQUETTE and REEDER, 1990; STANLEY, 2006; WALTER and MORSE, 1984). The distribution coefficient for magnesium varies with, for example, the growth rate and the magnesium and calcium concentrations (BERNER, 1978; BURTON and WALTER, 1991; BUSENBERG and PLUMMER, 1989; DE YOREO et al., 2009; MORSE et al., 2007; MORSE and BENDER, 1990; MUCCI and MORSE, 1983). Many studies have shown that the incorporation of magnesium into calcite reduces the thermodynamic stability

and increases the solubility of (magnesian) calcite (Figure 2.6, BUSENBERG and PLUMMER, 1989; DAVIS et al., 2000; KÖNIGSBERGER and GAMSJÄGER, 1992; KULIK, 2006). The decrease in calcite stability is caused by the introduction of a disorder in the calcite lattice due to the difference in size between the calcium and magnesium ions (BERNER, 1975; MUCCI and MORSE, 1983). Additionally, due to the smaller size of the magnesium compared to the calcium ion, the incorporation of magnesium also induces a decrease in the size of the unit cell of calcite (ALTHOFF, 1977; BISCHOFF et al., 1983; GOLDSMITH and GRAF, 1958; GOLDSMITH et al., 1961; PAQUETTE and REEDER, 1990).

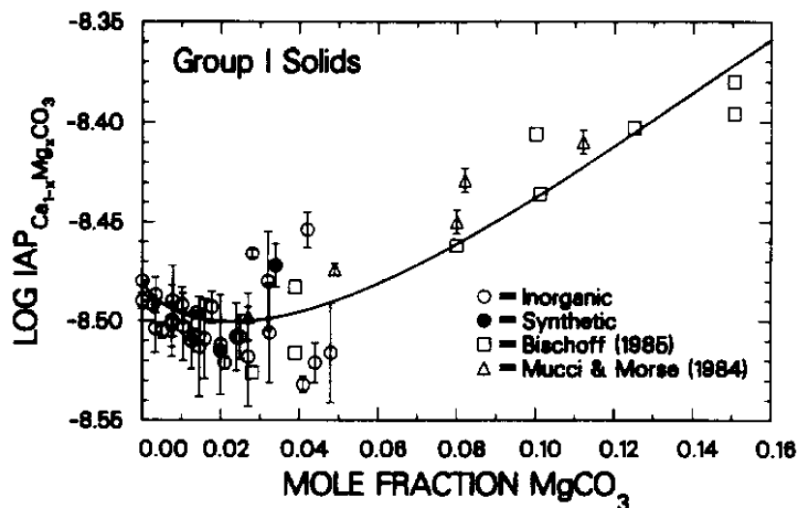


Figure 2.6 The effect of the incorporation of magnesium on the solubility product of calcite (BUSENBERG and PLUMMER, 1989), the figure includes data described by BISCHOFF et al. (1987) and MUCCI and MORSE (1984)

Magnesium ions are more strongly hydrated than calcium ions, which increases the kinetic barrier for calcite (and dolomite) nucleation and crystal growth when magnesium is adsorbed onto mineral surfaces by poisoning calcite (and dolomite) growth sites (DE YOREO et al., 2009; LIPPMANN, 1973; LOSTE et al., 2003). The adsorption of magnesium on aragonite is about 30 times less than on calcite (MUCCI and MORSE, 1985). Additionally, magnesium incorporation into aragonite is negligible (APPELO and POSTMA, 2005). From this it has been concluded that magnesium has no significant influence on the precipitation and thermodynamic stability of aragonite (BERNER, 1975; GUTJAHR et al., 1996). This indicates that the incorporation of magnesium into calcite reduces its stability with respect to

aragonite (BERNER, 1975; BUSENBERG and PLUMMER, 1989; DAVIS et al., 2000; GUTJAHR et al., 1996). An increase in the magnesium to calcium ratio in solution will thus promote the precipitation of aragonite over calcite and at aqueous magnesium to calcium ratios above about 1-2, only aragonite precipitates due to the inhibition and destabilization of calcite (DE CHOUDENS-SANCHEZ and GONZALEZ, 2009; FALINI et al., 1994; MORSE et al., 1997; PARK et al., 2008). Additionally, at ambient conditions, the formation of dolomite is inhibited even though dolomite is thermodynamically more stable than both calcite and aragonite (ARVIDSON and MACKENZIE, 1999; GARRELS et al., 1960). This is due to a combination of highly ordered magnesium layers in the dolomite structure, high adsorption of magnesium on dolomite surfaces and the strong hydration of magnesium ions, causing a high energetic barrier for dolomite precipitation to overcome (ALTHOFF, 1977). In contrast, due to the strong hydration of magnesium, the incorporation of magnesium into ACC increases the stability and formation of ACC (LOSTE et al., 2003).

In addition to the destabilizing effects of magnesium on calcite, the incorporation and adsorption of magnesium also affect the morphology of calcite. In the presence of magnesium, calcite rhombohedrals have a more rounded appearance than without magnesium. GIVEN and WILKINSON (1985) concluded that the supply rate of carbonate ions controls the calcite morphology and that the magnesium to calcite ratio is only an indirect factor, through influencing the rate of calcite precipitation. However, later studies showed that the adsorption and incorporation of magnesium at specific growth steps on calcite surfaces cause a change in calcite morphology (DAVIS et al., 2004; GUTJAHR et al., 1996; WASYLENKI et al., 2005). Calcite surfaces can have different types of steps, where smaller ions prefer the acute steps and larger ions prefer the obtuse steps. Hence, magnesium adsorbs preferentially on acute steps leading to a larger crystallization barrier at these steps compared to the obtuse steps. The step specific adsorption of magnesium decreases the calcite growth kinetics dominantly at the acute steps causing the calcite crystals to become elongated (DAVIS et al., 2004; MELDRUM and HYDE, 2001). Finally, the step specific incorporation of magnesium causes strain in the unit cell lattice predominantly along the acute steps, which causes the calcite crystals to become more rounded (DAVIS et al., 2004; FALINI et al., 1994; ZHANG and DAWE, 2000).

2.3.2 Sulfate

Sulfate substitutes for carbonate in the calcite structure when sulfate is present in solution (Figure 2.7, BUSENBERG and PLUMMER, 1985; KONTREC et al., 2004; PINGITORE et al., 1995). This indicates that the distribution coefficient is likely to be a function of the aqueous sulfate to carbonate ratio (BUSENBERG and PLUMMER, 1985; PINGITORE et al., 1995). Additionally, the incorporation of sulfate into calcite and aragonite decreases their thermodynamic stability and increases their solubility (Figure 2.8, BUSENBERG and PLUMMER, 1985; BUSENBERG and PLUMMER, 1989; FERNÁNDEZ-DÍAZ et al., 2010). Sulfate incorporation into calcite increases the size of the unit cell of calcite due to the substitution of a planer carbonate for a tetragonal sulfate ion (Figure 2.7, KONTREC et al., 2004).

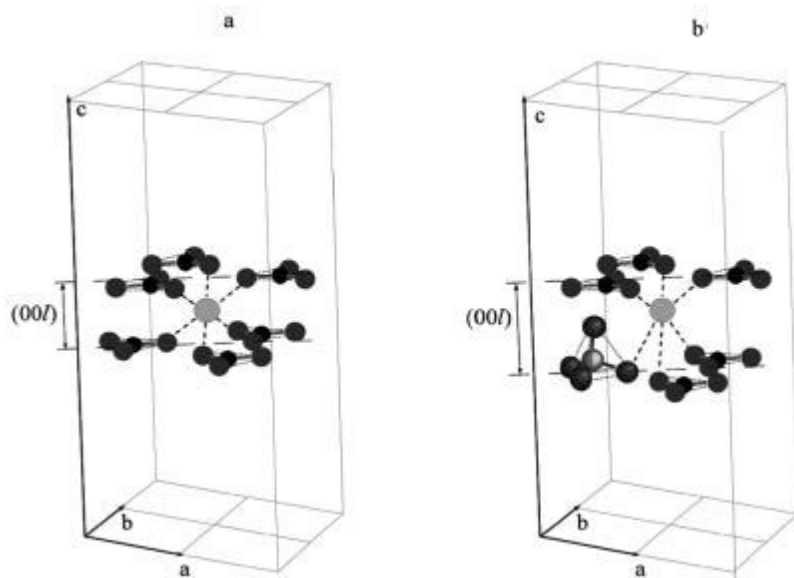


Figure 2.7 Schematics of the exchange of carbonate (a) and sulfate (b) in the calcite structure highlighting the increase in the length of the c axis ($00l$) caused by this exchange (KONTREC et al., 2004)

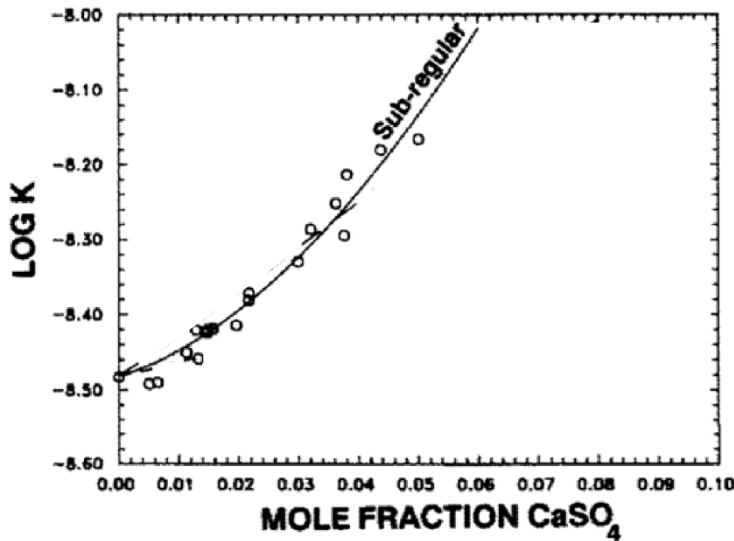


Figure 2.8 The effect of the incorporation of sulfate on the solubility product (K) of calcite (BUSENBERG and PLUMMER, 1989)

Sulfate incorporation into the calcite structure has been proposed to promote the amount of magnesium incorporation (BUSENBERG and PLUMMER, 1985; TAKANO, 1985) in order to compensate for the increase of the calcite unit cell caused by the incorporation of sulfate. However, the presence of sulfate has also been shown to decrease the incorporation of magnesium, but no explanation on the mechanism was given (BURTON and WALTER, 1991).

Similar to the effect of magnesium, sulfate decreases the calcite growth kinetics and has less effect on aragonite growth kinetics (BUSENBERG and PLUMMER, 1985; ZUDDAS and MUCCI, 1994). Additionally, BURTON (1993) used these differences in growth kinetics between calcite and aragonite to determine experimentally that aragonite preferentially precipitates when both sulfate and magnesium increase (Figure 2.9). However, only few studies tried to determine the effect of sulfate on the precipitated polymorphs directly (DONER and PRATT, 1969; FERNÁNDEZ-DÍAZ et al., 2010; KITANO, 1962; SIMKISS, 1964). These studies have shown that an increase in the sulfate concentration promoted the precipitation of either vaterite (due to the stabilization of vaterite by sulfate incorporation, DONER and PRATT, 1969; FERNÁNDEZ-DÍAZ et al., 2010; SIMKISS, 1964) or aragonite (but the mechanism was not discussed, KITANO, 1962) instead of calcite.

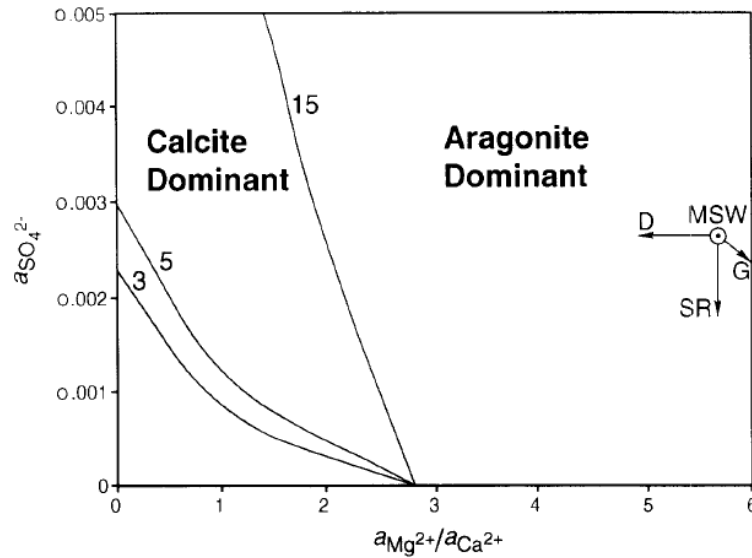


Figure 2.9 The effect of sulfate and the magnesium to calcium ratio in solution on the precipitation of calcite and aragonite as determined from seeded kinetic experiments; the curved lines represent the activities where calcite and aragonite formation kinetics are equal and the numbers along these lines represent the supersaturation (BURTON, 1993)

The incorporation of sulfate into vaterite has been determined to increase its thermodynamic stability and promote its formation by decreasing the vaterite lattice energy (FERNÁNDEZ-DÍAZ et al., 2010). However, sulfate does not significantly incorporate into the structure of ACC (AIZENBERG et al., 2001). Hence, sulfate is not likely to affect the structure and stability of ACC significantly.

In addition to the effects of sulfate on calcium carbonate mineralogy and kinetics, as described above, an increase in the sulfate concentration can cause the precipitation of calcium sulfate phases (DYDO et al., 2003). In nature, three calcium sulfate minerals occur: gypsum ($\text{CaSO}_4 \cdot 2\text{H}_2\text{O}$), bassanite ($\text{CaSO}_4 \cdot 0.5\text{H}_2\text{O}$) and anhydrite (CaSO_4) and to date no amorphous calcium sulfate phase has been identified. Gypsum has been determined to be stable at low temperature, anhydrite at high temperature and bassanite at high pressure and intermediate temperature (MIRWALD, 2008; YAMAMOTO and KENNEDY, 1969). Anhydrite is also stable at high ionic strength due to a decrease in the activity of water (HARDIE, 1991; HARVIE and WEARE, 1980; HARVIE et al., 1980; KRUMGALZ, 2001). A rare calcium sulfate – calcium carbonate phase, rapidcreekite ($\text{Ca}_2\text{SO}_4\text{CO}_3 \cdot 4\text{H}_2\text{O}$), has also been identified as a secondary mineral formed during the weathering of siderite (FeCO_3) (ROBERTS et al., 1986), but no information is available on the stability and solubility of

rapidcreekite. However, at ambient conditions, all (other) calcium sulfate mineral phases are ~3-4 orders of magnitude more soluble than calcium carbonate minerals (FREYER and VOIGT, 2003; PLUMMER and BUSENBERG, 1982). Because of the high solubility, calcium sulfate formation occurs predominantly in evaporitic environments like the Dead Sea (REZNIK et al., 2011; WARREN, 2010).

2.3.3 pH, alkalinity and pCO₂

Calcium carbonate growth has been observed to predominantly utilize calcium and bicarbonate in solution (Eq. 2.3, PLUMMER et al., 1979; PLUMMER et al., 1978). However, later studies showed that calcium carbonate growth is a function of the aqueous calcium to carbonate ratio (instead of bicarbonate), with maximum growth rates at ratios near unity (NEHRKE et al., 2007; STACK and GRANTHAM, 2010). This discrepancy, between growth via bicarbonate vs. carbonate, could be caused by the chemical conditions in the experimental methods. PLUMMER et al. (1978) determined the preference for bicarbonate in calcite growth via dissolution experiments at a pH < 7 (PLUMMER et al., 1979) when bicarbonate is the dominant carbonate species adsorbed on calcite surfaces (WOLTHERS et al., 2008). In contrast, the later studies followed calcite growth at a higher pH (pH = 10, NEHRKE et al., 2007; 8 < pH < 9.5, STACK and GRANTHAM, 2010). At pH above ~8.3, carbonate is the dominant species adsorbed on calcite surfaces (WOLTHERS et al., 2008). As calcite growth is heavily influenced by surface processes (TENG et al., 2000), the adsorption of either bicarbonate or carbonate could explain the observed differences.

Changes in the pH and alkalinity can also affect the incorporation of sulfate and magnesium. The incorporation of sulfate into calcite is thought to be a function of the aqueous sulfate to carbonate ratio (BUSENBERG and PLUMMER, 1985; TAKANO, 1985). Hence, a change in calcite growth via either carbonate or bicarbonate (due to variations in pH) could also change the incorporation of sulfate into calcite and affect calcite growth kinetics. Additionally, an increase in the concentration of bicarbonate decreases the amount of magnesium incorporated into the calcite structure (Figure 2.10, BURTON and WALTER, 1991), which could also destabilize calcite with respect to aragonite (DAVIS et al., 2000).

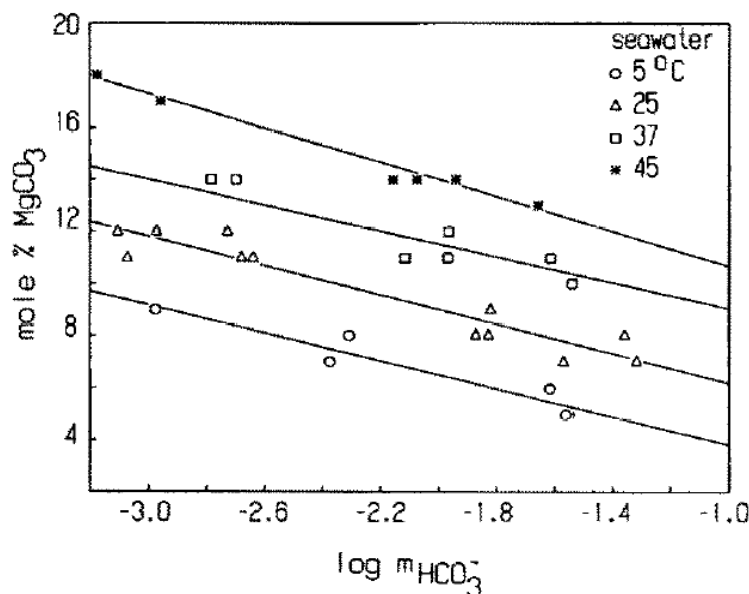


Figure 2.10 The effects of the concentration of bicarbonate on the magnesium incorporation into calcite (BURTON and WALTER, 1991)

It has also been suggested that an increase in the supersaturation caused by changes in the $p\text{CO}_2$ can promote aragonite precipitation by changing the calcium carbonate growth rates (GIVEN and WILKINSON, 1985). However, the study by GIVEN and WILKINSON (1985) was based on paleoceanographic models (section 2.4) and field data. In comparison, a recent experimental study indicated that an increase in alkalinity by an increase in $p\text{CO}_2$ would enhance the formation of calcite instead of aragonite (LEE and MORSE, 2010). However, this study used an experimental set-up characterized by large changes in the solution chemistry like the calcium and carbonate concentrations (MORSE et al., 1997). Contrastingly, LEE and MORSE (2010) determined the effects of alkalinity on the formation of calcium carbonate with magnesium and sulfate in the solutions. However, they did not take into account that the incorporation of sulfate into calcite (and aragonite), and hence the effect of sulfate on the stability of calcite (and aragonite), is likely to be a function of the sulfate to carbonate ratio (BUSENBERG and PLUMMER, 1985; PINGITORE et al., 1995).

GEBAUER et al. (2010) determined that the short range order of ACC formed in a solution with a pH of 8.75 resembles the structure of calcite and ACC formed in a solution with a pH of 9.8 resembles the structure of vaterite. Also, NEBEL et al. (2008) determined that ACC does not contain any bicarbonate.

2.3.4 Temperature

A large range of temperatures have been observed in natural aquatic environments; in modern environments, surface seawater temperatures can reach as high as ~29 °C near the equator while bottom seawater is generally ~4 °C (BERNER and BERNER, 1996). BURTON and WALTER (1991) determined that simultaneous to an increase in temperature the magnesium incorporation into calcite increased (Figure 2.10). This increased incorporation of magnesium into calcite inhibited calcite formation more than aragonite formation (BURTON and WALTER, 1987). As discussed in section 2.3.1, an increase in magnesium incorporation into calcite causes a decrease in the stability of calcite with respect to aragonite (Figure 2.6, BUSENBERG and PLUMMER, 1989). Hence, the magnesium to calcium ratio at which aragonite precipitation is preferred, decreases at elevated temperatures (Figure 2.11, MORSE et al., 1997). This relation has been used to explain the occurrence of predominantly low Mg-calcite in deep-sea sediments, and the dominance of aragonite and magnesian calcites (>4 mol% magnesium) in sediments in shallower and warmer seawater (MORSE et al., 1997).

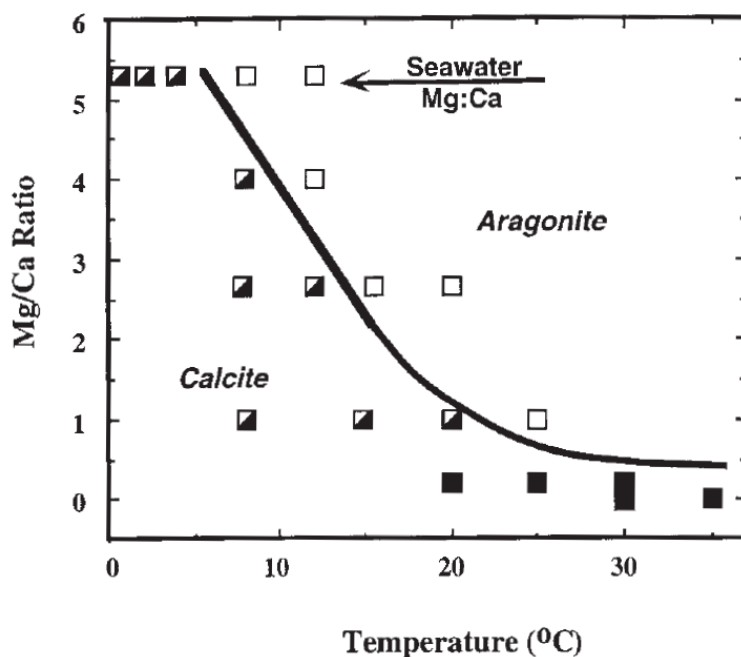


Figure 2.11 Temperature versus calcium carbonate mineralogy; the black squares represent the situation when only calcite precipitates, the white squares represent the situation when only aragonite precipitates and the split squares show when calcite precipitates and due to a change in the magnesium to calcium ratio in solution, caused by the experimental set-up, the calcite is overgrown by aragonite (MORSE et al., 1997)

High temperature alone also promotes the crystallization of aragonite directly by decreasing its nucleation energy (OGINO et al., 1987; WRAY and DANIELS, 1957). Finally, an increase in temperature can also promote dolomite precipitation. Due to a high activation energy, increasing the temperature can overcome the nucleation barrier for dolomite precipitation (ARVIDSON and MACKENZIE, 1999; FENTER et al., 2007).

2.4 The chemical evolution of Phanerozoic seawater

HARDIE (1996) showed that the dominant evaporite sequences formed during the Phanerozoic included either KCl (sylvite) or MgSO₄ (e.g. epsomite) evaporite minerals. It is also known that the chemical composition of the solutions from which evaporites form affect the dominant evaporite sequence (HARDIE, 1990; HARDIE, 1991). Hence, it was concluded that the changes in dominant evaporite sequence was caused by fluctuations in seawater composition, between CaCl₂ and MgSO₄

dominant seawater (LOWENSTEIN et al., 2003). HARDIE (1996) modelled the fluctuations in the seawater composition during the Phanerozoic (Figure 2.12) and proposed that they were predominantly caused by changes in mid-ocean ridge activity and river water input. At elevated oceanic ridge activity, more oceanic crust is formed and thus available for serpentinization, taking up magnesium and releasing calcium to the seawater. An increase in mid-ocean ridge activity also induces additional orogeny, which causes weathering and weathering fluxes of dissolved ions to the oceans to increase.

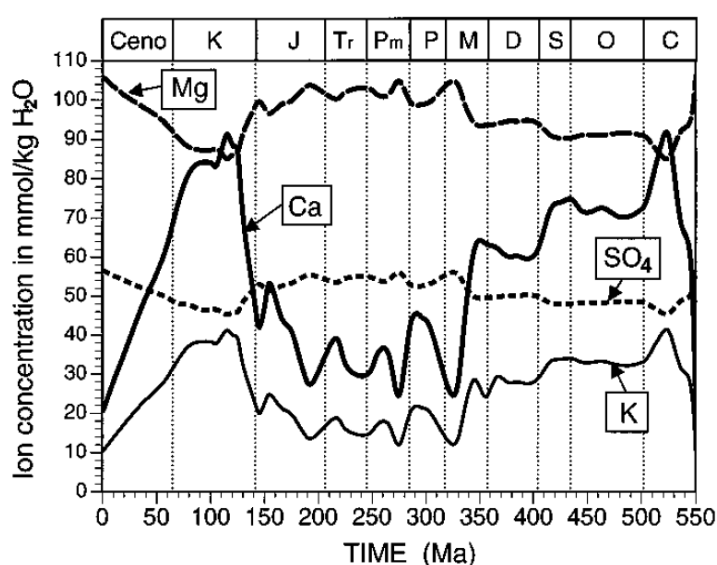


Figure 2.12 Evolution of seawater chemistry for major ions as predicted by HARDIE (1996)

Since the recognition that the seawater chemistry fluctuated significantly (HARDIE, 1996), much research has been done on the chemical evolution of seawater. However, only indirect evidence is available for Phanerozoic chemical composition of seawater. Much information on the composition of Phanerozoic seawater is based on calcium carbonates deposits (CICERO and LOHMANN, 2001; HARDIE, 1996; HASIUK and LOHMANN, 2008), biominerals (DICKSON, 2002; DICKSON, 2004; MARTIN, 1995) and evaporite sequences (HARDIE, 1996). The chemical composition of sedimentary (bio)minerals reflect the chemistry of the seawater composition in which they formed. However, diagenesis can alter their chemical composition significantly (BUDD and LAND, 1990; CORSETTI et al., 2006; STEUBER and VEIZER, 2002). Halite fluid inclusion composition has also been used

to extract information about the Phanerozoic seawater chemistry (HORITA et al., 2002; KOVALEVICH et al., 1998; LOWENSTEIN et al., 2003; LOWENSTEIN et al., 2001; TIMOFEEFF et al., 2006; ZIMMERMANN, 2000). Fluid inclusions in halite form during the evaporation of seawater and are preserved as relics of evaporated seawater (KOVALEVICH et al., 1998). Additionally, the composition of the fluid inclusions is affected by the degree of evaporation during halite formation and the simultaneous formation of other evaporitic phases like gypsum and anhydrite (HARDIE, 1990; KOVALEVICH et al., 1998; ZIMMERMANN, 2001). By performing back calculations and using several assumptions (e.g.: constant gypsum saturation state), HORITA et al. (2002), among others, estimated the chemical composition of the original seawater (HORITA et al., 2002; KOVALEVICH et al., 1998; ZIMMERMANN, 2001). In contrast to the model from HARDIE (1996) (Figure 2.12), HORITA et al (2002) determined that the potassium concentration remained approximately constant at ~10 mM throughout the Phanerozoic and that the magnesium and sulfate concentrations fluctuated significantly more (Figure 2.13 and 2.14). However, it is still debated whether halite fluid inclusions reflect the Phanerozoic seawater chemistry at the time of the halite deposition (HANOR and MCINTOSH, 2006; HOUSTON et al., 2011; LOWENSTEIN and TIMOFEEFF, 2008). Finally, sulphur stable isotope ratios (from e.g. carbonate associated sulfate) have been used to obtain information about the sulfate concentrations and redox state of the seawater during the Phanerozoic (GILL et al., 2007; GILL et al., 2011; KAH et al., 2004; NEWTON et al., 2011; PAYTAN et al., 1998; PAYTAN et al., 2004; WORTMANN and CHERNYAVSKY, 2007). These studies often reveal significantly lower sulfate concentrations (2-5 mM) than obtained from the fluid inclusion analyses shown in Figure 2.14 (GILL et al., 2007; GILL et al., 2011; KAH et al., 2004; NEWTON et al., 2004; WORTMANN and CHERNYAVSKY, 2007).

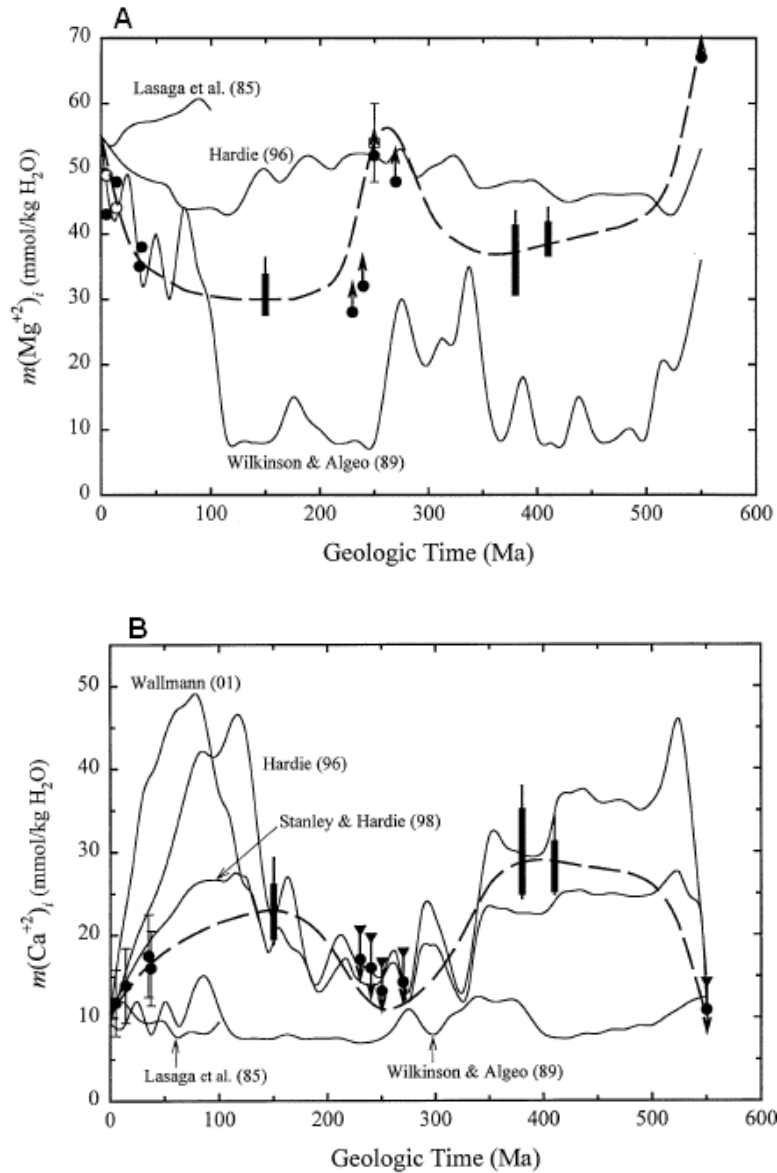


Figure 2.13 Chemical evolution of the magnesium (A) and calcium (B) concentration during the Phanerozoic as determined from halite fluid inclusions from: HORITA et al. (2002, dashed lines); the solid lines represent models from HARDIE (1996), STANLEY and HARDIE (1998), WALLMANN (2001) and WILKINSON and ALGEO (1989); figure reprinted from HORITA et al. (2002)

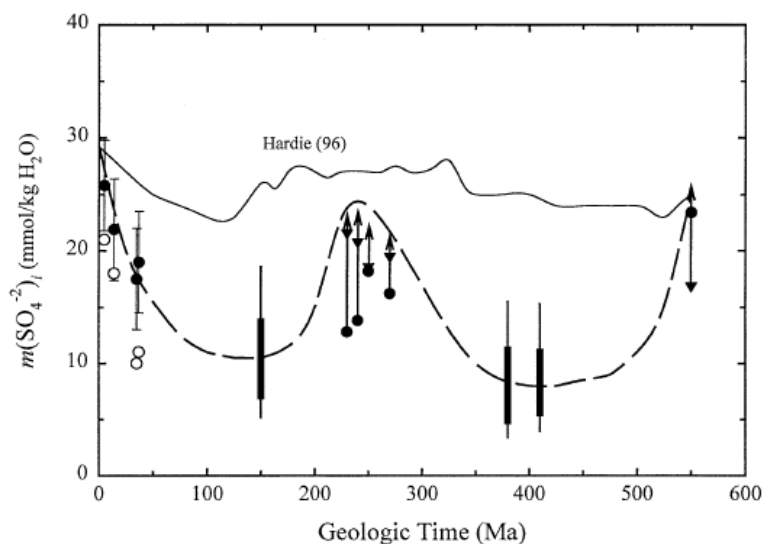


Figure 2.14 Chemical evolution of the sulfate concentration during the Phanerozoic as determined from halite fluid inclusions from: HORITA et al. (2002, dashed line); the solid line represents the model from HARDIE (1996); figure reprinted from HORITA et al. (2002)

There are many models of the composition of the Phanerozoic seawater (ARVIDSON et al., 2006b; BERNER, 2004; DEMICCO et al., 2005; MACKENZIE et al., 2008; STANLEY and HARDIE, 1998). These models show that the fluctuation in the Phanerozoic seawater chemistry is not solely influenced by processes at the mid ocean ridges and river water inputs. A combination of various processes, listed below, controlled the seawater chemistry during the Phanerozoic.

- (1) cation exchange between basalt and seawater due to cycling of seawater through mid-ocean ridges affects the calcium and magnesium concentration (ARVIDSON et al., 2006a; BERNER, 2004; DEMICCO et al., 2005; HOLLAND, 2005; HORITA et al., 2002; MACKENZIE et al., 2008; STANLEY, 2006; STANLEY and HARDIE, 1998; WILKINSON et al., 1985);
- (2) river water input varied through changes in weathering (caused by e.g. enhanced uplift) during the Phanerozoic (DEMICCO et al., 2005; HARDIE, 1996)
- (3) variation in reverse weathering from which products such as clay minerals and dissolved ions are transported to the oceans (ARVIDSON et al., 2006b; HOLLAND, 2005; MACKENZIE et al., 2008; MACKENZIE and KUMP, 1995);
- (4) changes in cation exchange on clay minerals (HOLLAND, 2005);
- (5) changes in precipitation abundance and composition of (bio)minerals (BERNER, 2004; MACKENZIE et al., 2008; RIDGWELL and ZEEBE, 2005;

STEUBER and VEIZER, 2002) and evaporites (WORTMANN and CHERNYAVSKY, 2007);

- (6) variations in $p\text{CO}_2$ which influences the concentrations of calcium, inorganic carbonate chemistry and pH, due to, for example, the enhanced dissolution or precipitation of carbonate (bio)minerals (MACKENZIE et al., 2008; RIDGWELL and ZEEBE, 2005; WALLMANN, 2001; WILKINSON et al., 1985);
- (7) dolomitization of precipitated calcium carbonates decreases the concentrations of magnesium in solution (ARVIDSON et al., 2006b; HOLLAND, 2005; HOLLAND et al., 1996; LOWENSTEIN et al., 2001; MACKENZIE et al., 2008).

The activity of mid-oceanic ridges has also been proposed as a predominantly indirect force on the seawater chemistry. For example, enhanced spreading rates can trigger evolution and cause changes in biomineralization due to sea level rise and the coinciding increase in the proportion of epicontinental seas, forming new niches for evolution (HOLLAND, 2005; HORITA et al., 2002; WILKINSON et al., 1985). Additionally, enhanced spreading rates can release CO_2 into the atmosphere and thus change the calcium carbonate equilibrium in seawater (WALLMANN, 2001; WILKINSON et al., 1985). Finally, although it is known that the temperature fluctuated during the Phanerozoic, precise determinations and modelling of the evolution of temperature and the surface seawater temperature is still debated (ROYER et al., 2004; WALLMANN, 2004).

2.4.1 Calcite vs. Aragonite seas

It is now recognized that, throughout the Phanerozoic, the primary abiotic marine calcium carbonate mineralogy oscillated between calcite and aragonite (Figure 2.15, SANDBERG, 1983) and possibly during the Proterozoic (HARDIE, 2003; RIES et al., 2008). These periods are known as calcite and aragonite seas (SANDBERG, 1983). However, the records now show that the calcium carbonate formed during the Phanerozoic was rarely purely calcite or aragonite but dominated by either calcite or aragonite (ADABI, 2004; WILKINSON et al., 1985; ZHURAVLEV and WOOD, 2009).

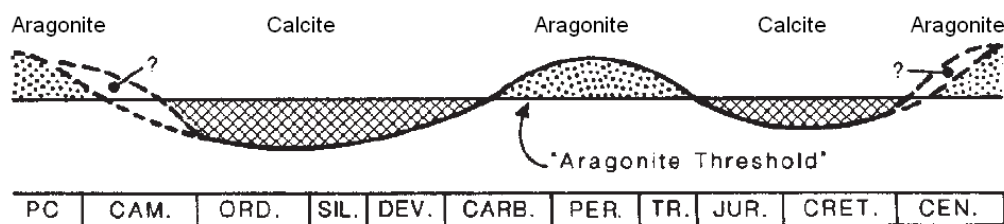


Figure 2.15 The distribution of the calcite and aragonite seas as determined by SANDBERG (1983)

The observed oscillations in calcium carbonate mineralogy coincided with the oscillations in the dominant evaporite sequences and seawater chemistry (HARDIE, 1996; LOWENSTEIN et al., 2003). Hence, the fluctuations of a range of chemical and physical parameters have been used to explain the oscillating trends in calcium carbonate mineralogy (either directly or by influencing other parameters):

- (1) fluctuations in the aqueous magnesium to calcium ratio (section 2.3.1, Figure 2.13, MORSE et al., 1997; STANLEY, 2006);
- (2) fluctuations in the sulfate concentration (section 2.3.2, Figure 2.14, RAILSBACK and ANDERSON, 1987);
- (3) fluctuations in the $p\text{CO}_2$ and subsequent variations in pH and alkalinity (section 2.3.3, LEE and MORSE, 2010; SANDBERG, 1983; WILKINSON et al., 1984; ZHURAVLEV and WOOD, 2009) and the affects on the calcium carbonate supersaturation (GIVEN and WILKINSON, 1985);
- (4) fluctuations in temperature by, for example, amplifying the effects of the magnesium to calcium ratios on the calcium carbonate mineralogy (section 2.2.4, BALTHASAR et al., 2011; BURTON and WALTER, 1987; MORSE et al., 1997).

It is now understood that the magnesium to calcium ratios is a dominant factor in determining the primary calcium carbonate polymorph formed from seawater by destabilizing calcite and inhibiting its formation (STANLEY, 2006, see also section 2.2.1). However, the precise magnesium to calcium ratio for the switch from calcite to aragonite seas is still debated; several ratios between 1 and 2 have been proposed to date (HARDIE, 1996; MORSE et al., 1997; WILKINSON and ALGEO, 1989). Furthermore, MORSE et al. (1997) determined that temperature influences the

magnesium to calcium ratio at which the switch from calcite to aragonite precipitation occurs (Figure 2.11). Most research on the influences on the calcite and aragonite seas has so far focussed on the magnesium to calcium ratio. Interestingly, the effect of the fluctuating sulfate concentration (Figure 2.14) on the oscillations between calcite and aragonite seas has largely been overlooked (LEE and MORSE, 2010). Additionally, the interactions of sulfate concentration (or the sulfate to carbonate/bicarbonate ratio) in combination with the magnesium to calcium ratio have only been determined by comparing the effect of sulfate and magnesium on the calcite and aragonite crystallization rates (section 2.3.2, BURTON, 1993).

2.5 Biomineralization

Most predominant calcareous biominerals are composed of calcite and aragonite (LOWENSTAM, 1981; WEINER and DOVE, 2003). However, in some cases vaterite is biomineralized (LOWENSTAM, 1981), like the spicules produced by a certain sea squirt (LOWENSTAM and ABBOTT, 1975) and several fish otoliths (TOMÁS and GEFFEN, 2003). Biominerals form either via an “organic matrix-mediated” or by a “biologically induced” process (LOWENSTAM, 1981). The “organic matrix-mediated” process is an intracellular process where the formation of the biomineral is (almost) completely genetically driven. During such a process the organism directs the precipitated polymorph with for example proteins (ADDADI and WEINER, 1992; BELCHER et al., 1996; DALBECK et al., 2006; FALINI et al., 1996; JI et al., 2010; LEVI et al., 1998; WEINER and TRAUB, 1984). Additionally, many calcium carbonate biomineralizing organisms utilize ACC to precisely control the shape and polymorph of the biominerals, like during mollusk shell and sea urchin spine formation (ADDADI et al., 2003; ADDADI and WEINER, 1992; AUZOUX-BORDENAVE et al., 2010; CUSACK and FREER, 2008; GAZEAU et al., 2010; MELDRUM and CÖLFEN, 2008; POLITI et al., 2004; TALMAGE and GOBLER, 2010; WEINER and DOVE, 2003; WEISS et al., 2002). For example, POLITI et al. (2008) observed that sea urchin larvae produce transient ACC, which dehydrates prior to controlled formation of single crystal calcite via a secondary nucleation process. Finally, organisms which form biominerals via an “organic matrix-mediated” process also (partly) control the chemical composition of the biomineral (ADDADI and WEINER, 1992;

CUSACK and FREER, 2008). During “biologically induced” biomineralization processes, the formation of the biominerals is generally extracellular and caused by changes in solution chemistry due to primary biological process (LOWENSTAM, 1981). For example, bacterial metabolic processes can change the chemistry in the vicinity of the cell walls which in turn can act as an active surface for the formation of calcium carbonates (FRANKEL and BAZYLINSKI, 2003). Due to the formation process of these biominerals, the organisms have much less control over the polymorph, shape and chemical composition of the minerals (LOWENSTAM, 1981).

2.5.1 Biomineralization throughout the Phanerozoic

During the Phanerozoic the mineralogy of many calcifying organisms oscillated significantly concurrent with the observed oscillations in abiotic calcium carbonate mineralogy (section 2.3.1) (STANLEY, 2006). However, not all marine fossils follow the oscillating trend of calcite and aragonite seas (e.g. bryozoans and rugose corals) (ADABI, 2004; BALTHASAR et al., 2011; WHEELEY et al., 2008; ZHURAVLEV and WOOD, 2009). ZHURAVLEV and WOOD (2009) showed that, in addition to the oscillations of seawater chemistry and temperature, extinctions had a major influence on the biomineralization of calcite or aragonite by emptying the ‘field’ for the evolution of new species. Additionally, RIES (2005), STANLEY (2006) and STANLEY et al (2005) recognized that changes in seawater chemistry can enhance the growth of organisms excreting preferential minerals or decrease the growth of organisms excreting less favourable minerals in their skeletons. Hence, newly evolved species adopted the dominant mineralogical form from the oceans in which they evolved to decrease the stress of forming thermodynamically unfavourable phases (STANLEY, 2006; ZHURAVLEV and WOOD, 2009). These observations suggest that the ocean chemistry had a profound effect on the evolution of calcifying organisms and their biomineralization products (KNOLL, 2003; MARTIN, 1995; PORTER, 2007; PORTER, 2010). However, species do generally not switch mineralogy after evolving to produce either calcite or aragonite if the seawater chemistry changes (RIES, 2005; STANLEY and HARDIE, 1998). This could explain the occurrence of calcite producing organisms in the present day oceans (which is an aragonite sea, Figure 2.15) (STANLEY and HARDIE, 1998).

In addition to the calcium carbonate polymorph formed by organisms, the chemical composition and temperature of seawater during the Phanerozoic (section 2.4) can affect the chemical composition of the biominerals (as discussed in section 2.3). The effects of the composition and temperature are widely used in the reconstruction of paleoenvironmental conditions (CUSACK and FREER, 2008). The seawater magnesium to calcium ratio can also (partly) control the amount of magnesium taken up in the calcite skeleton from several organisms (RIES, 2005; RIES, 2006; STANLEY, 2006; STANLEY et al., 2005). An increase in temperature has also been shown to enhance the incorporation of magnesium into biominerals (TAYLOR et al., 2009), yet $p\text{CO}_2$ has no significant affect on the incorporation of magnesium (ALLISON et al., 2011). The variations in the magnesium to calcium ratios have therefore been used for the reconstruction of the seawater chemistry (DICKSON, 2002; DICKSON, 2004; MARTIN, 1995) and temperature (LORENS and BENDER, 1980; OKAFOR et al., 2009). It has been suggested that the incorporation of sulfate into calcium carbonate minerals can provide useful information about the seawater sulfate to carbonate ratio during the Phanerozoic (PINGITORE et al., 1995). However, the correlation between seawater chemistry and sulfate incorporation into calcium carbonate biominerals is still unclear. Some field and (abiotic) experimental studies have suggested that either the incorporation of magnesium enhances the incorporation of sulfate (TAKANO, 1985) or that the presence of sulfate in solution causes a decrease in the magnesium incorporation (BURTON and WALTER, 1991). So far, sulfate incorporation into calcium carbonate biominerals has mainly been investigated using the sulphur isotope composition to obtain information about the sulfate chemistry and redox conditions of the Phanerozoic seawater (GILL et al., 2007; GILL et al., 2011; HETZEL et al., 2009; KAH et al., 2004; NEWTON et al., 2004; NEWTON et al., 2011; WORTMANN and CHERNYAVSKY, 2007).

Finally, diagenesis has the potential to alter the chemical signature of the biominerals significantly by, for example, equilibration of a solid solution to meteoric waters (BANNER and HANSON, 1990; BERNER, 1966). This would render any conclusions inferred from these biominerals incorrect. However, several geochemical signatures (e.g. strontium incorporation and the carbon and oxygen isotopic signature) can be used to distinguish between primary and diagenetically altered calcium carbonate (NEWTON et al., 2004; OKAFOR et al., 2009; THOMAS et al., 1999).

Chapter 3

Methods

In this chapter, the experimental and analytical methods are described. The descriptions here overlap with the method descriptions in later chapters. This is done to keep the results chapters self-explanatory. Additionally, the method development to analyse calcium and magnesium, using a spectrophotometer, and to analyse the chemical composition of solid calcium carbonate samples, using ion chromatography, are described at the end of this chapter. The methods described in this chapter are:

- 3.1. Laboratory based experimental methods
 - 3.1.1. Constant addition experiments
 - 3.1.2. Vaterite formation and ripening
- 3.2. Laboratory based analytical methods
 - 3.2.1. A spectrophotometric method to analyse Ca and Mg
 - 3.2.2. Ion Chromatography
 - 3.2.3. Scanning Electron Microscopy
 - 3.2.4. XRD
- 3.3. Synchrotron based Small and Wide Angle X-ray Scattering (SAXS/WAXS) and experimental methods
 - 3.3.1. Synchrotron radiation
 - 3.3.2. WAXS
 - 3.3.3. SAXS
 - 3.3.4. Experimental methods and data collection
- 3.4. Geochemical modelling using PHREEQC for windows
 - 3.4.1. Evaporation simulations
 - 3.4.2. Modelling the chemical evolution of the SAXS/WAXS experiments
- 3.5. Method development
 - 3.5.1. A spectrophotometric method to analyse Ca and Mg
 - 3.5.2. Measuring solid composition of CaCO₃ using Ion Chromatography

3.1 Laboratory based experimental methods

The two mineral synthesis methods described below were designed and used to examine the interaction between solution chemistry and the precipitated calcium carbonate mineralogy. The results from the constant addition experiments are described in chapter 4 and appendix C and the results from the vaterite formation and ripening experiments are described in chapter 6.

3.1.1 Constant addition experiments

The aim of these experiments was to investigate the effect of sulfate and magnesium on primary calcium carbonate mineralogy in relation to the Phanerozoic seawater composition. This was done by synthesizing calcium carbonate using constant addition experiments (21 ± 1 °C and 10 ± 1 °C). The experimental set-up was a modification of the method used by TESORIERO AND PANKOW (1996) (Figure 3.1). No seeds were used during the constant addition experiments to avoid seeded precipitation of either calcite or aragonite (WALTER, 1986). Instead, glass spheres with a diameter of 0.1 mm (BioSpec Products, Figure 3.2) were used as a reactive surface. This was done to mimic the precipitation on particles in seawater, akin to the formation of ooids. In all experiments, 1 g of glass beads was used in 500 ml of batch solution. The batch solutions contained 10 mM CaCl_2 and varying MgCl_2 (0-55 mM) and Na_2SO_4 (0-100 mM) concentrations. The magnesium to calcium ratio and sulfate concentration used during the experiments bracketed the proposed Phanerozoic seawater composition (HORITA et al., 2002). The solutions were adjusted to approximate seawater salinity (35‰) with NaCl to minimize the effect of ionic strength on the precipitation of calcium carbonate minerals. The batch solutions were made in two steps. The first step was the addition of NaCl, Na_2SO_4 and glass beads to 500 ml MiliQ water to reach approximate seawater salinity and the required sulfate concentration. To these solutions, 2 N NaOH was added and equilibrated with the atmosphere (for a minimum of 3 days) to reach a pH of ~8.1 and a carbonate alkalinity of ~1.6 mM. The second step consisted solely of the addition of $\text{CaCl}_2\cdot 2\text{H}_2\text{O}$ and $\text{MgCl}_2\cdot 6\text{H}_2\text{O}$ to the equilibrated solutions to reach the required calcium and magnesium concentrations. To ensure homogeneous conditions in the batch solutions, the Erlenmeyer flasks were shaken on an orbital

shaker at a rate of 270 rpm throughout the experiments. Two input solutions (one with elevated concentrations of $\text{CaCl}_2 \cdot 2\text{H}_2\text{O}$ and $\text{MgCl}_2 \cdot 6\text{H}_2\text{O}$ and one with elevated concentrations of Na_2CO_3 and Na_2SO_4) were added to the batch solutions during the experiments to promote calcium carbonate precipitation. A syringe pump was used to add the input solutions to the batch solutions at a rate of 1 ml/h. All the chemicals that were used during the constant addition experiments were analytical grade. Prior to, during, and at the end of the experiments the pH was measured and, simultaneously, solution samples were extracted from the batches and filtered using $0.2 \mu\text{m}$ syringe filters. Aliquots of the solution samples were either stored frozen (to analyze for sulfate) or acidified with concentrated HNO_3 and stored at room temperature (to analyze for calcium and magnesium). When terminating the experiments the solutions were filtered with $0.2 \mu\text{m}$ membrane filters using a vacuum pump to separate the precipitated CaCO_3 solids from the solutions. The solid samples were washed (using Milli-Q grade H_2O equilibrated with calcite) and filtered three successive times and dried at $95 \text{ }^\circ\text{C}$ overnight prior to further analyses.

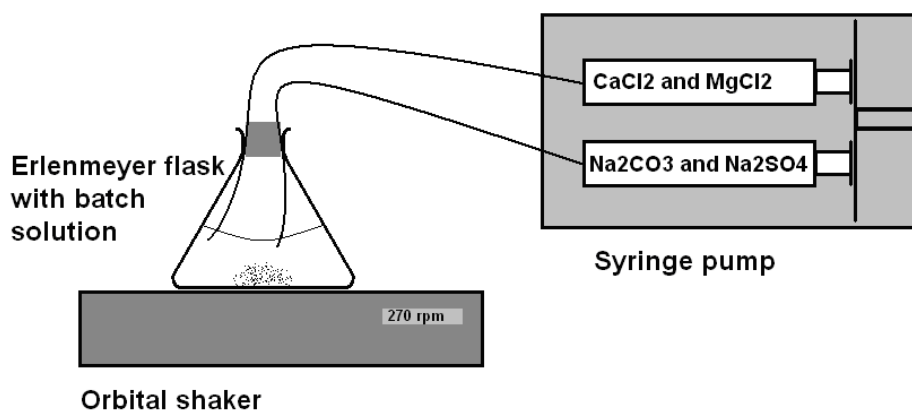


Figure 3.1 Schematic representation of the constant addition experiments

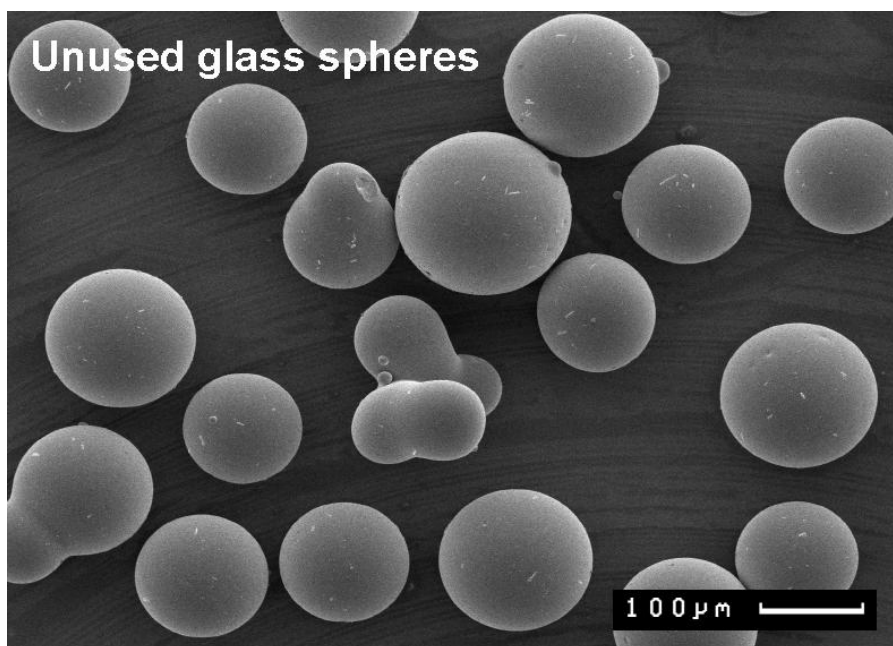


Figure 3.2 Scanning Electron Microscope image of the glass beads used during the constant addition experiments

3.1.2 Vaterite formation and ageing

A second set of calcium carbonate synthesis experiments were performed in order to study the effect of dissolved sulfate on the formation of vaterite. CaCO_3 was synthesized by rapidly mixing two solutions. 100 ml of a solution with 100 mM $\text{CaCl}_2 \cdot 2\text{H}_2\text{O}$ (analytical grade) was added to 100 ml of a solution containing 50 or 100 mM Na_2CO_3 (analytical grade) and 0 – 2 M Na_2SO_4 (analytical grade). The suspensions were continuously stirred using a magnetic stirrer (150 rpm) for the total duration of the experiments (~3 – 130 min). At the end of the experiments, the precipitates were separated from solution by filtering through 0.2 μm membrane filters and immediately washed with 18.2 M Ω Milli-Q grade H_2O (equilibrated with calcite and propan-2-ol). Subsequently, the samples were dried at room temperature prior to further analyses.

Additionally, the stability of vaterite was studied by performing ageing experiments. Vaterite formed during the formation experiment with 100 mM calcium, 50 mM carbonate and 1.25 M sulfate was used during the ageing experiments. The repining solutions contained 10 mM CaCl_2 , 0 – 200 mM Na_2SO_4 and 0 or 2 mM MgCl_2 . These solutions were prepared in the same way as the batch solutions used during the constant addition experiments (section 3.1.1).

Subsequently, 0.5 g vaterite was added and equilibrated with the solutions for ~1 – 17 h. Solution samples were taken before adding the solid to the solutions and at the end of the experiment. The solutions were filtered using a 0.2 µm syringe filter and aliquots of the solution samples were either stored frozen (to analyze for sulfate) or acidified with concentrated HNO₃ and stored at room temperature (to analyze for calcium). Solid samples were separated from the solutions by filtering the solution through a 0.2 µm membrane filter with a vacuum pump. Subsequently, the solid samples were washed with Milli-Q grade H₂O equilibrated with calcite and propan-2-ol and dried at room temperature prior to further analyses.

3.2 Laboratory based analytical methods

This section briefly describes the analytical methods used in this thesis.

3.2.1 A spectrophotometric method to analyse Ca and Mg

Solutions were analyzed for total calcium and magnesium using a spectrophotometric method modified after method 8030 (Hach Lange, Düsseldorf, Germany). A DR 2500 UV/VIS spectrophotometer was used to perform the analyses. Calmagite was used as an indicator and ethylene-diamine-tetraacetic acid (EDTA) and ethylene-glycol-tetraacetic acid (EGTA) were used as complexing agents. The concentrations of calcium and magnesium were determined by measuring the absorbance at a wavelength of 522 nm. The calcium concentration was calculated from the difference in absorbance of a solution with EGTA added and the same solution without both EGTA and EDTA. Additionally, the magnesium concentration was calculated from the difference in absorbance of a solution with EDTA and a solution with EGTA added. This method and the method development are described in more detail in section 3.5.1 and this method was used to determine calcium and magnesium concentrations in solution (chapter 4 and 7).

3.2.2 Ion Chromatography

Ion chromatography (IC) uses an ion exchange resin to separate ions based on their charge and their affinity to the specific resin. An ion chromatography set-up uses an eluent, a guard column, an analytical column and a suppressor and conductivity detector or a UV detector. A schematic representation of a standard set-up used in IC is shown in Figure 3.3.

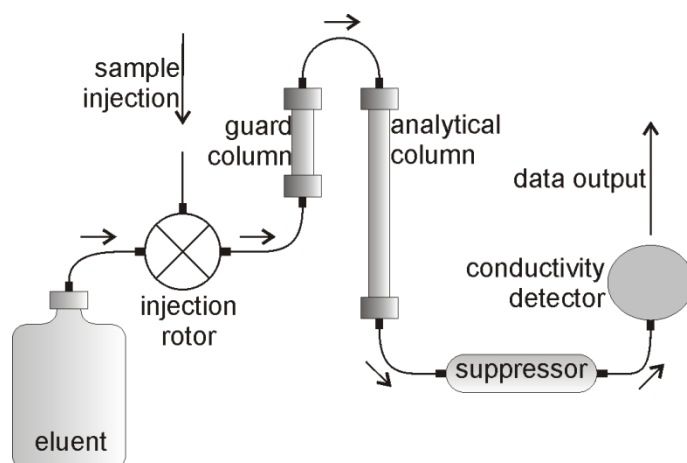


Figure 3.3 Schematic representation of a standard IC set-up

A sample is injected in a constant eluent flow (Figure 3.3). The relative affinity (to the ion-exchange resin used in the columns) of the solutes with respect to the eluent determines the residence time of the solutes on the columns. The differences in the relative affinity between all solutes determine the separation of the solutes by the guard and analytical column. A guard column is used to obtain an initial separation and to protect the analytical column against overloading by the solutes (Figure 3.3). When using a conductivity detector, a suppressor is generally used to reduce the conductivity of the eluent (Figure 3.3). Additionally, a suppressor also enhances the conductivity of the separated ions. Hence, this enhances the signal to noise ratio significantly. For analyses in this thesis, a Dionex DX500 system was used with a carbonate/bicarbonate eluent for the analyses of sulfate and a methanesulfonic acid eluent for the analyses of calcium and magnesium. The results from analyses with IC are described in chapter 4-8. Additionally, a full description of the method development to analyze the chemical composition (e.g.: Ca, Mg and SO_4) of solid calcium carbonate samples is presented in section 3.5.2.

3.2.3 Field Emission Gun-Scanning Electron Microscopy

When imaging with Field Emission Gun-Scanning Electron Microscopy (FEG-SEM) a high energy electron beam is used to scan samples. As a result of the high energy beam the sample material absorbs and the atoms in the sample material can become excited. This results in the emission of secondary electrons. The secondary electrons are accelerated towards a scintillating material. This causes the scintillating material to emit flashes of light, which are conducted to a photomultiplier. Subsequently, the electrical signal from the photomultiplier can be displayed as an analogue image or converted to a digital image.

When scanning samples, not all electrons in the high energy beam cause atoms in the sample material to become excited. This causes the sample material to charge. A conductive coating can be used to release the sample material from the surplus of electrons and thus prevent the sample material from charging. The samples presented in this thesis were coated with a conductive ~7 nm platinum coating. The samples presented in Figure 4.3 and 5.3 were imaged with a LEO 1530 Gemini FEG-SEM using a working distance of 3 mm and an accelerating voltage of 3 keV.

3.2.4 X-ray diffraction

X-ray diffraction (XRD) is a non-destructive elastic scattering technique using X-rays to analyse solid structures. XRD analyses can reveal structural and physical characteristics of crystalline phases. XRD relies on the repetitive character of crystal structures for the determination of the characteristics. The instrument used for the XRD analyses is a Bruker D8 X-Ray Diffractometer (Cu $k\alpha_1$). XRD was used for analyses of the solid samples obtained during the experiments described in chapter 4 and 7.

XRD uses the ability of interacting waves to cancel out or add up when they interfere. When two waves with the same frequency are synchronized, the amplitude of the waves will add up (constructive interference, Figure 3.4), while when a half wavelength phase shift occurs between these waves, they will cancel each other out (destructive interference, Figure 3.4). XRD uses these constructive and destructive interferences from diffracted X-rays (Figure 3.5). When the wavelength or a

multiple ($n\lambda$) of the incident beam is equal to $2d\sin\theta$ (i.e. $n\lambda$ is equal to the length of the line cab in Figure 3.5) than the scattered beams are in phase and a constructive interference results. Conversely, if $n\lambda \neq 2d\sin\theta$, a phase shift exists between the scattered beams and destructive interferences results from the interaction. Hence, if the d-spacing changes (Figure 3.5), so do the angles of the constructive interferences.

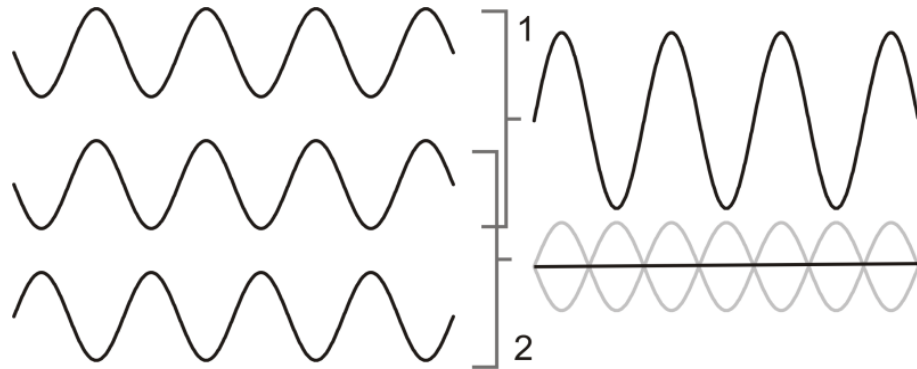


Figure 3.4 Graphic representation of the interactions of waves; 1) constructive interference and 2) destructive interference

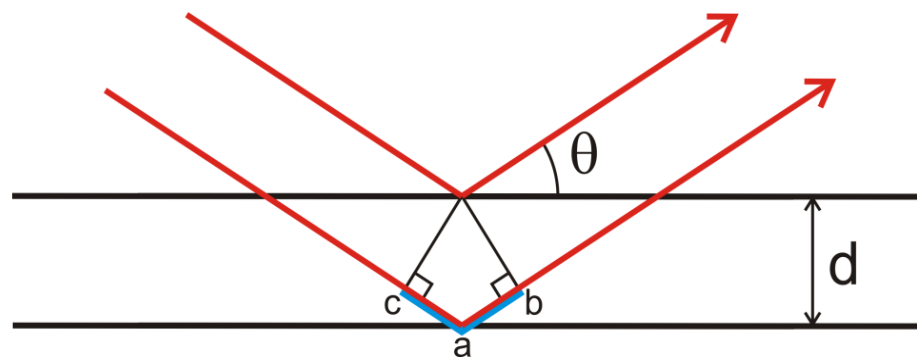


Figure 3.5 Bragg diffraction represented by a schematic representation of two parallel incident beams diffracted by two planes; $\sin \theta = ab/d = ca/d$, so: $d \sin \theta = ab = ca$

A mineral/crystal is built up from a lattice of repeating unit cells. A unit cell is the smallest repetitive 'unit' in a crystal structure. Unit cells have atom/ions in distinguishable positions. These features result in the appearance of (virtual) planes in the structure with miller indices representing these planes (PUTNIS, 1992). As an example the calcite unit cell is shown in Figure 3.6, with the (1 0 4) plane highlighted. Planes like the calcite (1 0 4) plane, act like the planes in Figure 3.5,

where the X-ray beams are scattered by atoms positioned in these planes (Figure 3.6B). Here, the above described mathematical relation ($n\lambda = 2d\sin\theta$, where $2d\sin\theta$ describes the length of the distance covered by the beam between points q and z) also explains the occurrence of constructive and destructive interference. This results in Bragg diffraction peaks in XRD patterns (bottom of Figure 3.6). Information can be extracted from an XRD pattern either to obtain a structural model from an unknown crystalline phase or to obtain physical information for a known structure via *Rietveld refinement*. *Rietveld refinement* on an XRD pattern can give information on: (1) the relative mass of the phases in a sample (HILL and HOWARD, 1987; RIETVELD, 1969), (2) crystallite size and strain of the crystalline phase (BALZAR and LEDBETTER, 1993) and (3) changes in the unit cell dimensions and the occupation of atomic positions in the unit cell (RIETVELD, 1969).

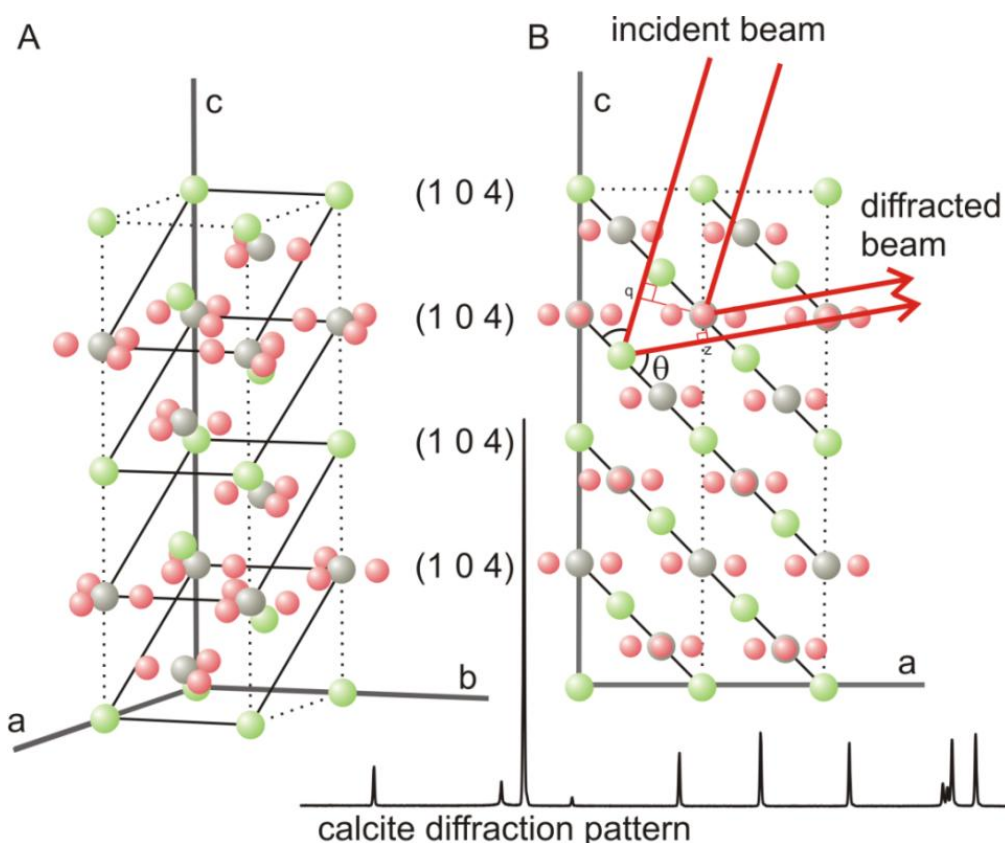


Figure 3.6 Calcite example on Bragg diffraction, the calcite unit cell is shown from two different angles, with the dotted lines representing the edges of the unit cell, the green spheres represent calcium, the grey spheres represent carbon and the red spheres represent oxygen, the carbonate ions only partly in the unit cells have been completed for ease, the structural information by MARKGRAF AND REEDER (1985) is used to construct the figure; A) 3D representation of a calcite unit cell, the black parallelograms show where the (1 0 4) planes are in the unit cell (these planes have the highest diffraction intensity); B) a view of two unit cells along the b axis, the tilted black lines show where the (1 0 4) planes are in this view, the red arrows represent the diffracted (X-ray) beams and at the bottom a typical diffraction pattern of calcite (with 7 weight% Si standard) is shown ($20 < 2\theta < 50$)

3.2.4.1 Relative mass of a phase in a sample

From the diffraction pattern, the *Rietveld scale factor* (S) can be calculated with Topas 4-2 (BRUKER_AXS, 2009). S relates a known crystalline structure to the integrated intensity of the Bragg peaks from the respective structure. Additionally S is proportional to the mass (m) in the sample (HILL and HOWARD, 1987; RIETVELD, 1969):

$$m_p \propto S_p(ZMV)_p$$

(Eq. 3.1)

where Z , M and V are the number of formula units per unit cell, the mass of the formula unit and the unit cell volume of phase p , respectively. This can subsequently be used to calculate the relative mass of all crystalline phases (m_p) in the diffraction pattern from a sample. Calculations on the relative mass of different phases were performed using Topas 4-2 (BRUKER_AXS, 2009) and are described in chapter 4 and 7 and appendix A.

3.2.4.2 Crystallite size and strain on the crystalline phase

In an infinitely large crystal (with an infinite amount of planes), when the angle deviates slightly from a perfect constructive interference ($2d \sin \theta \neq \lambda$, Figure 3.5), two diffracted beams have a half wavelength difference, causing a destructive interference (Figure 3.4). This results in infinitely narrow peaks at $n\lambda = 2d \sin \theta$ (GUINIER, 1963). A decrease in size of crystalline particles decreases this effect, causing the diffraction peaks to broaden (GUINIER, 1963). Strain induces a distortion of the lattice planes, due to external forces (e.g. stress) or internal forces (e.g. caused by the incorporation of magnesium or sulfate into calcite). Peak broadening caused by a decrease in crystallite size and due to strain can be separated because the broadening influence from the crystal size is length scale independent and strain acts more dominantly on smaller length scales (higher angles) (BALZAR and LEDBETTER, 1993).

3.2.4.3 Changes in the unit cell dimensions

The dimensions of a unit cell determine the d-spacing between planes causing the diffraction peaks, like the calcite (1 0 4) plane (Figure 3.6). When the dimensions of a unit cell change, so will the d-spacing causing Bragg diffraction peaks. The incorporation of foreign ions/atoms into the crystal structure can cause such a change in unit cell dimensions (in addition to causing strain, section 3.2.4.2) when the foreign ion/atom has a different size compared to the atom/ion it replaces. Magnesium has a smaller radius than calcium, so in addition to applying stress to the

calcite structure as described above, the calcite unit cell contracts (BISCHOFF et al., 1983; GOLDSMITH and GRAF, 1958; GOLDSMITH et al., 1961). Calculations on the lattice parameters were performed using Topas 4-2 (BRUKER_AXS, 2009). The results from these calculations are described in chapter 4 and 7. Additionally, Figure A.11 – A.13 and A.16 – A.18 (appendix A) visualize the effects of the incorporation of sulfate on the lattice parameters of calcite, aragonite and vaterite (A.11 – A.13 and A.16 – A.17) and the effect of magnesium on the lattice parameters of vaterite (Figure A.18).

3.3 Small and Wide Angle X-ray Scattering (SAXS/WAXS) and synchrotron based experimental methods

To study the kinetics and mechanisms of the transformation from ACC to crystalline calcium carbonate *in situ*, experiments have been performed at Diamond Light Source, Didcot, UK. These experiments were performed at the Small and Wide Angle X-ray Scattering (SAXS/WAXS) station, I22 (TERRILL et al., 2004). SAXS/WAXS, like XRD, is a non-destructive elastic scattering technique using X-rays that allows the characterization of solid phases. The results from the experiments at Diamond Light Source are discussed in chapter 5 and 6.

3.3.1 Synchrotron light

Performing experiments at synchrotron light sources has many advantages over laboratory-based X-ray sources. Due to the high brilliance of synchrotron light, the signal to noise ratio is very low. This allows time-resolved data collection with a time resolution of as low as 1 ms and the determination of disorder in amorphous phases like ACC. Additionally, because X-ray beams produced at a synchrotron light sources also have a low divergence, SAXS measurements can reach angles as low as $\sim 0.05^\circ$. Figure 3.7 shows a schematic representation of the layout of a Synchrotron. Below, a brief description of the production of synchrotron lights is presented.

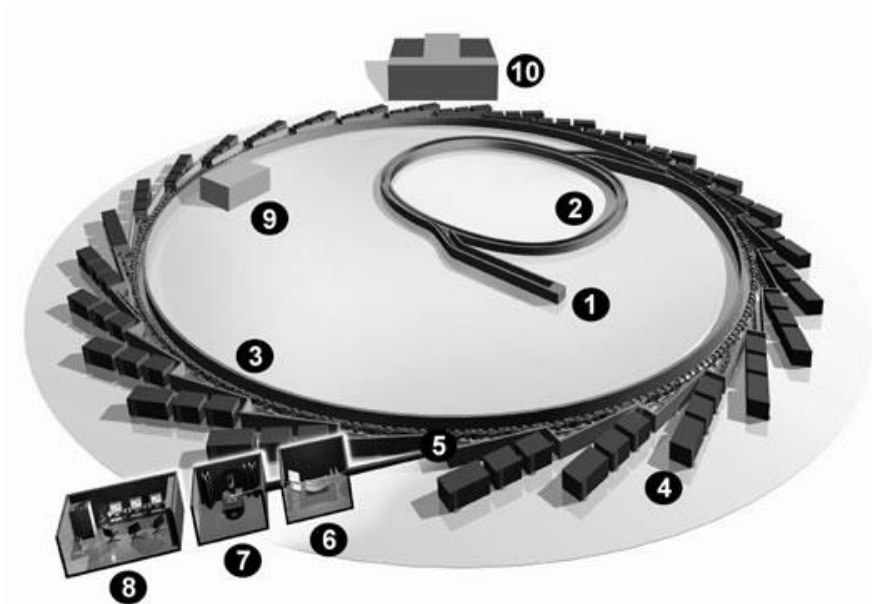


Figure 3.7 Schematic representation of Diamond Light Source
(www.diamond.ac.uk/Home/Technology.html)

The electron gun (1, Figure 3.7) in a synchrotron produces low energy electrons (90 keV), which are accelerated to gain energy in the linear accelerator (100 MeV). In the booster synchrotron (2, Figure 3.7), the electrons are accelerated further up to a maximum speed of close to the speed of light. The final energy before entering the storage ring (3, Figure 3.7) is 3 GeV, where the electrons are circulated using 48 bending magnets between equal amounts of straight sections. Synchrotron light is produced when the electrons pass through the bending magnets. Additionally, in the straight sections the electrons are oscillated by undulators and wigglers, which also produce synchrotron light. The synchrotron light is used in a wide range of beamlines with a wide range of applications (4-8, Figure 3.7). In each beamline, the synchrotron light is focussed and used for a wide variety of analytical techniques in the fields of imaging, scattering and spectroscopy. For the purpose of this project, experiments were performed at beamline I22 (SAXS/WAXS, Figure 3.8) because of the potential to perform solution based scattering experiments (chapter 5 and 6) at this versatile beamline.

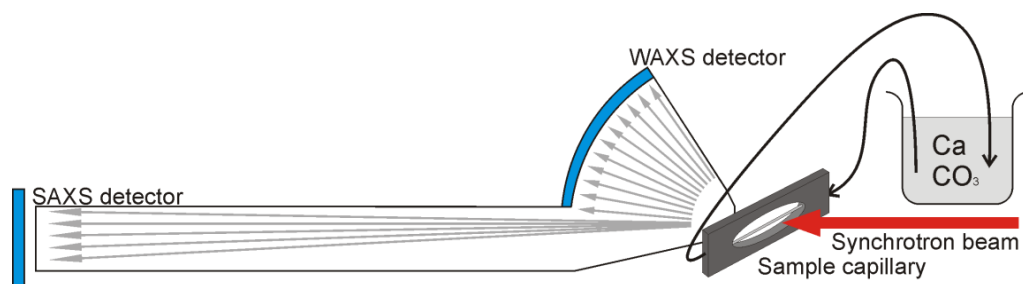


Figure 3.8 Schematic representation of the *in situ* experimental set-up at the SAXS/WAXS beamline at station I22

3.3.2 WAXS

Wide angle X-ray scattering is a technique based on the same principles as XRD (section 3.2.4). Therefore, in theory, all the analyses performed on XRD patterns can be performed on WAXS patterns as well (i.e. quantification of the phases present, determination of the unit cell parameters and the size and strain; section 3.2.4). However, the angle resolution in WAXS patterns (using a HOTWAXS detector) is much lower than can be obtained by conventional (powder) XRD. Hence, the results from WAXS analyses are far less accurate and precise as compared to regular (powder) XRD analyses (section 3.2.4). However, analyses of time-resolved WAXS patterns can provide valuable information on crystallization processes occurring in suspensions (e.g. AHMED et al., 2010; BEALE et al., 2006; BRAS et al., 2005; RYAN et al., 1995).

Using Topas 4-2 (BRUKER_AXS, 2009) the *Rietveld scale factor* (S) can be calculated. As discussed in section 3.2.4, S relates the structure of a known phase and the Bragg peaks in a WAXS (or XRD) pattern to the mass of the known phase in a sample (Eq. 3.1, HILL and HOWARD, 1987; RIETVELD, 1969). The *Rietveld scale factor* throughout the experiments ($S(t)$) can be normalized to the *Rietveld scale factor* at the end of the experiment (S_{final}). This results in the degree of reaction ($\alpha(t)$):

$$\alpha(t) = \frac{S(t)}{S_{final}}$$

(Eq. 3.2)

$\alpha(t)$ gives information about the reaction progress for the crystallizing phases (AHMED et al., 2010; RODRIGUEZ-BLANCO et al., 2011). However, when more than one crystalline phase forms during experiments, this definition of $\alpha(t)$ is not sufficient as it does not give information on the relative abundance of the crystalline phases throughout the experiments. The weight fraction (w) of phase (p) can be calculated with Topas 4-2 (section 3.2.4.1, BRUKER_AXS, 2009; HILL and HOWARD, 1987). The weight fraction at the end of the experiment ($w_{p,final}$) can then be used to normalize all phases to the final weight of the total amount of phases that are persistent until the end of the experiment:

$$\alpha_p(t) = \frac{S_p(t)}{S_{p,final}} \cdot w_{p,final}$$

(Eq. 3.3)

However, when an intermediate phase (i) forms during the experiment, this will not be sufficient. When the *Rietveld scale factor* of an intermediate phase (S_i) is at a maximum (i.e. at $t_{i,max}$) the relative weight fraction of the intermediate phase ($w_i(t_{i,max})$) compared to the relative weight fraction of one other phase present at the end of the experiment ($w_p(t_{i,max})$) and the previously calculated degree of reaction of this phase ($\alpha_p(t_{i,max})$, Eq. 3.3) can be used to obtain information about reaction progress of the intermediate phase via:

$$\alpha_i(t) = \frac{S_i(t)}{S_{i,final}} \cdot \left[\frac{w_i(t_{i,max})}{w_p(t_{i,max})} \cdot \alpha_p(t_{i,max}) \right]$$

(Eq. 3.4)

where the section between the square brackets represents a constant.

Finally, the decrease in the background intensity ($B(t)$) can be evaluated similarly to the intensity under the Bragg peaks. The background intensity at $t = 0$ (B_0) and the background intensity at the end of the experiment (B_{final}) can be used to calculate the degree of reaction for the breakdown of an amorphous phase (RODRIGUEZ-BLANCO et al., 2011):

$$\alpha(t) = \frac{B(t) - B_{final}}{B_0 - B_{final}}$$

(Eq. 3.5)

3.3.3 SAXS

As the name suggests, Small Angle X-ray Scattering (SAXS) acts on the smaller angles than WAXS. This means that SAXS patterns record larger scale features than WAXS and XRD (section 3.2.4). These features are generally not related to internal and structural features of crystalline phases (GLATTER and KRATKY, 1982; POROD, 1951). Initially, SAXS was developed for the study of biological material like proteins, however in this project SAXS was used to study the formation of inorganic solids (TOBLER et al., 2009). SAXS patterns (Figure 3.9) give information on the particle size, particle volume and morphological features and SAXS patterns are usually plotted against the scattering vector, q (\AA^{-1}):

$$q = \frac{4\pi}{\lambda} \sin \theta$$

(Eq. 3.6)

and:

$$q = \frac{2\pi}{d}$$

(Eq. 3.7)

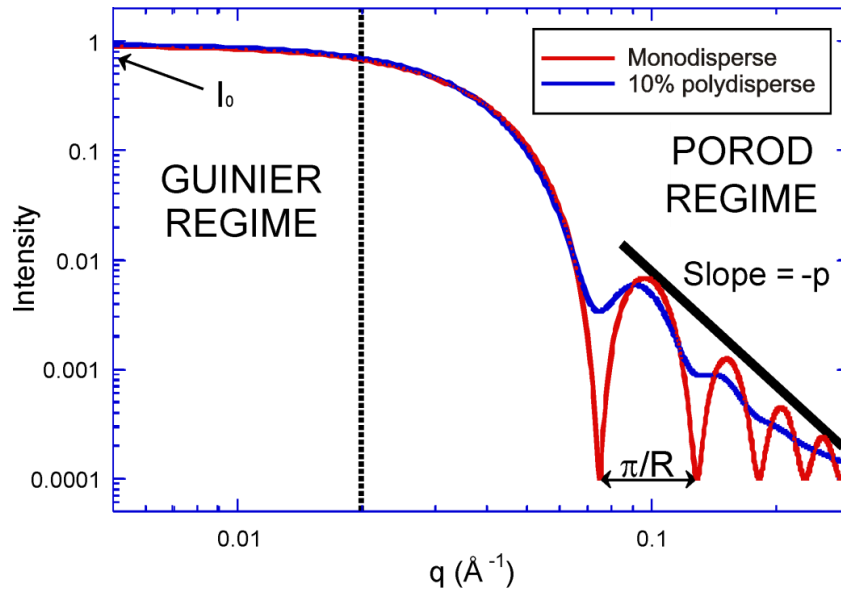


Figure 3.9 Examples of idealized SAXS patterns of a system with spherical particles with a radius (R) (modified from: <http://www.ansto.gov.au>)

In standard SAXS patterns, two regimes can be identified: the Guinier and the Porod regime (Figure 3.9). In the Guinier regime the measured intensity follows the following relationship (GLATTER and KRATKY, 1982; GUINIER, 1963; POROD, 1951):

$$I(q) = I_0 \exp \left[-\frac{q^2 R_g^2}{3} \right] \quad (\text{Eq. 3.8})$$

where I_0 is the (extrapolated) intensity at $q = 0$ and R_g is the radius of gyration. R_g is the weighed average radius of all cross sections through a particle and can be calculated from the slope of a $\ln(I(q))$ vs. q^2 plot of the Guinier region. When the particles are spherical, the following mathematical relationship can be used to calculate the radius (R) of the particles present in the system (GLATTER and KRATKY, 1982). Eq. 3.9 shows the relation between a spherical particle and the R_g . A list of relationships between R_g and the radii of particles is listed in GLATTER AND KRATKY (1982) for non-spherical particles. Additionally, R_g can be estimated using Eq. 3.8 and the slope in Figure 3.9 in the Guinier regime of the SAXS pattern. Additionally, R_g can be easily calculated using computer programs as GNOM (SVERGUN, 1992).

$$R_g^2 = \frac{3}{5}R^2$$

(Eq. 3.9)

When the analysed system is monodisperse, the particle diameter is easily determined from the SAXS patterns as shown in Figure 3.9. Polydispersity decreases the features in the Porod regime (Figure 3.9). However, when the system is still relatively monodisperse, the scattering from the particle population will still result in the appearance of at least one peak at low q ranges (Figure 3.9). The peak position at lowest q can then be used to estimate the particle diameter (d) (e.g., DE MOOR et al., 1999a; DE MOOR et al., 1999b) using Eq. 3.7.

Another parameter in Eq. 3.8 is I_0 , which can be estimated by extrapolation of the SAXS pattern to $q = 0$ (GLATTER, 1977; GUINIER, 1963). I_0 is related to the excess electrons in the scattering volume (GLATTER and KRATKY, 1982):

$$I_0 = (\Delta n_e)^2 = (\Delta\rho)^2 V^2$$

(Eq. 3.10)

where Δn_e is the excess electrons in the scattering volume, $\Delta\rho$ is the difference in electron density between the scattering particles and the medium and V is the scattering volume. The difference in electron density between the scattering particles and the medium is also related to the molecular weight of the scattering volume.

A third parameter that can be extracted from SAXS patterns is the invariant (Q) (BRAS et al., 2005; GLATTER and KRATKY, 1982; POROD, 1951). Q can be calculated using:

$$Q = \frac{1}{2\pi^2} \int_0^\infty I(q) q^2 dq$$

(Eq. 3.11)

The invariant is related to the volume fraction (Φ) of the scatterers and medium and the differences in electron density (BRAS et al., 2005; GLATTER and KRATKY, 1982; GOODISMAN and BRUMBERGER, 1971; LIU et al., 2010):

$$Q = \Phi(1 - \Phi)(\Delta\rho)^2$$

(Eq. 3.12)

If high quality data is collected and the particle density in the solution is low, the invariant (Q) and I_0 can be used to calculate the particle volume (V_p) of the scatterers with (GLATTER and KRATKY, 1982; GUINIER, 1963):

$$V_p \propto \frac{I_0}{Q}$$

(Eq. 3.13)

However, often the difficulties to calculate absolute intensities (KRATKY et al., 1966; PILZ, 1969; PILZ and KRATKY, 1967) and extrapolate to low and/or high q values prevent accurate I_0 and Q values to be derived. For example, if high q values are not measured, the invariant is difficult to evaluate, as the smallest particles might not be detected in the measured q range. Also, if the particles are too big to show significant features in the measured q range, I_0 and the scattering volume are highly underestimated. This limitation might be useful to study a nanoparticulate (by)product in the presence of large particles, when the large particles are not detected in the q range from the detector.

The last important parameter can be extracted from the Porod region (Figure 3.9) records information about the particle shape and morphology. POROD (1951) showed that the intensity of recorded SAXS patterns on a Log – Log plot decreases with a slope of 4. This was later determined only to hold for 3-dimensional particles with perfectly smooth surfaces. For all systems the following relation holds (BALE and SCHMIDT, 1984; BENNING and WAYCHUNAS, 2007; CICCARIELLO et al., 1988):

$$I(q) \propto q^{-p}$$

(Eq. 3.14)

where p is the Porod slope. From p information about the fractal dimension of a particle can be extracted (BALE and SCHMIDT, 1984; BENNING and WAYCHUNAS, 2007; SCHMIDT, 1991; TEIXEIRA, 1988). If $1 < p < 3$, the particle is a mass fractal and: p is the fractal dimension of a mass fractal (TEIXEIRA, 1988). If $3 < p < 4$, the particle has a fractal surface and: $p = 6 - D_s$, where D_s is the fractal dimension of the surface (Bale and Schmidt, 1984). Table 3.1 gives additional information on scatterers and their surface and mass dimensions.

Table 3.1 Table listing the fractal properties of scatterers (SCHMIDT, 1991) and relating these to the Porod slope, D is the fractal dimension, D_m is the mass fractal dimension, D_s is the surface fractal dimension and p is the Porod slope (Figure 3.9)

Scatterer	D_m	D_s	p
Mass fractal	D	D	1-3
Surface fractal	3	D_s	3-4
Extended scatterer	3	2	4
Thin platelet	2	2	2
Filament	1	1	1

3.3.4 Experimental methods and data collection

The crystallization of ACC was performed both off-line and on-line at room temperature by rapidly mixing equal volumes of two 1 M solutions of analytical grade calcium chloride ($\text{CaCl}_2 \cdot 2\text{H}_2\text{O}$) and sodium carbonate (Na_2CO_3). These ‘no additive’ experiments were complemented with sets of experiments performed with experiments where foreign (SO_4 , PO_4 and Mg) ions replaced either the CO_3 (SO_4 and PO_4) or the Ca (Mg) in the mixing solutions (‘replacement’ experiments, Figure 3.10A) or were added to either the CO_3 or the Ca in the mixing solutions (‘additive’ experiments, Figure 3.10B). During mixing and throughout the whole experimental time the suspensions were vigorously stirred to ensure rapid and continual homogenization.

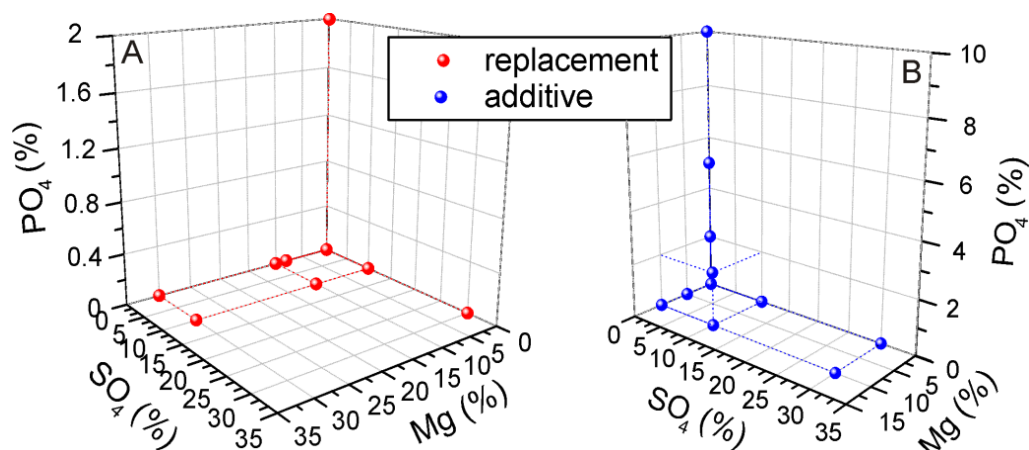


Figure 3.10 Graphical summary of all experimental conditions used in experiments performed at station I22 at Diamond Light Source

The on-line *in situ* experiments were performed at the small/wide angle X-ray scattering (SAXS/WAXS, Figure 3.8) beamline I22 at Diamond Light Source Ltd (UK). Immediately after mixing the suspensions were continuously pumped via a peristaltic pump through a capillary in line with the synchrotron beam. SAXS patterns were collected with a 2D RAPID detector (MARCHAL et al., 2009) or a 1D HOTSAXS detector (TERRILL et al., 2004) situated at 6 m from the sample capillary (Figure 3.8). Simultaneously WAXS patterns were collected with a HOTWAXS detector (Bateman et al., 2007) situated at 1.7 m from the sample capillary (Figure 3.8). Patterns were collected at one second / frame resolution for the total reaction duration of a minimum of ~35 min. The patterns were initially examined and exported to Excel with the computer program dream.jar (www.diamond.ac.uk). In Excel, the patterns were detector response corrected. This was done by dividing the experimental patterns by a silicon pattern (from which the silicon peaks were subtracted). Additionally, the collected patterns were background corrected by subtracting a sodium carbonate solution pattern (collected with the same instrument settings as the patterns from the respective experiment). For the calibration of the SAXS detectors, a pattern from a wet rat tail collagen standard was analysed. For the calibration of the WAXS detector, a pattern of a silicon standard was analysed.

To obtain additional information on the crystallization reactions, additional off-line experiments were performed. In the off-line experiments (chapter 5), the pH was continuously recorded (5 second time steps) and at specific time steps

(determined from the respective *in situ* experiment) aliquots of the suspensions were removed and filtered using a 0.2 μm membrane filters. The solids were immediately washed with isopropanol and dried (RODRIGUEZ-BLANCO et al., 2008) prior to further analyses. The results from the *in situ* and off-line experiments are described in chapter 5 and 6.

3.4 PHREEQC modelling

To complement the analytical data, simulations were performed using PHREEQC (http://wwwbrr.cr.usgs.gov/projects/GWC_coupled/phreeqc/, PARKHURST and APPELO, 1999). One set of simulations were performed to relate the calcium carbonate mineralogy to the fluctuations in Phanerozoic seawater composition (chapter 4 and appendix A). A second set of simulations was performed to derive chemical information that could not be analysed directly (e.g. saturation indices and chemical speciation), based on the analyses from the experimental solutions from the off-line experiments described (chapter 5 and Appendix B).

3.4.1 Evaporation simulations

PHREEQC evaporation simulations using the Pitzer equation (PARKHURST and APPELO, 1999) were carried out to evaluate the minerals formed from evaporating seawater with varying Mg and SO_4 concentrations as would have occurred during the Phanerozoic (HARDIE, 1996). The composition of the input solutions in the evaporation model solutions (2-20 mM Mg, 5-15 mM SO_4 , 10.5 mM Ca 10.4 mM K and 558 mM Cl; Na was adjusted to charge balance the solutions, Table A.1) were within the chemical range of the experimental solutions (Table 4.1). In addition, the Phanerozoic seawater composition from both calcite and aragonite seas, including compositions between these end members (8 mM SO_4 , 30 mM Ca and 29 mM Mg to 29 mM SO_4 , 10 mM Ca and 54 mM Mg, HORITA ET AL., 2002; Table A.2) were also used as input solutions in the evaporation simulations. The simulations were run by removing increasing amounts of H_2O from the solutions and allowing precipitation (Table A.3) of all major evaporite minerals (Table A.4, HARDIE, 1996). The evaporation simulations were validated comparing the PHREEQC simulation of

modern seawater (Figure A.9a and Figure A.10a) with the simulation by HARDIE (1991). There were no significant differences between the PHREEQC simulation and the simulation by HARDIE (1991).

3.4.2 Modelling the chemical evolution of the SAXS/WAXS experiments

As described in section 3.3.4, chapter 5 and Appendix B, off-line experiments were performed to complement the *in situ* SAXS/WAXS crystallization experiments. During these experiments, the pH was measured and at specific time steps, solution samples were analysed for the SO_4 and Ca concentrations. Due to the fast kinetics of the reaction and the necessity to take samples throughout the experiments, no alkalinity measurements were possible. To obtain information on the alkalinity and hence the saturation index (SI), PHREEQC simulations were performed.

Because of (potential) CO_2 exchange with the atmosphere, these simulations were not straightforward. To obtain close to realistic values for alkalinity and SI in a complex system, every step of the experiments was simulated in PHREEQC. The first step of the simulation was to create the initial solutions (Figure 3.10 and line 6-19 in Table 3.2). The second step was to mix these solutions (line 21-25, Table 3.2) and then the final step was to use the analysed solution data (pH, [Ca] and [SO_4]). In line 27-31 (Table 3.2), the precipitation of $\text{Ca}(\text{CO}_3)_{1-x}(\text{SO}_4)_x$ was simulated, where x is the mole fraction of SO_4 . The precipitation of $\text{Ca}(\text{CO}_3)_{1-x}(\text{SO}_4)_x$ was incorporated in the model, so that the simulated solution reached the measured [Ca] and [SO_4]. Finally, the exchange of dissolved carbonate with the atmosphere was simulated in order to reach the pH measured during the experiments (line 1-4 and line 32-34, Table 3.2). Results from these PHREEQC simulations are shown in Figure 6.5 and Appendix B.

Table 3.2 The first 29 lines of the input file for the PHREEQC simulations to model the chemical evolution during the SAXS/WAXS experiments, the example here is for the ‘replacement’ experiment described in chapter 5

1	Phases		
2	pH_fix		
3	H+ = H+		
4	Log_k	0	
5			
6	Solution 1		
7	Reaction 1		
8	Na2CO3	0.9	
9	Na2SO4	0.1	
10	1		
11	Save solution	1	
12	End		
13			
14	Solution 2		
15	Reaction 2		
16	CaCl2	1	
17	1		
18	Save solution	2	
19	End		
20			
21	Mix 1		
22	1	0.5	
23	2	0.5	
24	Save solution	3	
25	End		
26			
27	Use solution	3	
28	Reaction 3		
29	CaCO3	-0.41991	#-(0.5 – “measured Ca” – (0.05 – “measured SO ₄ ”))
30	CaSO4	-0.00464	#-(0.05 – “measured SO ₄ ”)
31	1		
32	Equilibrium_phases	3	
33	pH_fix	-8.757	CO2(g)
34	end		

3.5 Method development

This section describes developments/adjustments of methods to analyse solution and solid chemistry obtained from the experiments (chapter 4 and 7). The photospectrometric method described in section 3.5.1 was developed to obtain a fast and reliable method to analyse aqueous calcium and magnesium. This method is based on method 8030 from the Hach[®] DR/2500 manual. The method described in section 3.5.2 was developed to analyse the chemical composition of solid calcium carbonate phases accurately and precisely using ion chromatography. This method is

based on the column switching method to analyse nutrients in high salinity solution described by BRUNO et al. (2003) and the cation method to analyse the chemical composition of fish otoliths and seawater with a high precision and accuracy as described by MARINI et al. (2006)

3.5.1 A photospectrometric method to analyse Ca and Mg

3.5.1.1 Basic principles

The photospectrometric method described here is a modification of method 8030 from the Hach[®] DR/2500 manual, which uses calmagite (Figure 3.11) as complexing agent in the indicator solution. Calmagite colours an alkaline solution purple-blue. Calcium and magnesium present in solution complex to calmagite, which colours the solution red. In addition, EDTA forms stronger complexes with calcium and magnesium than calmagite. This then prevents colouring caused by calmagite complexed to calcium and magnesium. Similarly, EGTA forms stronger complexes to magnesium, preventing colouring caused by calmagite complexes with magnesium. The absorption of the three solutions described above was measured at a wavelength of 522 nm. The differences in the absorbance between the three solutions were used to calculate the calcium and magnesium concentrations.

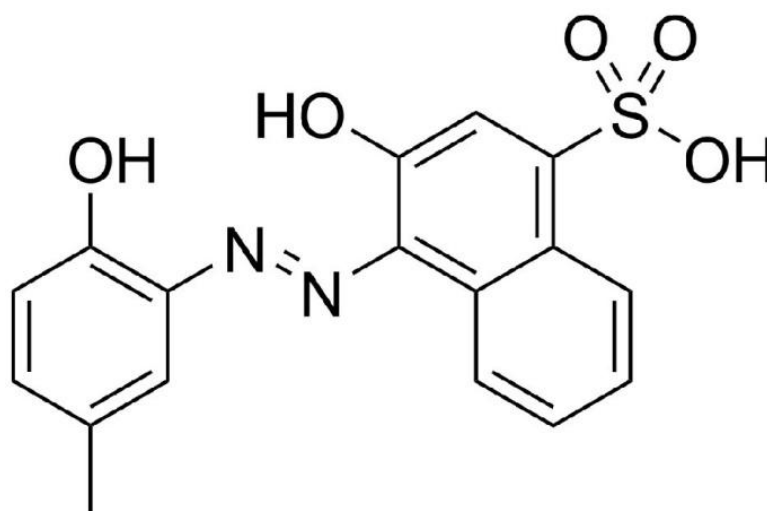


Figure 3.11 The chemical structure of Calmagite

3.5.1.2 Tests

Test 1

The calcium and magnesium concentrations of the standard solutions (~50 ml) used in the first test are listed in Table 3.3. To obtain a calibration for these concentrations, the following method was used:

- 1 Add approximately 0.5 ml of the Hach[®] calmagite solution
- 2 Add approximately 0.5 ml of the Hach[®] alkali solution
- 3 Mix the obtained solutions properly
- 4 Add:
 - a. 30 µL EDTA solution to 5 ml of the solution obtained at step 3 and mix
 - b. 30 µL EGTA solution to 5 ml of the solution obtained at step 3 and mix
- 5 Measure the absorbance of the solutions with calmagite, with calmagite and EDTA and with calmagite and EGTA
 - a. The difference between the absorbance from the solution with calmagite and EDTA and the solution with calmagite and EGTA corresponds to the magnesium concentration
 - b. The difference between the absorbance from the solution with calmagite and EGTA and the solution with only calmagite corresponds to the calcium concentration

Table 3.3 Concentrations of the first set of standard solutions tested including the respective absorbance measurements; the measured absorbance is for the solution with calmagite and EDTA (1), calmagite and EGTA (2) and only calmagite (3)

nr	Mg (ppm)	Ca (ppm)	Measured absorbance			Mg 2-1	Ca 3-2
			1	2	3		
1	0.25	0	0.512	0.681	0.690	0.169	0.009
2	0.02	0.03	0.504	0.521	0.528	0.017	0.007
3	0.75	0.25	0.499	0.928	0.984	0.429	0.056
4	0	0.5	0.490	0.504	0.602	0.014	0.098
5	0.5	1	0.506	0.820	0.851	0.314	0.031
6	1	1.5	0.513	0.852	0.965	0.339	0.113

The results from the first test are summarized in Table 3.3 and Figure 3.12. The calibration curves show a linear response up to 0.5 ppm calcium and 0.75 ppm magnesium. In sample number 5 and 6 (Table 3.3), the amount of calmagite was too low to complex all calcium and magnesium in the absence of EDTA and EGTA. However, when EGTA was added to the alkaline solution of sample number 5 and 6, the amount of calmagite was enough to complex all calcium. This caused the calcium Δ absorbance (see step 5b, above) to deviate from the linear response. Additionally in sample number 6 (Table 3.3) the amount of EGTA is too low to complex all magnesium in solution. This resulted in a deviation of the magnesium Δ absorbance (see step 5a, above) from the linear response (Figure 3.12).

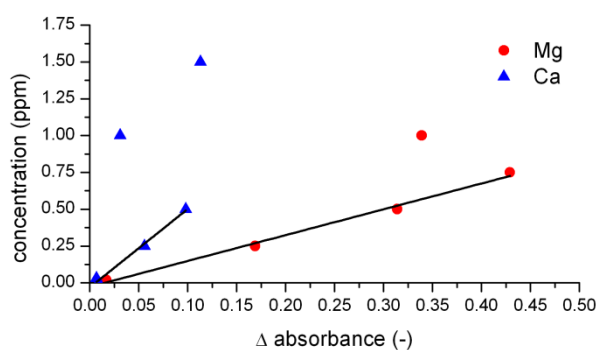


Figure 3.12 The calibration curves for the first set of standard solutions tested

Test 2

To overcome the above described problems the next method is used for the standard solutions (~50 ml) listed in Table 3.4:

- 1 Add approximately 1 ml of the Hach[®] calmagite solution
- 2 Add approximately 1 ml of the Hach[®] alkali solution
- 3 Mix the obtained solutions properly
- 4 Add:
 - a. 2 drops with a Pasteur pipette (~100 μ L) EDTA solution to 5 ml of the solution obtained at step 3 and mix
 - b. 2 drops with a Pasteur pipette (~100 μ L) EGTA solution to 5 ml of the solution obtained at step 3 and mix

- 5 Measure the absorbance of the solutions with calmagite, with calmagite and EDTA and with calmagite and EGTA
 - a. The difference between the absorbance from the solution with calmagite and EDTA and the solution with calmagite and EGTA corresponds to the magnesium concentration
 - b. The difference between the absorbance from the solution with calmagite and EGTA and the solution with only calmagite corresponds to the calcium concentration

Table 3.4 Concentrations in second set of standard solutions tested including the respective adsorbance measurements; the measured absorbance is for the solution with calmagite and EDTA (1), calmagite and EGTA (2) and only calmagite (3)

nr	Mg (ppm)	Ca (ppm)	Measured absorbance			Mg 2-1	Ca 3-2
			1	2	3		
1	0.25	0	0.818	1.001	1.019	0.183	0.018
2	0.05	0.05	0.847	0.887	0.909	0.040	0.022
3	0.75	0.25	0.854	1.379	1.440	0.525	0.061
4	0	0.5	0.860	0.864	0.977	0.004	0.113
5	0.5	1	0.855	1.214	1.411	0.359	0.197
6	1	1.5	0.860	1.520	1.710	0.660	0.190

The results from the second test are summarized in Table 3.4 and Figure 3.13. The calibration curves show a linear response up to 1 ppm Ca and Mg. In sample number 6 (Table 3.4) the amount of calmagite was still too low to complex all calcium and magnesium. However, when EGTA was added to the alkaline solution of sample number 6, the amount of calmagite was enough to complex all calcium. This caused the calcium Δ absorbance (see step 5b, above) to deviate from the linear response. Additionally, this method was used as test measurements on experimental solution samples. These tests indicated that occasionally calcium also complexed to EGTA, underestimating the calcium concentration and overestimating the magnesium concentration (see step 5, above).

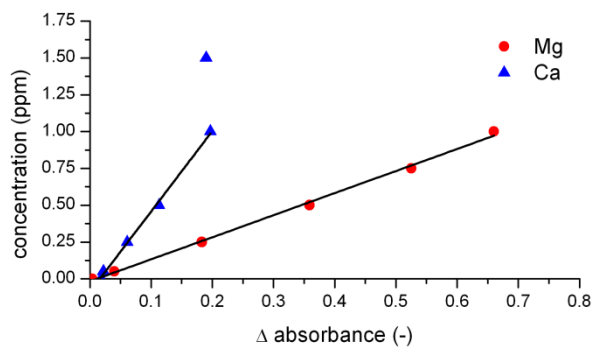


Figure 3.13 The calibration curves for the second set of standard solutions tested

3.5.1.3 Final method

The final method for the photospectrometric measurements of calcium and magnesium is described below and the results of analyses on the standard solutions are summarized in Table 3.5 and Figure 3.14. Additionally, to highlight the validity of this method, the analysed calcium and magnesium concentrations from a selection of constant addition experiments are plotted in Figure 3.15 (chapter 4: Table 4.1). This method has also been used to analyse the calcium and magnesium concentrations of the vaterite ageing experiments described in chapter 7.

- 1 Add approximately 1 ml of the Hach[®] calmagite solution to ~50 ml solution
- 2 Add approximately 1 ml of the Hach[®] alkali solution
- 3 Mix the obtained solutions properly
- 4 Add:
 - a. 2 drops (~100 μ L) EDTA solution to 5 ml of the solution obtained at step 3 and mix
 - b. 1 drop (~50 μ L) EGTA solution to 5 ml of the solution obtained at step 3 and mix
- 5 Measure the absorbance of the solutions with calmagite, with calmagite and EDTA and with calmagite and EGTA
 - a. The difference between the absorbance from the solution with calmagite and EDTA and the solution with calmagite and EGTA corresponds to the magnesium concentration
 - b. The difference between the absorbance from the solution with calmagite and EGTA and the solution with only calmagite corresponds to the calcium concentration

Table 3.5 Concentrations in final set of standard solutions tested including the respective adsorbance measurements; the measured absorbance is for the solution with calmagite and EDTA (1), calmagite and EGTA (2) and only calmagite (3)

nr	Mg (ppm)	Ca (ppm)	Measured absorbance			Mg 2-1	Ca 3-2
			1	2	3		
1	0.25	0.75	0.840	1.048	1.224	0.208	0.176
2	0.05	0.05	1.094	1.136	1.164	0.042	0.028
3	0.05	0.05	0.973	1.022	1.049	0.049	0.027
4	0.682	0.227	1.014	1.508	1.571	0.494	0.063
5	0	0.5	0.993	1.001	1.117	0.008	0.116
6	0.5	1	1.030	1.403	1.603	0.373	0.200
7	0.25	0	0.818	1.001	1.019	0.183	0.018
8	0.05	0.05	0.847	0.887	0.909	0.04	0.022
9	0.75	0.25	0.854	1.379	1.440	0.525	0.061
10	0	0.5	0.860	0.864	0.977	0.004	0.113
11	0.5	1	0.855	1.214	1.411	0.359	0.197

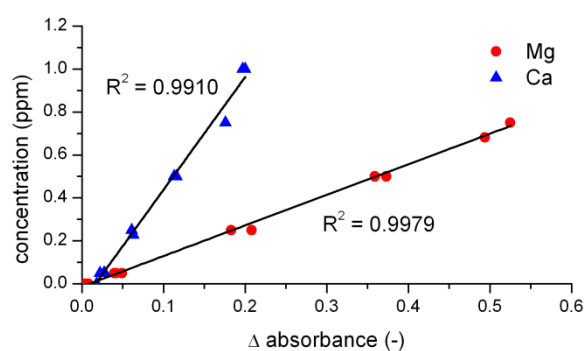


Figure 3.14 The final calibration curves

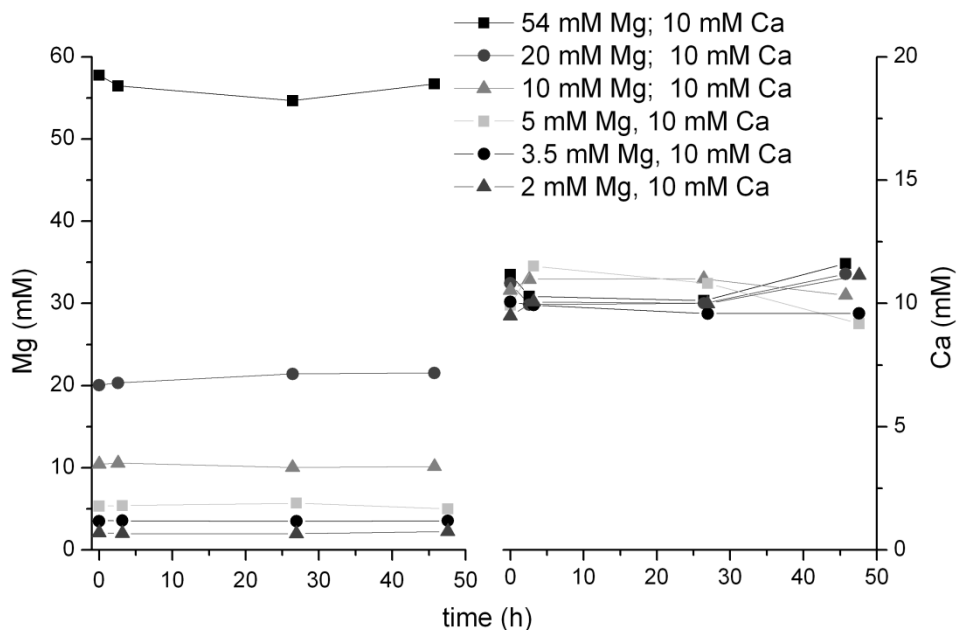


Figure 3.15 Magnesium and calcium concentrations from a selection of constant addition experiments (chapter 4) measured with the photospectrometric method; the legend states the chemistry of the solution as added before starting the experiments

3.5.2 Measuring solid composition of CaCO_3 using Ion Chromatography

Solid calcium carbonate samples were dissolved in diluted HCl to measure the chemical composition using IC (section 3.2.2). This dissolution approach was based on the method described by MARINI et al. (2006). Approximately 50 mg calcium carbonate was weighed and dissolved in 5 ml of 1.2 M HCl. The resulting solution was diluted with MilliQ water up to 15 ml. One aliquot of this solution was diluted 10 times to measure calcium and magnesium using the method described by MARINI et al. (2006) using a methanesulfonic acid (MSA) eluent. A second aliquot of this solution was diluted 2 times to measure sulfate following a column switching method described by BRUNO et al. (2003) with carbonate/bicarbonate eluents. All the measurements described here were performed on a Dionex[®] DX-500 ion chromatography system using a conductivity detector to detect the separated ions. The combined method described below was used for the measurements on the chemical composition of the calcium carbonate samples produced with the constant addition experiments (chapter 4).

3.5.2.1 Cations

MARINI et al. (2006) used an IonPac[®] CS12A chromatographic column, 18 mM MSA eluent with a flow rate of 1 ml/min and a sample injection volume of 100 μ l. The IonPac[®] CS12A chromatographic column has a medium capacity to alkaline earth and alkali metals and ammonium. The method did not include a guard column (Figure 3.3). To improve the ion separation between calcium and magnesium in the column, a less concentrated eluent was used (15 mM MSA). With this eluent, the first test measurements were performed on a series of acidified calibration standards and a test sample of dissolved CaCO₃ (Figure 3.16). The peaks of all the metal ions in the chromatographs from the test measurements are split. This caused the calcium peak to overlap the position of the magnesium peak. Hence, the magnesium peak could not be distinguished from the calcium peak (Figure 3.16B and 3.16C).

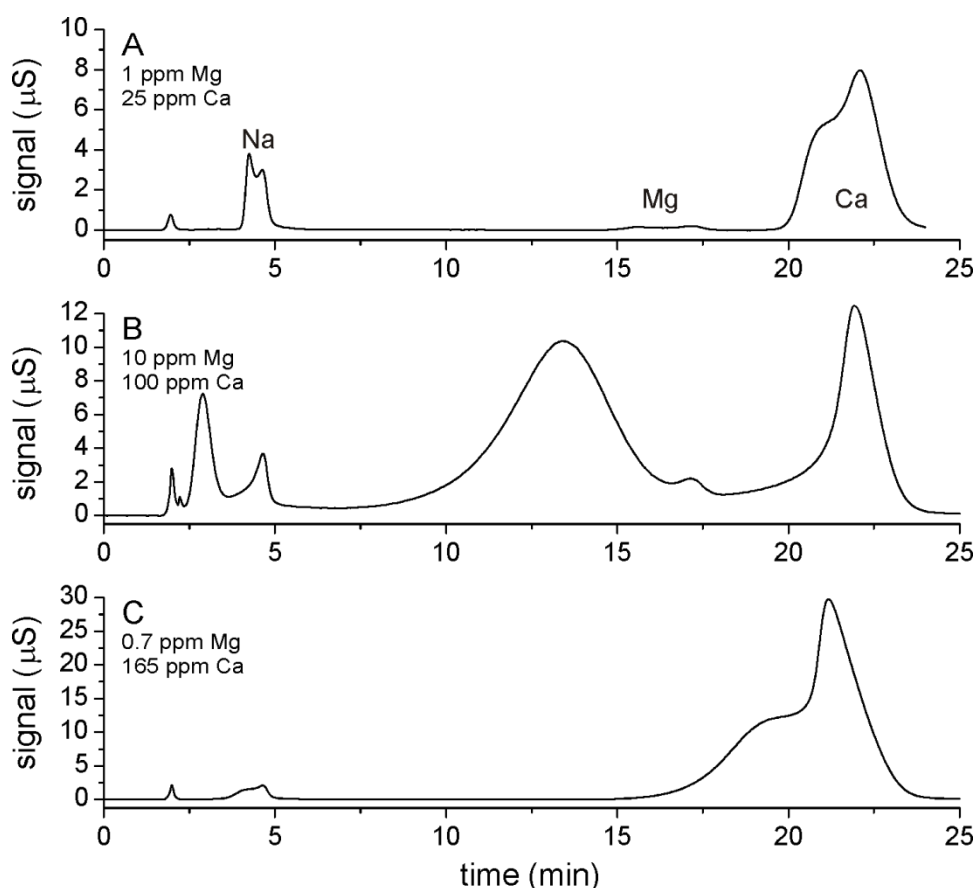


Figure 3.16 Chromatographs of the first test of the method to measure cations (A) a standard with: 2.5 ppm Na, 1 ppm Mg and 25 ppm Ca (B) a standard with: 10 ppm Na, 7.5 ppm Mg and 100 ppm Ca (C) a test sample from the constant addition experiments (chapter 4)

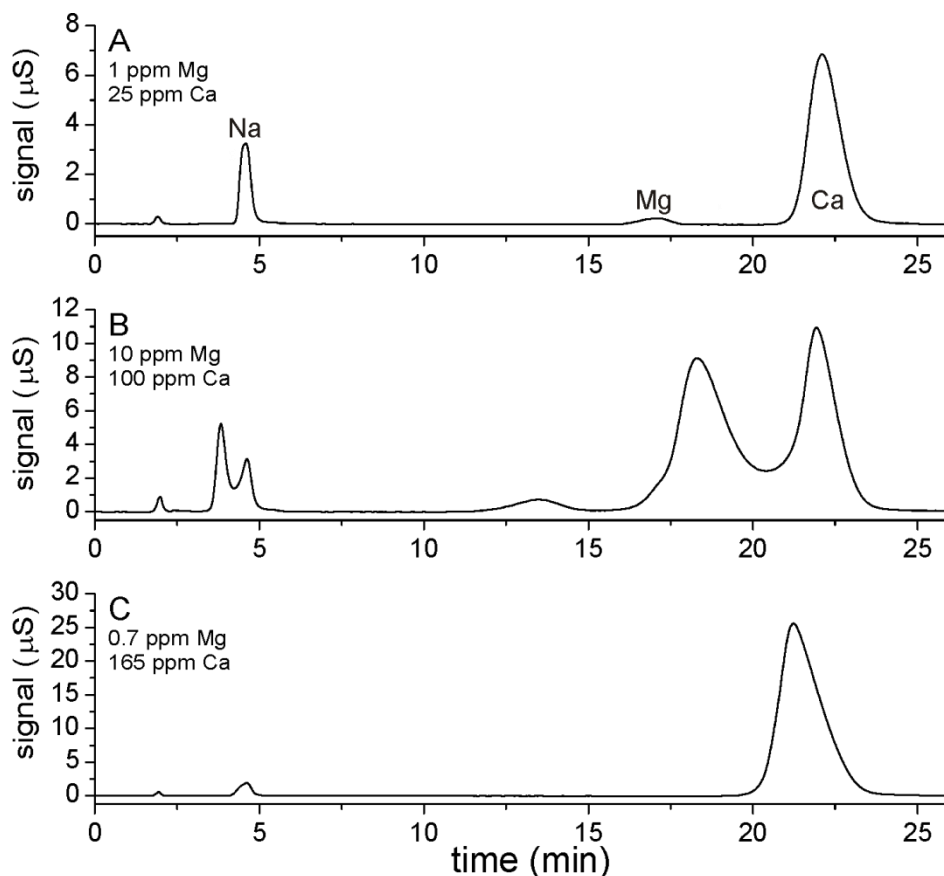


Figure 3.17 Chromatographs of the second test of the method to measure cations (A) a standard with: 2.5 ppm Na, 1 ppm Mg and 25 ppm Ca (B) a standard with: 10 ppm Na, 7.5 ppm Mg and 100 ppm Ca (C) a test sample from the constant addition experiments (chapter 4)

Split peaks in IC are generally caused by high acidity of samples. To counter this, a second test on the same samples was performed with a decreased injection volume (25 µl, Figure 3.17). Using a decreased injection volume greatly decreased the appearance of the split peaks. However the high calibration standards (Figure 3.17B) still showed split peaks in all cations included in the calibration standard. The split calcium peak in the high calibration standards still covered the position of the Mg peak (Figure 3.17B). However the low standards and the test sample (Figure 3.17A and 3.17C) did not show any split peaks. The split peaks in the high standards was caused by the use of more than 10% of a 1000 ppm calcium standard which was acidified with HNO₃. To decrease the acidity of the calibration standards a fresh 1000 ppm calcium standard was prepared from pure CaCO₃ dissolved identically to the dissolution of the experimental CaCO₃ samples as described above. When performing the measurements with calibration standards prepared with the freshly

prepared calcium standard no split peaks were observed in any chromatograph (Figure 3.18). In the chromatographs a good separation between the calcium and magnesium peaks can be observed in both, the calibration standards (Figure 3.18A and 3.18B) and the samples (Figure 3.18C and 3.18D). Additionally, this method did show a good regression between the calibration standards and the detected conductivity (Figure 3.19). Finally, the calcium and magnesium peak position shifted with increasing concentration (Figure 3.16 – 3.18). This, however, did not seem to influence the validity of the method. Hence, it was used to measure the calcium and magnesium composition of the solid samples produced in the constant addition experiments (chapter 4).

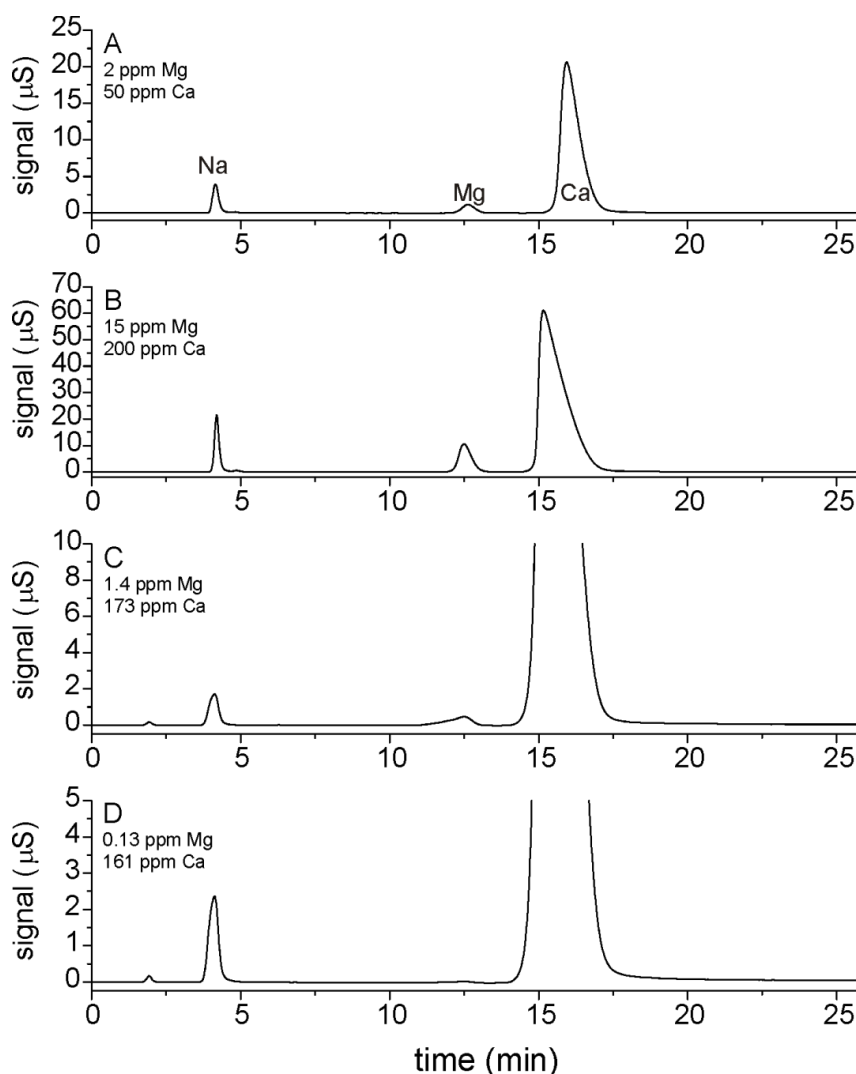


Figure 3.18 Chromatographs of the final method to measure the cation contents of dissolved calcium carbonate samples (A) a standard with: 2 ppm Na, 2 ppm Mg and 50 ppm Ca, (B) a standard with: 15 ppm Na, 15 ppm Mg and 200 ppm Ca (C) and (D) samples from the constant addition experiments (Table 4.1)

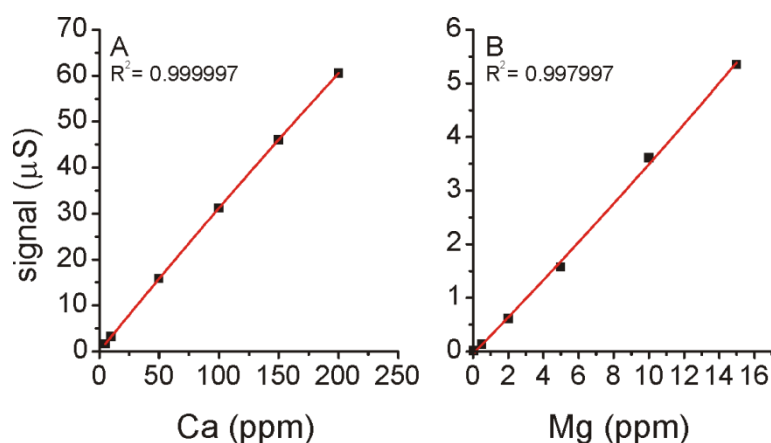


Figure 3.19 Calibration curves from the final method to measure cation content of dissolved carbonate samples

The use of this IC method to measure cations in dissolved carbonate is advantageous over the use of ICP-MS and ICP-AES for alkaline earth and alkali metals because of the small sample size needed for the analyses (25 μl instead of $>250 \mu\text{l}$, de VILLIERS et al., 2002; Yu et al., 2005). An additional advantage of this method is that an additional dilution step is not necessary, in contrast to analysing cation incorporation using ICP-MS (YU et al., 2005). It should also be noted that the method described here only includes the analyses of Na, Mg and Ca. However, Li, K, NH_3 , Mn, and Sr can also be analysed as described by MARINI et al. (2006).

Finally, calculations indicate that for this method the use of $<200 \mu\text{g}$ of calcium carbonate is needed to obtain 1 ml of solution for analyses. This mass is similar to the mass of shell material used when measuring Mg/Ca ratios in foraminiferal calcite using ICP-MS (OKAFOR et al., 2009). A test on this was performed using a sample of unwashed foraminifera. Seven aliquots of this sample were weighed ($\sim 0.09 - 0.21 \text{ mg}$) and dissolved in 10 μl 0.6 M HCl and diluted up to 0.5 – 1 ml. Figure 3.20 shows that the measured of the magnesium and strontium to calcium ratios lay between 3 and 3.5 mmole/mole and 0.75 and 0.9 mmole/mole respectively. The standard deviations (Figure 3.20) are similar to the standard deviations from measurements using ICP-MS (OKAFOR et al., 2009). Additionally, the inter-sample variation could be explained by residual evaporite or clay minerals, because the foraminiferal calcite was unwashed.

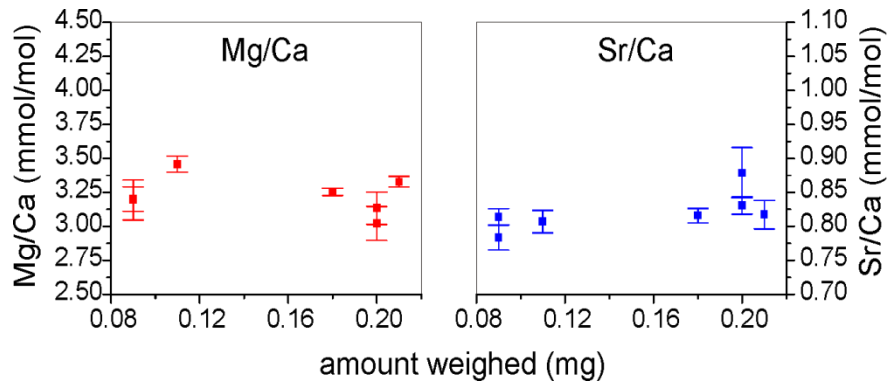


Figure 3.20 Test on the analyses of cations in an unwashed foraminifera sample as a function of the mass of material weighed, the symbols represent the averages of three analyses on the same dissolution and the error bars represent the respective standard deviations

The photospectrometric (section 3.5.1) and the ion chromatography method both allow simultaneous calcium and magnesium analyses. However, the photospectrometric method is quicker than the ion chromatography method. Hence, the photospectrometric method is more suitable to perform analyses on many samples. Additionally, the ion chromatography method is more precise and the concentration range is significantly larger compared to the photospectrometric method (Figure 3.14 and 3.19). Hence, when the magnesium and calcium concentrations are significantly different like in foraminiferal calcite (Figure 3.20) and when high precision is required the ion chromatography method is more suitable.

3.5.2.2 Anions

The IC method to analyse SO_4 used here was designed to analyse nutrients in saline solutions (BRUNO et al., 2003). The method used a high capacity analytical column (IonPac[®] AS9-HC) and two guard columns (IonPac[®] AG9-HC). During the analyses, a 14 mM carbonate – 3 mM bicarbonate eluent (EA) and a 9 mM carbonate eluent (EB) were used. Between the guard columns and the analytical column, a switching valve was located (Figure 3.21).

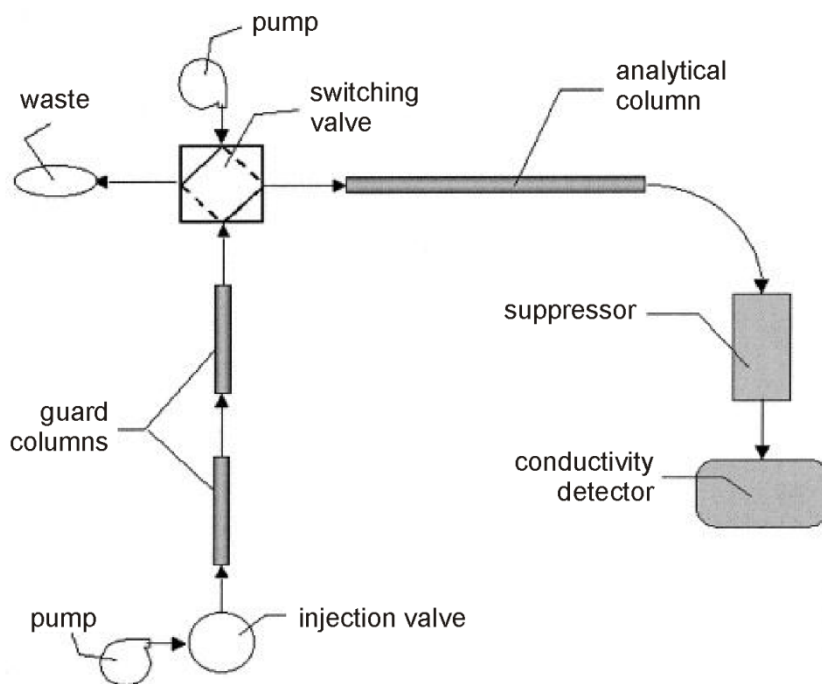


Figure 3.21 Column switching ion chromatography set-up used for the method to analyse anions in dissolved calcium carbonates, based on the method described by BRUNO et al. (2003)

An initial separation was achieved in the two guard columns using eluent EA. This allowed for the switching valve to selectively remove much of the chloride to waste while retaining the nutrients (BRUNO et al., 2003). The nutrients were further separated in the analytical column using eluent EB. This method was used in this method development because of the high chloride concentration in the solutions due to the use of HCl to dissolve the CaCO₃ samples. Finally, sulfate was analysed using a conductivity detector (BRUNO et al., 2003).

Initially, the position of the valve switch needed to be determined to eliminate most of the chloride from the measurement but to retain the SO₄. This was done by temporarily eliminating the analytical column and the valve switch from the set-up. This resulted in the chromatograph shown in Figure 3.22A. The conductivity signal from chloride and sulfate can be identified in this chromatograph. When implementing the valve switch at 1 min., most of the chloride signal is removed from the chromatograph and the sulfate signal is still detected by the conductivity detector (Figure 3.22B). Hence, the first test to analyse sulfate in the dissolved calcium carbonate samples was performed using the complete set-up including the analytical column (Figure 3.21) with the valve switch at 1 min (Figure 3.23).

The height of the chloride peak differed between the analyses of both calibration standards, yet the amount of chloride in both calibration standards was equal (Figure 3.23A and 3.23B). This indicates that the switching valve does not always switch at exactly 1 min as anticipated. This variability caused some of the sulfate in the injected sample to be removed to waste instead of separated on the analytical column. Due to this variability in the timing of the valve switch, the measurement is not stable with the switch at 1 min. This is shown in Figure 3.24A, where the detected signal of sulfate was not proportional to the amount of sulfate in the calibration standards. Hence, the valve switch was set at 0.85 min (Figure 3.25). This did show a good regression between the sulfate concentration in the calibration standards and the detected conductivity ($R^2 = 0.99994$, Figure 3.24B). Hence, this method was used to measure the sulfate composition of the solid samples produced in the constant addition experiments (chapter 4).

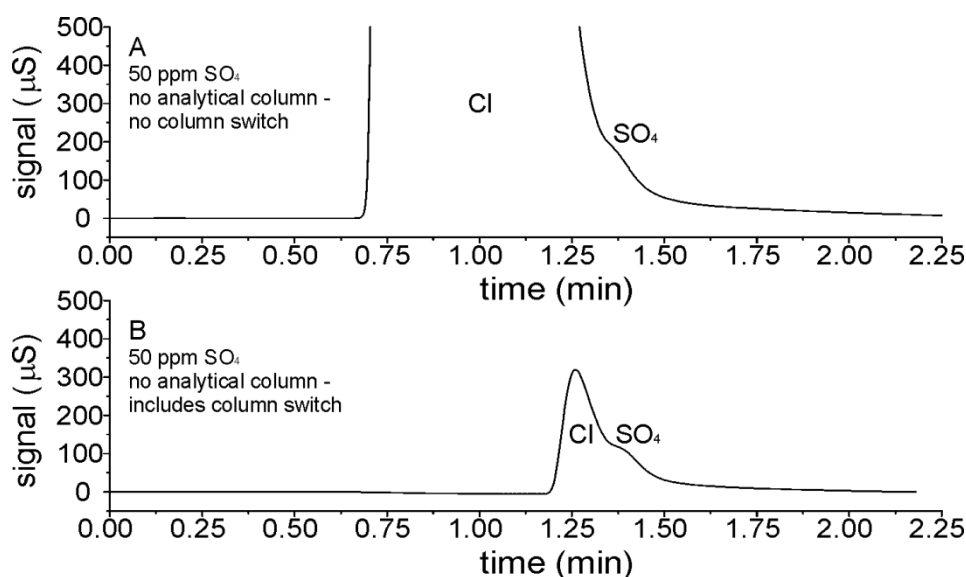


Figure 3.22 Test chromatographs of a standard with 50 ppm SO₄ to determine the timing of the column switch (A) chromatograph of the 50 ppm standard using only the guard columns in the set-up (B) chromatograph of the 50 ppm standard using the guard columns and the switching valve (at 1 min) without the analytical column

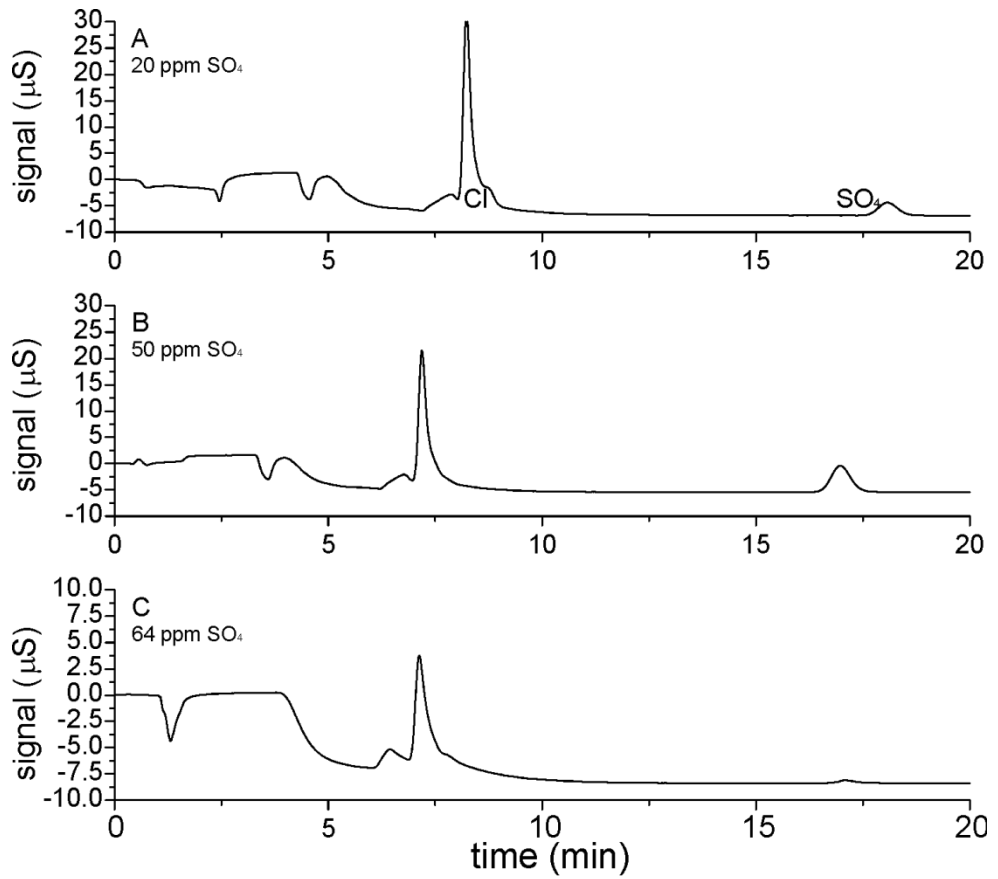


Figure 3.23 Chromatographs of the test with the analytical column in line and with the column switch at 1 min. (A) a standard with 20 ppm SO₄ (B) a standard with 50 ppm SO₄ (C) a CaCO₃ sample described in chapter 7

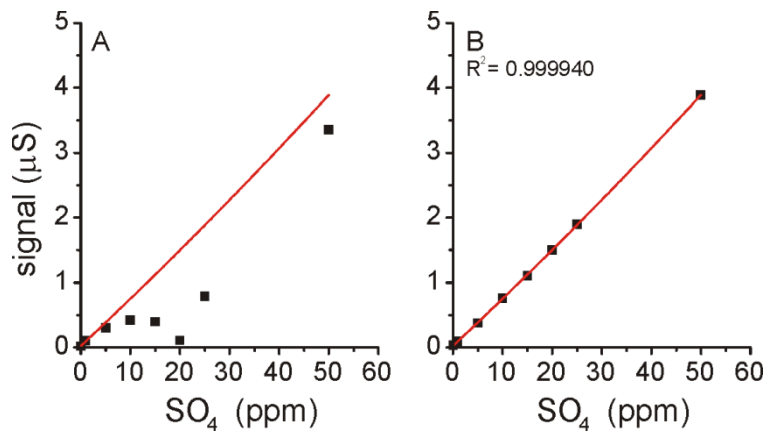


Figure 3.24 Two calibrations of the method to measure anions in dissolved calcium carbonate samples with the column switch at (A) 1 min. (Figure 3.23) (B) 0.85 min. (Figure 3.25); the red lines are the best fit for the calibration with the column switch at 0.85 min

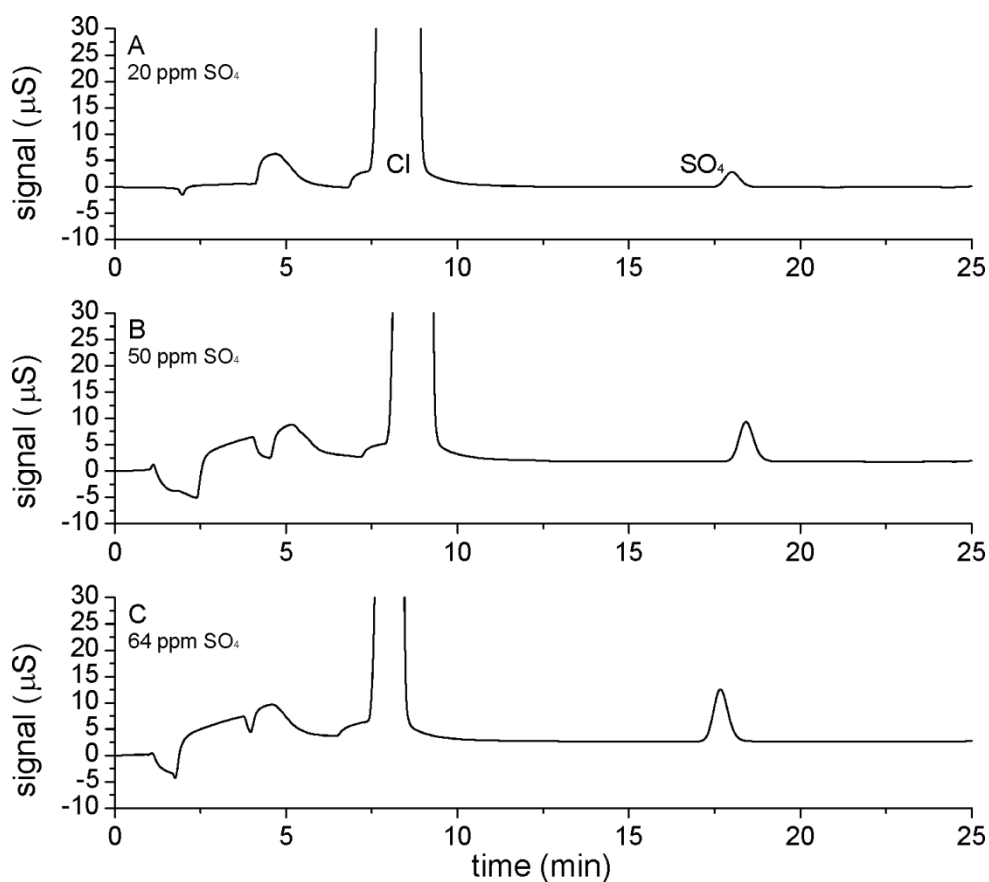


Figure 3.25 Chromatographs of the final method with the analytical column in line and with the column switch at 0.85 min. (A) a standard with 20 ppm SO₄ (B) a standard with 50 ppm SO₄ (C) a CaCO₃ sample described in chapter 7

The IC method described here is a simple method to analyse the sulfate composition of calcium carbonate samples, using the dissolution method described in section 3.5.2.1. Figure 3.26 shows the results from measurements of carbonate associated sulfate (CAS) in foraminiferal calcite. The results from the valve switching method show a similar trend as the results from the gravimetric method (Figure 3.26). However, two calcium carbonate samples do show a large difference between the CAS determined using IC and the gravimetrically determined CAS. For these, the gravimetric method resulted in a negative amount or exactly 0 ppm CAS (Figure 3.26). Hence, the CAS values obtained using the IC was likely to be better representative of the samples. Additionally, gravimetric determination on the amount of CAS in samples can have an error of up to 50% (OLCOTT et al., 2004). Finally, the dissolution method and the analyses described here to determine the chemical composition of calcium carbonate are less elaborate than gravimetric

methods (NEWTON et al., 2004). Hence, the valve switching method is likely to be suitable for CAS determinations.

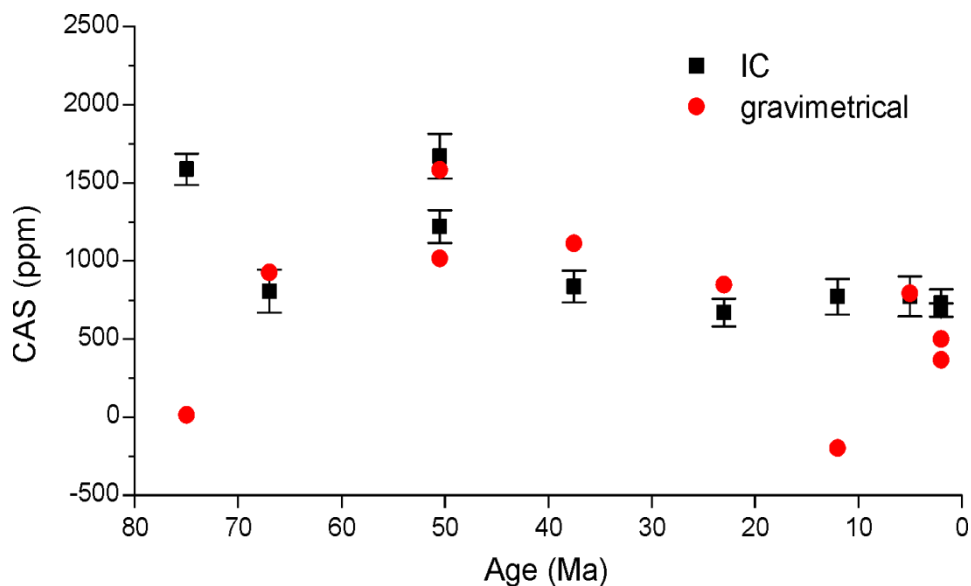


Figure 3.26 Measurements on the amount of CAS in foraminiferal calcite, the black squares represent the average of 4 separate analyses on the amount of CAS using IC and the error bars represent the respective standard deviation, the red circles represent the amount of CAS determined using the gravimetric method (CLERC, 2007); multiple analyses with the same age were performed on different size fractions of the same sample

Tests were also performed to determine the necessary amount of HCl needed to easily dissolve calcium carbonate samples. This resulted in the possibility to decrease the amount of HCl used to dissolve the calcium carbonate samples. Less HCl could additionally lead to eliminating the switching valve in the method. This would make the method much less prone to the variability of the valve switch as discussed above. This could decrease the standard deviation in the measurements significantly. Additionally, chromatographs of CAS analyses in foraminiferal calcite showed the possibility to analyse phosphate and nitrate in addition to sulfate for which the valve switching method was designed (BRUNO et al., 2003).

Chapter 4¹

The role of SO₄ in the switch from calcite to aragonite seas

4.1 Abstract

Throughout the Phanerozoic, the primary inorganic marine calcium carbonate mineralogy oscillated between calcite and aragonite, reflecting changes in seawater chemistry. These variations in seawater composition also appear to have influenced the evolution of calcifying organisms. However, the processes controlling these mineralogical and biological changes are poorly constrained: previous work has focused mainly on the Mg/Ca ratio in seawater as the primary driver. Here I examine the role of dissolved SO₄ in these processes by performing controlled laboratory precipitation experiments and geochemical modelling of evaporite formation. I show that an increase in dissolved SO₄ decreases the Mg/Ca ratio at which calcite is destabilized and aragonite becomes the dominant CaCO₃ polymorph. My data suggest that the Mg/Ca and SO₄ thresholds for forming a calcite sea are significantly lower than previous estimates and are mutually dependent. This shows that our understanding of Phanerozoic changes in seawater chemistry and the models relating this to primary CaCO₃ mineralogy need re-evaluation.

4.2 Introduction

The primary marine CaCO₃ polymorph in cements and ooids is documented to have oscillated between calcite and aragonite throughout the Phanerozoic

¹ The online supporting information (GSA data repository) to the published material is described in section 4.6 and the figures from the GSA data repository are deposited in Appendix A. The Appendix to this chapter (Appendix A) also contains the Topas Rietveld refinements (only described in the publication) and the results and description of unpublished test experiments performed at 10°C.

(SANDBERG, 1983). The periods recognized when predominantly abiotic calcite or aragonite formed are now known as calcite and aragonite seas. However, the records show that during the Phanerozoic, the CaCO_3 formed was rarely pure calcite or aragonite (WILKINSON et al., 1985; ZHURAVLEV and WOOD, 2009). Similar patterns in CaCO_3 biomineral formation have been reported for several, but not all, marine fossils (e.g. bryozoans and rugose corals). Most organisms adopted the dominant mineralogical form from the oceans in which they evolved (e.g., STANLEY, 2006; WILKINSON et al., 1985; ZHURAVLEV and WOOD, 2009), suggesting that the oceans had a profound effect on the evolution of calcifying organisms (PORTER, 2007). Explanations ranging from aqueous Mg/Ca (DAVIS et al., 2000; MORSE et al., 1997; STANLEY, 2006), to temperature (BURTON and WALTER, 1987), to pCO_2 , and subsequent changes in pH and alkalinity (SANDBERG, 1983; WILKINSON et al., 1984), have been invoked to explain the oscillating trends in CaCO_3 mineralogy. Currently, the aqueous Mg/Ca ratio is thought to have been the major driving force behind the changes (HARDIE, 1996; LOWENSTEIN et al., 2003; MORSE et al., 1997). Mg substitution for Ca in the calcite structure is a function of the Mg/Ca and temperature (BURTON and WALTER, 1991). Mg substitution affects the thermodynamic stability of calcite (DAVIS et al., 2000; KÖNIGSBERGER and GAMSJÄGER, 1992) and inhibits calcite growth (DAVIS et al., 2000). In addition, experimental studies have shown that Mg has a negligible effect on the stability of aragonite, causing aragonite to precipitate instead of calcite at an aqueous Mg/Ca higher than ~ 1.3 (MORSE et al., 1997). However, models of the chemical changes in seawater suggest that the switch from calcite to aragonite seas occurred at an aqueous Mg/Ca from ~ 1 (WILKINSON and ALGEO, 1989) to ~ 2 (HARDIE, 1996). These differences indicate that some uncertainty remains about the threshold level of Mg/Ca to induce a mineralogical change.

Coincident with the changes in CaCO_3 mineralogy, the evaporites that precipitated from marine brines during the same geological periods oscillated between KCl (calcite sea) and MgSO_4 (aragonite sea) types (HARDIE, 1996), which formed from seawater containing higher concentrations of dissolved CaCl_2 and MgSO_4 , respectively (LOWENSTEIN et al., 2003). Analyses of halite fluid inclusions indicated that SO_4 and Mg/Ca co-varied during the Phanerozoic in phase with the changes in CaCO_3 mineralogy (HORITA et al., 2002; LOWENSTEIN et al., 2003). These observations support the hypothesis that changes in solution chemistry (e.g.

Mg/Ca) were responsible for the oscillations between calcite and aragonite seas (e.g., STANLEY, 2006), but they also suggest that other dissolved ions (e.g. SO_4) might have a significant influence.

The concentration of SO_4 in the Phanerozoic sea has been determined to have fluctuated between ~5 and ~30 mM (HORITA et al., 2002; LOWENSTEIN et al., 2003), and experimental studies have shown that SO_4 decreases calcite stability and precipitation rate more markedly than for aragonite (BUSENBERG and PLUMMER, 1985; WALTER, 1986). This indicates that in addition to Mg/Ca, SO_4 may also act as a major influence on CaCO_3 precipitation (RAILSBACK and ANDERSON, 1987). However, the influence of SO_4 in addition to that of the Mg/Ca ratio on the calcite to aragonite seas has so far been largely overlooked (LEE and MORSE, 2010).

I quantified the effects of SO_4 and Mg/Ca ratio on the CaCO_3 mineralogy precipitated from solutions by performing laboratory-based CaCO_3 synthesis experiments at a range of SO_4 concentrations and Mg/Ca values. These experiments were combined with information from geochemical models of changes in evaporite mineralogy caused by fluctuations in seawater composition, allowing us to include SO_4 in, and re-evaluate, the existing models relating seawater chemistry to CaCO_3 mineralogy throughout the Phanerozoic.

4.3 Methods

Constant addition experiments were performed at 21 ± 1 °C using the method of TESORIERO AND PANKOW (1996). Glass spheres (100 μm Biospec Products©) were used to create a surface for nucleation and to mimic the inorganic precipitation of CaCO_3 on ooids. The initial solution for each experiment (500 mL) contained 10 mM CaCl_2 , 0–55 mM MgCl_2 , 0–100 mM Na_2SO_4 , and 2 g/L glass spheres. The total Mg and SO_4 concentrations bracketed proposed Phanerozoic seawater concentrations (HORITA et al., 2002). The salinity (ionic strength of ~0.6 M) and initial pH (~8.2, in equilibrium with the atmosphere) were adjusted to seawater values by the addition of NaCl and NaOH, respectively. While being continuously shaken on an orbital shaker (270 rpm), precipitation was induced by continuously injecting two solutions into the initial solutions via a syringe pump at 1 mL/h for ~48 h. These input solutions contained 250 mM CaCl_2 or 230 mM Na_2CO_3 . MgCl_2

(0–110 mM) or Na₂SO₄ (0–200 mM) was added to the input solutions to negate dilution of Mg and SO₄. At the start, during (~5 times), and at the end of the experiments, the pH of the reacted solutions was measured. Simultaneously, solution samples (~4 mL each) were removed and filtered through 0.2 μm filters and were either immediately acidified with HCl (for total Ca and Mg measurements) or stored frozen (for total SO₄ measurements). After the experiments were terminated (~48 h), the precipitated solids were separated from the solutions by filtering through 0.2 μm membrane filters. The resulting solids were washed three times with 18.2 MΩ Milli-Q grade H₂O equilibrated with calcite, filtered again, and dried at 95 °C for a minimum of 24 h.

The solutions were analyzed for total Ca and Mg using a spectrophotometric method using calmagite as an indicator (Method 8030, Hach Lange, Düsseldorf, Germany) and for total SO₄ by ion chromatography (IC) with a carbonate/bicarbonate eluent. The equilibrium alkalinity was calculated with PHREEQC (PARKHURST and APPELO, 1999) from the equilibrium pH, assuming equilibrium with the atmosphere. Powder X-ray diffraction (XRD) analyses of the solids were performed using a Bruker D8 X-Ray Diffractometer (Cu Kα1) with a silicon internal standard. The XRD patterns were analyzed with Topas4–2[®] (BRUKER_AXS, 2009) to determine the relative proportions of the precipitated CaCO₃ polymorphs and the CaCO₃ unit cell dimensions. Finally, aliquots of the precipitates were dissolved in 1.2 M HCl, and the resulting solutions were analyzed using IC methods modified after MARINI ET AL. (2006) to measure Ca and Mg, and after BRUNO ET AL. (2003) to measure SO₄. During most experiments, a mixture of calcite, aragonite, and/or vaterite precipitated (Table 4.1). If the solid samples contained more than 99% aragonite, the total SO₄ and Mg solid composition was assumed to represent the composition of aragonite. The aragonite compositions (as a function of the solution chemistry) were then used to calculate the aragonite composition in samples with less than 99% aragonite. The total composition and the estimated aragonite compositions were then used to calculate the calcite and vaterite composition in the samples where either calcite or vaterite was present alongside aragonite. This approach was used to determine the composition of the CaCO₃ polymorphs in all samples.

Table 4.1 Summary of the CaCO₃ mineralogy and composition from the constant addition experiments

Solution chemistry*		Solid composition after 48h										
SO ₄ (mM)	Mg/Ca (mM/mM)	Polymorph distribution [†]			Total composition		Calcite [§]		Aragonite [§]		Vaterite [§]	
		Calcite (%)	Aragonite (%)	Vaterite (%)	SO ₄ (mol%)	Mg (mol%)						
0.0	0.00	100.0	0.0	0.0	0.00	0.000	0.00	0.00	–	–	–	–
0.0	0.22	97.3	2.7	0.0	0.00	0.627	0.00	0.64	0.00	0.012	–	–
0.0	0.55	89.9	10.1	0.0	0.00	1.403	0.00	1.81	0.00	0.025	–	–
0.0	0.77	6.3	93.5	0.0	0.00	0.144	0.00	1.87	0.00	0.031	–	–
0.0	0.96	<1	99.5	0.0	0.00	0.028	–	–	0.00	0.028	–	–
0.0	1.99	0.0	100.0	0.0	0.00	0.057	–	–	0.00	0.057	–	–
0.0	5.22	0.0	100.0	0.0	0.00	0.088	–	–	0.00	0.088	–	–
5.1	0.21	94.0	6.0	0.0	1.02	0.602	1.07	0.64	0.25	0.012	–	–
5.1	0.36	37.2	62.8	0.0	0.43	0.361	0.74	0.94	0.25	0.018	–	–
4.9	0.52	6.6	93.5	0.0	0.25	0.103	0.44	1.25	0.24	0.024	–	–
5.3	0.77	<1	99.3	0.0	0.24	0.035	–	–	0.24	0.035	–	–
9.8	0.00	90.4	0.0	10.6	1.62	0.000	1.74	0.00	–	–	0.59	0.00
11.0	0.10	70.4	29.6	0.0	1.23	0.221	1.56	0.31	0.43	0.007	–	–
10.6	0.22	46.7	53.3	0.0	0.91	0.274	1.47	0.59	0.42	0.012	–	–
10.1	0.51	<1	99.1	0.0	0.38	0.022	–	–	0.38	0.022	–	–
9.7	0.75	<1	99.7	0.0	0.41	0.034	–	–	0.41	0.034	–	–
10.2	1.00	0.0	100.0	0.0	0.41	0.026	–	–	0.41	0.026	–	–
22.9	0.10	12.4	52.0	35.7	0.91	0.153	2.08	0.30	0.66	0.006	0.87	0.32
36.5	0.00	1.5	12.9	85.6	1.22	0.000	3.07	0.00	0.87	0.000	1.28	0.00
33.5	0.10	1.5	66.5	32.0	0.92	0.107	2.44	0.31	0.83	0.007	1.05	0.31
34.4	0.19	<1	99.5	0.0	0.86	0.011	–	–	0.86	0.011	–	–
31.8	0.51	<1	99.6	0.0	0.77	0.023	–	–	0.77	0.023	–	–
32.4	1.01	0.0	100.0	0.0	0.81	0.034	–	–	0.81	0.034	–	–
57.6	0.00	0.0	30.2	69.8	1.37	0.000	–	–	1.13	0.000	1.48	0.00
56.8	0.10	0.0	88.1	11.9	1.11	0.047	–	–	1.11	0.007	1.32	0.35
110.8	0.00	0.0	69.4	30.6	1.69	0.000	–	–	1.60	0.000	1.88	0.00
109.9	0.23	0.0	100.0	0.0	1.47	0.013	–	–	1.47	0.013	–	–
104.8	0.51	0.0	100.0	0.0	1.50	0.023	–	–	1.50	0.023	–	–
106.4	0.98	0.0	100.0	0.0	1.57	0.046	–	–	1.57	0.046	–	–

*The solutions in all experiments also contained 10mM Ca and had an ionic strength of ~0.6M

[†]<1 was used when 0–1% calcite was present.

[§]A hyphen was used when the composition for this polymorph is not relevant.

PHREEQC (PARKHURST and APPELO, 1999) evaporation simulations were carried out to evaluate the minerals formed from evaporating seawater with varying Mg and SO₄ concentrations, as would have occurred during the Phanerozoic (HARDIE, 1996). The method, starting solution compositions, and detailed results from the PHREEQC simulations are described in section 4.6.1 and Appendix A (Table A.1 – Table A.4; Figure A.1 – Figure A.10).

4.4 Results and discussion

The solution chemistry and solid composition for all experiments are summarized in Table 4.1. During most experiments, a mixture of calcite, aragonite, and/or vaterite precipitated. The dominant polymorph (>50%) as a function of Mg/Ca and SO₄ concentration is plotted in Figure 4.1. Note that 100% calcite only formed in experiments without Mg and SO₄ in solution (Table 4.1). With increasing

Mg in solution, the Mg substitution into calcite increased (Table 4.1). This change in composition caused the calcite stability to decrease and the aragonite to calcite ratio in the solid to increase (Table 4.1). In the absence of sulfate, only aragonite precipitated at $Mg/Ca > \sim 1.7$ (Figure 4.1), which is in accordance with results given by MORSE ET AL. (1997), while at $Mg/Ca > \sim 0.6-0.7$, aragonite became the most dominant phase precipitated (Figure 4.1). DAVIS ET AL. (2000) showed that when Mg exceeds ~ 1.8 mol% in calcite, aragonite becomes more stable than calcite, which is in agreement with the calculated calcite compositions in the samples when aragonite becomes dominant over calcite (Table 4.1). This suggests that the stability of the $CaCO_3$ polymorphs is marked by its dominance field in Figure 4.1.

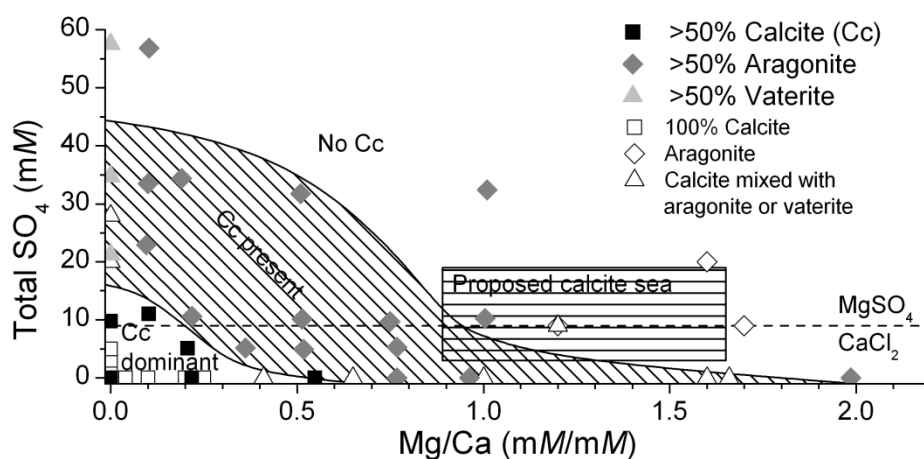


Figure 4.1 Polymorph distribution as a function of solution chemistry; closed symbols represent dominant $CaCO_3$ polymorph as measured in current study; open symbols represent previous research (DONER and PRATT, 1969, 26 °C; LEE and MORSE, 2010, 23 °C; MORSE et al., 1997, 20 °C; SIMKISS, 1964, 22 °C with an increase to 28 °C); diagonally shaded area highlights Mg/Ca and SO_4 field where calcite was present in solid phase after 48 h between 0% and 50%; horizontally shaded area represents proposed calcite sea concentrations (HORITA et al., 2002); and dashed horizontal line represents switch from KCl to $MgSO_4$ evaporites (LOWENSTEIN et al., 2003) as determined from PHREEQC evaporite simulations.

When the SO_4 concentration in calcite (Table 4.1) increased, there was an anisotropic change in the calcite unit cell parameters (1.5 mol% SO_4 incorporation caused the c-axis to increase by 0.22% and the a-axis to decrease by 0.035%; Figure A.11). This is indicative of the substitution of tetrahedral SO_4 for planar CO_3 ions in calcite (KONTREC et al., 2004). Hence, changes in pH or alkalinity will affect the

incorporation of SO_4 into the calcite structure (BUSENBERG and PLUMMER, 1985). The change in the calcite structure by SO_4 incorporation caused calcite solubility to increase (BUSENBERG and PLUMMER, 1985) and is likely to have decreased the calcite precipitation rate relative to aragonite (WALTER, 1986). Incorporation of SO_4 into aragonite was ~2–4 times lower than into calcite (Table 4.1). Furthermore, SO_4 had little effect on the aragonite structure (1.5 mol% SO_4 incorporation caused the c-axis to increase by ~0.07% and the b-axis to increase by ~0.02%; Figure A.12) compared to calcite. This demonstrates that SO_4 influenced the stability of aragonite different than calcite, causing aragonite to become more stable than calcite. This explains the precipitation of aragonite instead of calcite at lower Mg/Ca in the presence of SO_4 (e.g. Mg/Ca = 0.9 at 10 mM SO_4 ; Figure 4.1).

SO_4 incorporation into vaterite (a rare and unstable CaCO_3 mineral) did not significantly affect the unit cell parameters of vaterite (Figure A.13). This indicates that the precipitation of vaterite in the presence of SO_4 and absence of Mg (Table 4.1; Figure 4.1) (DONER and PRATT, 1969; SIMKISS, 1964) was likely to be caused by a positive effect of SO_4 on the stability of vaterite (FERNÁNDEZ-DÍAZ et al., 2010) relative to calcite. Mg incorporation into vaterite (Table 4.1) caused a significant decrease in the unit cell parameters (0.3 mol% Mg decreased the a-axis by 0.06% and the c-axis by 0.03%), while it did not affect the SO_4 incorporation. Vaterite inhibition at aqueous Mg/Ca \geq 0.2 is likely to be due to the changes in the vaterite structure caused by Mg incorporation.

4.5 Implications for Phanerozoic seawater chemistry

The mineralogical and morphological data indicate that SO_4 exerted a significant influence on CaCO_3 polymorphs (Figure 4.1; Figure 4.3). In contrary to previous experimental work, the current study used constant solution compositions (e.g. pH, $[\text{Ca}^{2+}]$) and a precipitation mechanism that mimicked oöid formation to give a good representation of abiotic calcium carbonate formation in Phanerozoic seawater (see section 4.6.2). My data show that SO_4 needs to be incorporated into the models relating Phanerozoic seawater chemistry with the switch from calcite to aragonite seas. PHREEQC evaporation simulations using input solutions in the experimental range predicted a switch between KCl and MgSO_4 evaporites

(coincident to CaCl_2 and MgSO_4 seas and calcite and aragonite seas) (HARDIE, 1996; LOWENSTEIN et al., 2003) at ~ 9 mM SO_4 , regardless of the aqueous Mg/Ca (Figure 4.1; Figure A.1 – A.8; Table A.1). This SO_4 concentration, combined with experimental results, indicates that the thresholds for calcite presence are within the lower range of the proposed calcite seawater concentrations (e.g. at 9 mM SO_4 , $\text{Mg/Ca} < \sim 1.1$; Figure 4.2). However, the primary CaCO_3 mineralogy during calcite and aragonite seas was rarely exclusively calcite or aragonite (WILKINSON et al., 1985; ZHURAVLEV and WOOD, 2009). I therefore propose that the thresholds for calcite seas are better represented by calcite dominance (e.g. at 5 mM SO_4 , $\text{Mg/Ca} < \sim 0.3$; Figure 4.2). The thresholds for calcite dominance do not overlap with the previously proposed seawater concentrations determined from halite fluid inclusions (Figure 4.2) (HORITA et al., 2002; LOWENSTEIN et al., 2003), but they are in agreement with SO_4 concentrations inferred from $\delta^{34}\text{S}$ isotope records from the Early Jurassic (< 5 mM) and Cretaceous (< 4 mM) (NEWTON et al., 2011; WORTMANN and CHERNYAVSKY, 2007). The Mg/Ca threshold is also compatible with Mg/Ca ratios from abiotic CaCO_3 minerals from the early Mississippian calcite sea of 0.2–0.3 (HASIUK and LOHMANN, 2008). Finally, the thresholds for the precipitation of 100% calcite (e.g. at 3 mM SO_4 , $\text{Mg/Ca} < \sim 0.15$; Figure 4.2) are unrealistic for seawater; therefore, it is highly unlikely that a pure calcite sea could have formed. The calcite threshold I propose (calcite dominance; Figure 4.2) demonstrates that either the primary CaCO_3 mineralogical information from ancient ooids needs re-evaluation or that Mg/Ca and SO_4 concentrations were much lower than proposed from halite fluid inclusions as indicated by recent studies (HASIUK and LOHMANN, 2008; NEWTON et al., 2011; WORTMANN and CHERNYAVSKY, 2007).

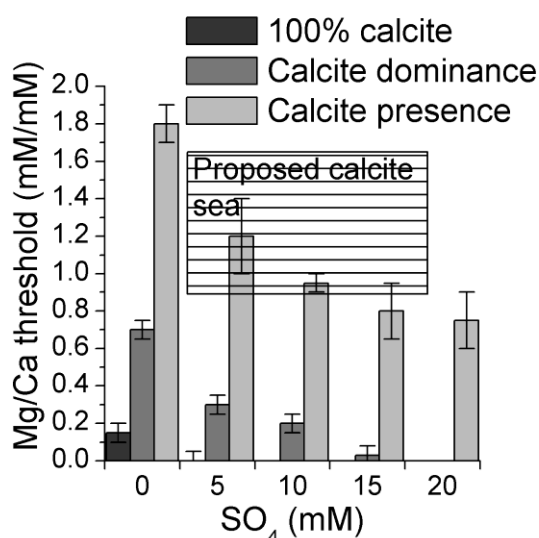


Figure 4.2 Mg/Ca thresholds for 100% calcite, calcite dominance, and presence; error bars are estimated from Figure 1, and horizontally shaded area represents proposed calcite sea chemistry (HORITA et al., 2002).

PHREEQC simulations using Phanerozoic seawater solutions (HORITA et al., 2002) revealed a large difference between the switch from KCl to MgSO₄ evaporites (Mg/Ca \approx 1.9 and SO₄ \approx 19 mM; Figure A.9 – A.10; Table A.2) and the calcite thresholds (Figure 4.2). One explanation is that the KCl and MgSO₄ evaporite types only seem to coincide with the calcite and aragonite seas, respectively, due to low time resolution of the mineralogical records. I could therefore predict that higher-resolution records will reveal that the switches in evaporites and CaCO₃ mineralogy are sequential rather than coincident. As shown previously herein, PHREEQC simulations using the experimental solutions did not reveal such a difference. Hence, the absolute Ca and Mg concentrations could have been lower than currently proposed for the calcite seas. Lower absolute Ca and Mg concentrations are not unlikely, because the high concentrations for calcite seas (as proposed from halite fluid inclusions) result from assumptions that the gypsum saturation state did not change significantly (HORITA et al., 2002). In addition, PHREEQC modelling indicates that from different starting compositions (i.e. Ca concentrations), equivalent final invariant solutions and similar evaporite sequences are obtained (e.g. simulation runs 14 and 20 in Table A.1 and Table A.2).

My work demonstrates that current seawater chemistry models cannot explain the distribution of inorganic marine carbonate minerals throughout the Phanerozoic. I propose new and lower limits on seawater chemistry during the calcite seas (e.g. at

5 mM SO₄, Mg/Ca < ~0.3; Fig. 2) as a result of inclusion of SO₄ and use of a more representative experimental approach combined with geochemical modelling on evaporite formation. These new limits require reevaluation of the geological evolution of important biogeochemical cycles (Ca, Mg, and S) and their relationship to primary CaCO₃ mineralogy.

4.6 GSA data repository

4.6.1 PHREEQC evaporation simulations

PHREEQC (PARKHURST and APPELO, 1999) evaporation simulations using the Pitzer equation were carried out to evaluate the minerals formed from evaporating seawater with varying Mg and SO₄ concentrations as would have occurred during the Phanerozoic (HARDIE, 1996). The composition of the input solutions in the evaporation models (2-20mM Mg, 5-15mM SO₄, 10.5mM Ca 10.4mM K, 558mM Cl and Na was adjusted to charge balance the solutions, Table A.1) were within the chemical range of the experimental solutions (Table 4.1). In addition, the Phanerozoic seawater composition from both calcite and aragonite seas, including compositions between these end members (8mM SO₄, 30mM Ca and 29mM Mg to 29mM SO₄, 10mM Ca and 54mM Mg, Horita et al., 2002; Table A.2) were also used as input solutions in the evaporation simulations. The simulations were run by removing increasing amounts of H₂O from the solutions and allowing precipitation (Table A.3). All simulated solutions contained Ca, Mg, SO₄, Na, Cl, CO₃ and K to allow precipitation of all major evaporite minerals, listed in Table A.4, during the simulations (HARDIE, 1996).

A summary of the results from the PHREEQC modelling are presented in Table A.1 and Table A.2. Figure A.1 – Figure A.4 and Figure A.9 show the evolution of the solution composition as a function of the remaining water as modelled by PHREEQC and Figure A.5 – Figure A.8 and Figure A.10 show the occurrence of the evaporite minerals in equilibrium with the evaporated solutions (Figure A.1 – Figure A.4 and Figure A.9). The evaporite type (HARDIE, 1996) was determined by examining the evaporite mineral sequence (Table A.1, Table A.2, Table A.4 and Figure A.5 – Figure A.8 and Figure A.10). When sylvite, and/or CaCl₂ minerals (Table A.4) were present during the evaporation of the modelled

solutions in the absence of MgSO_4 minerals, the evaporite type was determined to be KCl , and the evaporite type was determined to be MgSO_4 when polyhalite, and/or kieserite were present during the evaporation of the modelled solutions (HARDIE, 1996). For the purpose of this chapter I included the $\text{MgSO}_4 + \text{KCl}$ evaporite type in the MgSO_4 type because both of these evaporite types were coincident with the aragonite seas (HARDIE, 1996). The sea type (e.g. LOWENSTEIN et al., 2003) was determined from the composition of the final invariant solution (Table A.1 and Table A.2); when the Ca concentration exceeded the SO_4 concentration, the sea type was determined to be CaCl_2 and when the SO_4 concentration exceeded the Ca concentration, the sea type was determined to be MgSO_4 . Using the chemical divide (at which the switch from CaCl_2 to MgSO_4 precipitation occurs) that e.g. LOWENSTEIN et al. (2003) used does not result in the same sea type that the final invariant solution suggests. According to LOWENSTEIN et al. (2003) the CaSO_4 chemical divide, when the calcium and sulfate concentrations are equal in seawater, is the chemical boundary condition between different evaporite types; i.e. when the calcium concentrations is less than the sulfate concentration, sulfate is left in the evaporating solution and magnesium sulfate evaporites (e.g. kieserite, Table A.4) are able to precipitate resulting in a MgSO_4 evaporite sequence originating from a MgSO_4 sea. However, this does not take into account the precipitation of CaCl_2 minerals like antarcticite and tachyhydrite (Table A.1 and Table A.2 and Figure A.1 – Figure A.10), which form in addition to CaSO_4 minerals. This removes additional Ca from solution, therefore the Ca/SO_4 ratio at which additional SO_4 remains in solution to form MgSO_4 evaporites is >1 . (e.g. in a seawater solution with initial $[\text{Ca}] = 10.5\text{mM}$, the calculated chemical divide, separating between MgSO_4 and KCl evaporite types occurred at $\sim 9\text{mM SO}_4$, Table A.1).

4.6.2 Validation of the experimental method

Throughout the constant addition experiments, the solution chemistry (Mg , SO_4 and Ca , Table 4.1) remained constant ($\pm 5\%$). This is in contrast to free drift experiments (e.g., MORSE et al., 1997) in which major changes in solution chemistry occur during CaCO_3 formation (i.e., significant increases in Mg/Ca , MORSE et al., 1997). The CaCO_3 was precipitated onto glass spheres to mimic abiotic oöid formation in the ocean. In addition, the solids were imaged using a Field Emission

Gun Scanning Electron Microprobe (FEG-SEM) to obtain morphological information (Figure 4.3). CaCO_3 precipitated on the glass spheres show similar features compared to natural aragonite and calcite ooids, where aragonite needles precipitated tangentially on the glass spheres (Figure 4.3a – 4.3c) and calcite rhombohedras radially (Figure 4.3d – 4.3e) (e.g., SIMONE, 1980; WILKINSON et al., 1984). This emphasizes the applicability of my experimental approach to closely mimic abiotic CaCO_3 mineral formation in Phanerozoic seawater.

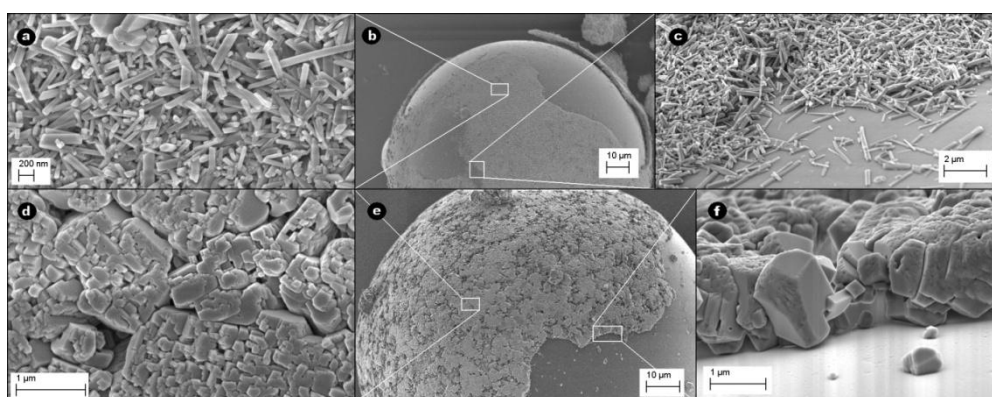


Figure 4.3 FEG-SEM images of aragonite (a-c) and calcite (d-e) precipitated on glass spheres.

MUCCI and MORSE (1983) determined that saturation state and precipitation kinetics do not influence the incorporation of Mg into calcite. This indicates that the mineral phases formed during the experiments were not influenced by the different absolute Ca (10mM) concentration used compared to proposed Phanerozoic seawater concentrations (up to 30mM Ca, HORITA et al., 2002). During the first 2–3h of each experiment, the injection of the NaCO_3 solutions caused the pH to increase to ~8.9. This was a consequence of an increase in alkalinity from ~1.8mM to ~4.5mM due to the lack of CaCO_3 precipitation. The initiation of CaCO_3 precipitation caused the pH to decrease rapidly and stabilize at ~8.2. Such a temporary increase in alkalinity has no significant effect on CaCO_3 precipitation (LEE and MORSE, 2010). Finally, model predictions for seawater alkalinity during the Phanerozoic (~2–~7mM, MACKENZIE et al., 2008) do not differ significantly from the alkalinity during my experiments (~1.8mM), and LEE and MORSE (2010) showed no significant effect on the precipitation on CaCO_3 within this range of alkalinities (1-7mM).

Chapter 5²

Mechanistic Insights into the Crystallization of Amorphous Calcium Carbonate (ACC)

5.1 Introduction

Calcium carbonates form in a wide variety of natural environments (e.g. soils and sediments) and they are ubiquitous at the Earth's surface, in the form of ancient limestone deposits or modern marine carbonate reefs. Most modern, natural calcium carbonate phases are formed by organisms as biominerals while fulfilling a wide variety of functions (e.g. stability, protection). Generally, the most predominant and most stable calcareous biominerals are calcite and aragonite (LOWENSTAM, 1981; WEINER and DOVE, 2003), yet, in some cases the less stable vaterite is also biomineralized (LOWENSTAM, 1981) (e.g. in spicules of a sea squirt (LOWENSTAM and ABBOTT, 1975) and various fish otoliths (TOMÁS and GEFFEN, 2003)). Conversely, synthetic calcium carbonates with specific size and shape properties are produced in large quantities in many industrial processes (e.g. paper manufacture, pharmaceuticals), while in some cases their precipitation leads to highly undesirable effects (e.g. scale formation in oil pipes), and this can lead to high repair and replacement costs. Despite their importance, a clear understanding of the fundamental process controlling the crystallization of calcium carbonate is still lacking.

The anhydrous, crystalline calcium carbonate (CaCO_3) polymorphs, which form under ambient conditions, are calcite, aragonite and vaterite. Their crystallization is often preceded by the formation and subsequent transformation of amorphous calcium carbonate (ACC). Many biomineralizing organisms utilize ACC to precisely control the shape and CaCO_3 polymorph (WEINER and DOVE, 2003)

² The online supporting information is inserted into the chapter where the data is first described and discussed (Figure 5.2E, Figure 5.4, Table 5.1 and Table 5.2) and a table with the summary of the evolution of the solution chemistry (calculated using PHREEQC) is deposited in Appendix B.

during the formation of their shells or spines (POLITI et al., 2004; WEISS et al., 2002). For example, sea urchin larvae produce highly elongated single crystals of calcite by the controlled deposition and transformation of ACC within their biological membrane (POLITI et al., 2008). Such natural biological processes have informed biomimetic studies of crystal growth and design and are now used to manipulate the shape and size of synthetic calcium carbonate particles (GOWER, 2008; MELDRUM and CÖLFEN, 2008).

The structure and chemistry of ACC is complex; several forms of ACC have been classified according to their water content, local order and mode of formation (e.g. abiotic *vs.* biogenic) (GEBAUER et al., 2010; RADHA et al., 2010), with the key variable being the amount of structural water. Hydrated-ACC can contain up to ~1.6 mole of water per mole CaCO₃, yet several less hydrated and even anhydrous forms of ACC have been described. For example, RADHA et al. (2010) produced both less ordered, more metastable and more ordered, less metastable ACC. Interestingly, a similar process has been observed by POLITI et al. (2008) during sea urchin spicule formation, where the initially transient, hydrated ACC transformed to anhydrous ACC before crystallizing to calcite via a secondary nucleation process. Furthermore, the enthalpies of the ACC phases in relation to the crystalline calcium carbonates show that energetically the sequence of increasing stability and therefore the crystallization pathway (following the Ostwald step rule, VAN SANTEN, 1984) should be as follows: disordered, hydrated ACC → less disordered, less hydrated ACC → anhydrous ACC → vaterite → aragonite → calcite (RADHA et al., 2010). This sequence highlights that all ACC phases have higher formation enthalpies than the crystalline polymorphs, thus ACC can act as a precursor to any of the anhydrous crystalline phases. However, in inorganic systems the transformation of ACC to its crystalline counterparts is often extremely rapid (seconds to minutes, RODRIGUEZ-BLANCO et al., 2011) and due to their inherent instability, the ACC precursors are difficult to characterize using *ex situ* techniques (e.g. TEM and FT-IR). Therefore, the proposed sequence of polymorph formation has not yet been observed or quantified in detail.

Abiotically synthesized ACC rapidly transforms to vaterite, calcite or aragonite, with the polymorph formed dependant on a number of factors including time, fluid composition and temperature (LAM et al., 2007; OGINO et al., 1987; RODRIGUEZ-BLANCO et al., in press). In most cases, pure ACC will transform to

calcite via a vaterite intermediate at low temperatures (<30°C, OGINO et al., 1987; RODRIGUEZ-BLANCO et al., 2011) and via an aragonite intermediate at higher temperatures (>60°C, OGINO et al., 1987). At low temperatures, the addition of magnesium tends to favour the direct formation of calcite from ACC, without a vaterite intermediate (RODRIGUEZ-BLANCO et al., in press). In contrast, sulfate has been shown to increase the stability and persistence of vaterite significantly at low temperatures (chapter 4, FERNÁNDEZ-DÍAZ et al., 2010).

The mechanisms and kinetics of the later stages of the crystallization pathways are controlled by the dissolution of vaterite and precipitation of calcite, with the rate controlled by the surface area of calcite (OGINO et al., 1990; RODRIGUEZ-BLANCO et al., 2011). However, the mechanism of the ACC to vaterite transformation is still not clear, with several possible mechanisms proposed. Many studies suggested that ACC dissolves and vaterite spheres formed via homogeneous nucleation of nanocrystalline vaterite particles, followed by fast aggregation to form μm sized polycrystalline spheres (SHEN et al., 2006; STÁVEK et al., 1992; VACASSY et al., 2000). A solid state mechanism for the ACC to vaterite crystallization has also been proposed, with the ACC particles dehydrating and recrystallizing to form vaterite (POUGET et al., 2010). Finally, a study based on imaging of inorganically precipitated vaterite suggested that vaterite forms via ACC dissolution coupled to spherulitic growth (ANDREASSEN, 2005). Resolving the mechanisms and kinetics of ACC crystallization in abiotic systems is key to developing a detailed understanding of how calcium carbonate phases form in both natural and synthetic processes. In particular, the mechanism of transformation between the individual phases forming as the system moves towards thermodynamic equilibrium from disordered hydrated ACC to fully crystalline calcite needs to be fully quantified.

In this study, I performed *in situ* small and wide angle X-ray scattering (SAXS/WAXS) experiments with a temporal resolution of 1 second and studied the direct transformation of ACC to vaterite in solution. Combined with off-line characterization of the solid phases and solution composition, I show that the crystallization of ACC to vaterite occurs in three distinct stages. ACC precipitates immediately from a supersaturated solution, but transforms quickly to vaterite via dehydration and rapid spherulitic growth of vaterite. This is followed by a second intermediate stage, where vaterite continues to form via the dissolution of remnant ACC, while finally the vaterite particles grow in a third stage only via surface-

controlled Ostwald ripening. Once all vaterite has fully formed the transformation to calcite via dissolution and re-precipitation takes place.

5.2 Methods

The crystallization of pure (without additive) ACC was performed both off-line and on-line by rapidly mixing equal volumes of molar solutions of calcium chloride ($\text{CaCl}_2 \cdot 2\text{H}_2\text{O}$, >99% purity) and sodium carbonate (Na_2CO_3 , >99% purity). These ‘no additive’ experiments were complemented with sets of experiments performed with either 10 mol% of the Na_2CO_3 replaced by Na_2SO_4 (‘replacement’ experiments) or with 10 mol% Na_2SO_4 added to the Na_2CO_3 solution (‘additive’ experiments). During mixing and throughout the whole experimental time the suspensions were vigorously stirred to ensure rapid and continual homogenization. The composition, solution volumes and saturation indices with respect to vaterite ($SI = \log(\{Ca^{2+}\}\{CO_3^{2-}\}/K_{sp,vaterite})$) of the starting solutions used for all experiments are listed in Table 5.1.

Table 5.1 Summary of the experimental conditions for all experiments

Experiment	CaCl ₂ solutions		Na ₂ CO ₃ /Na ₂ SO ₄ solutions			Solutions after mixing and prior to precipitation				
	Ca (M)	Volume (ml)	CO ₃ (M)	SO ₄ (M)	Volume (ml)	Ca (M)	CO ₃ (M)	SO ₄ (M)	Volume (ml)	SI
no additive	1	100	1	-	100	0.5	0.5	-	200	4.2
replacement	1	100	0.9	0.1	100	0.5	0.45	0.05	200	4.2
addition	2.5	40	0.625	0.0625	160	0.5	0.5	0.05	200	4.2

During all off-line experiments, the pH was continuously recorded (5-10 second time steps) and aliquots of the suspensions and solutions were removed at regular intervals and filtered using 0.2 μm membrane filters. The solids were immediately washed with isopropanol and dried (RODRIGUEZ-BLANCO et al., 2008). The solution samples were analyzed by ion chromatography (IC) for Ca and SO₄ (chapter 4) and together with the pH, the measured concentrations were used to calculate the aqueous carbonate and the saturation index (SI) with respect to vaterite over the whole length of the experiments using PHREEQC (PARKHURST and APPELO, 1999). The solid powders were imaged with a Field Emission Gun

Scanning Electron Microscope (LEO 1530 Gemini FEG-SEM) and the particle size distributions of ACC and vaterite were determined by measuring the diameters of ~100 particles.

The on-line, *in situ* experiments were performed using the simultaneous SAXS/WAXS data collection capability of beamline I22 at Diamond Light Source Ltd (UK). Immediately after mixing the suspensions were continuously pumped via a peristaltic pump through a capillary in line with the synchrotron beam. Simultaneous 2D SAXS (collected with a RAPID detector, MARCHAL et al., 2009) and 1D WAXS (collected with a HOTWAXS detector, BATEMAN et al., 2007) patterns were collected at one second/frame resolution for the total reaction duration of ~35min. SAXS patterns were only collected for the ‘no additive’ and ‘replacement’ experiments. Due to practical beamline operating procedures data collection started ~ 1 minute after mixing.

All SAXS and WAXS patterns were detector response corrected and background subtracted using a scattering pattern from the Na₂CO₃/Na₂SO₄ solution. Individual WAXS patterns were fitted using Topas 4-2 (BRUKER_AXIS, 2009) to obtain the *Rietveld scale factor* (S) for vaterite. The *Rietveld scale factor* relates the structure of a crystalline phase to the area under the Bragg peaks to obtain the amount of the respective phase in the sample (HILL and HOWARD, 1987; RIETVELD, 1969). Normalizing the *Rietveld scale factor* from the WAXS patterns throughout the experiments ($S(t)$) to the *Rietveld scale factor* at the end of the experiment (S_{final}) gives the degree of reaction for vaterite ($\alpha(t) = \frac{S(t)}{S_{final}}$, Eq. 3.2) (RODRIGUEZ-BLANCO et al., 2011). Similarly, the background intensity ($B(t)$) from the WAXS pattern normalized to the background intensity at $t = 0$ (B_0) and the end of the experiment (B_{final}) was used to calculate the degree of reaction for the ACC breakdown ($\alpha(t) = \frac{B(t)-B_{final}}{B_0-B_{final}}$, Eq. 3.5) (RODRIGUEZ-BLANCO et al., 2011). Finally, selected SAXS patterns were analyzed with GNOM (SVERGUN, 1992) to obtain information about the ACC particle size, while the change in vaterite crystallite size was determined from the scattering peak position in the SAXS patterns ($d = 2\pi/q$) where d (nm) is particle diameter and q (nm⁻¹) is the scattering vector (DE MOOR et al., 1999a; DE MOOR et al., 1999b).

2.3 Results

In all experiments, upon mixing a white gel-like precipitate formed instantaneously. At the start of data collection (~1 minute after mixing), no Bragg peaks were observed in the WAXS patterns; only a broad hump from the scattering of the ACC, the aqueous solution and air scatter was observed (Figure 5.1A). This confirms the initial formation of solely ACC, which is consistent with previous analyses on material synthesized using the exact same methodology (RODRIGUEZ-BLANCO et al., 2011). With time, the background intensity decreased and subsequently the growth of Bragg peaks was observed (Figure 5.1A). All Bragg peaks could be assigned to vaterite and no other crystalline phases were observed throughout the length of all experiments (max. 35 min). The time series SAXS patterns (Figure 5.1B) showed that simultaneous with the appearance of the Bragg peaks in the WAXS patterns (at ~1.5 min, Figure 5.1A), a peak in the SAXS patterns appeared. Over time, this peak migrated to lower q , indicating particle growth.

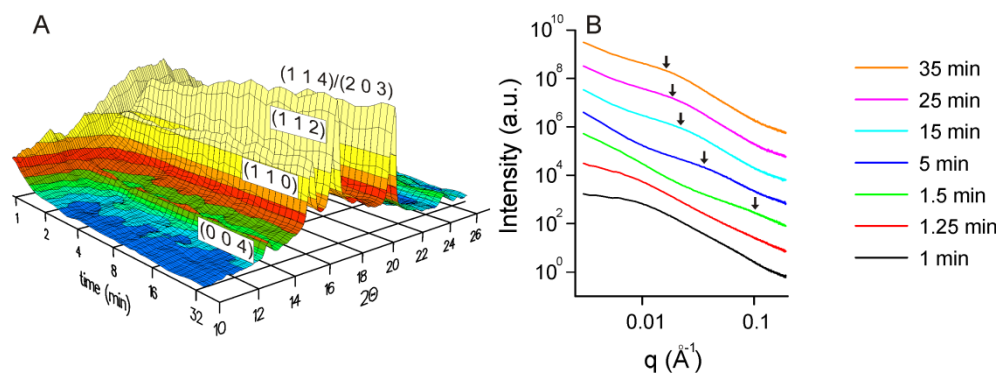


Figure 5.1 (A) 3D representations of the time resolved WAXS patterns from the ‘no additive’ experiment (time is plotted on a base 2 log scale for clarity); (B) stacked time series of selected SAXS patterns from the ‘no additive’ experiment, with the legend showing time in minutes and the arrows illustrating the position of the peaks caused by the scattering from the growing vaterite crystallites

The degree of reaction (α) for the crystallization of vaterite from pure ACC was extracted from the WAXS patterns (Figure 5.2A) as described above. Combining α_{ACC} and α_{vaterite} with the pH evolution from an equivalent off-line experiment revealed that the transformation occurred in three distinct stages (Figure

5.2A). The first stage was characterized by a rapid decrease in α_{ACC} up to ~80 seconds, with a concomitant rapid increase in α_{vaterite} between ~70 and ~90 seconds (Figure 5.2A). At the end of this first stage α_{vaterite} and α_{ACC} were ~0.8 and ~0.2 respectively (Figure 5.2A). During the second stage of the reaction, α_{ACC} decreased to zero after ~4-6 minutes and vaterite continued to form but at a slower rate reaching a plateau after ~6 minutes. Finally, during the third stage, the α_{vaterite} remained constant indicating that the crystallization from ACC was complete. The corresponding pH profile revealed a fast decrease from ~9.6 to ~8.3 during the first two stages of the reaction (Figure 5.2A) and stable value during stage three. Data for the crystallization of vaterite in the presence of sulfate (Figure 5.2B and 5.2E, 'additive' and 'replacement') followed an equivalent 3-stage reaction, with the initial formation of vaterite significantly delayed in the 'additive' experiment.

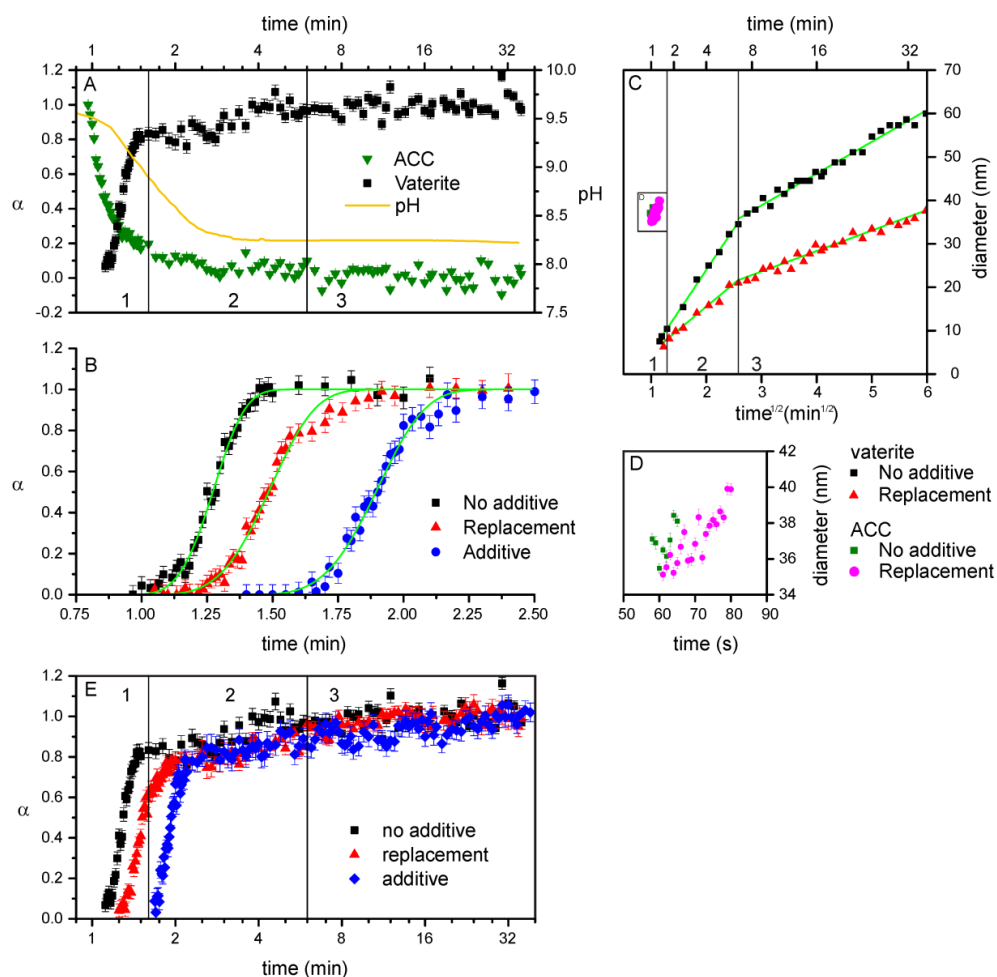


Figure 5.2 (A) α_{vaterite} and α_{ACC} vs. time (base 2 log scale) plot including a pH vs. time profile for the ACC to vaterite transformation for the ‘no additive’ experiment; (B) α_{vaterite} vs. time plots for the 1st stage of the crystallization of vaterite for all experiments with the best fit lines (see below) in green; (C) ACC nanoparticle and vaterite crystallite sizes derived from the SAXS data vs. time (on a time^{1/2} scale) for the ‘no additive’ and ‘replacement’ experiments; (D) detail of (C), showing ACC nanoparticle size vs. time (E) comparison of α_{vaterite} vs. time (base 2 log scale) of all three stages of all experiments; vertical lines and numbers in the figures (A) (C) and (E) represent the three different reaction stages

The particle diameters for vaterite and ACC, evaluated from the SAXS data are plotted in Figure 5.2C and 5.2D. The results reveal that in the early part of stage one (<70 seconds), when vaterite was not yet present, ACC particles with diameters of ~35-40 nm formed in both the ‘no additive’ and the ‘replacement’ experiment (Figure 5.2D). These values are comparable with the particle sizes evaluated from the FEG-SEM images (42±14 nm; Figure 5.3A). Although there is a slight increase in ACC particle size with time, the majority of ACC formed prior to the start of the SAXS/WAXS data collection (<60 seconds). The first vaterite particles that formed

during stage one (~70 seconds) had initial diameters of ~9 nm (Figure 5.2C) in both experiments ('no additive' and 'replacement'). During stage two (90 seconds to 6 minutes), the vaterite particle size increased rapidly to ~35 nm in the 'no additive' system and to ~20 nm in the 'replacement' system (Figure 5.2C). Finally, during stage three, although the α_{vaterite} remained constant (Fig 2A), the particle size continued to increase reaching a final diameter of ~60 nm in the 'no additive' system and ~40 nm in 'replacement' system (Figure 5.2C). FEG-SEM observation of solids collected during stage two (at 2 minutes) showed the vaterite as large ($1.3 \pm 0.4 \mu\text{m}$) polycrystalline spheres consisting of much smaller individual vaterite crystallites of $\sim 34 \pm 7 \text{ nm}$ in size (Figure 5.3B), yet some remnant ACC was still present in the samples as observed in Figure 5.3B. Finally, images of the sample from the end of stage three (at 35 minutes) showed similar large polycrystalline spheres, but consisting of crystallites of $58 \pm 16 \text{ nm}$ (Figure 5.3C) without any remnant ACC. Comparing the vaterite particles sizes from the SAXS and SEM analyses indicates that the vaterite peaks in the SAXS patterns recorded the size of the individual crystallites rather than the μm sized polycrystalline spheres. Hence, additional analyses of the SAXS patterns in terms of the time evolution of the Porod slope (p) (BALE and SCHMIDT, 1984; TEIXEIRA, 1988) showed a decrease in p during stage one from ~3.4 to ~2.5, and a gradual increase during stage three to ~2.9 (Figure 5.4).

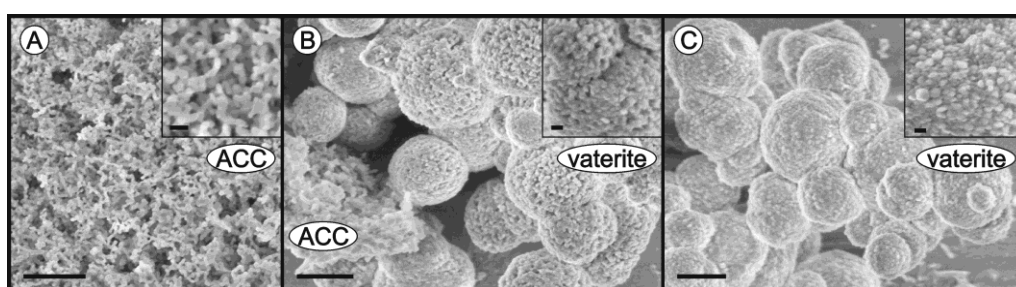


Figure 5.3 FEG-SEM images of solids quenched throughout the 'no additive' experiment; (A) 1 minute (B) 2 minutes (C) 35 minutes; the scale bar is $1 \mu\text{m}$ in the main images; the insets are enlargements of the dominant phase ((A) ACC and (B) and (C) vaterite) in the respective main image and the scale bar in the insets is 100 nm.

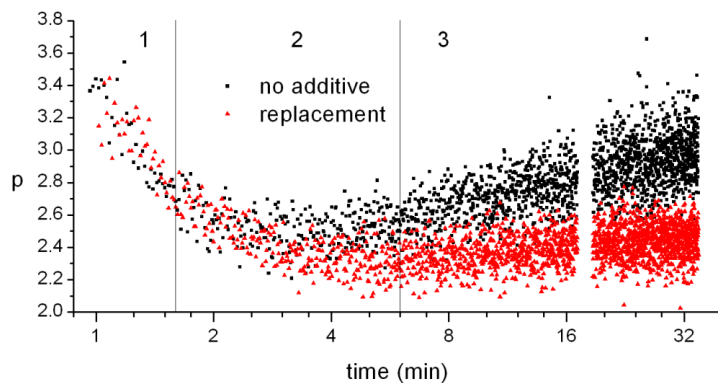


Figure 5.4 The slope of the Porod region ($I(q) \propto q^{-p}$) calculated from the SAXS patterns for the ‘no additive’ and ‘replacement’ experiments as a function of time (on a base 2 log scale)

The aqueous calcium concentrations measured immediately after mixing showed that ~80-95% of the initial calcium (500 mM, Table S1) was removed from solution during the precipitation of ACC (<60 seconds; Figure 5.5A). During stage two, the calcium concentrations reached a constant value, which was maintained for the whole duration of the experiments (Figure 5.5A). Comparing the three different experiments shows that the calcium concentrations were significantly higher throughout the ‘replacement’ experiment (~75 – 50 mM) compared to the ‘no additive’ and ‘additive’ experiments (~30 – 10 mM). This was due to an excess in calcium relative to carbonate in the starting solutions (Table S1). The evolution of the sulfate concentrations was similar in both the ‘additive’ and ‘replacement’ experiments (Figure 5.5B). In stage one, the sulfate concentrations decreased by 20-30% compared to the initial values (50 mM, Table S1), yet it also reached relatively constant values through stages two and three.

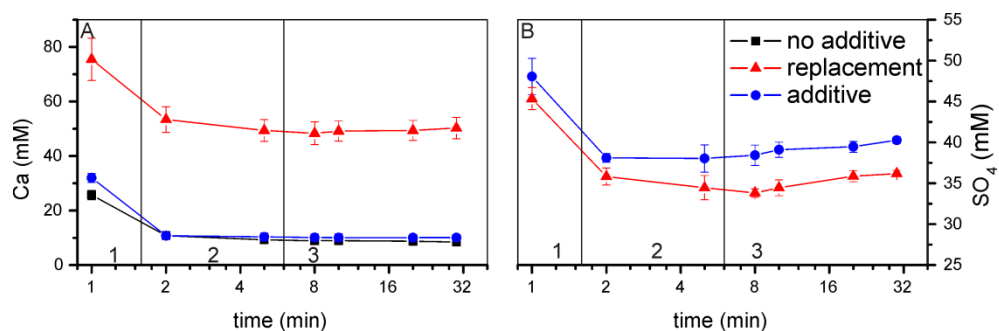


Figure 5.5 Evolution of the solution composition with time (base 2 log scale); (A) calcium and (B) sulfate; the black vertical lines and numbers in both figures indicate the different reaction stages and the errors bars represent the standard deviation of three measurements

5.4 Discussion

5.4.1 Stage one: ACC formation and vaterite spherulitic growth

Immediately upon mixing of the initial solutions ACC precipitated with particles sizes (35-40 nm; Figure 5.2D) consistent with a previous study where ACC was synthesized using the same synthesis protocol (20-45 nm, RODRIGUEZ-BLANCO et al., 2011). This is in contrast to other studies that have reported ACC with larger particle diameters e.g.: 90-110 nm (LIU et al., 2010), ~270 nm (BOLZE et al., 2002) and ~125 nm (RODRIGUEZ-BLANCO et al., 2008). However, in these previous studies ACC was precipitated from solutions of significantly lower supersaturation ($SI = 1.7-2.3$; $[Ca]$ and $[CO_3] = 3.5-10$ mM after mixing) compared to the initial supersaturation in this study ($SI = 4.2$, Table S1). As the number of nuclei increases with supersaturation (LAAKSONEN et al., 1995) and the amount of reactant in the system is finite, the final particles size of ACC will decrease with increasing supersaturation (BOLZE et al., 2004).

The rapid decrease in WAXS background intensity before the formation of vaterite (<70 seconds, Figure 5.1A) in conjunction with a decrease in the concentration of dissolved calcium suggests that the structure and/or composition of the ACC phase on my experiments changes during this 1st stage of the reaction. Recent thermodynamic (RADHA et al., 2010) and spectroscopic studies (KILLIAN et al., 2009; POLITI et al., 2008) of the crystallization of ACC in abiotic and biotic systems have shown that freshly precipitated, hydrated ACC transforms to a more

stable (lower enthalpy) dehydrated ACC prior to crystallization. This more thermodynamically stable form of ACC is also somewhat more structurally ordered compared to the less stable and more hydrated initial ACC phase (RADHA et al., 2010). The observed decrease in WAXS background intensity in the current study is also indicative of an increase in local order and dehydration of the initial ACC (RODRIGUEZ-BLANCO et al., 2011). I suggest that the dehydration process was driven by the lower enthalpy of the dehydrated ACC (RADHA et al., 2010). The formation of additional (more ordered and less hydrated) ACC prior to vaterite formation would lead to a continuous decrease in the carbonate concentration which lead to the observed decrease in pH during stage one (Figure 5.2A). Therefore the first step in the transformation of ACC to vaterite was the dehydration and ordering of ACC which occurred before significant crystallization of vaterite was observed (NAVROTSKY, 2004; RADHA et al., 2010). Finally, Figure 5.2D indicates that the ACC slightly increased in size prior to its crystallization. Although the recorded size increase was small (Figure 5.2D) this could have been caused by additional precipitation of less hydrated ACC. This increase in the size of ACC could decrease the stability of ACC and trigger its subsequent crystallization (RAITERI and GALE, 2010).

The transformation of ACC to vaterite as observed here must allow for a very rapid crystallization rate. In the pure system it only took ~20-30 seconds to reach $\alpha_{\text{vaterite}} \sim 0.8$ at the end of stage one (Figure 5.2A). Based primarily on electron microscopic observations, three possible mechanisms for the ACC to vaterite crystallization have so far been proposed:

- (i) homogeneous vaterite nucleation followed by fast aggregation (SHEN et al., 2006; STÁVEK et al., 1992; VACASSY et al., 2000)
- (ii) solid state transformation to vaterite (POUGET et al., 2010)
- (iii) fast spherulitic growth of vaterite polycrystalline spheres (ANDREASSEN, 2005)

The solid state transformation was mainly observed in the presence of an organic template and of dissolved ammonium (POUGET et al., 2009), which stabilized the (001) planes of vaterite and leads to large hexagonal plate-like vaterite particles, unlike the polycrystalline spheres in this study. Therefore, this solid state mechanism is not directly comparable to results in the current study. In contrast,

spherulitic growth has been shown to occur via growth front nucleation (GFN) (GRÁNÁSY et al., 2005), where new particles grow via the continuous nucleation of misaligned equivalent structural units (crystallites) on the surface of a growing spherulite (KEITH and PADDEN, 1963). Such a growth mechanism tends to result in polycrystalline spheres consisting of crystallites of approximately equal sizes. This is consistent with the vaterite morphology observed in the FEG-SEM images (Figure 5.3B), with μm sized spheres consisting of nm sized crystallites (Figure 5.2C). Additionally, the diameter of the vaterite crystallites that formed at the end of stage one (~ 9 nm) was similar to the ~ 10 nm \emptyset for the crystallites in spherulitically grown vaterite as reported by ANDREASSEN (2005).

In order for continuous nucleation to be the dominant growth process, spherulitic growth can only occur when the solution is continuously highly supersaturated with respect to the crystallizing phase. ANDREASSEN (2005) suggested that the spontaneous nucleation of vaterite, and therefore spherulitic growth will always occur in the presence of ACC. Nucleation of vaterite in the presence of ACC forces the highly soluble ACC ($K_{sp,ACC} = 10^{-6.3}$) (BREČEVIĆ and NIELSEN, 1989) to dissolve and maintain a high supersaturation ($SI = 1.4$) with respect to vaterite. The saturation index of the solution with respect to vaterite is high during stage one ($SI > 1.4$; Figure 5.6 and Appendix B) but reduces to less than 1.4 at the end of this stage. This clearly supports a spherulitic growth mechanism for vaterite during stage one. GRÁNÁSY et al. (2005) used theoretical calculations to determine that during spherulitic growth the extent of crystallization follows a Johnson-Mehl-Avrami-Kolmogorov (JMAK) (AVRAMI, 1939; AVRAMI, 1940; AVRAMI, 1941; JOHNSON and MEHL, 1939) kinetic model of the form:

$$\alpha(t) = \exp[1 - k(t - t_0)^n]$$

(Eq. 5.1)

where k is the kinetic constant (min^{-n}), t is the time (min), t_0 is the induction time (min) and n is the Avrami exponent. The Avrami exponent can be expressed as: $n = 1 + d$ (GRÁNÁSY et al., 2005), where d is the dimensionality during spherulitic growth. The images in Figure 5.3, show that the vaterite spherulites have grown in three dimensions, therefore an Avrami exponent of 4 would be expected (Figure

5.2B and Table 5.2). This model fits very well to the growth of vaterite during stage one ($R^2 > 0.98$, Table 5.2), which further strengthens my hypothesis that vaterite formed via a spherulitic growth mechanism.

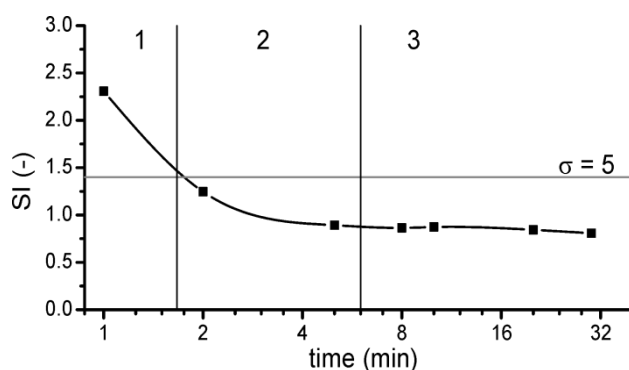


Figure 5.6 The evolution of the saturation indices vs. time (base 2 log scale) for the “no additive” system (based on PHREEQC calculations, further summarized in Appendix B); the vertical lines separate the three stages of the transformation reaction; not plotted is the SI for the initial solution (prior to ACC precipitation), which was ~ 4.2 (Table S1), calculated based on $K_{sp,vaterite} = 10^{-7.74}$ (PLUMMER and BUSENBERG, 1982), the horizontal line represents the relative supersaturation (σ) of 5

$$(\sigma = \sqrt{\{Ca^{2+}\}\{CO_3^{2-}\}/K_{sp,vaterite}}) \text{ (ANDREASSEN, 2005)}$$

Table 5.2 The kinetic constant (k) and the induction time (t_0) derived from the α data for vaterite to the JMAK model using an Avrami exponent (n) of 4 (Eq. 5.1)

Experiment	Variable	Value	Error
no additive	k (min^{-4})	48.7	8.8
Adj. $R^2 = 0.9888$	t_0 (min)	0.93	0.02
replacement	k (min^{-4})	11.7	2.5
Adj. $R^2 = 0.9828$	t_0 (min)	0.98	0.03
additive	k (min^{-4})	9.2	2.3
Adj. $R^2 = 0.9727$	t_0 (min)	1.37	0.03

The value of the slope (p) of the Porod region (high q values, Figure 5.4) can give information on the fractal dimensions of the scattering particles (BENNING and WAYCHUNAS, 2007; SCHMIDT, 1991; TOBLER et al., 2009). If: $1 < p < 3$, the scattering particles are mass fractals with a mass fractal dimension (TEIXEIRA, 1988):

$$D_m = p$$

(Eq. 5.2)

If: $3 < p < 4$, the scattering particles have fractal surfaces with a surface fractal dimension of (BALE and SCHMIDT, 1984):

$$D_s = 6 - p$$

(Eq. 5.3)

The Porod slope from the SAXS plots (p) is ~ 3.4 after 1 minute (Figure 5.4), corresponding to particles with a rough surface (BALE and SCHMIDT, 1984; BENNING and WAYCHUNAS, 2007). Conversely, after 2 minutes, p decreased to ~ 2.5 (Figure 5.4), which corresponds to fractal particles (i.e. porous and/or polycrystalline) (PIPICH et al., 2008). This change in p corresponds with the transformation from ACC particles ($\varnothing \sim 35$ nm, Figure 5.2D) with rough surfaces ($D_s = 2.6$, Eq. 5.3) to the polycrystalline fractal vaterite particles (i.e. μm sized polycrystalline spheres consistent of ~ 9 nm crystallites, $D_m = 2.5$, Eq. 5.2, Figure 5.3B).

5.4.1.1 The effect of sulfate on vaterite spherulitic growth

A significant decrease in the rate constant in both sulfate systems compared to the ‘no additive’ system was calculated using the JMAK model (‘no additive’: $48.7 \pm 8.8 \text{ min}^{-4}$, ‘replacement’: $11.7 \pm 2.5 \text{ min}^{-4}$ ‘additive’: $9.2 \pm 2.3 \text{ min}^{-4}$; Table 5.2). This could either be caused by sulfate (PLUMMER et al., 1979; PLUMMER et al., 1978) decreasing vaterite nucleation by surface interactions or by a decrease in the reaction enthalpy of the ACC crystallization to vaterite. Recent studies showed that sulfate stabilizes vaterite (chapter 4, FERNÁNDEZ-DÍAZ et al., 2010) and that it has no significant influence on the stability of ACC (AIZENBERG et al., 2001), thus increasing the reaction enthalpy for the ACC-vaterite transformation. This suggests that the observed decrease in rate constant (Table 5.2) was not a result of thermodynamic changes caused by the presence of sulfate. It is more likely that this decrease was due to adsorption of sulfate, which poisoned nucleation sites on the

growing vaterite spherulites and thus decreased the rate of the GFN of vaterite. A similar effect has been observed during calcite growth, with sulfate poisoning calcite growth sites (VAVOURAKI et al., 2008).

In my experiments vaterite spherulitic growth was only delayed in the ‘additive’ system (Figure 5.2B and 5.2E), which was likely caused by a similar poisoning effect as described above. However, vaterite spherulitic growth in the ‘replacement’ system was not significantly delayed by the presence of sulfate (Table 5.2). This indicates that the differences in induction time cannot be explained solely by the presence of sulfate. The calcium (Figure 5.5A) and calculated total inorganic carbon and bicarbonate concentrations (Appendix B) were larger in the ‘replacement’ compared to the ‘additive’ system during stage one. In addition, there is no significant difference in the *SI* between the ‘replacement’ and ‘additive’ systems (Appendix B). I infer therefore, that bicarbonate had a destabilizing effect on ACC, as previously suggested by NEBEL et al. (2008). A second reason for the differences in induction time (Table 5.2) is the consumption of bicarbonate rather than carbonate during vaterite nucleation, as previously also observed for calcite growth (PLUMMER et al., 1979; PLUMMER et al., 1978). These lines of evidence all indicate that the induction time for vaterite spherulitic growth is affected both by the amount of bicarbonate and by the presence of sulfate.

5.4.2 Stages two and three: vaterite growth and ripening

The vaterite crystallized during stage two (~20% of total, Figure 5.2A) formed under conditions closer to equilibrium than during stage one (Figure 5.6). During this stage virtually no increase in the large vaterite spherulite size was observed (Figure 5.3B and 5.3C), thus excluding further spherulitic growth of vaterite. Furthermore, the calcium concentration in solution (Figure 5.5A) decreased only slightly, indicating that little additional calcium carbonate precipitated from solution. At the end of stage one, the α_{ACC} of ~0.2 (Figure 5.2A) and the remnant ACC next to the vaterite spherulites (Figure 5.3B) suggest that the final 20% of vaterite formed predominantly via dissolution of the remaining ACC and reprecipitation on the pre-existing vaterite crystallites which nucleated during stage one. The lowered vaterite *SI* during stage two (< 1.2; Figure 5.6 and Appendix B) also suggests that the solubility of the remaining ACC was significantly reduced. I

argue that this was caused by the ordering/dehydration of ACC, which would lower the ACC crystallization enthalpy (RADHA et al., 2010). The decrease in p during stage two (up to ~4 minutes, Figure 5.4) can be attributed to the transformation of the remnant rough ACC particles in suspension to vaterite up to ~4 minutes (Figure 5.2A and 5.3B).

In stage two, the crystallite size of the vaterite particles making up the large spherulites also increased from ~9 nm to ~37 nm (Figure 5.2C). When assuming that this increase was only caused by 3D growth via ACC dissolution (retaining the same amount of vaterite crystallites), this would indicate a 70 times increase in total mass of vaterite. However, because the WAXS analyses showed that only ~20% of the total vaterite formed during stage two, I conclude that an alternative mechanism must be responsible for the majority of the increase in vaterite crystallite size. I suggest that this process is Ostwald ripening (LIFSHITZ and SLYOZOV, 1961; WAGNER, 1961). Ostwald ripening can either occur by a diffusion or surface controlled mechanism. When Ostwald ripening is diffusion controlled: $r(t) \propto t^{1/3}$ and when Ostwald ripening is surface/reaction controlled: $r(t) \propto t^{1/2}$ (LIFSHITZ and SLYOZOV, 1961; WAGNER, 1961). As the solutions were stirred continuously during the experiments (i.e., the suspensions were kept homogeneous), diffusion can be eliminated, and the Ostwald ripening process was likely to be surface controlled. This was also confirmed by the linearity of the plot of d versus $t^{1/2}$ (Figure 5.2C).

Finally, the vaterite crystallite growth in stage three was purely controlled by Ostwald ripening as no additional vaterite formed after stage two. Again, the linearity of the plot of d versus $t^{1/2}$ (Figure 5.2C) suggests a continued surface controlled ripening reaction. During stage three, the Porod slope (p) also increased from 2.5 to 2.9 (Figure 5.4). This was caused by a decrease in fractal appearance of the vaterite spherulites (PIPICH et al., 2008) due to Ostwald ripening, as the spherulites lose porosity due to the increasing crystallite size.

5.4.2.1 The effect of sulfate on vaterite growth and ripening

The final size of the vaterite crystallites was ~40% smaller in the 'replacement' compared to the 'no additive' system (Figure 5.2C). An increase in particle size caused by Ostwald ripening is proportional to the surface free energy

and the bulk solubility (LIFSHITZ and SLYOZOV, 1961; WAGNER, 1961). Furthermore, the surface free energy changes by the adsorption of dissolved ions (BUTT, 1996). Such a decrease in the surface free energy for vaterite was observed in the presence of silica (LAKSHTANOV and STIPP, 2010) and I assert that sulfate may have a similar effect on the surface free energy of the vaterite crystallites. Additionally, the stability of vaterite increased due to incorporation of sulfate (chapter 4, FERNÁNDEZ-DÍAZ et al., 2010) and hence its solubility decreased in the presence of sulfate. These changes in surface free energy and solubility could have ultimately decreased the rate of Ostwald ripening. However, a decrease in the rate of Ostwald ripening by surface poisoning effects cannot be excluded.

During stage three in the ‘replacement’ system, p remained at ~ 2.5 (BALE and SCHMIDT, 1984). This indicates that the fractal appearance of the vaterite spherulites did not change significantly during stage three (Eq. 5.3). The p and crystallite size in the ‘replacement’ system at the end of the experiment, correspond to the p and crystallite size at ~ 4 minutes in the ‘no additive’ system (Figure 5.2C and 5.4). This indicates that the decrease in Ostwald ripening caused by the presence of SO_4 was also recorded in the Porod slope.

5.5 Summary and conclusions

Combining the mechanisms presented above with previous results on the transformation of vaterite to calcite (OGINO et al., 1990; RODRIGUEZ-BLANCO et al., 2011) allowed us to elucidate the full abiotic transformation pathway from ACC via vaterite to calcite (Figure 5.7). In a first stage disordered hydrated ACC forms from a highly supersaturated solution. The local order within the ACC then increases concurrent to dehydration. This transition occurs due to the lower enthalpy of the more ordered less hydrated phase (RADHA et al., 2010). The large difference in solubility between ACC and vaterite in stage one keeps the supersaturation at a sufficient high level to allow continuous vaterite nucleation and spherulitic growth (ANDREASSEN, 2005). Once initiated, spherulitic growth is maintained as long as highly soluble ACC is present in the system. The ordering and increase in thermodynamic stability (lower enthalpy) of the ACC is also reinforced by an observed transition from spherulitic vaterite growth to surface particle growth in

stage two in the continued but decreasing presence of ACC. Once all the ACC has been consumed, the vaterite crystallite size continues to increase via Ostwald ripening (stage two and three). Because Ostwald ripening is a dissolution reprecipitation mechanism (LIFSHITZ and SLYOZOV, 1961; WAGNER, 1961), the further ripening of the vaterite is easily displaced by a dissolution-reprecipitation transformation mechanism leading to the final calcite (OGINO et al., 1990; RODRIGUEZ-BLANCO et al., 2011). This multi-step reaction pathway further validates the relative stability scheme for the various amorphous and crystalline calcium carbonate phases as described by RADHA et al. (2010).

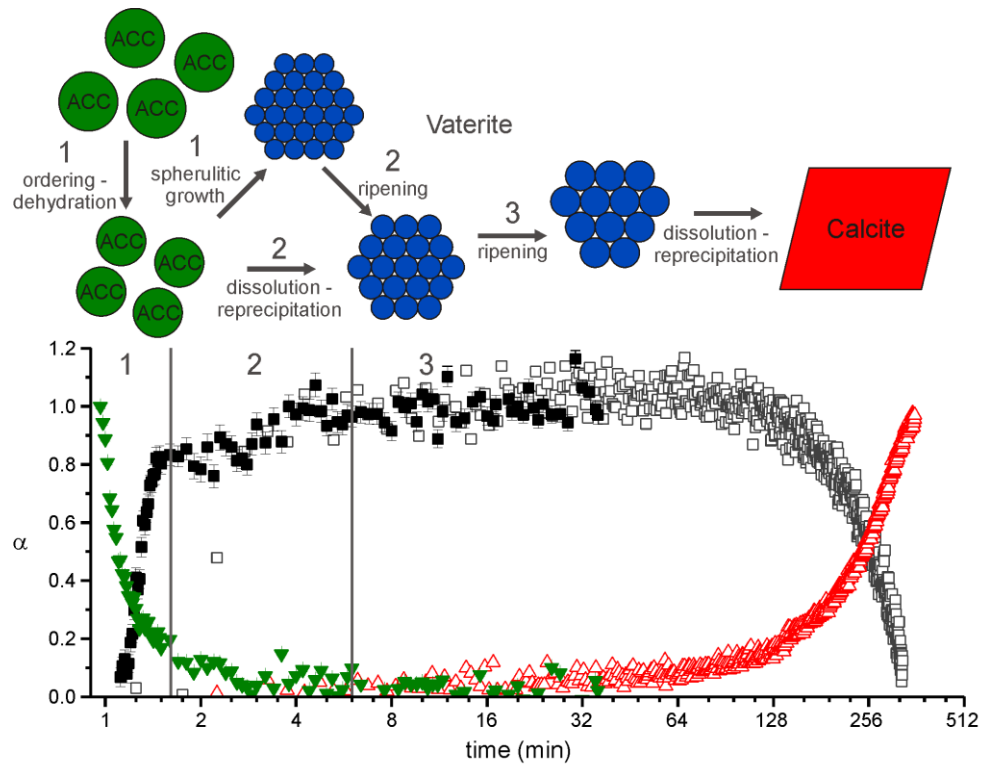


Figure 5.7 Schematic representation of the proposed multi stage ACC → Vaterite → Calcite crystallization pathway (top) with the underlying combined reaction progress, α_{ACC} , α_{vaterite} and α_{calcite} for the full crystallization reaction in the ‘no additive’ system (the green triangles and full black squares represent the ACC and vaterite from this study and the open squares and red triangles represent the vaterite and calcite from RODRIGUEZ-BLANCO et al. (2011)), stages 1, 2 and 3 of the reaction mechanism are labeled on the figure

The reaction pathway described above provides a comprehensive and complementary set of quantitative data about the abiotic mechanism of pure ACC crystallization. This multi-stage reaction process may represent the pathway of pure

ACC biomineralization, as seen in the observation of KILLIAN et al. (2009) who showed that calcitic sea urchin spicules form by secondary calcite nucleation within the ACC. This matches the secondary (vaterite) and tertiary (calcite) nucleation and growth processes observed in the abiotic reaction sequence. It should be noted that this study detailed the transformation in solution, either with or without the presence of sulfate. However, most biogenic calcium carbonates contain magnesium (5-10%) which leads to the direct formation of calcite from the ACC (LAM et al., 2007; RODRIGUEZ-BLANCO et al., in press). Additionally, sulfate has no large mechanistic influence on the ACC crystallization to vaterite, however sulfate has the capability to stabilize vaterite (chapter 4, FERNÁNDEZ-DÍAZ et al., 2010). This could help explain the existence of vaterite biomineralizing organisms (LOWENSTAM, 1981; LOWENSTAM and ABBOTT, 1975; TOMÁS and GEFFEN, 2003). In contrast to the transformation process described here, many biomineralization processes occur entirely within a biological membrane enclosed with little or no free water (WEINER and DOVE, 2003). This could significantly alter the transformation mechanism (MELDRUM and CÖLFEN, 2008). Finally, the results presented in this study demonstrate how fast time-resolved SAXS/WAXS data can be obtained and evaluated to gain an unprecedented detail into fast crystallization reactions when combined with additional off-line solid and solution characterization.

Chapter 6

Using WAXS to study intricate crystallization pathways – gypsum and vaterite crystallization via rapidcreekite

6.1 Introduction

Calcium carbonate and sulfate mineral phases like calcite (CaCO_3) and gypsum ($\text{CaSO}_4 \cdot 2\text{H}_2\text{O}$) are common in modern and ancient environments, for example, in coral reefs and massive evaporite deposits (MORSE and MACKENZIE, 1990; WARREN, 2010). They also form as unwanted by-products (scale) during many industrial processes like during desalination of seawater to produce drinking water (DYDO et al., 2003; MOGHADASI et al., 2004; UCHYMIK et al., 2008).

Natural calcium carbonate phases occur as three anhydrous CaCO_3 minerals: calcite, aragonite and vaterite (MORSE and MACKENZIE, 1990). From these phases, calcite is the stable polymorph, whereas aragonite and vaterite are metastable (PLUMMER and BUSENBERG, 1982). In nature, vaterite is the least common of the three anhydrous calcium carbonate minerals. However, vaterite has been observed in nature, for example, as a secondary product from ikaite ($\text{CaCO}_3 \cdot 6\text{H}_2\text{O}$) decomposition (ITO et al., 1999) and at low temperatures in the presence of gypsum (GRASBY, 2003). Experimentally, vaterite has been identified as a product from the interaction of alkaline solutions with gypsum (FERNÁNDEZ-DÍAZ et al., 2009a; FLÖRKE and FLÖRKE, 1961; RONCAL-HERRERO et al., 2011) and as a calcium carbonate crystallization product in the presence of sulfate (chapter 4). The persistence of vaterite in these systems/environments is likely to be caused by the stabilizing effect of sulfate on vaterite (FERNÁNDEZ-DÍAZ et al., 2010, see also chapter 4 and 7).

The abiotic formation of gypsum in nature occurs predominantly in evaporitic environments like the dead sea (REZNIK et al., 2011). Many large gypsum formations have been found in the geological record (WARREN, 2010). Among the

many evaporite minerals found in nature, rapidcreekite is a hydrated calcium sulfate-calcium carbonate solid solution ($\text{Ca}_2\text{SO}_4\text{CO}_3 \cdot 4\text{H}_2\text{O}$). However, due to its rarity in nature, very little is known about this phase. Rapidcreekite has only been found in nature at two localities and always in association with gypsum and other carbonate minerals (ROBERTS et al., 1986; WALENTA and DUNN, 1989). Rapidcreekite is thought to be a secondary mineral and formed in an iron rich environment (Rapid Creek area, northern Yukon Territory, Canada, ROBERTS et al., 1986). However, no iron phases were identified in the second locality (a silver and uranium mine in the Black Forest, Germany) where rapidcreekite was found (WALENTA and DUNN, 1989). Finally, rapidcreekite was only found in one experimental desalination study at a low aqueous carbonate to sulfate ratio (DYDO et al., 2003) and nothing is known about its thermodynamic stability.

The structure of gypsum can be represented by hydrated sheets of alternate double chains of Ca and SO_4 ; these double planes are held together with H-bridges (DE VILLIERS, 1971; SCHOFIELD et al., 1996). The structure of rapidcreekite as determined from a natural sample is similar to the structure of gypsum (COOPER and HAWTHORNE, 1996). In relation to the structure of gypsum, in rapidcreekite alternate double chains of SO_4 are replaced by CO_3 ions (COOPER and HAWTHORNE, 1996).

Nucleation and formation pathways of CaSO_4 phases are poorly understood (FREYER and VOIGT, 2003; VAN DRIESSCHE et al., in review). Additionally, only little information is available on the effects of SO_4 on the formation of vaterite (chapter 4 and 5, FERNÁNDEZ-DÍAZ et al., 2010). This chapter reports further on the effect of SO_4 on vaterite formation in combination with the formation of CaSO_4 phases. This was done by performing *in situ* time resolved crystallization experiments using the wide angle X-ray scattering (WAXS) capability of beamline I22 (SAXS/WAXS) at Diamond Light Source in order to quantify the formation of vaterite and gypsum via a rapidcreekite intermediate.

6.2 Methods

Crystallization experiments following the method described by RODRIGUEZ-BLANCO et al (2010) and in chapter 5 were used. In brief, 40 ml of a 2.5 M calcium chloride solutions ($\text{CaCl}_2 \cdot 2\text{H}_2\text{O}$, analytical grade) was rapidly injected into 160 ml

of a 0.625 M sodium carbonate/sulfate (Na_2CO_3 , analytical grade / Na_2SO_4 , analytical grade). To inject the calcium chloride solution in the sodium carbonate/sulfate solution, a stopped flow device was used. The crystallization experiments were performed in three different chemical conditions:

- (1) ‘replacement’: 30% of CO_3 was replaced by SO_4 (the amount of calcium was equal to the amount of carbonate and sulfate);
- (2) ‘additive’: 30% SO_4 was added to the CO_3 solution (that the amount of calcium was equal to the amount of carbonate) and
- (3) ‘additive-Mg’: identical to (2) including 10% Mg (as $\text{MgCl}_2 \cdot 2\text{H}_2\text{O}$) added to the Ca solution.

The chemical conditions used are described in more detail in Table 6.1. Throughout the experiments (up to ~80 min), the formed suspensions were stirred vigorously by an overhead stirrer to ensure homogeneous conditions. During the ‘replacement’ experiment the pH was recorded.

Table 6.1 Summary of the experimental conditions for all experiments

Exp.	Ca solution			CO ₃ /SO ₄ solution		
	Ca (M)	Mg (M)	V (ml)	CO ₃ (M)	SO ₄ (M)	V (ml)
Replacement	2.5	-	40	0.4375	0.1875	160
Additive	2.5	-	40	0.625	0.1875	160
Additive-Mg	2.5	0.25	40	0.625	0.1875	160

Exp.	Mixed solution				
	Ca (M)	Mg (M)	CO ₃ (M)	SO ₄ (M)	V (ml)
Replacement	0.5	-	0.35	0.15	200
Additive	0.5	-	0.5	0.15	200
Additive-Mg	0.5	0.05	0.5	0.15	200

The experiments were performed at the small/wide angle X-ray scattering (SAXS/WAXS) beamline I22 at Diamond Light Source. Immediately after mixing, the suspensions were continuously pumped through a capillary in line with the synchrotron beam using a peristaltic pump. WAXS patterns were collected at one second / frame resolution with a HOTWAXS detector (BATEMAN et al., 2007), for a total duration up to ~80 min. The collected patterns were detector response corrected and background subtracted. Individual WAXS patterns were fitted using Topas 4-2

(BRUKER_AXS, 2009) to obtain the *Rietveld scale factor* (S) of the Bragg peaks for each phase detected in the patterns. S relates the structural model with the intensity under the Bragg peaks to obtain the relative mass (w) of the respective phase in the sample (HILL AND HOWARD, 1987; RIETVELD, 1969). Subsequently, the degree of reaction ($\alpha(t)$) was calculated for all crystalline phases (present at the end of the experiment (p) and as an intermediate(i)) using Eq. 6.1 and 6.2 (see also section 3.3.2):

$$\alpha_p(t) = \frac{S_p(t)}{S_p(t_{final})} \cdot w_p(t_{final})$$

(Eq. 6.1)

$$\alpha_i(t) = \frac{S_i(t)}{S_i(t_{i,max})} \cdot \left[\frac{w_i(t_{i,max})}{w_p(t_{i,max})} \cdot \alpha_p(t_{i,max}) \right]$$

(Eq. 6.2)

where t_{final} represents the time at which the data collection was terminated and the crystalline phases p were present. Additionally, $t_{i,max}$ represents the time at which the *Rietveld scale factor* (S) corresponding to a crystalline intermediate phase (i) reached a maximum. Finally, $\alpha_p(t)$ is recalculated using each phase's molar weight ($M_{w,p}$) to the mole % of crystalline phases in the system compared to the final amount of moles using Eq. 6.3.

$$mole \%_p(t) = 100\% \cdot \frac{\alpha_p(t)/M_{w,p}}{\sum(\alpha(t)/M_w)}$$

(Eq. 6.3)

6.3 Results and discussion

In all experiments after mixing, the solutions were highly supersaturated with respect to all known calcium carbonate and sulfate phases. Additionally,

immediately after mixing a white suspension formed in all experiments. Figure 6.1A shows a 3D representation of the WAXS results from the ‘replacement’ experiment. The absence of any Bragg peaks shows that no crystalline phase was present during the first 4 minutes. Due to the absence of Bragg peaks and the presence of a white suspension, the broad hump in the background of the WAXS patterns during the first 4 minutes (Figure 6.1) is likely to be caused by scattering from amorphous calcium carbonate (ACC), water and air (chapter 5, RODRIGUEZ-BLANCO et al., 2011). To date, no amorphous calcium sulfate phase has been identified, but scattering caused by a small amount of nanocrystalline calcium sulfate (VAN DRIESSCHE et al., in review) cannot be excluded.

In the ‘replacement’ experiment, Bragg peaks appeared after ~4 minutes and grew while the background intensity in the WAXS patterns decreased (Figure 6.1). Four averaged WAXS patterns (Figure 6.1B) show that the first phases growing from the amorphous precursor were vaterite and rapidcreekite, while at the end of the experiment gypsum and vaterite were the only crystalline phases present. In comparison, during the ‘additive’ and ‘additive-Mg’ experiments, the first phase growing from the amorphous precursor was gypsum followed by rapidcreekite and vaterite (and calcite in the ‘additive-Mg’ experiment). Also at the end of these experiments, the only crystalline phases present were gypsum and vaterite (and calcite in the ‘additive-Mg’ experiment). To the best of our knowledge, this is the first time that rapidcreekite is observed as an intermediate in gypsum and vaterite formation.

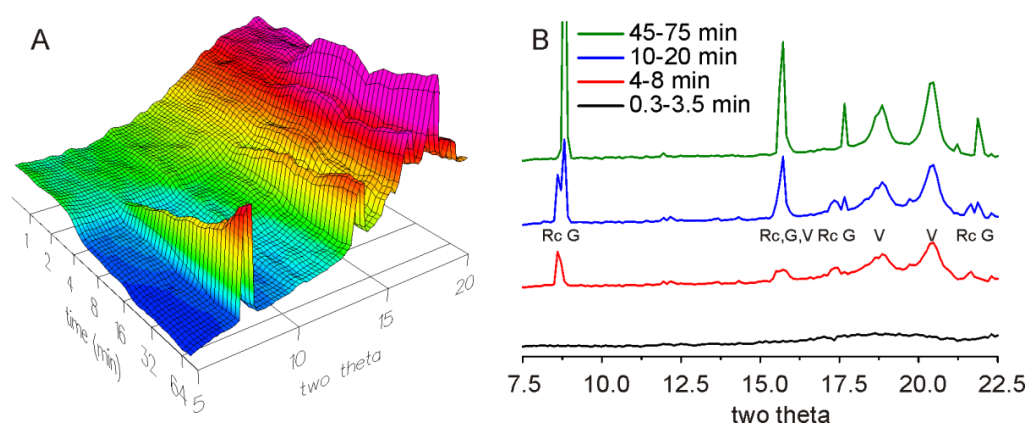


Figure 6.1 (A) 3D plot of the time resolved WAXS patterns with time on a base 2 log scale and (B) averaged WAXS patterns over 4 time intervals from the ‘replacement’ experiment; the position of the main peaks for gypsum, rapidcreekite and vaterite are labelled with G, Rc and V, respectively

6.3.1 ‘Replacement’ experiment

Figure 6.2A shows the $\alpha(t)$ extracted from the WAXS patterns collected during the ‘replacement’ experiment using Eq. 6.1 and 6.2 (Figure 6.1). During the ‘replacement’ experiment after the formation of ACC, $\alpha(t)$ for vaterite started to increase at ~ 3.5 min and for rapidcreekite at ~ 4 min. After the initial increase in $\alpha(t)$ for vaterite and rapidcreekite, the $\alpha(t)$ for gypsum started to increase at ~ 6 min and further increased throughout the experimental time. After ~ 15 min, the $\alpha(t)$ for rapidcreekite and decreased up to ~ 40 min, simultaneously $\alpha(t)$ for vaterite increased. Additionally, Figure 6.3 shows the recorded pH during the ‘replacement’ experiment and a comparison to the $\alpha(t)$ for gypsum. Prior to an increase in $\alpha(t)$ for gypsum formation the pH decreased from ~ 9.1 to ~ 7.7 . Subsequently, during the initial increase in $\alpha(t)$ for gypsum, the pH increased from ~ 7.7 to ~ 7.9 while the $\alpha(t)$ for rapidcreekite and vaterite remained constant (Figure 6.2A).

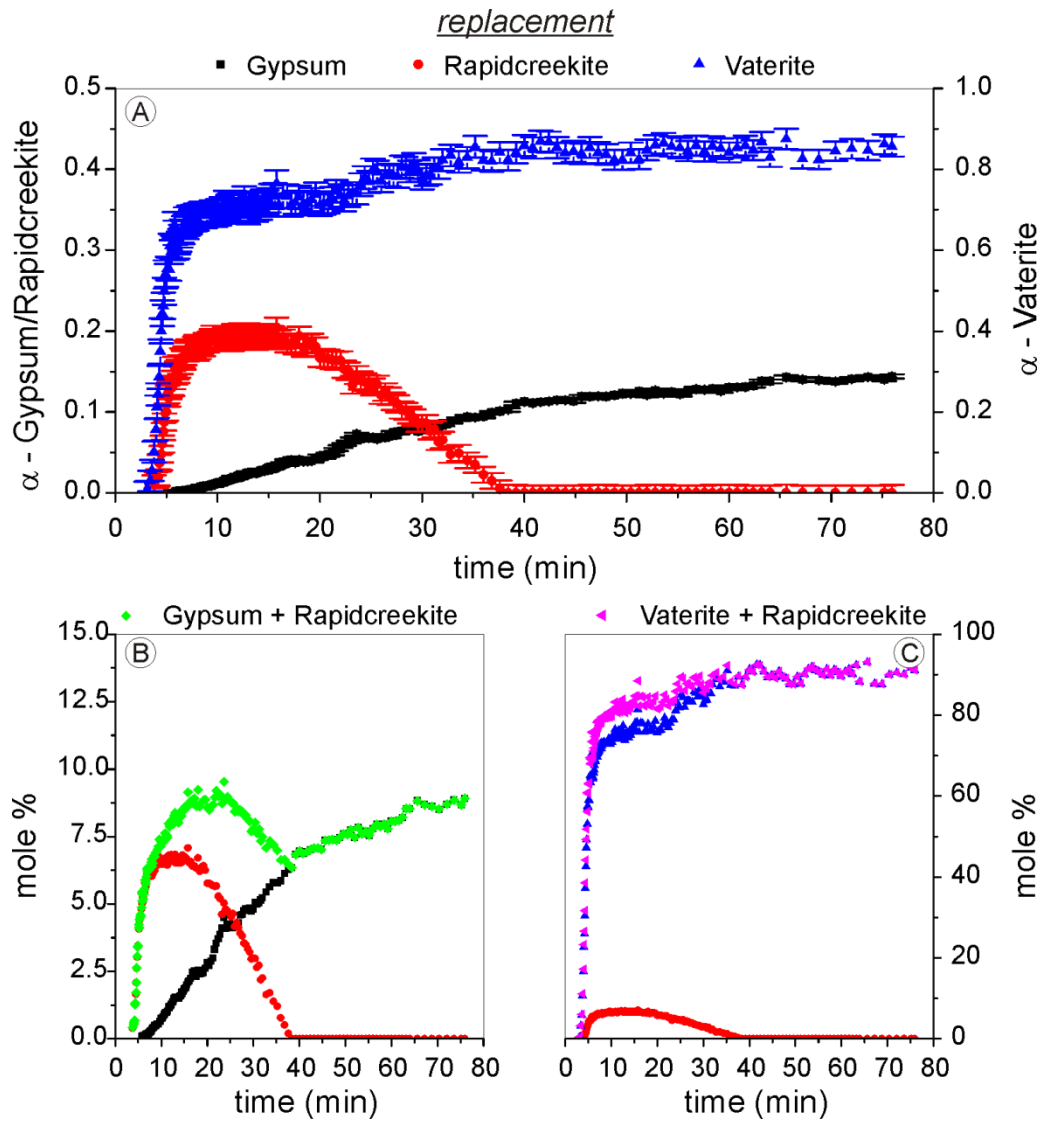


Figure 6.2 $\alpha(t)$ plots for vaterite, gypsum and rapidcreekite from the ‘replacement’ experiment (A) $\alpha(t)$ calculated using Eq. 6.1 and 6.2; (B) and (C): $\alpha(t)$ recalculated to the mole % of crystalline phases in the system using Eq. 6.3, including the sum of mole % of (B) gypsum and rapidcreekite and (C) vaterite and rapidcreekite

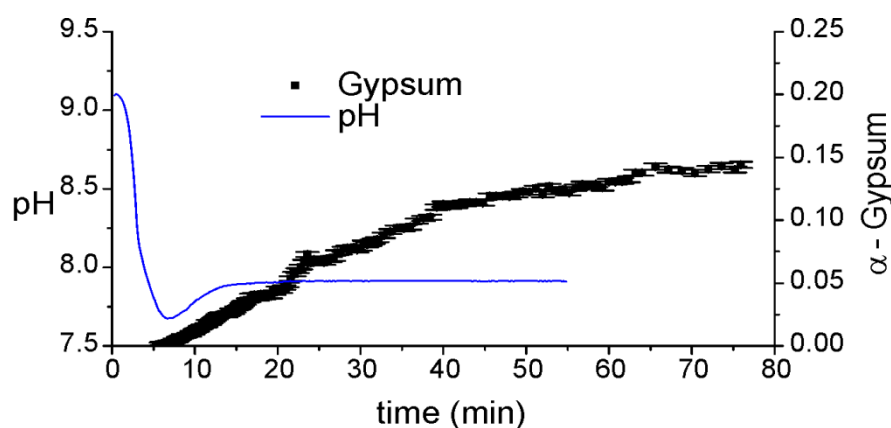
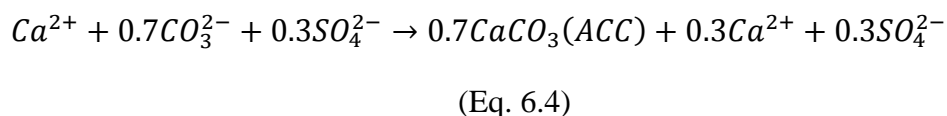


Figure 6.3 The pH and $\alpha(t)$ for gypsum (Figure 6.2A) during the ‘replacement’ experiment

Previous research indicated that SO_4 does not significantly replace CO_3 in the structure of ACC (chapter 5, Figure 5.5, AIZENBERG et al., 2001). This indicates that the formation of ACC in the ‘replacement’ experiment (where 30% CO_3 was replaced by SO_4 , Table 6.1) can be represented by Eq. 6.4. The fractions in Eq. 6.4 represent the ion fractions with respect to the calcium ion if all carbonate would precipitate as ACC.

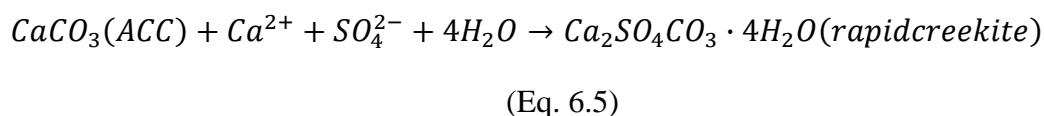


Eq. 6.4 indicates that subsequent to ACC formation, the remaining Ca and SO_4 concentrations were significantly larger than the CO_3 concentration (in line with the results from experiments described in chapter 5, Table 6.2). Hence, the formation of rapidcreekite in the ‘replacement’ experiment corresponds well with the observation from DYDO et al. (2003) that rapidcreekite forms from a solution with a low CO_3/SO_4 ratio (0.0045).

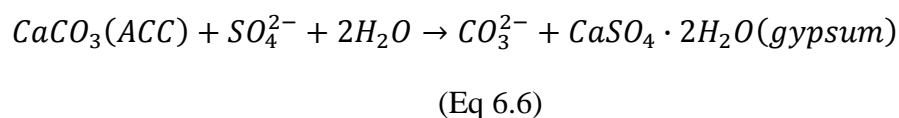
Table 6.2 Extract from Table D.1 on the solution chemistry prior to the formation of vaterite, from the results of experiments described in chapter 5 with no additive or 10% SO₄ in the initial carbonate solution instead of 30% ('no additive', 'replacement (10%)' and 'additive (10%)')

	pH	Total concentrations (mM)			Aqueous speciation (mM)			
		Ca	TIC	SO ₄	Ca ²⁺	CO ₃ ²⁻	HCO ₃ ⁻	SO ₄ ²⁻
No additive	9.5	26	30	0	20	4.0	7.3	0
Replacement (10%)	8.8	75	45	45	57	2.1	22	23
Additive (10%)	9.6	32	39	48	22	5.4	8.5	27

As shown in Eq. 6.4, the carbonate concentration is likely to be low and rapidcreekite is a carbonate containing phase. Hence, the formation of rapidcreekite is likely to have formed at the expense of ACC as represented in Eq. 6.5.

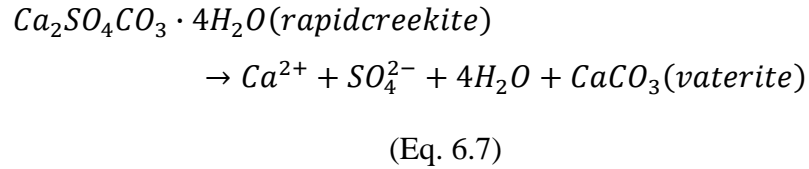


Following the formation of rapidcreekite, gypsum started to crystallize at ~6 min. and simultaneously the pH increased from ~7.7 to ~7.9 between ~6 and ~15 min (Figure 6.3) during which $\alpha(t)$ for rapidcreekite and vaterite remained constant (Figure 6.2A). Hence, the increase in pH cannot be explained by a release of CO₃ from the break down of rapidcreekite. This indicates that the initial gypsum crystallization occurred at the expense of any remaining ACC, as an increase in CO₃ in solution (caused by the dissolution of ACC) could explain the observed increase in pH (Eq. 6.6 and Figure 6.3).

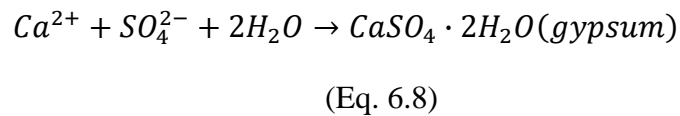


Between ~15 min and ~40 min, the $\alpha(t)$ for rapidcreekite decreased while the $\alpha(t)$ for gypsum and vaterite increased (Figure 6.2A). Additionally, the sum of the gypsum and rapidcreekite mole % decreased with rapidcreekite disappearance (Figure 6.2B). Hence, the total amount of solid CaSO₄ in the system decreased. This indicates that the amount of SO₄ in solution increased (caused by the disappearance

of rapidcreekite, Eq. 6.7). In contrast, the sum of the vaterite and rapidcreekite mole % increased continuously throughout the experiment (Figure 6.2C). This indicates that the disappearance of rapidcreekite was caused by the formation of additional vaterite and concurrently releasing Ca and SO₄ into the solution following Eq. 6.7.



Finally, when all rapidcreekite disappeared, gypsum continued to form (at ~ 40 min, Figure 6.2A and 6.2B). In addition, the pH remained constant after all rapidcreekite dissolved and no more vaterite crystallized during the experiment (Figure 6.2 and 6.3). This indicates that no more ACC was present in the system and the additional gypsum crystallized from solution (Eq. 6.8).



6.3.2 ‘Additive’ and ‘additive-Mg’ experiments

Figure 6.4A and 6.5A show the $\alpha(t)$ extracted from the WAXS patterns collected during the ‘additive’ and *additive-Mg* experiment, respectively, using Eq. 6.1 and 6.2. During the ‘additive’ experiment, the $\alpha(t)$ for gypsum started to increase at ~3 min (Figure 6.4A), while the $\alpha(t)$ for rapidcreekite and vaterite started to increase at ~4 and ~4.5 min respectively. The $\alpha(t)$ for rapidcreekite reached a maximum of ~0.05 at ~7 min and decreased to 0 after ~12 min. During the ‘additive’ -Mg experiment, the $\alpha(t)$ for gypsum started to increase at ~1 min, the $\alpha(t)$ for rapidcreekite at ~2 min and the $\alpha(t)$ for vaterite at ~5 min (Figure 6.5A). The $\alpha(t)$ for rapidcreekite reached a maximum of ~0.18 at ~7 min and decreased to 0 after ~30 min.

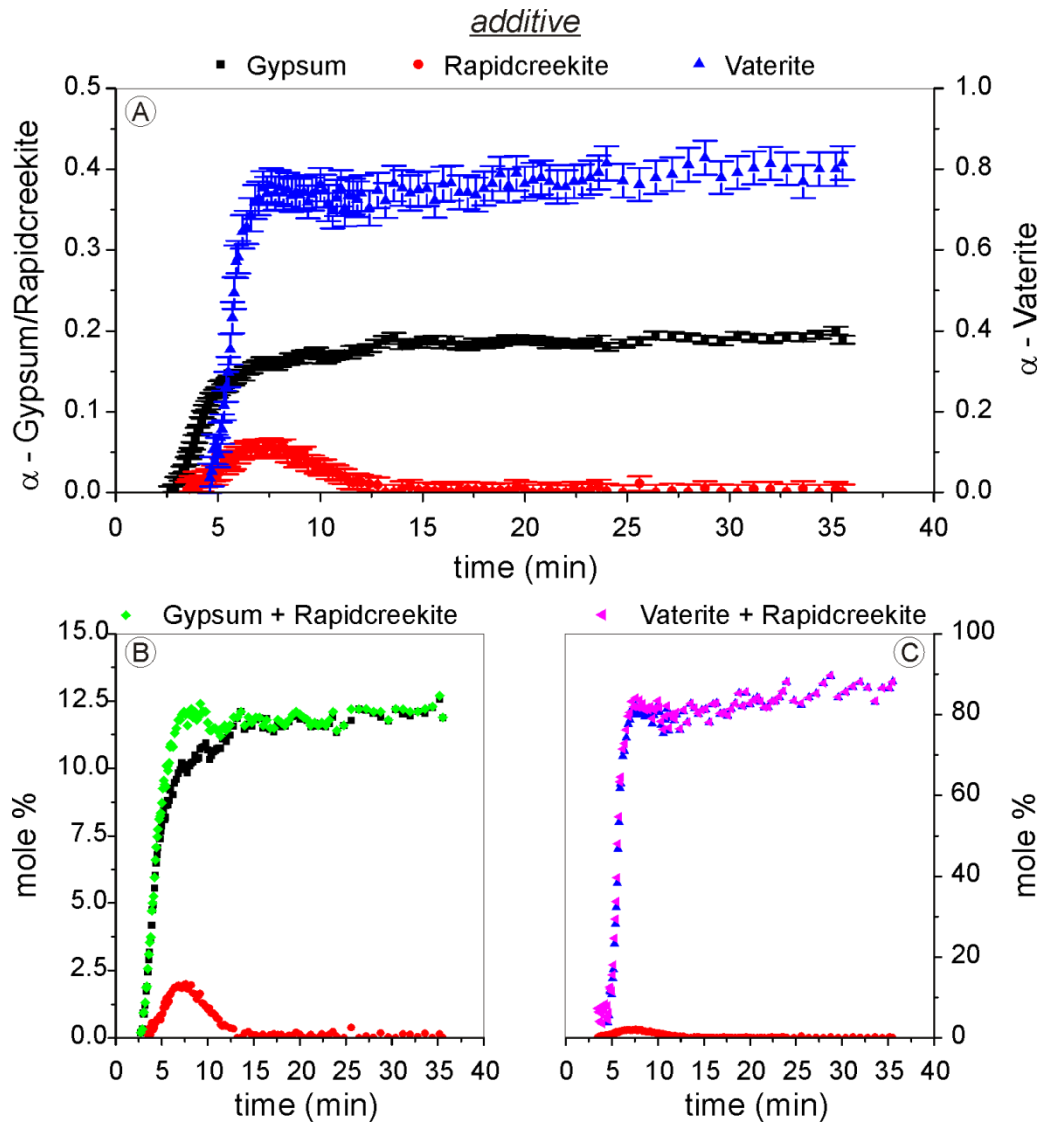


Figure 6.4 $\alpha(t)$ plots for vaterite, gypsum and rapidcreekite from the ‘additive’ experiment (A) $\alpha(t)$ calculated using Eq. 6.1 and 6.2; (B) and (C): $\alpha(t)$ recalculated to the mole % of crystalline phases in the system using Eq. 6.3, including the sum of mole % of (B) gypsum and rapidcreekite and (C) vaterite and rapidcreekite

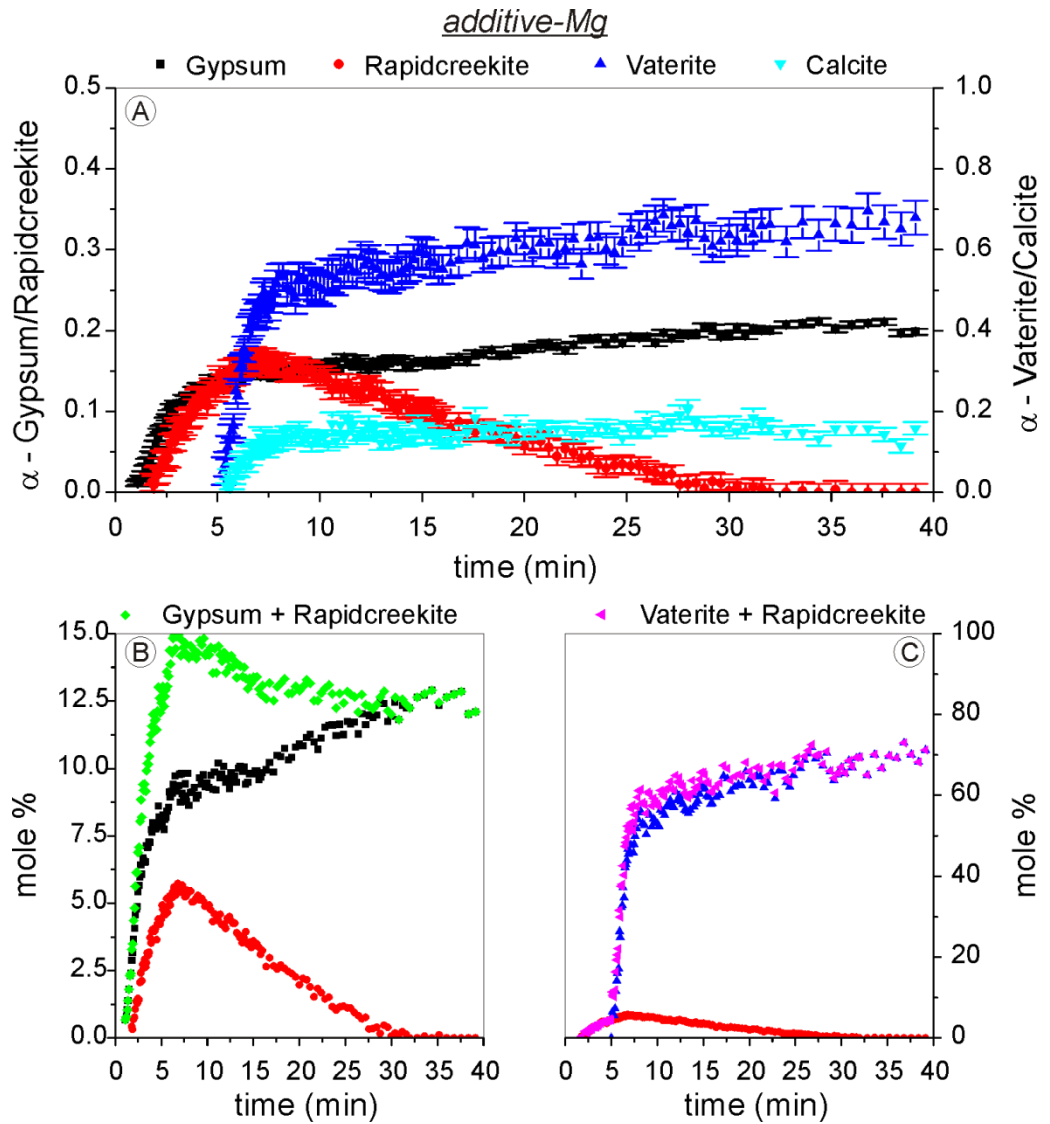
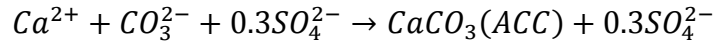
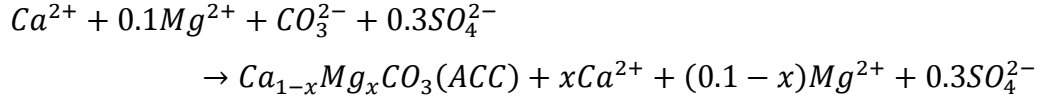


Figure 6.5 $\alpha(t)$ plots for vaterite, calcite, gypsum and rapidcreekite from the ‘additive-Mg’ experiment (A) $\alpha(t)$ calculated using Eq. 6.1 and 6.2; (B) and (C): $\alpha(t)$ recalculated to the mole % of crystalline phases in the system using Eq. 6.3, including the sum of mole % of (B) gypsum and rapidcreekite and (C) vaterite and rapidcreekite

Similar to the ‘replacement’ experiments, the first phase that formed in the ‘additive’ and ‘additive-Mg’ experiment was an ACC phase, which can be represented by Eq. 6.9 (‘additive’) and 6.10 (‘additive-Mg’). The fractions in Eq. 6.9 and 6.10 represent the ion fractions with respect to the calcium ion if all carbonate precipitated as ACC and Mg would replace Ca in the structure of ACC.



(Eq. 6.9)



(Eq. 6.10)

As shown in Figure 6.4 and 6.5, the first phase that formed in the ‘additive’ and *additive-Mg* experiments was gypsum. The formation of gypsum during the ‘additive’ experiment compared to the ‘replacement’ experiment was significantly faster (~90% gypsum formed during the first 10 min in the ‘additive’ experiment compared to ~20% during the ‘replacement’ experiment, Figure 6.2A and 6.4A). Table 6.2 and Eq. 6.4 and 6.9 indicate that the aqueous Ca/SO₄ ratio after ACC formed was lower in the ‘additive’ experiment compared to the ‘replacement’ experiment. ZHANG and NANCOLLAS (1992) determined that the hydration of gypsum facilitates the incorporation of Ca (which ions are more strongly hydrated than SO₄) more than the incorporation of SO₄. This causes the gypsum formation kinetics to increase in decreasing low Ca/SO₄ ratio (ZHANG and NANCOLLAS, 1992). Hence, the difference in the aqueous Ca/SO₄ ratios (Eq. 6.4 and 6.9) caused the increase in the gypsum formation kinetics in the ‘additive’ experiment compared to the ‘replacement’ experiment. The faster kinetics of gypsum formation at a low Ca/SO₄ ratio can also explain the gypsum (a decrease in the induction time) crystallization before rapidcreekite and vaterite in the ‘additive’ experiment (Figure 6.4A).

Mg has been shown to incorporate into the structure of ACC (Eq. 6.10, LOSTE et al., 2003) stabilizing the precipitated amorphous phase (LOSTE et al., 2003; RODRIGUEZ-BLANCO et al., in press). This could increase the amount of ACC formed initially, which could lead to a decreased Ca concentration leading to a decrease in the Ca/SO₄ ratio. As discussed above, this could cause a decrease in the gypsum induction time in the ‘additive-Mg’ (~1 min) compared to the ‘additive’ experiment (~3 min) (Figure 6.4A and 6.5A). In the ‘additive-Mg’ experiment both the induction time for rapidcreekite and gypsum decreased. Because the structures of

gypsum and rapidcreekite are similar (COOPER and HAWTHORNE, 1996), the decrease in the induction time for rapidcreekite in the ‘additive-Mg’ experiment compared to the ‘additive’ experiment could also be caused by a lowering in the aqueous Ca/SO₄ ratio as described above.

During the ‘additive’ and ‘additive-Mg’ experiments, rapidcreekite crystallization ended when the initial (rapid) vaterite formation finished (i.e. most carbonate from solution was consumed by either rapidcreekite or vaterite formation, Figure 6.4A and 6.5A). Subsequently, rapidcreekite breakdown was coupled with the formation of additional vaterite (section 6.3.1 and Eq. 6.7) releasing Ca and SO₄ back into the solution (Figure 6.4C and 6.5C) allowing further gypsum formation (Eq. 6.7, Figure 6.4 and 6.5). During the ‘replacement’ and ‘additive-Mg’ experiment the sum of the mole % of rapidcreekite and gypsum decreased during the dissolution of rapidcreekite (Figure 6.5B). This indicates that not all Ca and SO₄ released back into solution by the breakdown of rapidcreekite resulted in additional formation of gypsum. Furthermore, rapidcreekite only started forming after more than 75% of the gypsum had crystallized (Figure 6.4 and 6.5). These observations indicate that rapidcreekite solubility is lower than gypsum solubility. However, CaCO₃ minerals are about four orders of magnitude less soluble than gypsum (FREYER and VOIGT, 2003; PLUMMER and BUSENBERG, 1982). Hence, the formation of CaCO₃ minerals is likely to be favoured over the formation of rapidcreekite or cause the breakdown of rapidcreekite.

6.3.3 Vaterite formation mechanisms and kinetics

Figure 6.6 shows the $\alpha(t)$ for the initial stage of the vaterite formation including the best fit with the Johnson-Mehl-Avrami-Kolmogorov (JMAK) equation (Eq. 6.11, AVRAMI, 1939; AVRAMI, 1940; AVRAMI, 1941; JOHNSON and MEHL, 1939):

$$\alpha(t) = 1 - \exp[-k(t - t_0)^n]$$

(Eq. 6.11)

where k is the kinetic constant (min⁻ⁿ), t is the time (min), t_0 is the induction time

(min) and n is the Avrami exponent. The Avrami exponent can be expressed as: $n = 1 + d$ (GRÁNÁSY et al., 2005), where d is the dimensionality during spherulitic growth. The JMAK parameters fitted with $n = 4$ (chapter 5) are listed in Table 6.3. The kinetic constant in all experiments was lower and the induction time higher for all experiments compared to the experiments described in chapter 5 ('no additive', 'replacement (10%)' and 'additive (10%)' in Table 6.3). Additionally, the induction time in the 'additive' and 'additive-Mg' experiments was higher than in the 'replacement' experiment and the kinetic constant was lower in the 'additive-Mg' experiment than in the 'replacement' and 'additive' experiments (Table 6.3).

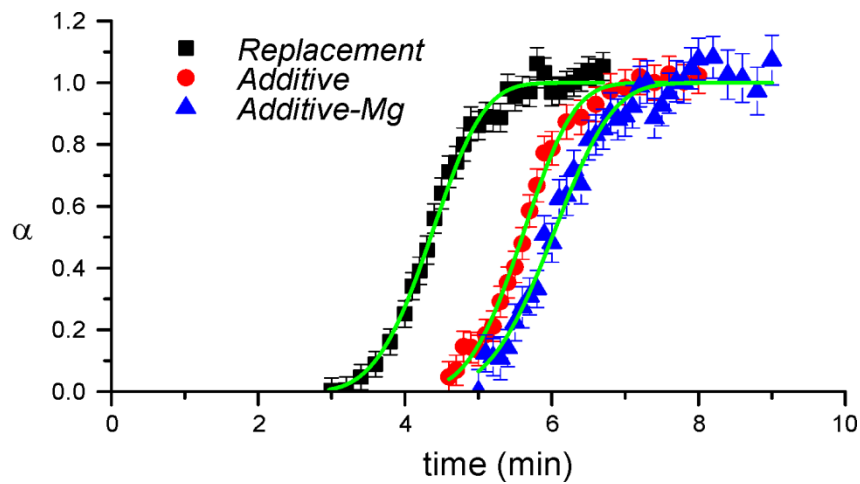


Figure 6.6 $\alpha(t)$ for the initial stage of vaterite formation in the 'replacement', 'additive' and 'additive-Mg' experiments with the JMAK fits superimposed

Table 6.3 JMAK fitted parameters (with $n = 4$) for the spherulitic growth of vaterite of the experiments described in this chapter (with ‘(30%)’ as suffix); including a reproduction of the fitted parameters from the experiments discussed in chapter 5 and Table 5.2 (‘no additive’, ‘replacement (10%)’ and ‘additive (10%)’) for comparison

Experiment	Variable	Value	Standard error
no additive	k (min ⁻⁴)	48.7	8.8
Adj. R ² = 0.9888	t_0 (min)	0.93	0.02
replacement (10%)	k (min ⁻⁴)	11.7	2.5
Adj. R ² = 0.9828	t_0 (min)	0.98	0.03
additive (10%)	k (min ⁻⁴)	9.2	2.3
Adj. R ² = 0.9727	t_0 (min)	1.37	0.03
replacement (30%)	k (min ⁻⁴)	0.0425	0.0075
Adj. R ² = 0.993	t_0 (min)	2.34	0.09
additive (30%)	k (min ⁻⁴)	0.0469	0.0082
Adj. R ² = 0.993	t_0 (min)	3.63	0.08
additive-Mg (30%)	k (min ⁻⁴)	0.0256	0.0060
Adj. R ² = 0.982	t_0 (min)	3.72	0.13

As discussed in chapter 5, the ACC crystallization to vaterite occurred via a spherulitic growth mechanism (ANDREASSEN, 2005), which can be described by the JMAK model (GRÁNÁSY et al., 2005). Additionally, the JMAK model fits with an Avrami coefficient (n) of 4 (Figure 6.6 and Table 6.3). This indicates that the vaterite formation followed 3D spherulitic growth kinetics (chapter 5, GRÁNÁSY et al., 2005). The increase in SO₄ concentration decreased the spherulitic rate constant (k , Table 6.3) by ‘poisoning’ the vaterite spherulitic growth nucleation sites further compared to the experiments with 10% SO₄ (chapter 5), which also caused the increase in the induction time (t_0 , Table 6.3). Similar to the solution composition described in chapter 5 (Table 6.2), the bicarbonate concentration was likely higher in the ‘replacement’ experiment than in the ‘additive’ and ‘additive-Mg’ experiments. This could have caused a shorter induction time in the ‘replacement’ experiment compared to the ‘additive’ and ‘additive-Mg’ experiments (Table 6.3), either by destabilizing ACC (chapter 5, NEBEL et al., 2008) or by the consumption of bicarbonate rather than carbonate during the formation of vaterite (chapter 5).

Only in the ‘additive-Mg’ experiment, calcite formed in addition to vaterite (Figure 6.5A). In similar experiments with Mg present (without SO₄) ACC crystallized directly to calcite without vaterite as an intermediate (RODRIGUEZ-BLANCO et al., in press). This is caused by the strong destabilizing affect Mg exerts on vaterite (chapter 4). However, the destabilization of Mg on vaterite is

counteracted by the stabilization of vaterite by SO_4 and the destabilization and inhibition of calcite by SO_4 (chapter 4 and 7, FERNÁNDEZ-DÍAZ et al., 2010), hence in the ‘additive-Mg’ experiment the formation of vaterite occurred. The JMAK model also shows that the addition of Mg decreased the kinetic constant (k) in the ‘additive-Mg’ experiment compared to the ‘additive’ and ‘replacement’ experiments by ~40% (Table 6.3). LOSTE et al. (2003) determined that the incorporation of Mg significantly stabilized the ACC structure and chapter 4 shows that the incorporation of Mg destabilized vaterite. This resulted in a decrease in the vaterite crystallization enthalpy, which caused k to decrease (Table 6.3).

6.4 Concluding remarks

Even though the solubility of rapidcreekite is likely to be lower than that of gypsum, rapidcreekite has only been found at two localities (ROBERTS et al., 1986; WALENTA and DUNN, 1989) as a secondary mineral. The rarity of rapidcreekite is likely to be caused by the lower solubility of CaCO_3 minerals compared to the solubility of rapidcreekite. This indicates that generally, CaCO_3 phases will be preferred over rapidcreekite. Thus, rapidcreekite is also likely to be associated with calcium carbonate phases in nature (ROBERTS et al., 1986; WALENTA and DUNN, 1989) and during CaSO_4 scaling in the presence of CO_3 (DYDO et al., 2003). Additionally, although vaterite formed experimentally in this study, in nature the occurrence of aragonite, as determined by ROBERTS et al. (1986), can also be explained by the presence of Mg as well as SO_4 (chapter 4). The results presented in this study indicate that rapidcreekite can form easily prior to the full crystallization of gypsum and CaCO_3 phases when both SO_4 and CO_3 are present in solution and that rapidcreekite might be an important intermediate in alkaline brines and evaporitic environments.

Finally, this study highlights the applicability of synchrotron based WAXS experiments to study complex crystallization processes. For a more complete determination of all processes that occur during the crystallization, off-line solution and solid data is required (e.g. solution chemistry and electron microscopy, chapter 5).

Chapter 7

Vaterite, formation and the effect of sulfate

7.1 Introduction

Calcium carbonates (CaCO_3) minerals precipitate in a wide variety of environments (MORSE and MACKENZIE, 1990). In most natural settings CaCO_3 phases are dominated by either calcite or aragonite (MORSE and MACKENZIE, 1990). However, a third rare metastable anhydrous CaCO_3 mineral (vaterite) can occur in nature. Examples of vaterite occurrence in nature are: in the presence of gypsum (GRASBY, 2003) and as an Ikaite ($\text{CaCO}_3 \cdot 6\text{H}_2\text{O}$) dehydration product (ITO et al., 1999). Additionally, several organisms have been determined to produce vaterite as a biomineralization product (LOWENSTAM, 1981). For example, the mineralized parts of a specific sea squirt (*Herdmania momus*, LOWENSTAM and ABBOTT, 1975) and the otoliths of some fish species (TOMÁS and GEFFEN, 2003) are exclusively made of vaterite.

Several studies have attempted to refine the structure of vaterite (KAMHI, 1963; LE BAIL et al., 2011; MEDEIROS et al., 2007; MEYER, 1960; MEYER, 1969; WANG and BECKER, 2009). Even though no agreement has been reached on the precise structure, some features of the vaterite structure are identical between all refinements. The calcium ions are positioned in a hexagonal sub-lattice, the carbonate ions are aligned in planes parallel to the c-axis and there is a considerable amount of disorder in the position and alignment of the carbonate ions in the structure.

Experimentally, in the absence of any additives, vaterite transforms into calcite (KRALJ et al., 1997; OGINO et al., 1987; OGINO et al., 1990; RODRIGUEZ-BLANCO et al., 2011) or aragonite (BISCHOFF, 1968; OGINO et al., 1987) within a few hours. This transient nature of vaterite can explain the rarity of vaterite in natural settings and the difficulties in structural determinations. However, experimental studies on the carbonation of gypsum also resulted in the formation and persistence of vaterite (FERNÁNDEZ-DÍAZ et al., 2009b; FLÖRKE and FLÖRKE, 1961; RONCAL-HERRERO et

al., 2011). Vaterite has also been observed to preferentially form and persist for longer periods in the presence of sulfate (chapter 4, DONER and PRATT, 1969; FERNÁNDEZ-DÍAZ et al., 2010; SIMKISS, 1964). Additionally, BISCHOFF (1968) determined that the transformation kinetics of vaterite to aragonite decreased in the presence of sulfate in solution. FERNÁNDEZ-DÍAZ et al. (2010) used vaterite formation experiments, in the presence of varying sulfate concentrations, in combination with atomistic simulation models to determine that the incorporation of sulfate enhances the stability of vaterite and concurrently decreases the stability of calcite and aragonite. From this FERNÁNDEZ-DÍAZ et al. (2010) determined that the vaterite to calcite and aragonite transformation energy decreases in the presence of sulfate, explaining the observed decrease in transformation kinetics (BISCHOFF, 1968; FERNÁNDEZ-DÍAZ et al., 2010). However, the exact mechanisms of the interaction of sulfate with vaterite and the effects on the structure of vaterite have not been determined experimentally.

For comparison, ammonium has been shown to stabilize vaterite via adsorption and by acting as a template by binding preferentially on specific vaterite lattice faces (POUGET et al., 2010). Additionally, in biomimetic studies, organic substances have also been shown to promote the precipitation and stabilization of vaterite (DUPONT et al., 1997; OLDERØY et al., 2009; THOMPSON et al., 2011; XYLEA et al., 1991; ZHU et al., 2009). Although the specific process is not well understood, organic substances may define the crystallizing polymorph and direction of growth by, for example, adsorption with calcium or carbonate ions or poisoning nucleation sites (MELDRUM and CÖLFEN, 2008).

To determine the mechanisms of the effects of SO_4 on the formation, stability and structure of vaterite were tested by via a series of synthesis and ageing experiments. Additionally, conventional analytical methods were supplemented by synchrotron based analytical methods.

7.2 Methods

7.2.1 Synthesis experiments

Calcium carbonate was synthesized by rapidly mixing 200 ml of 100 mM calcium chloride ($\text{CaCl}_2 \cdot 2\text{H}_2\text{O}$, analytical grade) with 200 ml of 50-100 mM sodium carbonate (Na_2CO_3 , analytical grade) containing 0-2M sodium sulphate (Na_2SO_4 , analytical grade). The chemical composition of the solutions used in the synthesis experiments are summarized in Table 7.1. During all experiments, the solutions were continuously stirred by a magnetic stirrer at 150 rpm for ~15 minutes at room temperature ($21 \pm 1^\circ\text{C}$). At the end of the experiments, the precipitates were separated from solution by filtration (0.2 μm membrane filter). The precipitates were immediately washed with 18.2 M Ω Milli-Q grade H_2O equilibrated with calcite, then with propan-2-ol and subsequently dried at room temperature. X-Ray Diffraction (XRD) analyses of the solids were performed using a Bruker D8 X-Ray Diffractometer ($\text{Cu K}\alpha 1$). On all collected XRD patterns, Rietveld refinements were performed using Topas V4.2 (BRUKER_AXS, 2009). The XRD patterns revealed that experiment 5 ($\text{SO}_4/\text{CO}_3 = 25$, Table 7.1) produced solely vaterite. Additionally, the chemical composition of the solid sample from experiment 5 was analyzed using a Cameca microprobe with integrated Wavelength Dispersive X-ray Spectroscopy (WDS) and via the dissolution of the solid sample in HCl and subsequent analyzed with Ion Chromatography (IC) as described in section 3.5.2. Finally, the structure of the vaterite formed in experiment 5 was characterized with X-ray absorption spectroscopy (XAS) and high-resolution XRD (HR-XRD) at Diamond Light Source (at station I18 and I11, respectively). Also on the collected HR-XRD pattern, Rietveld refinement was performed using Topas V4.2 (BRUKER_AXS, 2009). Experiment 5 was also repeated 5 times for 3.33 – 140 minutes. The pH was also recorded during one of the repeat experiments (140 min). The solid products of these repeat experiments were washed, dried and characterized with XRD as described above.

Table 7.1 Summary of the solutions used for the formation experiments

Exp.	Ca solution	CO ₃ / SO ₄ solution		
	CaCl ₂ (mM)	Na ₂ CO ₃ (mM)	Na ₂ SO ₄ (M)	SO ₄ /CO ₃
1	100	100	0	0
2	100	100	0.42	4.2
3	100	100	1	10
4	100	50	1	20
5	100	50	1.25	25
6	100	50	1.5	30
7	100	50	2	40

7.2.2 Ageing experiments

In addition to the synthesis experiments, aging experiments were performed to determine the persistence and stability of the formed vaterite. Because experiment 5 produced solely vaterite, the vaterite formed in this experiment was also used in subsequent ageing experiments. These ageing experiments were performed with solutions containing 10 mM CaCl₂ and 0-200 mM Na₂SO₄ and 0-2 mM MgCl₂ concentrations. The pH (in equilibrium with the atmosphere) was adjusted to ~8.1 using a 2N NaOH solution. The ageing experiments were performed by adding 0.5 g of the solid produced in experiment 5 to 200 ml of the solutions described in above and in Table 7.2. The suspensions were continuously stirred by a magnetic stirrer at 150 rpm for up to 17 hours (Table 7.2). All ageing experiments were performed at room temperature (21±1°C). At the end of each experiment, solid samples were separated from the solutions in the same way as described above, and characterized with XRD. On all collected XRD patterns, Rietveld refinements were performed using Topas V4.2 (BRUKER_AXS, 2009) to determine the weight percentage of calcite and vaterite present in the samples. Solution samples were taken before adding the solid to the solutions and at the end of the experiments. To confirm the solution chemistry (Table 7.2), the solution samples were analysed for Ca and Mg photospectrometrically using calmagite as an indicator (section 3.5.1) and SO₄ using ion chromatography (IC) with a carbonate/bicarbonate eluent.

Table 7.2 Solution chemistry of the ageing experiments

Exp.	Time (h)	CaCl ₂ (mM)	MgCl ₂ (mM)	Na ₂ SO ₄ (mM)
A1	1.0	10	0	0
A2	3.4	10	0	0
B1	1.0	10	0	30
B2	3.5	10	0	30
C1	1.4	10	0	100
C2	3.0	10	0	100
D1	1.5	10	0	200
D2	5.2	10	0	200
E1	2.3	10	2	0
E2	16.8	10	2	0
F1	2.5	10	2	100
F2	17.0	10	2	100

7.3 Results and discussion

7.3.1 Synthesis experiments

All Bragg peaks from the XRD patterns could be assigned to calcium carbonate phases (i.e.: calcite and vaterite, Figure 7.1). At a SO₄/CO₃ ratio of 0, ~39% calcite and ~61% vaterite formed. With an increase in the SO₄/CO₃ ratio, the percentage of calcite decreased and above a SO₄/CO₃ ratio of 25, vaterite was the only phase that formed (Figure 7.1). This shows that the presence of sulfate in solution promoted the formation of vaterite over calcite. This trend has also been reported by FERNÁNDEZ-DÍAZ et al. (2010). However, the highest SO₄/CO₃ ratio used by FERNÁNDEZ-DÍAZ et al. (2010) was 0.5, which is significantly lower than the SO₄/CO₃ ratios used in this study (Table 7.1). This could explain why FERNÁNDEZ-DÍAZ et al. (2010) did not produce solely vaterite and only achieved a maximum of ~90% vaterite. The IC and microprobe WDS analyses revealed the SO₄ content of the vaterite from experiment 5 (SO₄/CO₃ = 25, Table 7.1) to be 4.0 mol% ± 0.2, which is significantly higher than previously observed for the incorporation of sulfate into the structure of vaterite (<1.9 mol%, chapter 4 and <2.2 mol%, FERNÁNDEZ-DÍAZ et al., 2010). The vaterite sample formed in experiment 5, at a SO₄/CO₃ of 25, will henceforth be referred to as ‘4%SO₄ vaterite’.

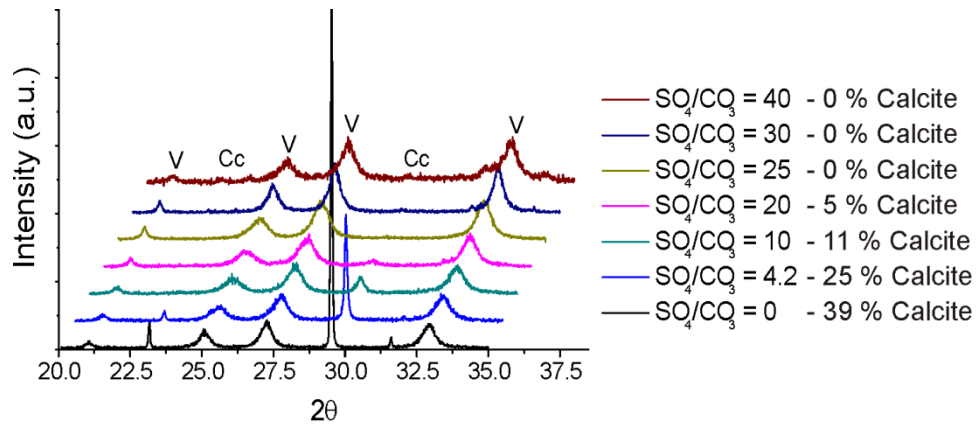


Figure 7.1 Stacked XRD patterns showing the effect of SO_4/CO_3 on the formation of calcium carbonate; the legend represents the initial SO_4/CO_3 ratio and the calculated weight percentage of calcite

In the XRD patterns of the repeats of experiment 5 ($\text{SO}_4/\text{CO}_3 = 25$, Table 7.1) all Bragg peaks can be assigned to vaterite (Figure 7.2). The patterns from the solids that were separated from solution at 3.33 and 4.33 minutes had a relatively high background intensity (with a maximum intensity at $2\theta \approx 32^\circ$) and low intensity vaterite Bragg peaks. Between 4.33 and 9 minutes, the background intensity decreased and remained low beyond 9 minutes (Figure 7.2). Additionally, the pH profile of the repeat of experiment 5 ($\text{SO}_4/\text{CO}_3 = 25$, Table 7.1, Figure 7.3) shows that the pH initially decreased from $\sim 10.5 - 10.3$ up to ~ 7 minutes followed by a subsequent larger decrease in pH from $\sim 10.3 - 9$ (from 9 minutes onwards, Figure 7.3). Such a pH evolution with two subsequent decreases in pH during the formation of crystalline calcium carbonate phases, has previously also been reported by OGINO et al. (1987).

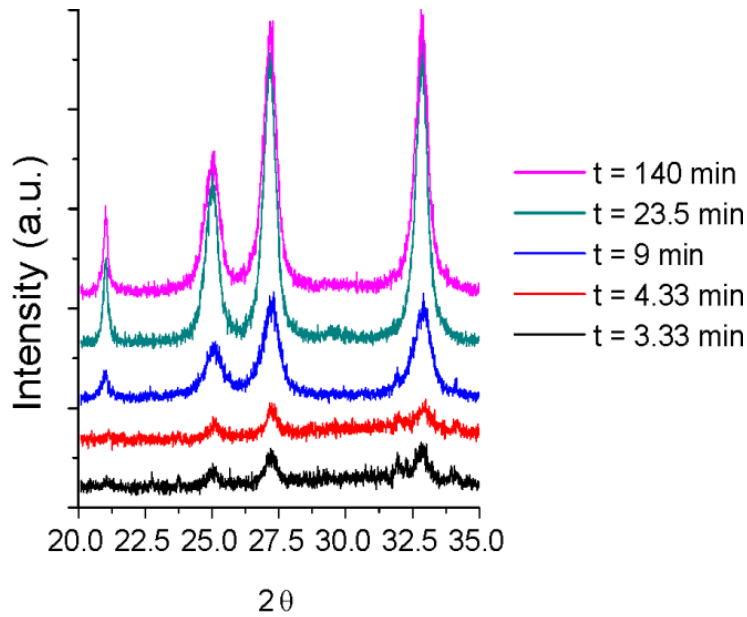


Figure 7.2 Stacked XRD patterns from five repeats of experiment 5 ($\text{SO}_4/\text{CO}_3 = 25$); the legend represents the time after mixing that the solid sample was separated from solution and the patterns show the development of only vaterite Bragg peaks

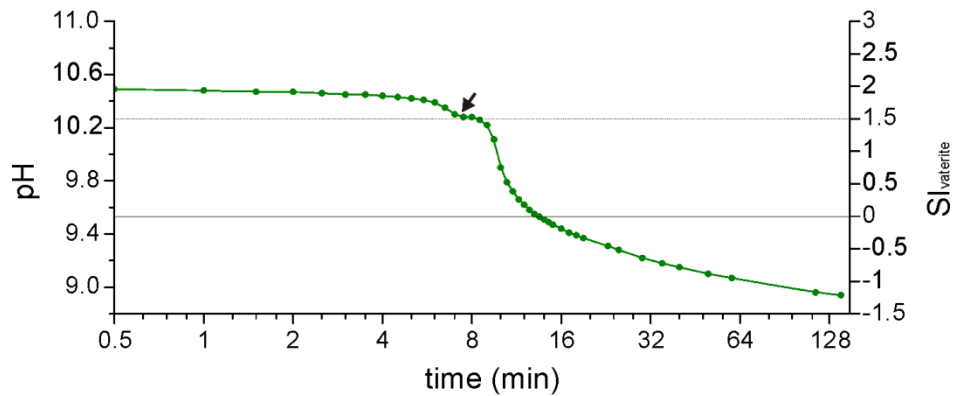


Figure 7.3 pH evolution during experiment 5 ($\text{SO}_4/\text{CO}_3 = 25$, Table 7.1), including the saturation index with respect to vaterite (SI_{vaterite}) as calculated using PHREEQC, assuming no CO_2 exchange with the atmosphere (PARKHURST and APPELO, 1999), the arrow represents the inflection point (OGINO et al., 1987), the dotted horizontal line represents the SI_{vaterite} required for spherulitic growth and the solid horizontal line represents the ‘solubility’ of vaterite if no CO_2 exchange with the atmosphere occurred

Amorphous calcium carbonate (ACC) has no long range order ($>15 \text{ \AA}$), resulting in the absence of Bragg peaks in XRD patterns combined with a broad maximum at $2\theta \approx 30^\circ$ (FAATZ et al., 2004; RODRIGUEZ-BLANCO et al., 2008). Hence, the XRD results indicate that during the synthesis experiments initially ACC formed

which crystallized to vaterite (chapter 5, OGINO et al., 1987; RODRIGUEZ-BLANCO et al., 2011). The decrease in the background intensity between 4.33 and 9 minutes indicates that ACC fully crystallized prior to 9 minutes, corresponding with previous results on the crystallization of ACC (chapter 5, OGINO et al., 1987; RODRIGUEZ-BLANCO et al., 2011). The full crystallization of ACC was concurrent to the initial decrease in pH from 10.5 – 10.3 (Figure 7.3). Additional PHREEQC (PARKHURST and APPELO, 1999) calculations were performed by assuming that changes in pH were caused by the formation of CaCO_3 only, to obtain information on the saturation state during the experiment (Figure 7.3). These calculations revealed that up to ~7 minutes, the supersaturation of the solution with respect to vaterite was high enough to sustain vaterite spherulitic growth ($\text{SI} > 1.5$, Figure 7.3, chapter 5, ANDREASSEN, 2005). The supersaturation with respect to vaterite combined with the presence of ACC (at 3.33 and 4.33 minutes) during the formation experiment (Figure 7.2 and 7.3) support an initial vaterite formation (<7 – 9 minutes) via spherulitic growth from ACC as discussed in chapter 5 and by ANDREASSEN (2005).

During the second decrease in pH (~9 minutes onwards, Figure 7.3), the calculated supersaturation with respect to vaterite decreased below the threshold for vaterite spherulitic growth ($\text{SI} < 1.5$, Figure 7.3, chapter 5, ANDREASSEN, 2005). Additionally, no ACC was detected in the XRD patterns in the formation experiment at 9 minutes (Figure 7.2) and the PHREEQC calculations indicate that an additional ~20% calcium carbonate formed after ~9 minutes. This suggests that additional vaterite formed, predominantly via direct precipitation from solution.

7.3.2 Structural analyses of vaterite

High Resolution-XRD (HR-XRD) pattern from the '4%SO₄ vaterite' obtained at Diamond Light Source beamline I11 is shown in Figure 7.4. Corresponding to the offline XRD pattern from the '4%SO₄ vaterite' sample (Figure 7.1), all Bragg peaks in the HR-XRD pattern (Figure 7.4) can be assigned to vaterite, confirming the presence of only vaterite the '4%SO₄ vaterite' sample. The results from the refinements on the HR-XRD pattern are summarized in Table 7.3 (KAMHI, 1963; MEYER, 1969) and the Rietveld refinement with the structural model from KAMHI (1963) is plotted in Figure 7.4. The Rietveld refinements of the vaterite using the structure file from KAMHI (1963) showed that the calculated lattice parameters did

not significantly differ from the previously reported lattice parameters for vaterite (Table 7.3) produced via the dehydration of ikaite (TANG et al., 2009). Additionally, the lattice parameters calculated with the Le Bail refinement (which uses the symmetry of the unit cell only without any assumption on the position of the atoms to refine the lattice parameters) using the supercell from MEYER (1969) showed no significant differences with lattice parameters from vaterite (Table 7.3) produced via the biomimetic formation in the presence of amino acids (THOMPSON et al., 2011). These comparisons suggest that the crystal structure of the '4%SO₄ vaterite' was not affected by the presence of SO₄ in the solid sample. Furthermore, no additional crystalline (SO₄) phase was present in the vaterite sample. This in agreement with previous results of the effect of SO₄ on the structure of vaterite (chapter 4, FERNÁNDEZ-DÍAZ et al., 2010).

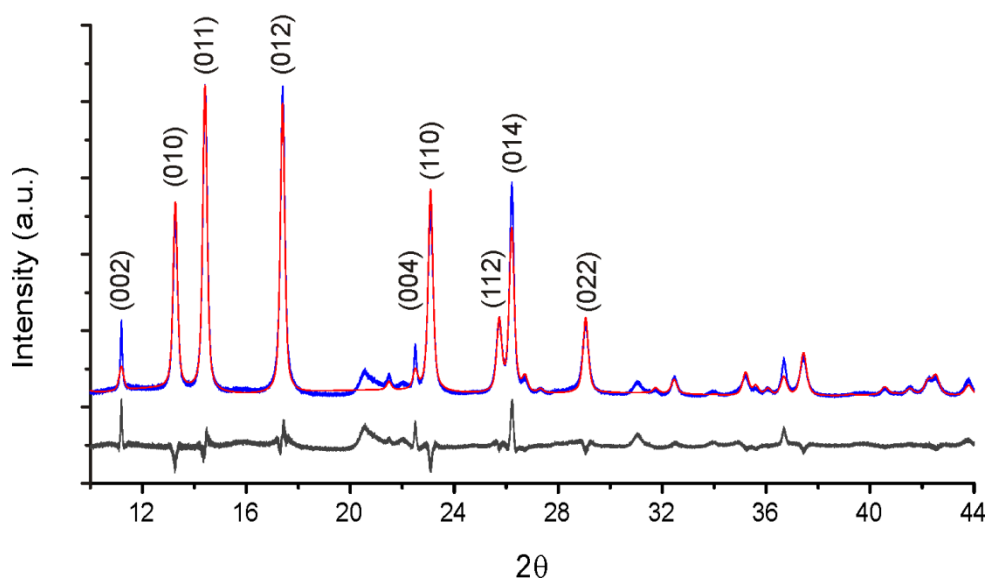


Figure 7.4 HR-XRD pattern of the '4%SO₄ vaterite' in blue (measured with a $\lambda = 0.826404 \text{ \AA}$), fitted vaterite pattern using the structural model by KAMHI et al. (1963) in red and the difference plot in grey; a selection of the Miller indices are shown above the corresponding Bragg peaks

Table 7.3 Summary of the Rietveld refinement on the HR-XRD pattern of the ‘4%SO₄ vaterite’; *the Rietveld refinement using the structural model from MEYER (1969) did not result in a fit, hence this structural model was fitted with performing a Le Bail refinement resulting in a low R_{Bragg}

Crystal sysmtem	R _{Bragg}	Unit cell axis	Refined values (Å)	Literature values (Å)	Reference
Hexagonal	4.551	a	4.1287	4.13	(KAMHI, 1963)
		c	8.4706	8.49	
		a		4.1228	(TANG et al., 2009)
		c		8.4654	
Hexagonal	0.515*	a	7.1517	7.15	(MEYER, 1969)
		c	16.9409	16.94	(THOMPSON et al., 2011)
		a		7.1532	
		c		16.9323	

The XANES spectrum from the ‘4%SO₄ vaterite’, collected at Diamond Light Source beamline I18, and a comparison to an aragonite and calcite standard are plotted in Figure 7.5. The XANES spectrum from the vaterite sample and calcite standard both show two peaks at ~4050 and ~4058 eV. The XANES spectrum from aragonite only exhibits one main peak at ~4050 eV and a smaller broad peak between 4060 and 4065 eV. Additionally, all the XANES spectra show a pre-edge peak at ~4040 eV and a shoulder on the ~4045 eV. The vaterite XANES spectrum differs significantly from the calcite and aragonite standards (Figure 7.5) and the vaterite XANES spectrum is identical to a previously reported XANES spectrum from vaterite without the incorporation of foreign ions like sulfate (LAM et al., 2007). This suggests that, like the structure of the ‘4%SO₄ vaterite’, the local order environment of calcium in the ‘4%SO₄ vaterite’ was not affected by the presence of SO₄ in the sample.

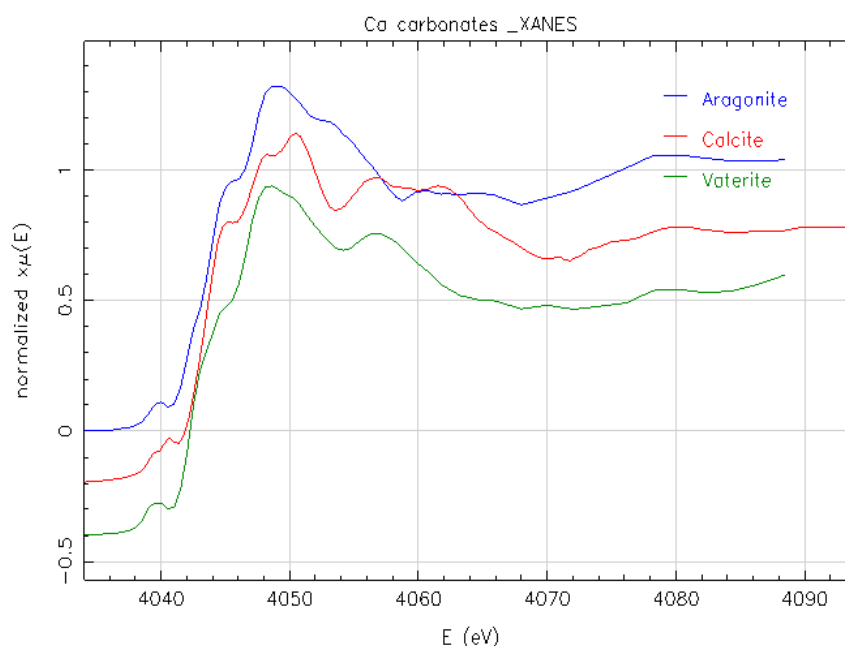


Figure 7.5 XANES spectrum at the Ca K-edge from the vaterite from experiment '4%SO₄ vaterite', including a calcite and aragonite standard

7.3.3 Vaterite ageing

During the ageing experiments using the '4%SO₄ vaterite', in the solutions with 0 mM SO₄ and 0 mM Mg (experiment A1 and A2, Table 7.2), the final weight percentage of calcite was ~1% and ~4% after 1.0 and 3.4 hours, respectively (Figure 7.6). In the solutions with 0 mM SO₄ and 2 mM Mg (experiment E1 and E2, Table 7.2), the final weight percentage of calcite was ~0.7% and ~47% after respectively 2.5 and 16.8 hours (Figure 7.6). In contrast, during all ageing experiments when SO₄ was added to the ageing solutions (Table 7.2), no calcite formed up to 17 hours (Figure 7.6).

The solution analyses on the collected solutions from all ageing experiments confirmed the initial solution composition throughout the experiments (Table 7.2). However, during the experiments without sulfate in the initial solution (experiment A1, A2, E1 and E2, Table 7.2), the SO₄ concentration at the end of the experiments increased from 0 mM to ~0.8 – 0.9 mM while the Ca concentration remained constant at ~10 mM (Figure 7.7).

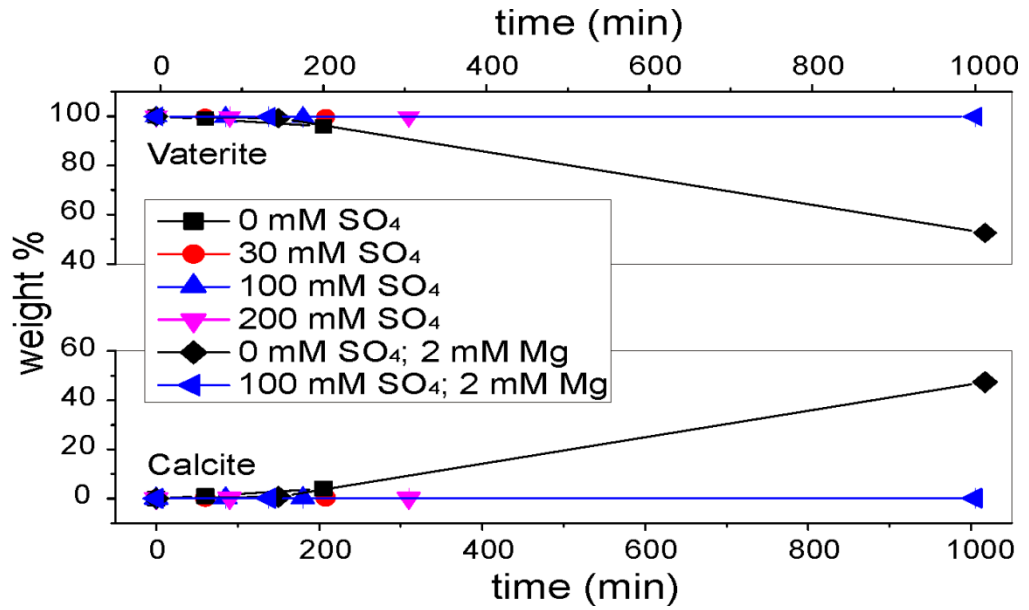


Figure 7.6 Polymorph distribution vs. time during all vaterite ripening experiments; the legend represents the SO_4 and Mg concentration in solution as described in Table 7.2

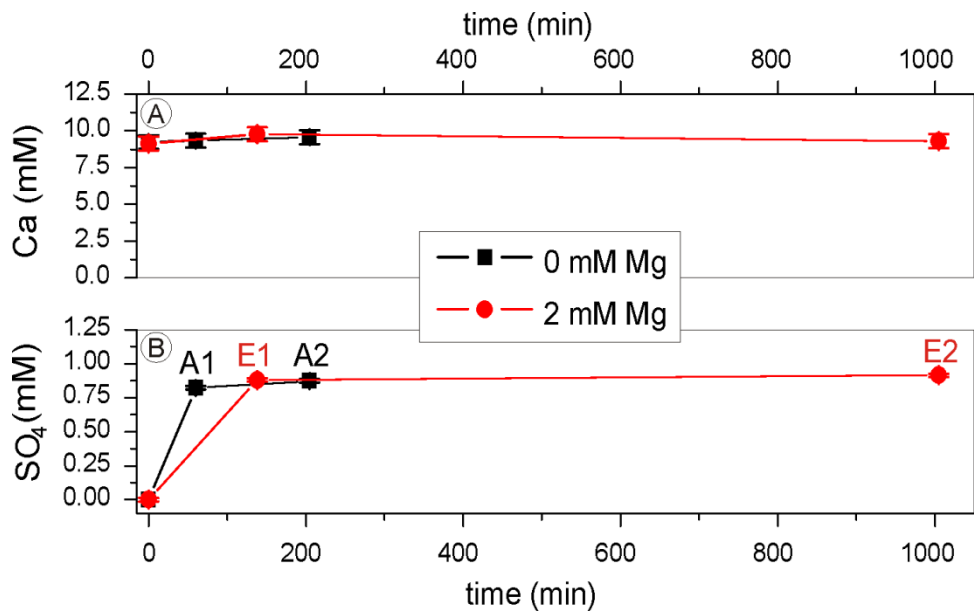


Figure 7.7 The Ca (A) and SO_4 (B) concentration in the ageing experiments without SO_4 present in the initial solutions; the legend represents the Mg concentration in solution as described in Table 7.2, the numbering in (B) represents the experiment number as listed in Table 7.2 and the error bars represent the standard deviation from triplicate measurements

Figure 7.7 shows that SO_4 was released into the solution during the formation of calcite (Figure 7.6) in the experiments without SO_4 in the initial solution. The

release of SO_4 into the solution, in combination with a constant Ca concentration, indicates that vaterite transformed to calcite instead of primary calcite formation from solution. An increase in the SO_4 concentration to ~ 0.85 mM in 1 hour (experiment A1, Table 7.2, Figure 7.7) was caused by a release of ~ 85 % of the SO_4 (associated with the '4% SO_4 vaterite') into the solution, while only ~ 1 % vaterite transformed to calcite (Figure 7.6). This indicates that the analyzed SO_4 was predominantly associated with the surface of the '4% SO_4 vaterite'. Additionally, without SO_4 and Mg in the initial solution (experiment A2, Table 7.2), ~ 4 % of the vaterite transformed to calcite in ~ 3.4 hours (Figure 7.6). In comparison, RODRIGUEZ-BLANCO et al. (2011) determined that in a system without any SO_4 ~ 30 % vaterite transformed to calcite in 3 hours. This indicates that less than 1 mM SO_4 in solution decreased the rate of vaterite to calcite transformation. In the presence of Mg in solution (Experiments E1 and E2, Table 7.2), ~ 48 % of the '4% SO_4 vaterite' transformed after ~ 17 h (Figure 7.6). However, 0.7% vaterite transformed to calcite after 2.5 hours compared to 1% and 4% after 1 and 3.4 hours in the absence of Mg (and SO_4) in solution. This indicates that in the presence of Mg, the transformation of vaterite to calcite was inhibited even though Mg has been shown to destabilize vaterite (chapter 4). Finally, no calcite formed when ≥ 30 mM SO_4 was present in solution; thus, the vaterite transformation was completely inhibited for up 17 hours (Figure 7.6).

7.3.4 The effects on vaterite stability

SO_4 incorporation has been determined to decrease the stability of calcite and increase the stability of vaterite (chapter 4, BUSENBERG and PLUMMER, 1985; FERNÁNDEZ-DÍAZ et al., 2010). This could cause a decrease in the vaterite to calcite transformation kinetics (FERNÁNDEZ-DÍAZ et al., 2010). However, as shown above, SO_4 was predominantly associated to the surfaces of vaterite, instead of incorporated into the structure. Hence, the presence of sulfate likely caused the formation of calcite to be inhibited (VAVOURAKI et al., 2008), preventing the transformation of vaterite to calcite as observed in the ageing experiments (Figure 7.6). During the experiments with SO_4 in the initial solutions, calcite was further destabilized due to the presence of SO_4 inhibiting the formation and growth of calcite (VAVOURAKI et al., 2008). However, inhibition of the transformation of vaterite to calcite due to

small amounts of SO_4 incorporation into the structure of vaterite and adsorption of SO_4 onto vaterite surfaces cannot be excluded.

As indicated above, 2 mM Mg in solution caused a small inhibition of the transformation of vaterite to calcite. BISCHOFF (1968) determined that no decrease in the vaterite to aragonite transformation occurred with up to 5 mM Mg in solution. However, Mg in solution has been shown to inhibit the formation of calcite via adsorption onto calcite surfaces and the incorporation of Mg into calcite (chapter 4, BISCHOFF and FYFE, 1968; DAVIS et al., 2000). Thus the presence of Mg in solution could cause an additional decrease in the reaction kinetics by inhibiting calcite formation.

As observed in Figure 7.1, sulfate caused the preferential formation of vaterite over calcite. The incorporation of sulfate into the calcite structure has also been shown to decrease the calcite formation and growth from sulfate containing solutions (chapter 4, VAVOURAKI et al., 2008). However, adsorption of sulfate onto vaterite has previously been determined to decrease vaterite nucleation and growth via poisoning its nucleation and growth sites (chapter 5). Thus, for the formation of solely vaterite (at $\text{SO}_4/\text{CO}_3 \geq 25$, Figure 7.1), calcite nucleation and growth needed to be inhibited more strongly than vaterite, likely due to the destabilization (BUSENBERG and PLUMMER, 1985; FERNÁNDEZ-DÍAZ et al., 2010) and inhibition (chapter 4, VAVOURAKI et al., 2008) of calcite formation and growth as discussed above. An increase in the preferential formation of vaterite over calcite due to stabilizing effects caused by small amounts of SO_4 incorporation into the structure of vaterite (FERNÁNDEZ-DÍAZ et al., 2010) can however not be excluded.

7.4 Concluding remarks

Vaterite formed initially via a spherulitic growth mechanism, followed by secondary vaterite formation directly from solution. An increase in the SO_4/CO_3 ratio promoted the formation of vaterite over calcite. Additionally, SO_4 was predominantly associated to the surfaces of vaterite rather than incorporated into the vaterite structure. Hence, the formation of solely vaterite in high SO_4 concentrations ($\text{SO}_4/\text{CO}_3 \geq 25$, Figure 7.1) and the inhibition of the transformation of vaterite to calcite were likely to be primarily caused by the inhibition of calcite formation. This

is contrary to the formation of vaterite in the presence of ammonium and in biomimetic studies where ammonium and organics cause the preferential formation of vaterite dominantly by templating effects. The results in this study can help explain the occurrence of vaterite in different environmental settings.

Finally, the presence of SO_4 during the formation of vaterite did not affect the local order and the crystal structure significantly. This shows that the vaterite produced in this study was structurally identical to pure vaterite.

Chapter 8

Summary and concluding remarks

This thesis describes the effects of solution composition on calcium carbonate formation and mineralogy, tested via a variety of experimental approaches. The effect of the solution composition was tested on: (1) the mineralogy and formation of calcium carbonate phases (chapter 4 and 7) and (2) the crystallization mechanism of calcium carbonate from an amorphous precursor (ACC, chapter 5 – 7). The results improve our knowledge of the influences of variations in solution composition (sulfate and magnesium) on the formation and mineralogy of calcium carbonate minerals. This will aid understanding of the processes influencing the primary calcium carbonate formation during the Phanerozoic and processes influencing biomineralization.

8.1 Effects of solution composition (sulfate and magnesium) on the precipitated calcium carbonate polymorph

In the constant addition experiments, the effects of solution composition (sulfate and magnesium) on heterogeneous calcium carbonate formation were studied (chapter 4). The results from these experiments confirmed that magnesium replaces calcium in the structure of calcite and vaterite, while magnesium does not replace calcium in the structure of aragonite (<0.1 mol% magnesium). Concurrent with the incorporation of magnesium into calcite and vaterite, the unit cell size decreased due to the smaller size of the magnesium compared to calcium ions, causing both phases to destabilize with respect to aragonite. Hence, with an increase in the magnesium to calcium ratio in solution, aragonite formed from solution instead of calcite or vaterite. At magnesium to calcium ratios higher than ~0.6-0.7, aragonite was the dominant calcium carbonate mineral formed.

When sulfate was present in the solutions during the constant addition experiments (chapter 4), sulfate replaced carbonate in the structure of all calcium carbonate minerals. Due to the replacement of planar carbonate by larger tetragonal sulfate ions, the unit cell of calcite increased. The same, but to a lesser extent,

occurred when sulfate replaced carbonate in aragonite. From the changes in the calcite and aragonite unit cell sizes, it was concluded that the incorporation of sulfate decreased the stability of calcite and, to a lesser extent, the stability of aragonite. Due to the changes in the stability of calcite and aragonite, the magnesium to calcium ratio at which calcite became less stable than aragonite decreased in the presence of sulfate, even though the incorporation of sulfate into the structure of calcite decreased in the presence of magnesium. This caused the formation of dominantly aragonite instead of calcite at lower magnesium to calcium ratios (e.g. at 5 mM SO_4 , $\text{Mg}/\text{Ca} = \sim 0.3$).

The results from the constant addition experiments (chapter 4) also revealed that the vaterite unit cell size did not change with the incorporation of up to 1.9 mol% sulfate. This lack of any structural changes concurrent with the incorporation of sulfate into vaterite is likely to have caused the stability of vaterite to increase. Thus in the presence of sulfate in solution (and no aqueous magnesium) vaterite was the dominant polymorph formed from solution. However, the formation and ageing experiments (with varying sulfate to carbonate ratios) described in chapter 7 indicate that sulfate in solution predominantly adsorbed onto vaterite surfaces rather than incorporated into the vaterite structure. This indicates that the formation of vaterite was predominantly caused via the destabilization of calcite. However, the results described in chapter 4 and chapter 7 cannot be directly compared because of the differences in the kinetics and mechanism of vaterite formation (slow formation on reactive surfaces (chapter 4) vs. fast spherulitic growth (chapter 7)).

8.2 Amorphous calcium carbonate crystallization and the effect of the sulfate concentration

Amorphous calcium carbonate (ACC) crystallization was studied using a set of experiments with high initial supersaturation to allow for the crystallization process to be followed *in situ* using X-ray scattering techniques. Combined with additional information on the solution composition (e.g.: calcium and pH) and imaging of the solids, the crystallization mechanism could be extracted. The initial calcium carbonate in a highly supersaturated system was a highly soluble disordered ACC (chapter 5, 6 and 7). In the presence of the disordered ACC, the solution remained

highly supersaturated with respect to the crystalline calcium carbonate polymorphs. During this stage vaterite formation was initiated, likely via the destabilization of ACC due to its continuous growth. The initial stage of vaterite formation occurred via a spherulitic growth mechanism (chapter 5), which was maintained as long as highly soluble ACC was present in the system, allowing the solution composition to exceed supersaturation needed for spherulitic growth ($SI_{vaterite} > 1.5$). The initially formed disordered ACC subsequently dehydrated, which caused the local order in the structure to increase. This caused the thermodynamic stability of the ACC to increase and the supersaturation to decrease below the limit for vaterite spherulitic growth. Hence, the final stage of vaterite formation occurred via ACC dissolution coupled to vaterite precipitation (chapter 5). After vaterite was fully formed and no more ACC was present, vaterite particle growth (Ostwald ripening) was the only remaining process occurring in the system (chapter 5). Subsequently, the vaterite eventually transformed to the thermodynamically most stable phase calcite via a dissolution reprecipitation mechanism (OGINO et al., 1990; RODRIGUEZ-BLANCO et al., 2011). The ACC crystallization pathway described here followed the Ostwald step rule (VAN SANTEN, 1984) and validated the relative stability of various amorphous and crystalline calcium carbonate phases as described by RADHA et al. (2010).

In addition to the mechanism of ACC crystallization to vaterite, the effects of solution composition on ACC crystallization have been quantified (chapter 5, 6 and 7). In contrast to the crystalline calcium carbonate phases (chapter 4), sulfate in solution during the formation of ACC did not replace carbonate in the structure of ACC (chapter 5). Hence, sulfate had no significant effect on the mechanism of ACC crystallization to vaterite. However, sulfate in solution did cause an increase in the induction time of vaterite nucleation and reduced its spherulitic growth rate, likely by poisoning nucleation and growth sites (chapter 5). Sulfate also caused the vaterite Ostwald ripening process to slow down, either via the incorporation of sulfate into vaterite (chapter 4) or via the adsorption of sulfate onto vaterite surfaces (chapter 5 and 7). Additionally, preferential crystallization to vaterite over calcite was likely caused by the destabilization of calcite in the presence sulfate (chapter 7).

When the sulfate concentration in solution exceeded the solubility for calcium sulfate phases (i.e.: >50 mM sulfate, chapter 6), rapidcreekite ($\text{Ca}_2\text{SO}_4\text{CO}_3\cdot 4\text{H}_2\text{O}$) and gypsum ($\text{CaSO}_4\cdot 2\text{H}_2\text{O}$) formed in addition to ACC and vaterite (chapter 6). The

formation of these phases did not affect the initial vaterite spherulitic growth. However, the dissolution of rapidcreekite, instead of less hydrated, more ordered ACC (chapter 5), dominated the vaterite formation in the dissolution reprecipitation stage (chapter 6). Additionally, the formation of rapidcreekite after >75% of gypsum formed and the disappearance of rapidcreekite coupled to the formation of additional vaterite (instead of gypsum) indicates that the solubility of rapidcreekite is lower than the solubility of gypsum.

Conversely, magnesium incorporated into the structure of ACC stabilized this phase significantly (LOSTE et al., 2003). Magnesium also promoted the formation of calcite over vaterite (chapter 6, RODRIGUEZ-BLANCO et al., in press) and decreased the vaterite spherulitic growth kinetics without inducing a delay in vaterite formation (chapter 6). The decrease in the kinetics of vaterite spherulitic growth and the promotion of calcite over vaterite in the presence of 50 mM magnesium was likely caused by a decrease in the stability of vaterite due to magnesium incorporation (chapter 4). The results from chapter 5 and 6 also indicate that bicarbonate decreased the induction time for vaterite spherulitic growth by destabilizing ACC or promoting vaterite growth (chapter 5 and 6).

8.3 Relating the experimental results to natural calcium carbonate formation

As shown in section 2.4, the Phanerozoic seawater composition oscillated, which caused oscillations in the dominant calcium carbonate polymorph precipitated during the Phanerozoic (calcite and aragonite seas, HARDIE, 1996; SANDBERG, 1983). To date, previous experimental research showed that the magnesium to calcium ratio was the dominant factor in the oscillations between the calcite and aragonite seas (MORSE et al., 1997). However, the results from chapter 5 show that sulfate in addition to the magnesium to calcium ratio can influence the primary calcium carbonate polymorph. These results show that for calcite to form during a calcite sea period, the magnesium to calcium ratio need to have been lower than ~0.3, in the presence of 5 mM sulfate. These values are less than the magnesium to calcium ratios and at the lower most limit for the sulfate concentrations for the calcite seas, inferred from fluid inclusion analyses (HORITA et al., 2002;

LOWENSTEIN et al., 2005). Additionally, PHREEQC modelling (chapter 5) indicates that fluid inclusion analyses (LOWENSTEIN et al., 2005) can result in Phanerozoic seawater composition significantly different to what was inferred previously from the fluid inclusion composition (Appendix A). The above indicates that either the calcite and aragonite seas or the evolution of the seawater composition throughout the Phanerozoic needs to be re-evaluated.

The solution composition in seawater throughout the Phanerozoic has also been suggested to have influenced the evolution of biomineralizing organisms (PORTER, 2007; PORTER, 2010). Many newly evolved organisms preferentially crystallize the thermodynamically favourable calcium carbonate polymorph (STANLEY, 2006; ZHURAVLEV and WOOD, 2009). Organisms often utilize ACC as a precursor to thermodynamically more stable crystalline phase to control the shape of the crystalline products (CUSACK and FREER, 2008; GOWER, 2008; MELDRUM and CÖLFEN, 2008). The ACC crystallization mechanism described in chapter 5 can represent the abiotic equivalent of the pathway by which many biomineralization processes occur. Similar multi-step processes of ACC to calcite transformation have already been observed in, for example, sea urchin spicules (KILLIAN et al., 2009). However, in contrast to the transformation process described in chapter 5, biomineralization processes often occur entirely enclosed within a membrane in the presence of proteins and little or no free water (WEINER and DOVE, 2003) and these factors will significantly alter the transformation mechanism (MELDRUM and CÖLFEN, 2008).

The presence of magnesium in solution inhibits ACC crystallization to vaterite (chapter 6, LAM et al., 2007; RODRIGUEZ-BLANCO et al., in press). This may explain why most biomineralization processes either produce calcite or aragonite (LOWENSTAM, 1981) because of the ubiquitous presence of aqueous magnesium in modern and Phanerozoic environments (BERNER and BERNER, 1996; HORITA et al., 2002). Sulfate has been shown to exert little influence on the mechanism of ACC crystallization to vaterite (chapter 5 and 6). However, the presence of sulfate in crystallizing solutions has been shown to promote the formation and enhance the stability of vaterite (chapter 4 and 7, FERNÁNDEZ-DÍAZ et al., 2010). Thus, the presence of sulfate could help explain the existence of several vaterite biomineralizing organisms (LOWENSTAM, 1981; LOWENSTAM and ABBOTT, 1975; TOMÁS and GEFFEN, 2003).

Finally, the results from chapter 6 indicate that the solubility of rapidcreekite is lower than the solubility of gypsum, however, rapidcreekite is rarely found in natural settings (ROBERTS et al., 1986; WALENTA and DUNN, 1989). This is likely to be caused by the low solubility of all calcium carbonate phases compared to calcium sulfate phases, such as gypsum (FREYER and VOIGT, 2003; PLUMMER and BUSENBERG, 1982). These results indicate that rapidcreekite might act as an intermediate to gypsum formation in alkaline systems. Additionally, rapidcreekite is found in nature in the presence of aragonite (ROBERTS et al., 1986; WALENTA and DUNN, 1989). This could be explained by the presence of magnesium in solution in such environments, as magnesium has been shown to promote the formation of aragonite (chapter 4) and rapidcreekite (chapter 6).

8.4 Outlook

To better understand the effect of sulfate on calcium carbonate formation and stability, additional information on the incorporation into and adsorption of sulfate onto all calcium carbonate polymorphs is needed. The incorporation of sulfate has been determined to influence the stability of all anhydrous calcium carbonate phases via a computational study (FERNÁNDEZ-DÍAZ et al., 2010). However, information on sulfate incorporation has only been reported previously for calcite (BUSENBERG and PLUMMER, 1985) over a small pH range (7.1 – 7.7). Additionally, different studies suggest that pH and alkalinity of the solution determine whether calcium carbonate forms via the direct incorporation of carbonate (NEHRKE et al., 2007; STACK and GRANTHAM, 2010) or the adsorption of bicarbonate followed by deprotonation (PLUMMER et al., 1978). Because sulfate incorporation in calcite is thought to be dependent on the sulfate to carbonate ratio (BUSENBERG and PLUMMER, 1985; PINGITORE et al., 1995), the incorporation of sulfate into calcium carbonate phases should depend strongly on pH and alkalinity. Furthermore, the influence of magnesium on the incorporation of sulfate into calcite and vice versa has so far provided an incoherent story. The results in chapter 4 show that the sulfate incorporation decreases in the presence of magnesium. However, previous studies suggested that the incorporation of magnesium decreases with sulfate present (BURTON and WALTER, 1991) or that the sulfate incorporation increases in the

presence of magnesium incorporation (TAKANO, 1985). Hence, the co-dependency between the incorporation of sulfate and magnesium also needs to be quantified. The effect of temperature on the incorporation (and adsorption) of sulfate also needs to be investigated to explain the preliminary 10°C results shown in appendix A.3 in comparison to the 21°C experiments described in chapter 4. Additionally, chapter 4 assumes that sulfate stabilizes vaterite through the incorporation of sulfate while chapter 7 indicates that surface associated sulfate promotes the formation of vaterite over calcite.

The above shows that additional information is needed on the effects of sulfate on the formation and stability of vaterite, for example, a distinction between the adsorption and incorporation of sulfate. This could be investigated by performing similar constant addition batch experiments, as described in chapter 4, varying solution chemistry (and temperature) and using calcium carbonate seeds to direct the formation of the calcium carbonate phases. Mineralogical and surface sensitive analytical techniques (e.g. XRD and X-ray photoelectron spectroscopy) combined with solid and solution chemical analyses can then be used to extract information on the incorporation (and adsorption) of sulfate and the effects of magnesium, alkalinity, pH and temperature on the incorporation and adsorption.

The experiments performed at Diamond Light Source could also be extended to look into more detail on how organisms modify ACC crystallization. Organisms often use proteins and other organic molecules to direct the formation of crystalline calcium carbonates (ADDADI and WEINER, 1992; AIZENBERG et al., 2001; BELCHER et al., 1996; CUSACK and FREER, 2008; JI et al., 2010; WOLF et al., 2011). Hence, when proteins are included in the solution composition, information could be obtained on how the abiotic transformation mechanism and kinetics are modified and which calcium carbonate polymorphs are then preferred. This could provide more information on the control (or lack of control) organisms have on the composition and structure of the biominerals they form (DICKSON, 2002; RIES, 2004; RIES et al., 2008). Particularly it requires *in situ* measurements combined with thorough off-line mineralogical and chemical analyses of the crystalline products formed during these experiments.

Because rapidcreekite both crystallizes and breaks down during the experiments described in chapter 6, measuring the chemical evolution of the solution

composition (e.g.: the calcium and sulfate concentrations and the pH) during this multi step reaction would provide limits for the solubility of rapidcreekite. Finally, the mechanisms of gypsum formation are not well understood. The results in chapter 6 show that when using *in situ* wide angle X-ray scattering techniques, information on the formation of gypsum is obtained. This suggests crystalline calcium sulfate phases can form via a precursor phase, similar to the formation of crystalline calcium carbonate (e.g. GEBAUER et al., 2008). Additional, *in situ* measurements on crystallization experiments under alkaline conditions, more representative of natural environments (e.g. lower calcium and carbonate concentrations), could confirm whether rapidcreekite can form as a precursor to gypsum in nature.

References

- Adabi, M. H., 2004. A re-evaluation of aragonite versus calcite seas. *Carbonates and Evaporites* **19**, 133-141.
- Addadi, L., Raz, S., and Weiner, S., 2003. Taking Advantage of Disorder: Amorphous Calcium Carbonate and Its Roles in Biomineralization. *Advanced Materials* **15**, 959-970.
- Addadi, L. and Weiner, S., 1992. Control and Design Principles in Biological Mineralization. *Angewandte Chemie-International Edition in English* **31**, 153-169.
- Ahmed, I. A. M., Benning, L. G., Kakonyi, G., Sumoondur, A. D., Terrill, N. J., and Shaw, S., 2010. Formation of Green Rust Sulfate: A Combined in Situ Time-Resolved X-ray Scattering and Electrochemical Study. *Langmuir* **26**, 6593-6603.
- Aizenberg, J., Lambert, G., Weiner, S., and Addadi, L., 2001. Factors Involved in the Formation of Amorphous and Crystalline Calcium Carbonate: A Study of an Ascidian Skeleton. *Journal of the American Chemical Society* **124**, 32-39.
- Albright, J. N., 1971. Vaterite Stability. *American Mineralogist* **56**, 620-624.
- Allison, N., Austin, H., Austin, W., and Paterson, D. M., 2011. Effects of seawater pH and calcification rate on test Mg/Ca and Sr/Ca in cultured individuals of the benthic, calcitic foraminifera *Elphidium williamsoni*. *Chemical Geology* **289**, 171-178.
- Althoff, P. L., 1977. Structural refinements of dolomite and a magnesian calcite and implications for dolomite formation in the marine environment. *American Mineralogist* **62**, 772-783.
- Andreassen, J.-P., 2005. Formation mechanism and morphology in precipitation of vaterite--nano-aggregation or crystal growth? *Journal of Crystal Growth* **274**, 256-264.
- Appelo, C. A. J. and Postma, D., 2005. *Geochemistry, Groundwater and Pollution*. A.A. Balkema Publishers, Leiden/London/New York/Philadelphia/Singapore.

Arvidson, R. S., Guidry, M., and Mackenzie, F. T., 2006a. The control of Phanerozoic atmosphere and seawater composition by basalt-seawater exchange reactions. *Journal of Geochemical Exploration* **88**, 412-415.

Arvidson, R. S. and Mackenzie, F. T., 1999. The dolomite problem; control of precipitation kinetics by temperature and saturation state. *American Journal of Science* **299**, 257-288.

Arvidson, R. S., Mackenzie, F. T., and Guidry, M., 2006b. MAGic: A Phanerozoic Model for the Geochemical Cycling of Major Rock-Forming Components. *American Journal of Science* **306**, 135-190.

Auzoux-Bordenave, S., Badou, A., Gaume, B., Berland, S., Helléouet, M. N., Milet, C., and Huchette, S., 2010. Ultrastructure, chemistry and mineralogy of the growing shell of the European abalone *Haliotis tuberculata*. *Journal of Structural Biology* **171**, 277-290.

Avrami, M., 1939. Kinetics of phase change, I. General Theory. *Journal of Chemical Physics* **7**, 1103-1112.

Avrami, M., 1940. Kinetics of phase change, II. Transformation-Time Relations for Random Distribution of Nuclei. *Journal of Chemical Physics* **8**, 212-224.

Avrami, M., 1941. Kinetics of Phase Change, III. Granulation, Phase Change, and Microstructure. *Journal of Chemical Physics* **9**, 177-184.

Bale, H. D. and Schmidt, P. W., 1984. Small-Angle X-Ray-Scattering Investigation of Submicroscopic Porosity with Fractal Properties. *Physical Review Letters* **53**, 596.

Balthasar, U., Cusack, M., Faryma, L., Chung, P., Holmer, L. E., Jin, J., Percival, I. G., and Popov, L. E., 2011. Relic aragonite from Ordovician-Silurian brachiopods: Implications for the evolution of calcification. *Geology* **39**, 967-970.

Balzar, D. and Ledbetter, H., 1993. Voigt-Function Modeling in Fourier-Analysis of Size-Broadened and Strain-Broadened X-Ray-Diffraction Peaks. *Journal of Applied Crystallography* **26**, 97-103.

Banner, J. L. and Hanson, G. N., 1990. Calculation of simultaneous isotopic and trace element variations during water-rock interaction with applications to carbonate diagenesis. *Geochimica et Cosmochimica Acta* **54**, 3123-3137.

Bateman, J. E., Derbyshire, G. E., Diakun, G., Duxbury, D. M., Fairclough, J. P. A., Harvey, I., Helsby, W. I., Lipp, J. D., Marsh, A. S., Salisbury, J., Sankar, G., Spill, E. J., Stephenson, R., and Terrill, N. J., 2007. The HOTWAXS detector. *Nuclear Instruments and Methods in Physics Research Section A: Accelerators, Spectrometers, Detectors and Associated Equipment* **580**, 1526-1535.

Beale, A. M., van der Eerden, A. M. J., Jacques, S. D. M., Leynaud, O., O'Brien, M. G., Meneau, F., Nikitenko, S., Bras, W., and Weckhuysen, B. M., 2006. A Combined SAXS/WAXS/XAFS Setup Capable of Observing Concurrent Changes Across the Nano-to-Micrometer Size Range in Inorganic Solid Crystallization Processes. *Journal of the American Chemical Society* **128**, 12386-12387.

Belcher, A. M., Wu, X. H., Christensen, R. J., Hansma, P. K., Stucky, G. D., and Morse, D. E., 1996. Control of crystal phase switching and orientation by soluble mollusc-shell proteins. *Nature* **381**, 56-58.

Benning, L. G. and Waychunas, G. A., 2007. Nucleation, Growth, and Aggregation of Mineral Phases: Mechanisms and Kinetic Controls. In: Brantley, S., Kubicki, J., and White, A. Eds.), *Kinetics of Water-Rock Interactions*. Springer-Verlag, New-York.

Berner, E. K. and Berner, R. A., 1996. *Global Environment: Water, Air, and Geochemical Cycles*. Prentice Hall, Upper Saddle River, NJ.

Berner, R. A., 1966. Chemical diagenesis of some modern carbonate sediments. *American Journal of Science* **264**, 1-36.

Berner, R. A., 1975. The role of magnesium in the crystal growth of calcite and aragonite from sea water. *Geochimica et Cosmochimica Acta* **39**, 489-494.

Berner, R. A., 1978. Equilibrium, kinetics, and the precipitation of magnesian calcite from seawater; discussion. *American Journal of Science* **278**, 1475-1477.

Berner, R. A., 2004. A Model for Calcium, Magnesium and Sulfate in Seawater over Phanerozoic Time. *American Journal of Science* **304**, 16.

Bischoff, J. L., 1968. Catalysis Inhibition and Calcite-Aragonite Problem .2. Vaterite-Aragonite Transformation. *American Journal of Science* **266**, 80-90.

Bischoff, J. L., Fitzpatrick, J. A., and Rosenbauer, R. J., 1993. The Solubility and Stabilization of Ikaite ($\text{CaCO}_3 \cdot 6\text{H}_2\text{O}$) from 0° to 25°C: Environmental and Paleoclimatic Implications for Thinolite Tufa. *The Journal of Geology* **101**, 21-33.

Bischoff, J. L. and Fyfe, W. S., 1968. Catalysis Inhibition and Calcite-Aragonite Problem .I. Aragonite-Calcite Transformation. *American Journal of Science* **266**, 65-79.

Bischoff, W. D., Bishop, F. C., and Mackenzie, F. T., 1983. Biogenically Produced Magnesian Calcite Inhomogeneities in Chemical and Physical-Properties Comparison with Synthetic Phases. *American Mineralogist* **68**, 1183-1188.

Bischoff, W. D., Mackenzie, F. T., and Bishop, F. C., 1987. Stabilities of synthetic magnesian calcites in aqueous solution: Comparison with biogenic materials. *Geochimica et Cosmochimica Acta* **51**, 1413-1423.

Bolze, J., Peng, B., Dingenouts, N., Panine, P., Narayanan, T., and Ballauff, M., 2002. Formation and Growth of Amorphous Colloidal CaCO_3 Precursor Particles as Detected by Time-Resolved SAXS. *Langmuir* **18**, 8364-8369.

Bolze, J., Pontoni, D., Ballauff, M., Narayanan, T., and Cölfen, H., 2004. Time-resolved SAXS study of the effect of a double hydrophilic block-copolymer on the formation of CaCO_3 from a supersaturated salt solution. *Journal of Colloid and Interface Science* **277**, 84-94.

Bras, W., Greaves, G. N., Oversluizen, M., Clark, S. M., and Eeckhaut, G., 2005. The development of monodispersed alumino-chromate spinel nanoparticles in doped cordierite glass, studied by in situ X-ray small and wide angle scattering, and chromium X-ray spectroscopy. *Journal of Non-Crystalline Solids* **351**, 2178-2193.

Brečević, L. and Nielsen, A. E., 1989. Solubility of amorphous calcium carbonate. *Journal of Crystal Growth* **98**, 504-510.

Bruker_AXS, 2009. *TOPAS V4.2: General Profile and Structure Analysis Software for Powder Diffraction Data. User's Manual*. Bruker AXS, Karlsruhe, Germany, 2009.

Bruno, P., Caselli, M., de Gennaro, G., De Tommaso, B., Lastella, G., and Mastrolitti, S., 2003. Determination of nutrients in the presence of high chloride concentrations by column-switching ion chromatography. *Journal of Chromatography A* **1003**, 133-141.

Budd, D. A. and Land, L. S., 1990. Geochemical Imprint of Meteoric Diagenesis in Holocene Ooid Sands, Schooner Cays, Bahamas - Correlation of Calcite Cement Geochemistry with Extant Groundwaters. *Journal of Sedimentary Petrology* **60**, 361-378.

Burton, E. A., 1993. Controls on marine carbonate cement mineralogy: review and reassessment. *Chemical Geology* **105**, 163-179.

Burton, E. A. and Walter, L. M., 1987. Relative precipitation rates of aragonite and Mg calcite from seawater: Temperature or carbonate ion control? *Geology* **15**, 111-114.

Burton, E. A. and Walter, L. M., 1991. The effects of PCO_2 and temperature on magnesium incorporation in calcite in seawater and MgCl_2 - CaCl_2 solutions. *Geochimica et Cosmochimica Acta* **55**, 777-785.

Busenberg, E. and Plummer, N. L., 1985. Kinetic and thermodynamic factors controlling the distribution of SO_4^{2-} and Na^+ in calcites and selected aragonites. *Geochimica et Cosmochimica Acta* **49**, 713-725.

Busenberg, E. and Plummer, N. L., 1989. Thermodynamics of magnesian calcite solid-solutions at 25°C and 1 atm total pressure. *Geochimica et Cosmochimica Acta* **53**, 1189-1208.

Butt, H.-J., 1996. A Sensitive Method to Measure Changes in the Surface Stress of Solids. *Journal of Colloid and Interface Science* **180**, 251-260.

Ciccariello, S., Goodisman, J., and Brumberger, H., 1988. On the Porod law. *Journal of Applied Crystallography* **21**, 117-128.

Cicero, A. D. and Lohmann, K. C., 2001. Sr/Mg variation during rock-water interaction: implications for secular changes in the elemental chemistry of ancient seawater. *Geochimica et Cosmochimica Acta* **65**, 741-761.

Clerc, C., 2007, Controls on the incorporation of carbonate associated sulphate (CAS), University of Leeds

Cooper, M. A. and Hawthorne, F. C., 1996. The crystal structure of rapidcreekite, $\text{Ca}_2(\text{SO}_4)(\text{CO}_3)(\text{H}_2\text{O})_4$, and its relation to the structure of gypsum. *Canadian Mineralogist* **34**, 99-106.

Corsetti, F. A., Kidder, D. L., and Marenco, P. J., 2006. Trends in oolite dolomitization across the Neoproterozoic-Cambrian boundary: A case study from Death Valley, California. *Sedimentary Geology* **191**, 135-150.

Cusack, M. and Freer, A., 2008. Biomineralization: Elemental and Organic Influence in Carbonate Systems. *Chemical Reviews* **108**, 4433–4454.

Dahl, K. and Buchardt, B., 2006. Monohydrocalcite in the arctic Ikka fjord, SW Greenland: First reported marine occurrence. *Journal of Sedimentary Research* **76**, 460-471.

Dalbeck, P., England, J., Cusack, M., Lee, M. R., and Fallick, A. E., 2006. Crystallography and chemistry of the calcium carbonate polymorph switch in *M. edulis* shells. *European Journal of Mineralogy* **18**, 601-609.

Davis, K. J., Dove, P. M., and De Yoreo, J. J., 2000. The Role of Mg^{2+} as an Impurity in Calcite Growth. *Science* **290**, 1134-1137.

Davis, K. J., Dove, P. M., Wasylenki, L. E., and De Yoreo, J. J., 2004. Morphological consequences of differential Mg^{2+} incorporation at structurally distinct steps on calcite. *American Mineralogist* **89**, 714-720.

De Choudens-Sanchez, V. and Gonzalez, L. A., 2009. Calcite and Aragonite Precipitation Under Controlled Instantaneous Supersaturation: Elucidating the Role of CaCO_3 Saturation State and Mg/Ca Ratio on Calcium Carbonate Polymorphism. *Journal of Sedimentary Research* **79**, 363-376.

de Moor, P., Beelen, T. P. M., Komanschek, B. U., Beck, L. W., Wagner, P., Davis, M. E., and van Santen, R. A., 1999a. Imaging the assembly process of the organic-mediated synthesis of a zeolite. *Chemistry-a European Journal* **5**, 2083-2088.

de Moor, P., Beelen, T. P. M., and van Santen, R. A., 1999b. In situ observation of nucleation and crystal growth in zeolite synthesis. A small-angle X-ray scattering investigation on Si-TPA-MFI. *Journal of Physical Chemistry B* **103**, 1639-1650.

De Villiers, J. P. R., 1971. Crystal Structures of Aragonite, Strontianite, and Witherite. *American Mineralogist* **56**, 758-767.

de Villiers, S., Greaves, M., and Elderfield, H., 2002. An intensity ratio calibration method for the accurate determination of Mg/Ca and Sr/Ca of marine carbonates by ICP-AES. *Geochem. Geophys. Geosyst.* **3**, 1001.

De Yoreo, J. J., Zepeda-Ruiz, L. A., Friddle, R. W., Qiu, S. R., Wasylenki, L. E., Chernov, A. A., Gilmer, G. H., and Dove, P. M., 2009. Rethinking Classical Crystal Growth Models through Molecular Scale Insights: Consequences of Kink-Limited Kinetics. *Crystal Growth & Design* **9**, 5135-5144.

Demicco, R. V., Lowenstein, T. K., Hardie, L. A., and Spencer, R. J., 2005. Model of seawater composition for the Phanerozoic. *Geology* **33**, 877-880.

Dickson, J. A. D., 2002. Fossil Echinoderms As Monitor of the Mg/Ca Ratio of Phanerozoic Oceans. *Science* **298**, 1222-1224.

Dickson, J. A. D., 2004. Echinoderm skeletal preservation: Calcite-aragonite seas and the Mg/Ca ratio of phanerozoic oceans. *Journal of Sedimentary Research* **74**, 355-365.

Doerner, H. A. and Hoskins, W. M., 1925. Co-precipitation of radium and barium sulfates. *American Journal of the Chemical Society* **47**, 662-675.

Doner, H. E. and Pratt, P. F., 1969. Solubility of Calcium Carbonate Precipitated in Aqueous Solutions of Magnesium and Sulfate Salts. *Soil Science Society of America Journal* **33**, 690-693.

Drever, J. I., 1997. *The geochemistry of natural waters: surface and groundwater environments*. Prentice Hall, Upper Saddle River, New Jersey.

Drits, V., Srodon, J., and Eberl, D. D., 1997. XRD measurement of mean crystalline thickness of illite and illite/smectite: Reappraisal of the Kubler index and the Scherrer equation. *Clay Clay Min.* **45**, 461-475.

Dupont, L., Portemer, F., and late Michel Figlarz, t., 1997. Synthesis and study of a well crystallized CaCO₃ vaterite showing a new habitus. *Journal of Materials Chemistry* **7**, 797-800.

Dydo, P., Turek, M., and Ciba, J., 2003. Scaling analysis of nanofiltration systems fed with saturated calcium sulfate solutions in the presence of carbonate ions. *Desalination* **159**, 245-251.

Faatz, M., Gröhn, F., and Wegner, G., 2004. Amorphous Calcium Carbonate: Synthesis and Potential Intermediate in Biomineralization. *Advanced Materials* **16**, 996-1000.

Falini, G., Albeck, S., Weiner, S., and Addadi, L., 1996. Control of aragonite or calcite polymorphism by mollusk shell macromolecules. *Science* **271**, 67-69.

Falini, G., Gazzano, M., and Ripamonti, A., 1994. Crystallization of calcium carbonate in presence of magnesium and polyelectrolytes. *Journal of Crystal Growth* **137**, 577-584.

Fenter, P., Zhang, Z., Park, C., Sturchio, N. C., Hu, X. M., and Higgins, S. R., 2007. Structure and reactivity of the dolomite (104)-water interface: New insights into the dolomite problem. *Geochimica et Cosmochimica Acta* **71**, 566-579.

Fernández-Díaz, L., Fernandez-Gonzalez, A., Carneiro, J., and Prieto, M., 2009a. On the interaction between gypsum and carbonate-bearing aqueous solutions: Implications for the polymorphism of CaCO₃. *Geochimica Et Cosmochimica Acta* **73**, A367-A367.

Fernández-Díaz, L., Fernández-González, Á., and Prieto, M., 2010. The role of sulfate groups in controlling CaCO₃ polymorphism. *Geochimica et Cosmochimica Acta* **74**, 6064-6076.

Fernández-Díaz, L., Pina, C. M., Astilleros, J. M., and Sanchez-Pastor, N., 2009b. The carbonatation of gypsum: Pathways and pseudomorph formation. *American Mineralogist* **94**, 1223-1234.

Flörke, W. and Flörke, O. W., 1961. Vateritbildung aus Gips in Sodalösung. *Neues Jahrbuch für Mineralogie - Monatshefte*, 179-181.

Frankel, R. B. and Bazylinski, D. A., 2003. Biologically Induced Mineralization by Bacteria. In: Dove, P. M., De Yoreo, J. J., and Weiner, S. Eds.), *Biomineralization*. Mineralogical Society of America.

Freyer, D. and Voigt, W., 2003. Crystallization and phase stability of CaSO₄ and CaSO₄-based salts. *Monatshefte Fur Chemie* **134**, 693-719.

Gamsjäger, H., Königsberger, E., and Preis, W., 2000. Lippmann Diagrams: Theory and Application to Carbonate Systems. *Aquatic Geochemistry* **6**, 119-132.

Garrels, R. M., Thompson, M. E., and Siever, R., 1960. Stability of some carbonates at 25 degrees C and one atmosphere total pressure. *American Journal of Science* **258**, 402-418.

Gazeau, F., Gattuso, J. P., Dawber, C., Pronker, A. E., Peene, F., Peene, J., Heip, C. H. R., and Middelburg, J. J., 2010. Effect of ocean acidification on the early life stages of the blue mussel *Mytilus edulis*. *Biogeosciences* **7**, 2051-2060.

Gebauer, D., Gunawidjaja, P. N., Ko, J. Y. P., Bacsik, Z., Aziz, B., Liu, L., Hu, Y., Bergström, L., Tai, C.-W., Sham, T.-K., Edén, M., and Hedin, N., 2010. Proto-Calcite and Proto-Vaterite in Amorphous Calcium Carbonates. *Angewandte Chemie International Edition*, n/a-n/a.

Gebauer, D., Völkel, A., and Cölfen, H., 2008. Stable Prenucleation Calcium Carbonate Clusters. *Science* **322**, 1819-1822.

Gill, B. C., Lyons, T. W., and Saltzman, M. R., 2007. Parallel, high-resolution carbon and sulfur isotope records of the evolving Paleozoic marine sulfur reservoir. *Palaeogeography, Palaeoclimatology, Palaeoecology* **256**, 156-173.

Gill, B. C., Lyons, T. W., Young, S. A., Kump, L. R., Knoll, A. H., and Saltzman, M. R., 2011. Geochemical evidence for widespread euxinia in the Later Cambrian ocean. *Nature* **469**, 80-83.

Given, R. K. and Wilkinson, B. H., 1985. Kinetic Control of Morphology, Composition, and Mineralogy of Abiotic Sedimentary Carbonates. *Journal of Sedimentary Petrology* **55**, 109-119.

Glatter, O., 1977. New Method for Evaluation of Small-Angle Scattering Data. *Journal of Applied Crystallography* **10**, 415-421.

Glatter, O. and Kratky, O., 1982. *Small Angle X-Ray Scattering*. Academic Press, London.

Glynn, P. D., 2000. Solid-solution solubilities and thermodynamics: Sulfates, carbonates and halides. In: Alpers, C. N., Jambor, J. L., and Nordstrom, D. K. Eds.), *Sulfate Minerals/minerals: Crystallography, Geochemistry and Environmental*

Significance. Mineralogical Society of America, Reviews in Mineralogy and Geochemistry.

Glynn, P. D. and Reardon, E. J., 1990. Solid-solution aqueous-solution equilibria; thermodynamic theory and representation. *American Journal of Science* **290**, 164-201.

Goldsmith, J. R. and Graf, D. L., 1958. Relation between Lattice Constants and Composition of the Ca-Mg Carbonates. *American Mineralogist* **43**, 84-101.

Goldsmith, J. R., Graf, D. L., and Heard, H. C., 1961. Lattice Constants of the Calcium-Magnesium Carbonates. *American Mineralogist* **46**, 453-457.

Goodisman, J. and Brumberger, H., 1971. Scattering from a Multiphase System. *Journal of Applied Crystallography* **4**, 347-351.

Goodwin, A. L., Michel, F. M., Phillips, B. L., Keen, D. A., Dove, M. T., and Reeder, R. J., 2010. Nanoporous Structure and Medium-Range Order in Synthetic Amorphous Calcium Carbonate. *Chemistry of Materials* **22**, 3197-3205.

Gower, L. B., 2008. Biomimetic Model Systems for Investigating the Amorphous Precursor Pathway and Its Role in Biomineralization. *Chemical Reviews* **108**, 4551-4627.

Graf, D. L., 1961. Crystallographic Tables for the Rhombohedral Carbonates. *American Mineralogist* **46**, 1283-1316.

Gránásy, L., Pusztai, T., Tegze, G., Warren, J. A., and Douglas, J. F., 2005. Growth and form of spherulites. *Physical Review E* **72**.

Grasby, S. E., 2003. Naturally precipitating vaterite ($[\mu]$ -CaCO₃) spheres: unusual carbonates formed in an extreme environment. *Geochimica et Cosmochimica Acta* **67**, 1659-1666.

Guinier, A., 1963. *X-ray Diffraction in Crystals, Imperfect Crystals, and Amorphous Bodies*. W. H. Freeman, San Francisco.

Gutjahr, A., Dabringhaus, H., and Lacmann, R., 1996. Studies of the growth and dissolution kinetics of the CaCO₃ polymorphs calcite and aragonite II. The influence of divalent cation additives on the growth and dissolution rates. *Journal of Crystal Growth* **158**, 310-315.

Hanor, J. S. and McIntosh, J. C., 2006. Are secular variations in seawater chemistry reflected in the compositions of basinal brines? *Journal of Geochemical Exploration* **89**, 153-156.

Hardie, L. A., 1990. The roles of rifting and hydrothermal CaCl₂ brines in the origin of potash evaporites; an hypothesis. *American Journal of Science* **290**, 43-106.

Hardie, L. A., 1991. On the Significance of Evaporites. *Annual Review of Earth and Planetary Sciences* **19**, 131-168.

Hardie, L. A., 1996. Secular variation in seawater chemistry: An explanation for the coupled secular variation in the mineralogies of marine limestones and potash evaporites over the past 600 my. *Geology* **24**, 279-283.

Hardie, L. A., 2003. Secular variations in Precambrian seawater chemistry and the timing of Precambrian aragonite seas and calcite seas. *Geology* **31**, 785-788.

Harvie, C. E. and Weare, J. H., 1980. The prediction of mineral solubilities in natural waters: the Na---K---Mg---Ca---Cl---SO₄---H₂O system from zero to high concentration at 25° C. *Geochimica et Cosmochimica Acta* **44**, 981-997.

Harvie, C. E., Weare, J. H., Hardie, L. A., and Eugster, H. P., 1980. Evaporation of Seawater - Calculated Mineral Sequences. *Science* **208**, 498-500.

Hasiuk, F. J. and Lohmann, K. C., 2008. Mississippian paleocean chemistry from biotic and abiotic carbonate, Muleshoe Mound, Lake Valley formation, New Mexico, USA. *Journal of Sedimentary Research* **78**, 147-160.

Henderson, L. M. and Kracek, F. C., 1927. The fractional precipitation of barium and radium chromates. *Journal of the American Chemical Society* **49**, 738-749.

Hetzel, A., Böttcher, M. E., Wortmann, U. G., and Brumsack, H.-J., 2009. Paleo-redox conditions during OAE 2 reflected in Demerara Rise sediment geochemistry (ODP Leg 207). *Palaeogeography, Palaeoclimatology, Palaeoecology* **273**, 302-328.

Hill, R. J. and Howard, C. J., 1987. Quantitative phase analysis from neutron powder diffraction data using the Rietveld method. *Journal of Applied Crystallography* **20**, 467-474.

Holland, H. D., 2005. Sea level, sediments and the composition of seawater. *American Journal of Science* **305**, 220-239.

Holland, H. D., Horita, J., and Seyfried, W. E., 1996. On the secular variations in the composition of Phanerozoic marine potash evaporites. *Geology* **24**, 993-996.

Horita, J., Zimmermann, H., and Holland, H. D., 2002. Chemical evolution of seawater during the Phanerozoic: Implications from the record of marine evaporites. *Geochimica et Cosmochimica Acta* **66**, 3733-3756.

Houston, S., Smalley, C., Laycock, A., and Yardley, B. W. D., 2011. The relative importance of buffering and brine inputs in controlling the abundance of Na and Ca in sedimentary formation waters. *Marine and Petroleum Geology* **28**, 1242-1251.

Hull, H. and Turnbull, A. G., 1973. Thermochemical Study of Monohydrocalcite. *Geochimica Et Cosmochimica Acta* **37**, 685-694.

Ito, T., Matsubara, S., and Miyawaki, R., 1999. Vaterite after ikaite in carbonate sediment. *Journal of Mineralogy, Petrology and Economic Geology* **94**, 176-182.

Jansen, J. H. F., Woensdregt, C. F., Kooistra, M. J., and van der Gaast, S. J., 1987. Ikaite pseudomorphs in the Zaire deep-sea fan: An intermediate between calcite and porous calcite. *Geology* **15**, 245-248.

Ji, B., Cusack, M., Freer, A., Dobson, P. S., Gadegaard, N., and Yin, H., 2010. Control of crystal polymorph in microfluidics using molluscan 28 kDa Ca(2+)-binding protein. *Integrative Biology* **2**, 528-535.

Johnson, W. A. and Mehl, R. F., 1939. Reaction kinetics in processes of nucleation and growth. *Transactions of the American Institute of Mining, Metallurgical and Petroleum Engineers* **135**, 416-442.

Kah, L. C., Lyons, T. W., and Frank, T. D., 2004. Low marine sulphate and protracted oxygenation of the proterozoic biosphere. *Nature* **431**, 834-838.

Kamhi, S. R., 1963. On the Structure of Vaterite, CaCO₃. *Acta Crystallography* **16**, 770-772.

Keith, H. D. and Padden, F. J., 1963. A Phenomenological Theory of Spherulitic Crystallization. *journal article* **34**, 2409-2421.

Killian, C. E., Metzler, R. A., Gong, Y. U. T., Olson, I. C., Aizenberg, J., Politi, Y., Wilt, F. H., Scholl, A., Young, A., Doran, A., Kunz, M., Tamura, N., Coppersmith, S. N., and Gilbert, P. U. P. A., 2009. Mechanism of Calcite Co-Orientation in the Sea Urchin Tooth. *Journal of the American Chemical Society* **131**, 18404-18409.

Kitano, Y., 1962. Behavior of Inorganic Ions in the Separation of CaCO₃ from Bicarbonate Solution. *Bulletin of the Chemical Society of Japan* **35**, 1973-1980.

Knoll, A. H., 2003. Biomineralization and evolutionary history. In: Dove, P. M., de Yoreo, J. J., and Weiner, S. Eds.), *Biomineralization*. Mineralogical Society of America, Washington, DC.

Königsberger, E. and Gamsjäger, H., 1992. Solid-solute phase equilibria in aqueous solution: VII. A re-interpretation of magnesian calcite stabilities. *Geochimica et Cosmochimica Acta* **56**, 4095-4098.

Kontrec, J., Kralj, D., Brečević, L., Falini, G., Fermani, S., Nöthig-Laslo, V., and Mirosavljevic, K., 2004. Incorporation of inorganic anions in calcite. *European Journal of Inorganic Chemistry*, 4579-4585.

Kornicker, W. A., Presta, P. A., Paige, C. R., Johnson, D. M., Hileman Jr, O. E., and Snodgrass, W. J., 1991. The aqueous dissolution kinetics of the barium/lead sulfate solid solution series at 25 and 60°C. *Geochimica et Cosmochimica Acta* **55**, 3531-3541.

Kovalevich, V. M., Peryt, T. M., and Petrichenko, O. I., 1998. Secular Variation in Seawater Chemistry during the Phanerozoic as Indicated by Brine Inclusions in Halite. *Journal of Geology* **106**, 695-712.

Kralj, D., Brečević, L., and Kontrec, J., 1997. Vaterite growth and dissolution in aqueous solution III. Kinetics of transformation. *Journal of Crystal Growth* **177**, 248-257.

Kratky, O., Pilz, I., and Schmitz, P. J., 1966. Absolute intensity measurement of small angle x-ray scattering by means of a standard sample. *Journal of Colloid and Interface Science* **21**, 24-34.

Krumgalz, B. S., 2001. Application of the Pitzer ion interaction model to natural hypersaline brines. *Journal of Molecular Liquids* **91**, 3-19.

Kulik, D. A., 2006. Dual-thermodynamic estimation of stoichiometry and stability of solid solution end members in aqueous-solid solution systems. *Chemical Geology* **225**, 189-212.

Kulik, D. A., Vinograd, V. L., Paulsen, N., and Winkler, B., 2010. (Ca,Sr)CO₃ aqueous-solid solution systems: From atomistic simulations to thermodynamic modelling. *Physics and Chemistry of the Earth* **35**, 217-232.

Laaksonen, A., Talanquer, V., and Oxtoby, D. W., 1995. Nucleation - Measurements, Theory, and Atmospheric Applications. *Annu. Rev. Phys. Chem.* **46**, 489-524.

Lakshatanov, L. Z. and Stipp, S. L. S., 2010. Interaction between dissolved silica and calcium carbonate: 1. Spontaneous precipitation of calcium carbonate in the presence of dissolved silica. *Geochimica et Cosmochimica Acta* **74**, 2655-2664.

Lam, R. S. K., Charnock, J. M., Lennie, A., and Meldrum, F. C., 2007. Synthesis-dependant structural variations in amorphous calcium carbonate. *Crystengcomm* **9**, 1226-1236.

Le Bail, A., Ouhenia, S., and Chateigner, D., 2011. Microtwinning hypothesis for a more ordered vaterite model. *Powder Diffraction* **27**, 16-21.

Lee, J. and Morse, J. W., 2010. Influences of alkalinity and pCO₂ on CaCO₃ nucleation from estimated Cretaceous composition seawater representative of "calcite seas". *Geology* **38**, 115-118.

Lennie, A. R., Tang, C. C., and Thompson, S. P., 2004. The structure and thermal expansion behaviour of ikaite, CaCO₃·6H₂O, from T = 114 to T = 293 K. *Mineralogical Magazine* **68**, 135-146.

Levi, Y., Albeck, S., Brack, A., Weiner, S., and Addadi, L., 1998. Control over aragonite crystal nucleation and growth: An in vitro study of biomineralization. *Chemistry-a European Journal* **4**, 389-396.

Lifshitz, I. M. and Slyozov, V. V., 1961. The kinetics of precipitation from supersaturated solid solutions. *Journal of Physics and Chemistry of Solids* **19**, 35-50.

Lippmann, F., 1973. *Sedimentary Carbonate Minerals*. Springer Verlag, New York.

Liu, J., Pancera, S., Boyko, V., Shukla, A., Narayanan, T., and Huber, K., 2010. Evaluation of the Particle Growth of Amorphous Calcium Carbonate in Water by Means of the Porod Invariant from SAXS. *Langmuir* **26**, 17405-17412.

Lorens, R. B. and Bender, M. L., 1980. The impact of solution chemistry on *Mytilus edulis* calcite and aragonite. *Geochimica et Cosmochimica Acta* **44**, 1265-1278.

Loste, E., Wilson, R. M., Seshadri, R., and Meldrum, F. C., 2003. The role of magnesium in stabilising amorphous calcium carbonate and controlling calcite morphologies. *Journal of Crystal Growth* **254**, 206-218.

Lowenstam, H. A., 1981. Minerals Formed by Organisms. *Science* **211**, 1126-1131.

Lowenstam, H. A. and Abbott, D. P., 1975. Vaterite: A Mineralization Product of the Hard Tissues of a Marine Organism (Ascidacea). *Science* **188**, 363-365.

Lowenstein, T. K., Hardie, L. A., Timofeeff, M. N., and Demicco, R. V., 2003. Secular variation in seawater chemistry and the origin of calcium chloride basinal brines. *Geology* **31**, 857-860.

Lowenstein, T. K. and Timofeeff, M. N., 2008. Secular variations in seawater chemistry as a control on the chemistry of basinal brines: test of the hypothesis. *Geofluids* **8**, 77-92.

Lowenstein, T. K., Timofeeff, M. N., Brennan, S. T., Hardie, L. A., and Demicco, R. V., 2001. Oscillations in Phanerozoic Seawater Chemistry: Evidence from Fluid Inclusions. *Science* **294**, 1086-1088.

Lowenstein, T. K., Timofeeff, M. N., Kovalevych, V. M., and Horita, J., 2005. The major-ion composition of Permian seawater. *Geochimica et Cosmochimica Acta* **69**, 1701-1719.

Mackenzie, F. T., Arvidson, R. S., and Guidry, M., 2008. Phanerozoic time chemostatic modes of the ocean-atmosphere-sediment system through Phanerozoic time. *Mineralogical Magazine* **72**, 333-335.

Mackenzie, F. T. and Kump, L. R., 1995. Reverse Weathering, Clay Mineral Formation, and Oceanic Element Cycles. *Science* **270**, 586.

Marchal, J., Tartoni, N., and Nave, C., 2009. Synchrotron applications of pixel and strip detectors at Diamond Light Source. *Nuclear Instruments and Methods in Physics Research Section A: Accelerators, Spectrometers, Detectors and Associated Equipment* **604**, 123-126.

Marini, M., Campanelli, A., and Abballe, F., 2006. Measurement of alkaline and earthy ions in fish otolith and sea water using a high performance ion chromatography. *Marine Chemistry* **99**, 24-30.

Markgraf, S. A. and Reeder, R. J., 1985. High-temperature structure refinements of calcite and magnesite. *American Mineralogist* **70**, 590-600.

Marland, G., 1975. The stability of $\text{CaCO}_3 \cdot 6\text{H}_2\text{O}$ (ikaite). *Geochimica et Cosmochimica Acta* **39**, 83-91.

Martin, R. E., 1995. Cyclic and secular variation in microfossil biomineralization: clues to the biogeochemical evolution of Phanerozoic oceans. *Global and Planetary Change* **11**, 1-23.

Medeiros, S. K., Albuquerque, E. L., Maia Jr, F. F., Caetano, E. W. S., and Freire, V. N., 2007. First-principles calculations of structural, electronic, and optical absorption properties of CaCO_3 Vaterite. *Chemical Physics Letters* **435**, 59-64.

Meldrum, F. C. and Cölfen, H., 2008. Controlling Mineral Morphologies and Structures in Biological and Synthetic Systems. *Chemical Reviews* **108**, 4332-4432.

Meldrum, F. C. and Hyde, S. T., 2001. Morphological influence of magnesium and organic additives on the precipitation of calcite. *Journal of Crystal Growth* **231**, 544-558.

Meyer, H. J., 1960. Über Vaterit und seine Struktur. *Fortschritte der Mineralogie* **38**, 186-187.

Meyer, H. J., 1969. Structure and Disorder in Vaterite. *Zeitschrift Fur Kristallographie Kristallgeometrie Kristallphysik Kristallchemie* **128**, 183-212.

Meyer, H. J., 1984. The influence of impurities on the growth rate of calcite. *Journal of Crystal Growth* **66**, 639-646.

Michel, F. M., MacDonald, J., Feng, J., Phillips, B. L., Ehm, L., Tarabrella, C., Parise, J. B., and Reeder, R. J., 2008. Structural characteristics of synthetic amorphous calcium carbonate. *Chemistry of Materials* **20**, 4720-4728.

Mirwald, P. W., 2008. Experimental study of the dehydration reactions gypsum-bassanite and bassanite-anhydrite at high pressure: Indication of anomalous behavior of H₂O at high pressure in the temperature range of 50-300 degrees C. *Journal of Chemical Physics* **128**.

Moghadas, J., Müller-Steinhagen, H., Jamialahmadi, M., and Sharif, A., 2004. Model study on the kinetics of oil field formation damage due to salt precipitation from injection. *Journal of Petroleum Science and Engineering* **43**, 201-217.

Morse, J. W., Arvidson, R. S., and Lutge, A., 2007. Calcium carbonate formation and dissolution. *Chemical Reviews* **107**, 342-381.

Morse, J. W. and Bender, M. L., 1990. Partition coefficients in calcite: Examination of factors influencing the validity of experimental results and their application to natural systems. *Chemical Geology* **82**, 265-277.

Morse, J. W. and Mackenzie, F. T., 1990. *Geochemistry of Sedimentary Carbonates*. Elsevier, Amsterdam.

Morse, J. W., Wang, Q. W., and Tsio, M. Y., 1997. Influences of temperature and Mg:Ca ratio on CaCO₃ precipitates from seawater. *Geology* **25**, 85-87.

Mucci, A., 1986. Growth kinetics and composition of magnesian calcite overgrowths precipitated from seawater: Quantitative influence of orthophosphate ions. *Geochimica et Cosmochimica Acta* **50**, 2255-2265.

Mucci, A. and Morse, J. W., 1983. The incorporation of Mg²⁺ and Sr²⁺ into calcite overgrowths: influences of growth rate and solution composition. *Geochimica et Cosmochimica Acta* **47**, 217-233.

Mucci, A. and Morse, J. W., 1984. The solubility of calcite in seawater solutions of various magnesium concentration, It = 0.697 m at 25 °C and one atmosphere total pressure. *Geochimica et Cosmochimica Acta* **48**, 815-822.

Mucci, A. and Morse, J. W., 1985. Auger spectroscopy determination of the surface-most adsorbed layer composition on aragonite, calcite, dolomite, and magnesite in synthetic seawater. *American Journal of Science* **285**, 306-317.

Navrotsky, A., 2004. Energetic clues to pathways to biomineralization: Precursors, clusters, and nanoparticles. *Proceedings of the National Academy of Sciences of the United States of America* **101**, 12096-12101.

Nebel, H., Neumann, M., Mayer, C., and Epple, M., 2008. On the Structure of Amorphous Calcium Carbonate—A Detailed Study by Solid-State NMR Spectroscopy. *Inorganic Chemistry* **47**, 7874-7879.

Nehrke, G., Reichart, G. J., Van Cappellen, P., Meile, C., and Bijma, J., 2007. Dependence of calcite growth rate and Sr partitioning on solution stoichiometry: Non-Kossel crystal growth. *Geochimica et Cosmochimica Acta* **71**, 2240-2249.

Newton, R. J., Pevitt, E. L., Wignall, P. B., and Bottrell, S. H., 2004. Large shifts in the isotopic composition of seawater sulphate across the Permo-Triassic boundary in northern Italy. *Earth and Planetary Science Letters* **218**, 331-345.

Newton, R. J., Reeves, E. P., Kafousia, N., Wignall, P. B., Bottrell, S. H., and Sha, J.-G., 2011. Low marine sulfate concentrations and the isolation of the European epicontinental sea during the Early Jurassic. *Geology* **39**, 7-10.

Njegic-Dzakula, B., Falini, G., Brecevic, L., Skoko, Z., and Kralj, D., 2010. Effects of initial supersaturation on spontaneous precipitation of calcium carbonate in the presence of charged poly-l-amino acids. *Journal of Colloid and Interface Science* **343**, 553-563.

Ogino, T., Suzuki, T., and Sawada, K., 1987. The formation and transformation mechanism of calcium carbonate in water. *Geochimica et Cosmochimica Acta* **51**, 2757-2767.

Ogino, T., Suzuki, T., and Sawada, K., 1990. The rate and mechanism of polymorphic transformation of calcium carbonate in water. *Journal of Crystal Growth* **100**, 159-167.

Okafor, C. U., Thomas, D. J., Wade, B. S., and Firth, J., 2009. Environmental change in the subtropics during the late middle Eocene greenhouse and global implications. *Geochem. Geophys. Geosyst.* **10**, Q07003.

Olcott, A. N., Lorentz, N. J., Corsetti, F. A., and Berelson, W. M., 2004. Reevaluating gravimetric determination of carbonate associated sulfate concentrations. *2004 Denver Annual Meeting*. Geological Society of America, Denver.

Olderøy, M. Ø., Xie, M., Strand, B. L., Flaten, E. M., Sikorski, P., and Andreassen, J.-P., 2009. Growth and Nucleation of Calcium Carbonate Vaterite Crystals in Presence of Alginate. *Crystal Growth & Design* **9**, 5176-5183.

Paquette, J. and Reeder, R. J., 1990. Single-crystal X-ray structure refinements of two biogenic magnesian calcite crystals. *American Mineralogist* **75**, 1151-1158.

Park, W. K., Ko, S.-J., Lee, S. W., Cho, K.-H., Ahn, J.-W., and Han, C., 2008. Effects of magnesium chloride and organic additives on the synthesis of aragonite precipitated calcium carbonate. *Journal of Crystal Growth* **310**, 2593-2601.

Parkhurst, D. L. and Appelo, C. A. J., 1999. *User's guide to PHREEQC (version 2) — a computer program for speciation, batch-reaction, one-dimensional transport, and inverse geochemical calculations*. U.S. Geological Survey Denver, Colorado.

Paytan, A., Kastner, M., Campbell, D., and Thiemens, M. H., 1998. Sulfur Isotopic Composition of Cenozoic Seawater Sulfate. *Science* **282**, 1459-1462.

Paytan, A., Kastner, M., Campbell, D., and Thiemens, M. H., 2004. Seawater Sulfur Isotope Fluctuations in the Cretaceous. *Science* **304**, 1663-1665.

Pilz, I., 1969. Absolute Intensity Measurement of Small-Angle X-Ray Scattering by Means of a Standard Sample .3. *Journal of Colloid and Interface Science* **30**, 140-&.

Pilz, I. and Kratky, O., 1967. Absolute intensity measurement of small-angle X-ray scattering by means of a standard sample, II. *Journal of Colloid and Interface Science* **24**, 211-218.

Pingitore, N. E., Meitzner, G., and Love, K. M., 1995. Identification of sulfate in natural carbonates by x-ray absorption spectroscopy. *Geochimica et Cosmochimica Acta* **59**, 2477-2483.

Pipich, V., Balz, M., Wolf, S. E., Tremel, W., and Schwahn, D., 2008. Nucleation and Growth of CaCO₃ Mediated by the Egg-White Protein Ovalbumin: A Time-Resolved in situ Study Using Small-Angle Neutron Scattering. *Journal of the American Chemical Society* **130**, 6879-6892.

Plummer, L. N. and Busenberg, E., 1982. The solubilities of calcite, aragonite and vaterite in CO₂-H₂O solutions between 0 and 90°C, and an evaluation of the aqueous model for the system CaCO₃-CO₂-H₂O. *Geochimica et Cosmochimica Acta* **46**, 1011-1040.

Plummer, L. N., Parkhurst, D. L., and Wigley, T. M. L., 1979. Critical Review of the Kinetics of Calcite Dissolution and Precipitation, *Chemical Modeling in Aqueous Systems*. American Chemical Society.

Plummer, L. N., Wigley, T. M. L., and Parkhurst, D. L., 1978. The kinetics of calcite dissolution in CO₂-water systems at 5 degrees to 60 degrees C and 0.0 to 1.0 atm CO₂. *American Journal of Science* **278**, 179-216.

Politi, Y., Arad, T., Klein, E., Weiner, S., and Addadi, L., 2004. Sea urchin spine calcite forms via a transient amorphous calcium carbonate phase. *Science* **306**, 1161-1164.

Politi, Y., Metzler, R. A., Abrecht, M., Gilbert, B., Wilt, F. H., Sagi, I., Addadi, L., Weiner, S., and Gilbert, P. U. P. A., 2008. Transformation mechanism of amorphous calcium carbonate into calcite in the sea urchin larval spicule. *Proceedings of the National Academy of Sciences of the United States of America* **105**, 20045-20045.

Porod, G., 1951. Die Rontgenkleinwinkelstreuung Von Dichtgepackten Kolloiden Systemen .1. *Kolloid-Zeitschrift and Zeitschrift Fur Polymere* **124**, 83-114.

Porter, S. M., 2007. Seawater Chemistry and Early Carbonate Biomineralization. *Science* **316**, 1302.

Porter, S. M., 2010. Calcite and aragonite seas and the de novo acquisition of carbonate skeletons. *Geobiology* **8**, 256-277.

Pouget, E. M., Bomans, P. H. H., Dey, A., Frederik, P. M., de With, G., and Sommerdijk, N. A. J. M., 2010. The Development of Morphology and Structure in Hexagonal Vaterite. *Journal of the American Chemical Society* **132**, 11560-11565.

Prieto, M., 2009. Thermodynamics of Solid Solution-Aqueous Solution Systems. In: Oelkers, E. and Schott, J. Eds.), *Thermodynamics and Kinetics of Water-Rock Interaction*. The Mineralogical Society of America.

Prieto, M., Fernandez-Gonzalez, A., Becker, U., and Putnis, A., 2000. Computing Lippmann diagrams from direct calculation of mixing properties of solid solutions: Application to the barite-celestite system. *Aquatic Geochemistry* **6**, 133-146.

Putnis, A., 1992. *Introduction to Mineral Sciences*. Cambridge University Press, Cambridge.

Quigley, D. and Rodger, P. M., 2008. Free energy and structure of calcium carbonate nanoparticles during early stages of crystallization. *The Journal of Chemical Physics* **128**, 221101-4.

Radha, A. V., Forbes, T. Z., Killian, C. E., Gilbert, P. U. P. A., and Navrotsky, A., 2010. Transformation and crystallization energetics of synthetic and biogenic amorphous calcium carbonate. *Proceedings of the National Academy of Sciences* **107**, 16438-16443.

Railsback, L. B. and Anderson, T. F., 1987. Control of Triassic seawater chemistry and temperature on the evolution of post-Paleozoic aragonite-secreting faunas. *Geology* **15**, 1002-1005.

Raiteri, P. and Gale, J. D., 2010. Water Is the Key to Nonclassical Nucleation of Amorphous Calcium Carbonate. *Journal of the American Chemical Society* **132**, 17623-17634.

Reznik, I. J., Gavrieli, I., Antler, G., and Ganor, J., 2011. Kinetics of gypsum crystal growth from high ionic strength solutions: A case study of Dead Sea - seawater mixtures. *Geochimica Et Cosmochimica Acta* **75**, 2187-2199.

Ridgwell, A. and Zeebe, R. E., 2005. The role of the global carbonate cycle in the regulation and evolution of the Earth system. *Earth and Planetary Science Letters* **234**, 299-315.

Ries, J. B., 2004. Effect of ambient Mg/Ca ratio on Mg fractionation in calcareous marine invertebrates: A record of the oceanic Mg/Ca ratio over the Phanerozoic. *Geology* **32**, 981-984.

Ries, J. B., 2005. Aragonite production in calcite seas: effect of seawater Mg/Ca ratio on the calcification and growth of the calcareous alga *Penicillus capitatus*. *Paleobiology* **31**, 445-458.

Ries, J. B., 2006. Mg fractionation in crustose coralline algae: Geochemical, biological, and sedimentological implications of secular variation in the Mg/Ca ratio of seawater. *Geochimica Et Cosmochimica Acta* **70**, 891-900.

Ries, J. B., Anderson, M. A., and Hill, R. T., 2008. Seawater Mg/Ca controls polymorph mineralogy of microbial CaCO₃: A potential proxy for calcite-aragonite seas in Precambrian time. *Geobiology* **6**, 106-119.

Rietveld, H. M., 1969. A profile refinement method for nuclear and magnetic structures. *Journal of Applied Crystallography* **2**, 65-71.

Roberts, A. C., Ansell, H. G., Jonasson, I. R., Grice, J. D., and Ramik, R. A., 1986. Rapidcreekite, a New Hydrated Calcium-Sulfate Carbonate from the Rapid Creek Area, Yukon Territory. *Canadian Mineralogist* **24**, 51-54.

Rodriguez-Blanco, J. D., Bots, P., Roncal-Herrero, T., Shaw, S., and Benning, L. G., in press. The role of pH and Mg on the stability and crystallization of amorphous calcium carbonate. *Journal of Alloys and Compounds*.

Rodriguez-Blanco, J. D., Shaw, S., and Benning, L. G., 2008. How to make 'stable' ACC: protocol and preliminary structural characterization. *Mineralogical Magazine* **72**, 283-286.

Rodriguez-Blanco, J. D., Shaw, S., and Benning, L. G., 2011. The kinetics and mechanisms of amorphous calcium carbonate (ACC) crystallization to calcite, via vaterite. *Nanoscale* **3**, 265-271.

Roncal-Herrero, T., Bots, P., Rodriguez-Blanco, J. D., Shaw, S., and Benning, L. G., 2011. The role of inorganic additives in evaporitic carbonate precipitation. *Mineralogical Magazine* **75**, 1748.

Royer, D. L., Berner, R. A., Montañez, I. P., Tabor, N. J., and Beerling, D. J., 2004. CO₂ as a primary driver of Phanerozoic climate. *GSA Today* **14**, 4-10.

Ruiz-Agudo, E., Putnis, C. V., Jiménez-López, C., and Rodriguez-Navarro, C., 2009. An atomic force microscopy study of calcite dissolution in saline solutions: The role of magnesium ions. *Geochimica et Cosmochimica Acta* **73**, 3201-3217.

Ryan, A. J., Hamley, I. W., Bras, W., and Bates, F. S., 1995. Structure Development in Semicrystalline Diblock Copolymers Crystallizing from the Ordered Melt. *Macromolecules* **28**, 3860-3868.

Sandberg, P. A., 1983. An oscillating trend in Phanerozoic non-skeletal carbonate mineralogy. *Nature* **305**, 19-22.

Schmidt, P. W., 1991. Small-Angle Scattering Studies of Disordered, Porous and Fractal Systems. *Journal of Applied Crystallography* **24**, 414-435.

Schofield, P. F., Knight, K. S., and Stretton, I. C., 1996. Thermal expansion of gypsum investigated by neutron powder diffraction. *American Mineralogist* **81**, 847-851.

Shahar, A., Bassett, W. A., Mao, H.-k., Chou, I. M., and Mao, W., 2005. The stability and Raman spectra of ikaite, $\text{CaCO}_3 \cdot 6\text{H}_2\text{O}$, at high pressure and temperature. *American Mineralogist* **90**, 1835-1839.

Shen, Q., Wei, H., Zhou, Y., Huang, Y., Yang, H., Wang, D., and Xu, D., 2006. Properties of Amorphous Calcium Carbonate and the Template Action of Vaterite Spheres. *The Journal of Physical Chemistry B* **110**, 2994-3000.

Shtukenberg, A. G., Punin, Y. O., and Azimov, P., 2006. Crystallization kinetics in binary solid solution-aqueous solution systems. *American Journal of Science* **306**, 553-574.

Simkiss, K., 1964. Variations in the Crystalline Form of Calcium Carbonate precipitated from Artificial Sea Water. *Nature* **201**, 492-493.

Simone, L., 1980. Ooids: A review. *Earth-Science Reviews* **16**, 319-355.

Stack, A. G. and Grantham, M. C., 2010. Growth Rate of Calcite Steps As a Function of Aqueous Calcium-to-Carbonate Ratio: Independent Attachment and Detachment of Calcium and Carbonate Ions. *Crystal Growth & Design* **10**, 1409-1413.

Stanley, S. M., 2006. Influence of seawater chemistry on biomineralization throughout phanerozoic time: Paleontological and experimental evidence. *Palaeogeography, Palaeoclimatology, Palaeoecology* **232**, 214-236.

Stanley, S. M. and Hardie, L. A., 1998. Secular oscillations in the carbonate mineralogy of reef-building and sediment-producing organisms driven by tectonically forced shifts in seawater chemistry. *Palaeogeography, Palaeoclimatology, Palaeoecology* **144**, 3-19.

Stanley, S. M., Ries, J. B., and Hardie, L. A., 2005. Seawater chemistry, coccolithophore population growth, and the origin of Cretaceous chalk. *Geology* **33**, 593-596.

Stávek, J., Šípek, M., Hirasawa, I., and Toyokura, K., 1992. Controlled double-jet precipitation of sparingly soluble salts. A method for the preparation of high added value materials. *Chemistry of Materials* **4**, 545-555.

Steuber, T. and Veizer, J., 2002. Phanerozoic record of plate tectonic control of seawater chemistry and carbonate sedimentation.

Svergun, D., 1992. Determination of the regularization parameter in indirect-transform methods using perceptual criteria. *Journal of Applied Crystallography* **25**, 495-503.

Swainson, I. P., 2008. The structure of monohydrocalcite and the phase composition of the beachrock deposits of Lake Butler and Lake Fellmongery, South Australia. *2008* **93**, 1014-1018.

Takano, B., 1985. Geochemical implications of sulfate in sedimentary carbonates. *Chemical Geology* **49**, 393-403.

Talmage, S. C. and Gobler, C. J., 2010. Effects of past, present, and future ocean carbon dioxide concentrations on the growth and survival of larval shellfish. *Proceedings of the National Academy of Sciences* **107**, 17246-17251.

Tang, C. C., Thompson, S. P., Parker, J. E., Lennie, A. R., Azough, F., and Kato, K., 2009. The ikaite-to-vaterite transformation: new evidence from diffraction and imaging. *Journal of Applied Crystallography* **42**, 225-233.

Taylor, P. D., James, N. P., Bone, Y., Kuklinski, P., and Kyser, T. K., 2009. Evolving Mineralogy of Cheilostome Bryozoans. *Palaios* **24**, 440-452.

Teixeira, J., 1988. Small-Angle Scattering by Fractal Systems. *Journal of Applied Crystallography* **21**, 781-785.

Teng, H. H., Dove, P. M., and De Yoreo, J. J., 2000. Kinetics of calcite growth: surface processes and relationships to macroscopic rate laws. *Geochimica et Cosmochimica Acta* **64**, 2255-2266.

Terrill, N. J., Grant, A. F., Marshall, A. R., Smith, A. D., and Sawhney, K. J., 2004. The non-crystalline Diffraction beamline for Diamond – An Update. *Fibre Diffraction Review* **12**, 9-14.

Tesoriero, A. J. and Pankow, J. F., 1996. Solid solution partitioning of Sr²⁺, Ba²⁺, and Cd²⁺ to calcite. *Geochimica Et Cosmochimica Acta* **60**, 1053-1063.

Thomas, D. J., Bralower, T. J., and Zachos, J. C., 1999. New Evidence for Subtropical Warming During the Late Paleocene Thermal Maximum: Stable Isotopes from Deep Sea Drilling Project Site 527, Walvis Ridge. *Paleoceanography* **14**, 561-570.

Thompson, S. P., Parker, J. E., Marchal, J., Potter, J., Birt, A., Yuan, F., Fearn, R. D., Lennie, A. R., Street, S. R., and Tang, C. C., 2011. Fast X-ray powder diffraction on I11 at Diamond. *Journal of Synchrotron Radiation* **18**, 637-648.

Timofeeff, M. N., Lowenstein, T. K., da Silva, M. A., and Harris, N. B., 2006. Secular variation in the major-ion chemistry of seawater: Evidence from fluid inclusions in Cretaceous halites. *Geochimica Et Cosmochimica Acta* **70**, 1977-1994.

Tobler, D. J., Shaw, S., and Benning, L. G., 2009. Quantification of initial steps of nucleation and growth of silica nanoparticles: An *in situ* SAXS and DLS study. *Geochimica et Cosmochimica Acta* **73**, 5377-5393.

Tomás, J. and Geffen, A. J., 2003. Morphometry and composition of aragonite and vaterite otoliths of deformed laboratory reared juvenile herring from two populations. *Journal of Fish Biology* **63**, 1383-1401.

Tribello, G. A., Bruneval, F., Liew, C., and Parrinello, M., 2009. A Molecular Dynamics Study of the Early Stages of Calcium Carbonate Growth. *The Journal of Physical Chemistry B* **113**, 11680-11687.

Uchymiak, M., Lyster, E., Glater, J., and Cohen, Y., 2008. Kinetics of gypsum crystal growth on a reverse osmosis membrane. *Journal of Membrane Science* **314**, 163-172.

Vacassy, R., Lemaître, J., Hofmann, H., and Gerlings, J. H., 2000. Calcium carbonate precipitation using new segmented flow tubular reactor. *AIChE Journal* **46**, 1241-1252.

Van Driessche, A. E. S., Benning, L. G., Rodriguez-Blanco, J. D., Ossorio, M., Bots, P., and García-Ruiz, J. M., in review. The role, and implications, of bassanite as a precursor phase to gypsum precipitation *Science*.

Van Santen, R. A., 1984. The Ostwald step rule. *The Journal of Physical Chemistry* **88**, 5768-5769.

Vavouraki, A. I., Putnis, C. V., Putnis, A., and Koutsoukos, P. G., 2008. An Atomic Force Microscopy study of the growth of calcite in the presence of sodium sulfate. *Chemical Geology* **253**, 243-251.

Wagner, C., 1961. Theorie der Alterung von Niederschlägen durch Umlösen (Ostwald-Reifung). *Zeitschrift für Elektrochemie, Berichte der Bunsengesellschaft für physikalische Chemie* **65**, 581-591.

Walenta, K. and Dunn, P. J., 1989. Camgasite, a new calcium-magnesium arsenate mineral of the $\text{CaMg}(\text{AsO}_4)(\text{OH})\cdot 5\text{H}_2\text{O}$ composition from Wittichen in medium Black Forest (FRG). *Der Aufschluß* **40**, 369-372.

Wallmann, K., 2001. Controls on the cretaceous and cenozoic evolution of seawater composition, atmospheric CO_2 and climate. *Geochimica et Cosmochimica Acta* **65**, 3005-3025.

Wallmann, K., 2004. Impact of atmospheric CO_2 and galactic cosmic radiation on Phanerozoic climate change and the marine delta $\text{O}-18$ record. *Geochemistry Geophysics Geosystems* **5**.

Walter, L. M., 1986. Relative Efficiency of Carbonate Dissolution and Precipitation During Diagenesis: A Progress Report on the Role of Solution Chemistry. In: Gautier, D. L. (Ed.), *Roles of Organic Matter in Sediment Diagenesis*. Society of Economic Paleontologists and Mineralogists Special Publication

Walter, L. M. and Morse, J. W., 1984. Magnesian calcite stabilities: A reevaluation. *Geochimica et Cosmochimica Acta* **48**, 1059-1069.

Wang, J. W. and Becker, U., 2009. Structure and carbonate orientation of vaterite (CaCO_3). *American Mineralogist* **94**, 380-386.

Warren, J. K., 2010. Evaporites through time: Tectonic, climatic and eustatic controls in marine and nonmarine deposits. *Earth-Science Reviews* **98**, 217-268.

Wasylenki, L. E., Dove, P. M., and De Yoreo, J. J., 2005. Effects of temperature and transport conditions on calcite growth in the presence of Mg^{2+} : Implications for paleothermometry. *Geochimica et Cosmochimica Acta* **69**, 4227-4236.

Weiner, S. and Dove, P. M., 2003. An overview of biomineralization processes and the problem of the vital effect. In: Dove, P. M., de Yoreo, J. J., and Weiner, S. Eds.), *Biomineralization*. Mineralogical Society of America, Washington, DC.

Weiner, S. and Traub, W., 1984. Macromolecules in Mollusk Shells and Their Functions in Biomineralization. *Philosophical Transactions of the Royal Society of London Series B-Biological Sciences* **304**, 425-&.

Weiss, I. M., Tuross, N., Addadi, L., and Weiner, S., 2002. Mollusc larval shell formation: amorphous calcium carbonate is a precursor phase for aragonite. *Journal of Experimental Zoology* **293**, 478-491.

Wheeley, J. R., Cherns, L., and Wright, V. P., 2008. Provenance of microcrystalline carbonate cement in limestone-marl alternations (LMA): aragonite mud or molluscs? *Journal of the Geological Society* **165**, 395-403.

Wilkinson, B. H. and Algeo, T. J., 1989. Sedimentary Carbonate Record of Calcium Magnesium Cycling. *American Journal of Science* **289**, 1158-1194.

Wilkinson, B. H., Buczynski, C., and Owen, R. M., 1984. Chemical control of carbonate phases; implications from Upper Pennsylvanian calcite-aragonite ooids of southeastern Kansas. *Journal of Sedimentary Research* **54**, 932-947.

Wilkinson, B. H., Owen, R. M., and Carroll, A. R., 1985. Submarine hydrothermal weathering, global eustasy, and carbonate polymorphism in Phanerozoic marine oolites. *Journal of Sedimentary Research* **55**, 171-183.

Wolf, S. E., Leiterer, J., Pipich, V., Barrea, R., Emmerling, F., and Tremel, W., 2011. Strong stabilization of liquid amorphous calcium carbonate by ovalbumin: gaining insight into the mechanism of 'polymer-induced liquid precursor' processes. *Journal of the American Chemical Society*, null-null.

Wolthers, M., Charlet, L., and Van Cappellen, P., 2008. The surface chemistry of divalent metal carbonate minerals; a critical assessment of surface charge and potential data using the charge distribution multi-site ion complexation model. *American Journal of Science* **308**, 905-941.

Wortmann, U. G. and Chernyavsky, B. M., 2007. Effect of evaporite deposition on Early Cretaceous carbon and sulphur cycling. *Nature* **446**, 654-656.

Wray, J. L. and Daniels, F., 1957. Precipitation of Calcite and Aragonite. *Journal of the American Chemical Society* **79**, 2031-2034.

Xyla, A. G., Giannimaras, E. K., and Koutsoukos, P. G., 1991. The precipitation of calcium carbonate in aqueous solutions. *Colloids and Surfaces* **53**, 241-255.

Yamamoto, H. and Kennedy, G. C., 1969. Stability Relations in System CaSO₄-H₂O at High Temperatures and Pressures. *American Journal of Science* **267**, 550-&.

Yu, J., Day, J., Greaves, M., and Elderfield, H., 2005. Determination of multiple element/calcium ratios in foraminiferal calcite by quadrupole ICP-MS. *Geochem. Geophys. Geosyst.* **6**, Q08P01.

Zhang, J. and Nancollas, G. H., 1992. Influence of calcium/sulfate molar ratio on the growth rate of calcium sulfate dihydrate at constant supersaturation. *Journal of Crystal Growth* **118**, 287-294.

Zhang, Y. and Dawe, R. A., 2000. Influence of Mg²⁺ on the kinetics of calcite precipitation and calcite crystal morphology. *Chemical Geology* **163**, 129-138.

Zhu, Y., Liu, Y., Ruan, Q., Zeng, Y., Xiao, J., Liu, Z., Cheng, L., Xu, F., and Zhang, L., 2009. Superstructures and Mineralization of Laminated Vaterite Mesocrystals via Mesoscale Transformation and Self-Assembly. *The Journal of Physical Chemistry C* **113**, 6584-6588.

Zhuravlev, A. Y. and Wood, R. A., 2009. Controls on carbonate skeletal mineralogy: Global CO₂ evolution and mass extinctions. *Geology* **37**, 1123-1126.

Zimmermann, H., 2000. Tertiary seawater chemistry; implications from primary fluid inclusions in marine halite. *American Journal of Science* **300**, 723-767.

Zimmermann, H., 2001. On the origin of fluids included in Phanerozoic marine halite--basic interpretation strategies. *Geochimica et Cosmochimica Acta* **65**, 35-45.

Zuddas, P. and Mucci, A., 1994. Kinetics of calcite precipitation from seawater: I. A classical chemical kinetics description for strong electrolyte solutions. *Geochimica et Cosmochimica Acta* **58**, 4353-4362.

Appendix A

Supplementary information to chapter 4

A.1 Tables and figures from the PHREEQC evaporation simulations

Table A.1 Table with input and output solutions from the evaporation simulations on solutions in the concentration range from the experimental set-up, including the sea type (LOWENSTEIN et al., 2003), the evaporite type (HARDIE, 1996) and the evaporite mineral sequence as they occur in the simulations

Solution nr	Starting chemistry of modelling solutions (mM)							Chemistry of invariant solutions (M)						
	Ca	Mg	SO ₄	Na	Cl	K	DIC	Ca	Mg	SO ₄	Na	Cl	K	DIC
1	10.5	2.0	5.0	535	558	10.4	2.47	6.84	0.55109	1.19E-05	0.0310	15.1	0.312	9.81E-05
2	10.5	2.0	8.0	541	558	10.4	2.47	6.84	0.55115	1.19E-05	0.0310	15.1	0.312	9.81E-05
3	10.5	2.0	10.0	545	558	10.4	2.47	0.00268	4.52	0.154	0.460	8.93	0.492	0.367
4	10.5	2.0	15.0	555	558	10.4	2.47	0.00817	0.30514	0.330	4.90	6.87	2.011	0.00715
5	10.5	5.0	5.0	529	558	10.4	2.46	6.84	0.55109	1.19E-05	0.0310	15.1	0.312	9.81E-05
6	10.5	5.0	8.0	535	558	10.4	2.46	6.84	0.55108	1.19E-05	0.0310	15.1	0.312	9.81E-05
7	10.5	5.0	10.0	539	558	10.4	2.46	0.00268	4.52	0.154	0.460	8.93	0.492	0.367
8	10.5	5.0	15.0	549	558	10.4	2.46	0.00268	4.52	0.154	0.460	8.93	0.492	0.367
9	10.5	10.0	5.0	519	558	10.4	2.45	6.84	0.55108	1.19E-05	0.0310	15.1	0.312	9.81E-05
10	10.5	10.0	8.0	525	558	10.4	2.45	6.84	0.55117	1.19E-05	0.0310	15.1	0.312	9.81E-05
11	10.5	10.0	10.0	529	558	10.4	2.45	0.00268	4.52	0.154	0.460	8.93	0.492	0.367
12	10.5	10.0	15.0	539	558	10.4	2.45	0.000784	6.81	0.319	0.253	9.40	0.174	1.978
13	10.5	20.0	5.0	499	558	10.4	2.43	5.22	2.54	3.94E-06	0.0190	15.6	0.0221	0.000233
14	10.5	20.0	8.0	505	558	10.4	2.43	5.22	2.54	3.94E-06	0.0190	15.6	0.0221	0.000233
15	10.5	20.0	10.0	509	558	10.4	2.43	0.00113	8.72	0.0467	0.0744	11.7	0.0184	2.802
16	10.5	20.0	15.0	519	558	10.4	2.43	0.00113	8.72	0.0467	0.0744	11.7	0.0184	2.802
	Sea type*		Evaporite type [†]				Evaporite mineral sequence [‡]							
1	CaCl ₂		KCl				Cc, G, A, H, Syl, Car, Ant							
2	CaCl ₂		KCl				Cc, G, A, H, Syl, Car, Ant							
3	MgSO ₄		MgSO ₄				Cc, G, A, H, Car, Pol, Syl							
4	MgSO ₄		MgSO ₄				Cc, G, A, H, Gl, Pol, Syl							
5	CaCl ₂		KCl				Cc, G, A, H, Syl, Car, Ant							
6	CaCl ₂		KCl				Cc, G, A, H, Syl, Car, Ant							
7	MgSO ₄		MgSO ₄				Cc, G, A, H, Car, Pol, Syl							
8	MgSO ₄		MgSO ₄				Cc, G, A, H, Car, Gl, Pol, Syl							
9	CaCl ₂		KCl				Cc, G, A, H, Syl, Car, Ant							
10	CaCl ₂		KCl				Cc, G, A, H, Syl, Car, Ant							
11	MgSO ₄		MgSO ₄				Cc, G, A, H, Car, Pol, Syl							
12	MgSO ₄		MgSO ₄				Cc, G, A, H, Car, Gl, Pol, Syl, Ki							
13	CaCl ₂		KCl				Cc, G, A, H, Syl, Bi, Car, Tac							
14	CaCl ₂		KCl				Cc, G, A, H, Syl, Bi, Car, Tac							
15	MgSO ₄		MgSO ₄				Cc, G, A, H, Bi, Car, Pol, Syl							
16	MgSO ₄		MgSO ₄				Cc, G, A, H, Bi, Car, Pol, Syl, Ki							

* The sea type was determined from the invariant solutions where Ca>SO₄ represents a CaCl₂ type sea and Ca<SO₄ represents a MgSO₄ type sea.

[†] The evaporite type is determined from the evaporite mineral sequence; when sylvite is present without any MgSO₄ mineral the evaporite type is KCl and when polyhalite and/or kieserite is present the evaporite type is MgSO₄ (HARDIE, 1996)

[‡] The evaporite mineral sequences are determined from Figure A.5 to Figure A.8; the abbreviations of the mineral phases and their chemical formula are listed in Table A.4.

Table A.2 Table with input and output solutions from the evaporation simulations on solutions between the cretaceous and the present day chemistry as proposed by for example HORITA et al. (2003), including the sea type (LOWENSTEIN et al., 2003), the evaporite type (HARDIE, 1996) and the evaporite mineral sequence as they occur in the simulations

Solution nr	Starting chemistry of modelling solutions (mM)							Chemistry of invariant solutions (M)						
	Ca	Mg	SO ₄	Na	Cl	K	DIC	Ca	Mg	SO ₄	Na	Cl	K	DIC
17	10.5	54.3	28.9	478	558	10.4	2.37	0.00113	8.72	0.0467	0.0744	11.7	0.0184	2.80
18	13.8	50.0	25.3	473	558	10.4	2.37	0.00113	8.72	0.0467	0.0744	11.7	0.0184	2.80
19	19.2	43.0	19.6	465	558	10.4	2.36	0.00113	8.72	0.0467	0.0744	11.7	0.0184	2.80
20	20.8	41.0	17.9	462	558	10.4	2.36	5.22	2.54	3.94E-06	0.0190	15.6	0.0221	0.000233
21	25.4	35.0	13.0	455	558	10.4	2.35	5.22	2.54	3.94E-06	0.0190	15.6	0.0221	0.000233
22	29.9	29.0	8.0	448	558	10.4	2.18	5.90	2.06	3.72E-06	0.0164	16.0	0.0306	0.000178
	Sea type*		Evaporite type [#]			Evaporite mineral sequence [§]								
17	MgSO ₄		MgSO ₄			Cc, G, A, H, Gl, Pol, E, Hx, Ki, Car, Bi								
18	MgSO ₄		MgSO ₄			Cc, G, A, H, Pol, Car, Ki, Bi								
19	MgSO ₄		MgSO ₄			Cc, G, A, H, Syl, Car, Ki, Bi								
20	CaCl ₂		KCl			Cc, G, A, H, Syl, Car, Bi, Tac								
21	CaCl ₂		KCl			Cc, G, A, H, Syl, Car, Bi, Tac								
22	CaCl ₂		KCl			Cc, G, A, H, Syl, Bi, Car, Tac, Ant								

* The sea type was determined from the invariant solutions where Ca>SO₄ represents a CaCl₂ type sea and Ca<SO₄ represents a MgSO₄ type sea.

[#] The evaporite type is determined from the evaporite mineral sequence; when sylvite is present without any MgSO₄ mineral the evaporite type is KCl and when polyhalite and/or kieserite is present the evaporite type is MgSO₄ (HARDIE, 1996)

[§] The evaporite mineral sequences are determined from Figure A.10; the abbreviations of the mineral phases and their chemical formula are listed in Table A.4.

Table A.3 The first 77 lines of one input file for the PHREEQC evaporation calculations (PARKHURST and APPELO, 1999); additional lines were added to continuously remove water from the solutions saved in the previous part from the model.

phases		epsomite	0	0
Tachyhydrite		hexahydrite	0	0
CaMg2Cl6:12H2O = Ca+2 + 2Mg+2 + 6Cl- + 12H2O		kieserite	0	0
log_k 17.1439		polyhalite	0	0
Antarcticite		glauberite	0	0
CaCl2:6H2O = Ca+2 + 2Cl- + 6H2O		calcite	1	0
log_k 4.0933		CO2(g)	-3.412	10000
selected_output		save solution	1	
-water true		save equilibrium_phases	1	
-distance false		end		
-time false				
-file Z:\Min-Gro\experiments\constant		solution	2	
addition\PHREEQC-evaporation\m2-15.xls		save solution	2	
-totals S(6) Ca Mg K Na Cl C(4)		end		
-equilibrium_phases halite sylvite antarcticite				
bischofite tachyhydrite carnallite gypsum anhydrite		mix	1	
epsomite hexahydrite kieserite polyhalite		1	1	
glauberite calcite		2	-0.1	
-saturation_indices halite sylvite antarcticite		use equilibrium_phases	1	
bischofite tachyhydrite carnallite gypsum anhydrite		save solution	1	
epsomite hexahydrite kieserite polyhalite		save equilibrium_phases	1	
glauberite calcite		end		
solution 1		mix	2	
-pH 7		1	1	
-Temp 21		2	-0.09	
-water 1		use equilibrium_phases	1	
reaction 1		save solution	1	
MgCl2 2.0		save equilibrium_phases	1	
Na2SO4 15.0		end		
NaCl 522.6				
CaCl2 10.5		mix	3	
KCl 10.4		1	1	
NaHCO3 2		2	-0.0405	
Na2CO3 0.3		use equilibrium_phases	1	
0.001		save solution	1	
equilibrium_phases 1		save equilibrium_phases	1	
halite 0 0		end		
sylvite 0 0				
antarcticite 0 0				
bischofite 0 0				
tachyhydrite 0 0				
carnallite 0 0				
gypsum 0 0				
anhydrite 0 0				

Table A.4 List with possible evaporite minerals, their abbreviation as used in Table A.1 and Table A.2 and their chemical formula.

Mineral	Abbreviation	Chemical formula
calcite	Cc	CaCO_3
gypsum	G	$\text{CaSO}_4 \cdot 2\text{H}_2\text{O}$
anhydrite	A	CaSO_4
halite	H	NaCl
sylvite	Syl	KCl
carnallite	Car	$\text{KMgCl}_3 \cdot 6\text{H}_2\text{O}$
antarcticite	Ant	$\text{CaCl}_2 \cdot 6\text{H}_2\text{O}$
tachyhydrite	Tac	$\text{CaMg}_2\text{Cl}_6 \cdot 12\text{H}_2\text{O}$
bischofite	Bi	$\text{MgCl}_2 \cdot 6\text{H}_2\text{O}$
glauuberite	Gl	$\text{Na}_2\text{Ca}(\text{SO}_4)_2$
polyhalite	Pol	$\text{K}_2\text{Ca}_2\text{Mg}(\text{SO}_4)_4 \cdot 2\text{H}_2\text{O}$
epsomite	E	$\text{MgSO}_4 \cdot 7\text{H}_2\text{O}$
hexahydrite	Hx	$\text{MgSO}_4 \cdot 6\text{H}_2\text{O}$
kieserite	Ki	$\text{MgSO}_4 \cdot \text{H}_2\text{O}$

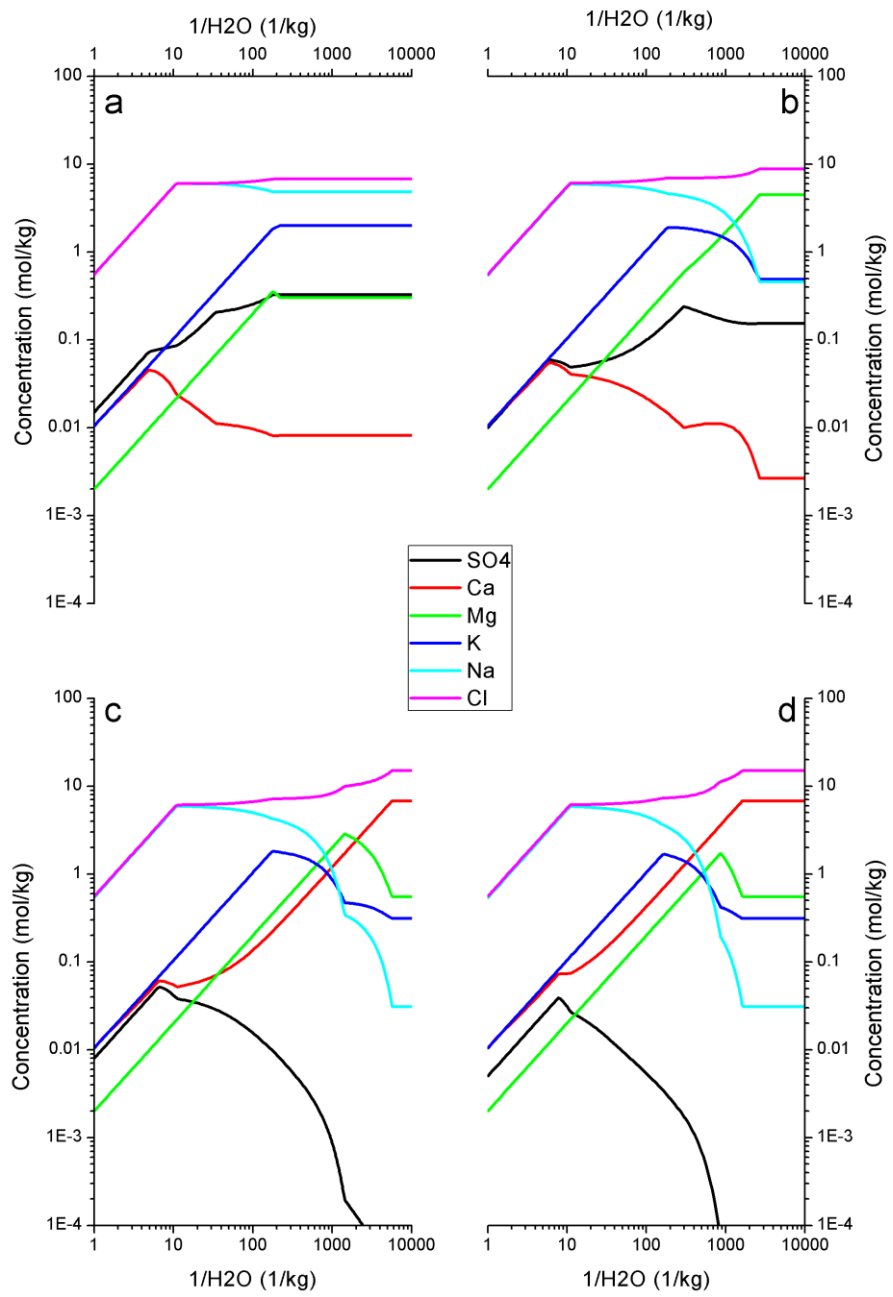


Figure A.1 The evolution of the solution from simulation runs 1-4; 2mM Mg and a. 15mM SO₄, b. 10mM SO₄, c. 8mM SO₄ and d. 5mM SO₄ (Table A.1).

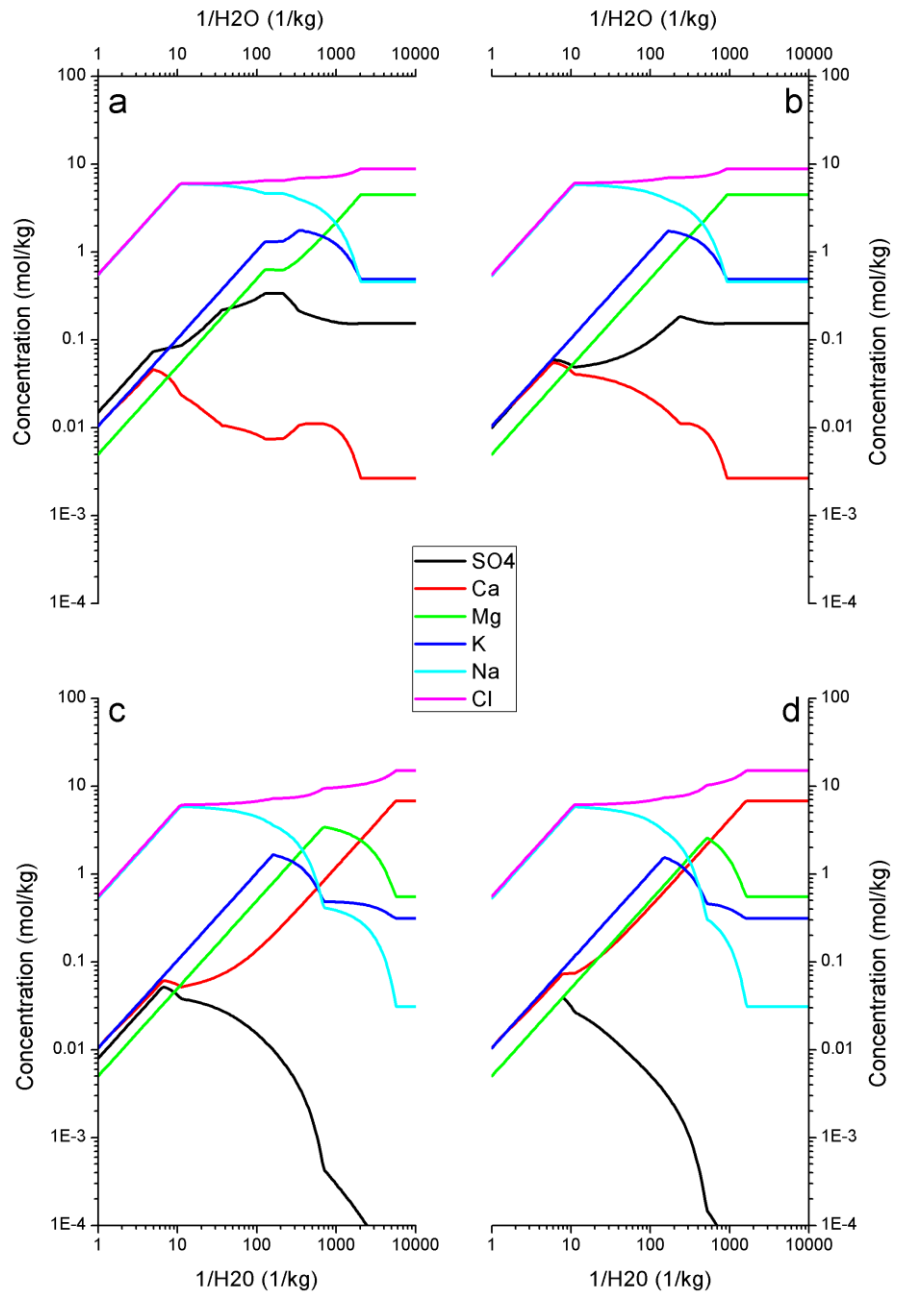


Figure A.2 The evolution of the solution from simulation runs 2-8; 5mM Mg and a. 15mM SO₄, b. 10mM SO₄, c. 8mM SO₄ and d. 5mM SO₄ (Table A.1).

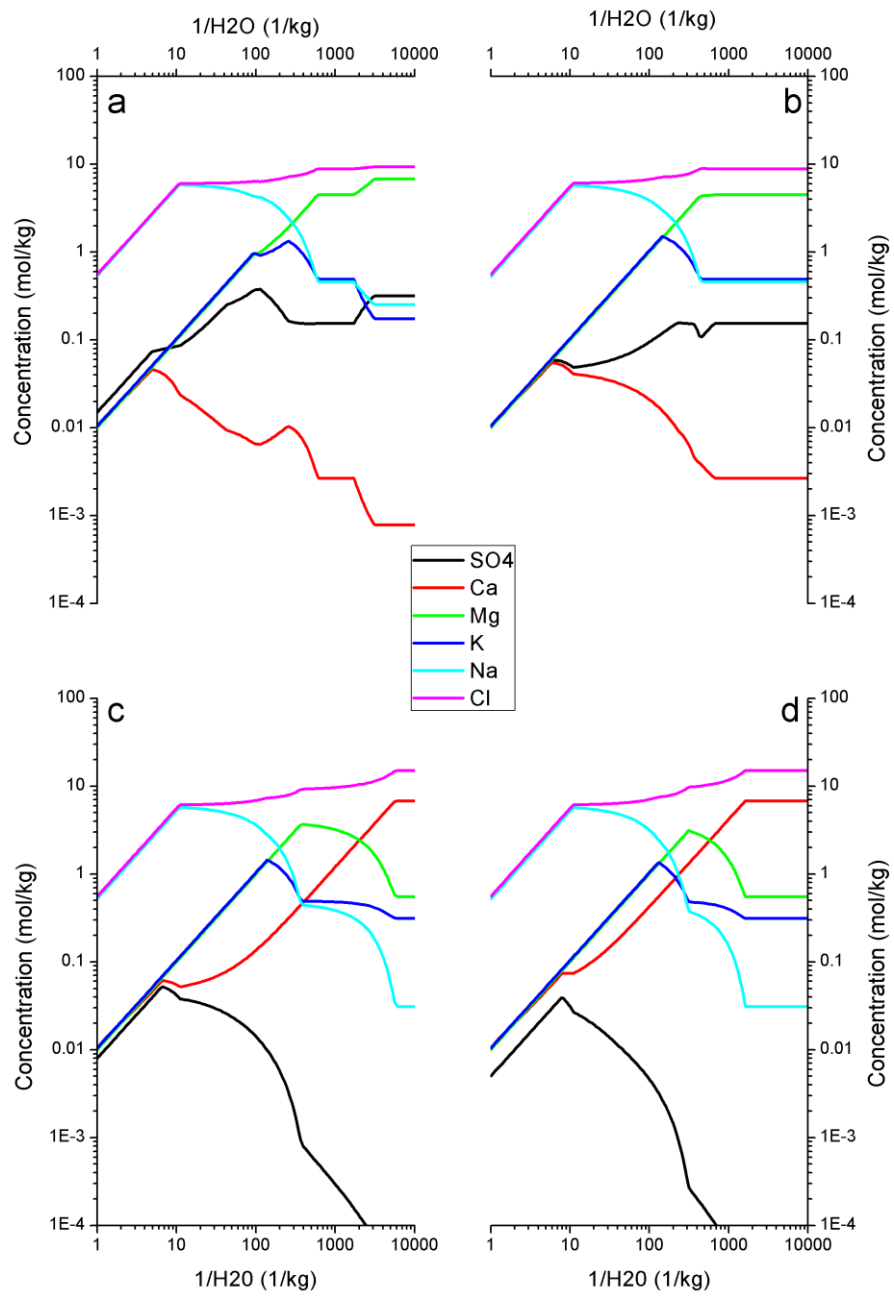


Figure A.3 The evolution of the solution from simulation runs 9-12; 10mM Mg and a. 15mM SO₄, b. 10mM SO₄, c. 8mM SO₄ and d. 5mM SO₄ (Table A.1).

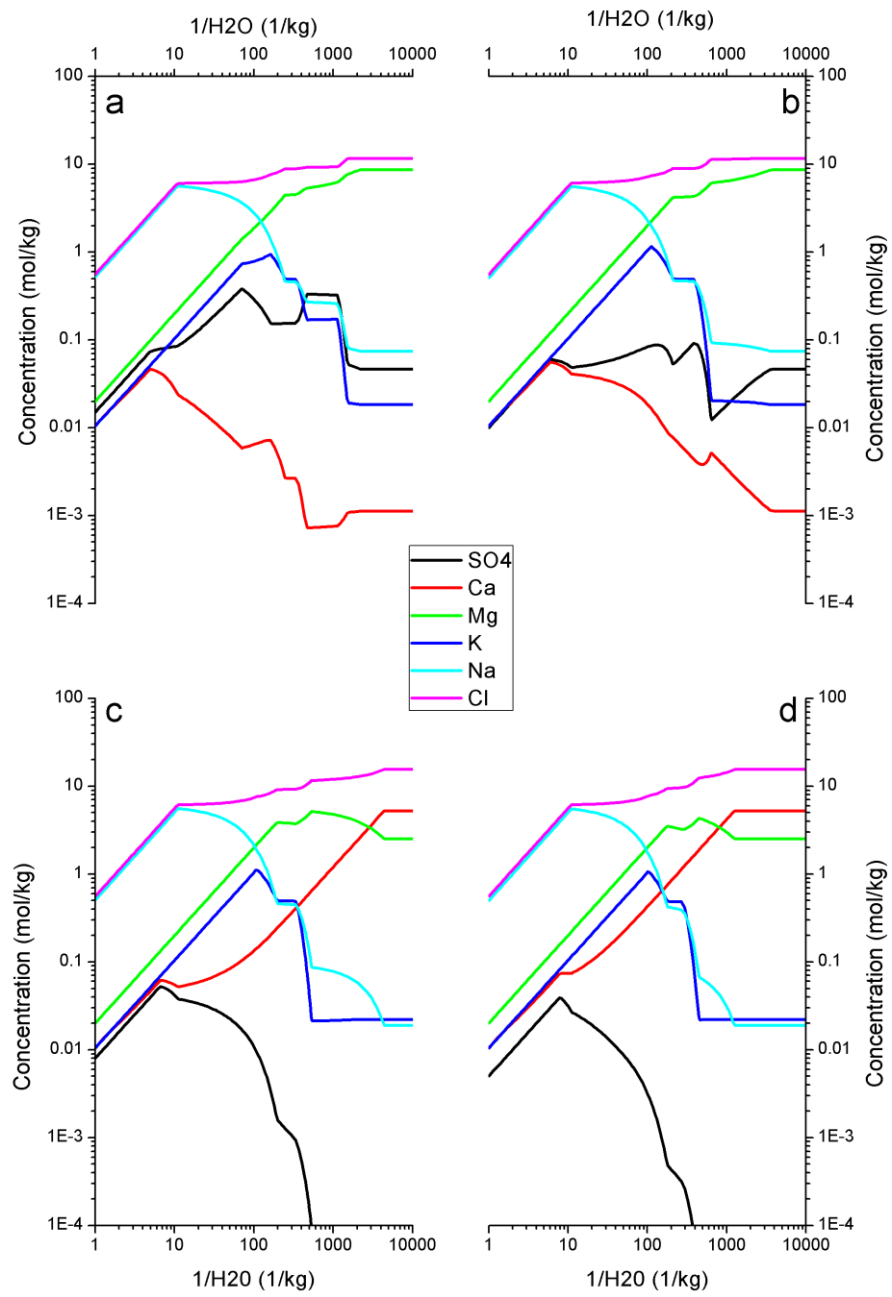


Figure A.4. The evolution of the solution from simulation runs 13-16; 20mM Mg and a. 15mM SO₄, b. 10mM SO₄, c. 8mM SO₄ and d. 5mM SO₄ (Table A.1).

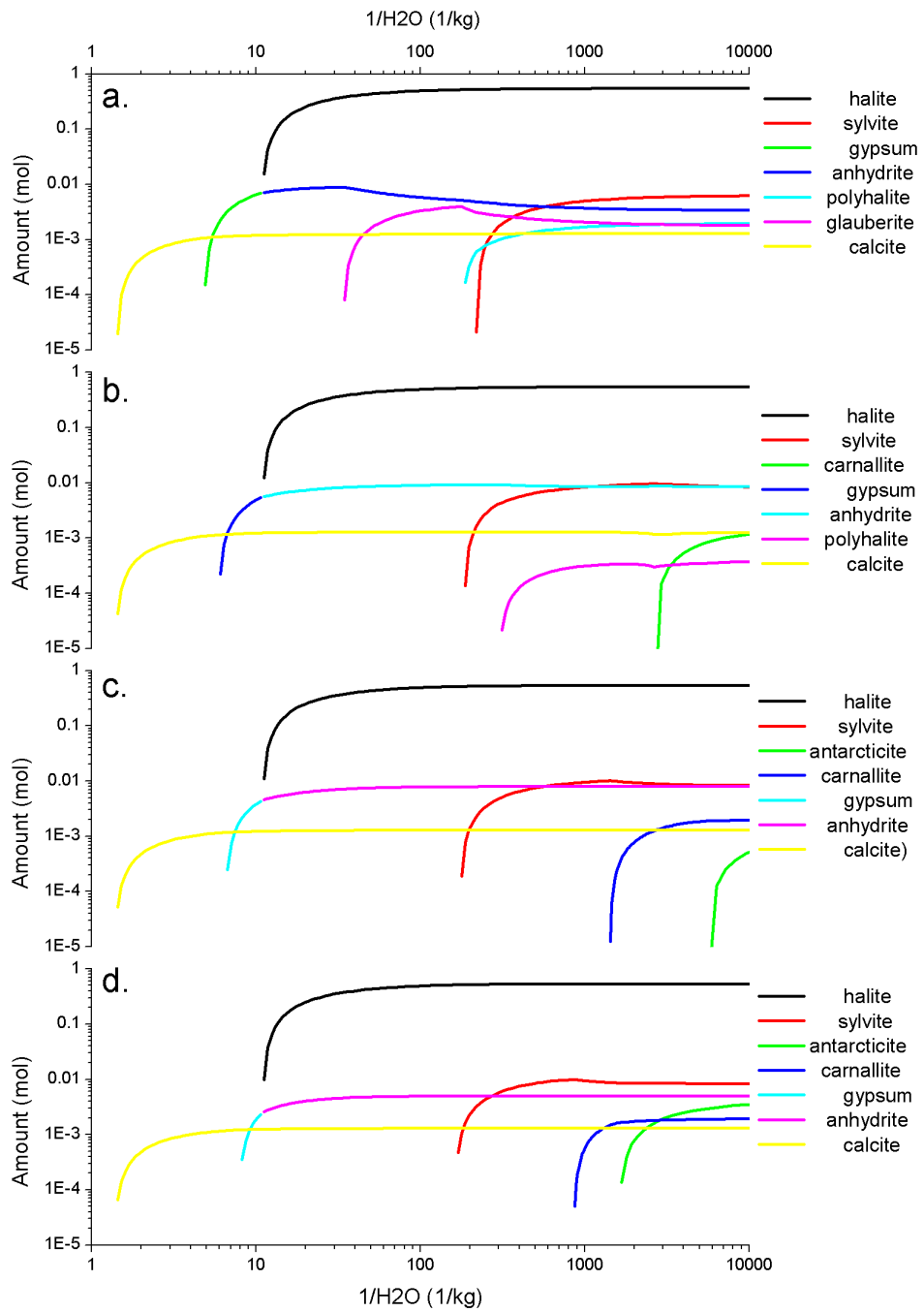


Figure A.5 The evaporite sequence from simulation runs 1-4; 2mM Mg and a. 15mM SO₄, b. 10mM SO₄, c. 8mM SO₄ and d. 5mM SO₄ (Table A.1); note that the colour coding for the mineral phases is not the same in each graph it is dependent on the evaporite sequence.

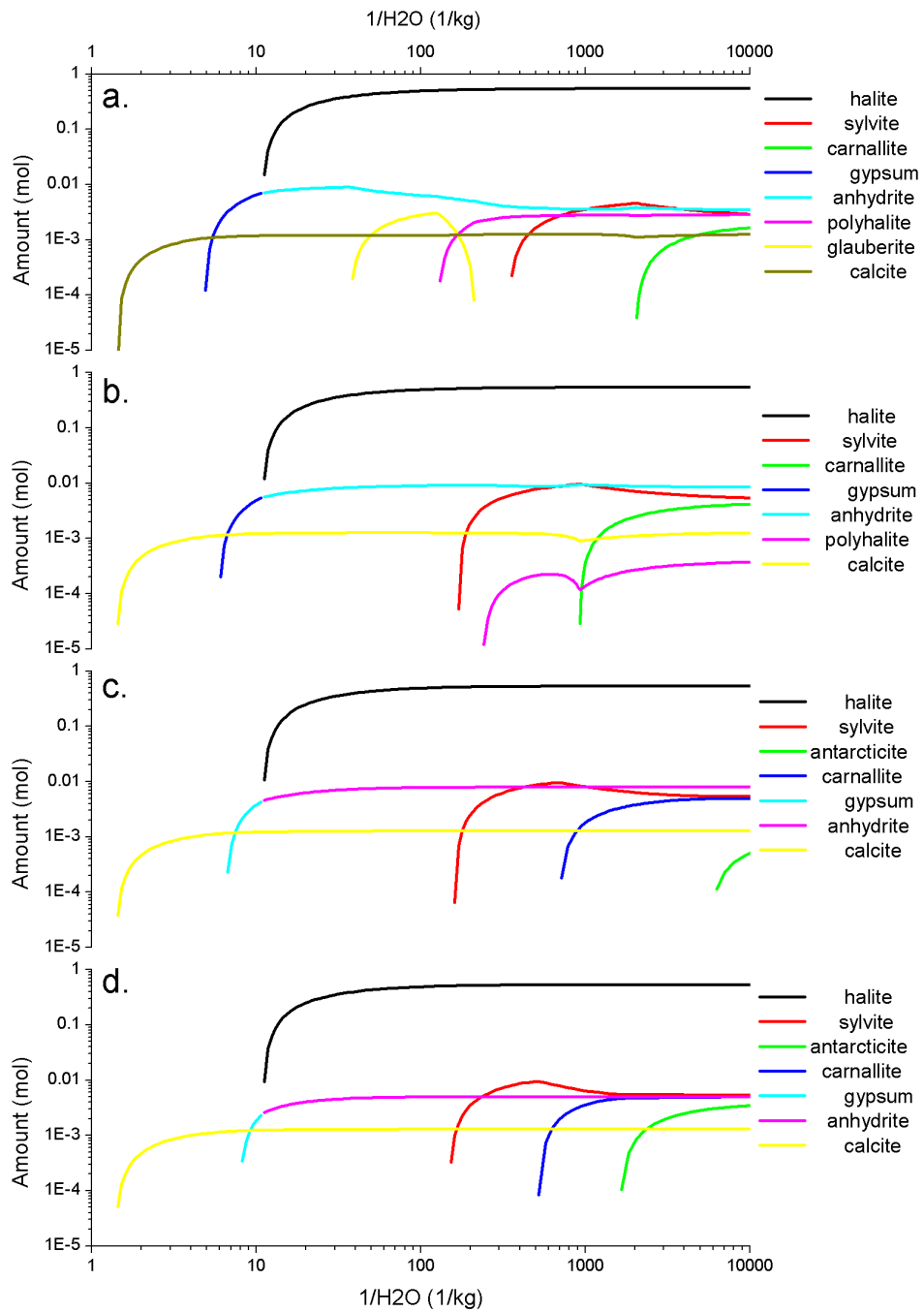


Figure A.6 The evaporite sequence from simulation runs 5-8; 5mM Mg and a. 15mM SO₄, b. 10mM SO₄, c. 8mM SO₄ and d. 5mM SO₄ (Table A.1); note that the colour coding for the mineral phases is not the same in each graph it is dependent on the evaporite sequence.

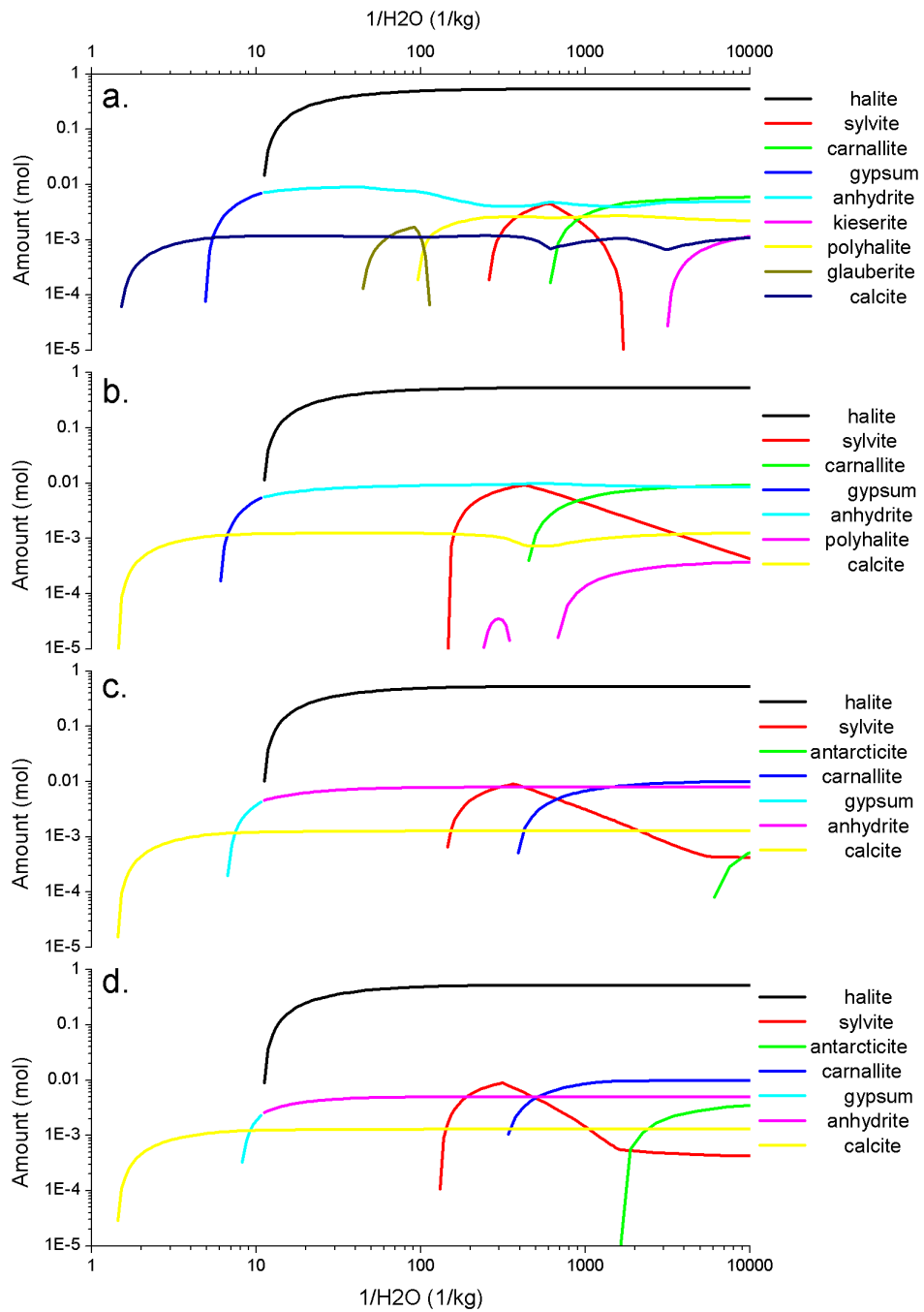


Figure A.7 The evaporite sequence from simulation runs 9-12; 10mM Mg and a. 15mM SO₄, b. 10mM SO₄, c. 8mM SO₄ and d. 5mM SO₄ (Table A.1); note that the colour coding for the mineral phases is not the same in each graph it is dependent on the evaporite sequence.

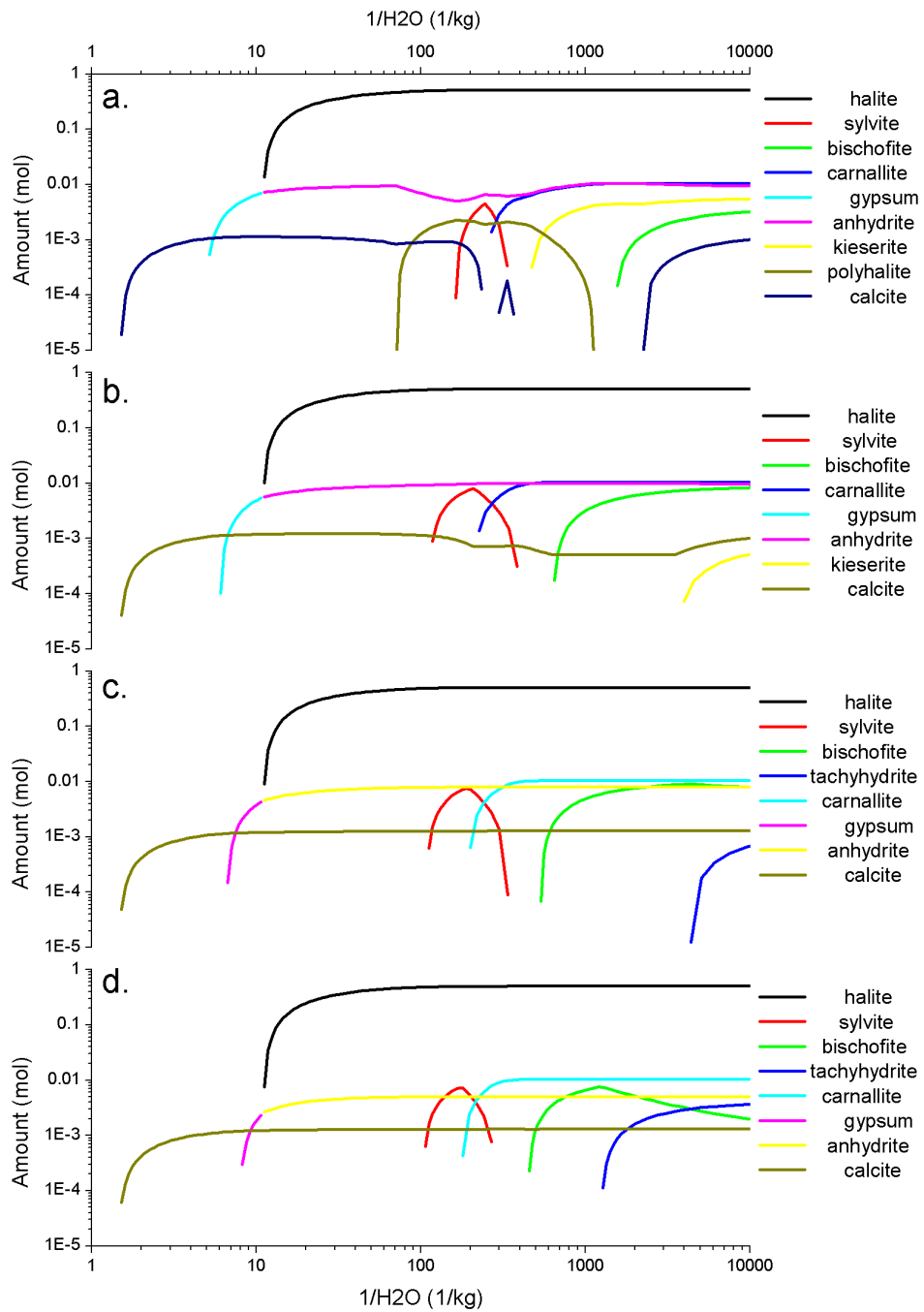


Figure A.8 The evaporite sequence from simulation runs 13-16; 20mM Mg and a. 15mM SO₄, b. 10mM SO₄, c. 8mM SO₄ and d. 5mM SO₄ (Table A.1); note that the colour coding for the mineral phases is not the same in each graph it is dependent on the evaporite sequence.

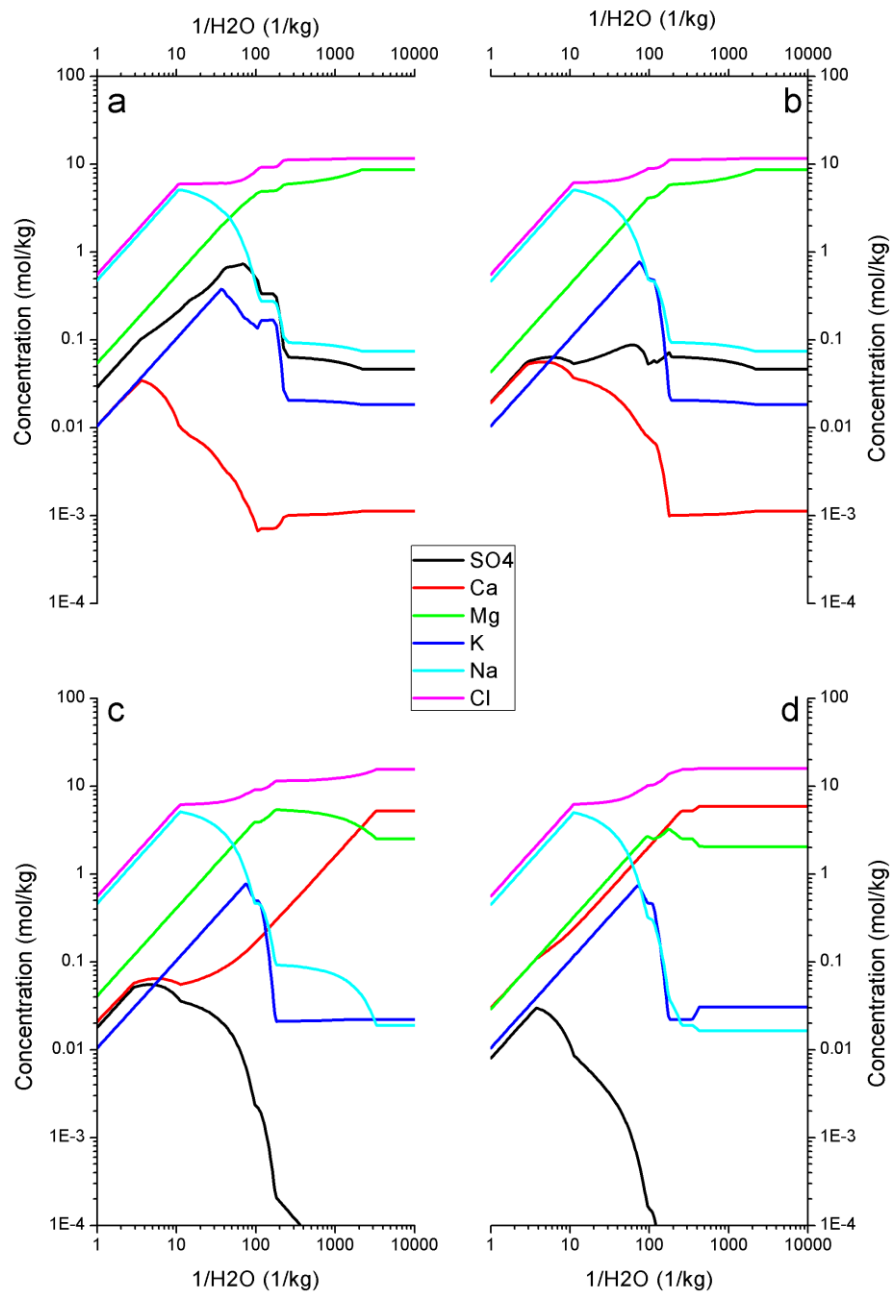


Figure A.9 The evolution of the solution from simulation runs a: 17, b: 19, c: 20 and d: 22 (Table A.2).

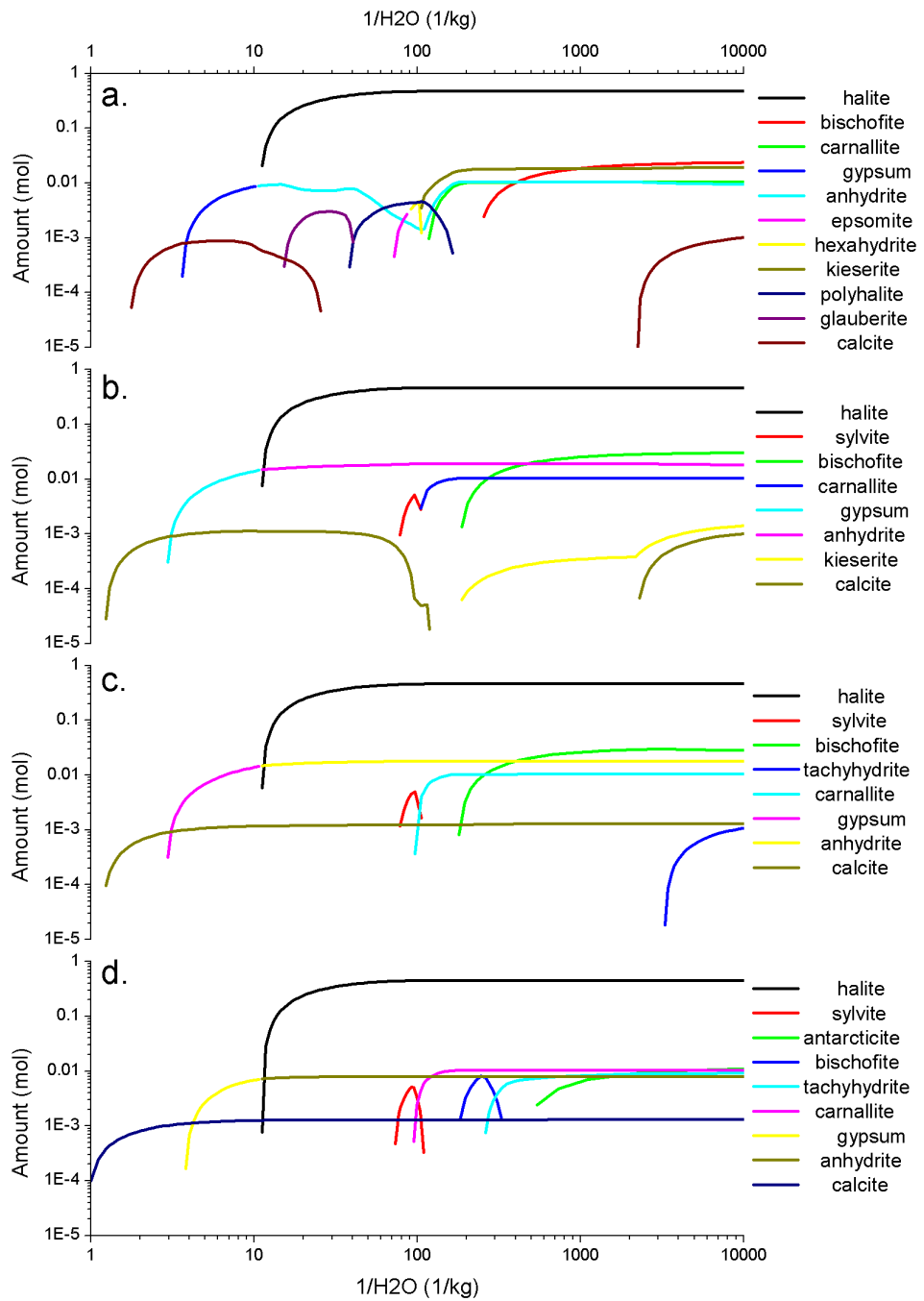


Figure A.10 The evaporite sequence from simulation runs a: 17, b: 19, c: 20 and d: 22 (Table A.2); note that the colour coding for the mineral phases is not the same in each graph it is dependent on the evaporite sequence.

A.2 Unpublished Rietveld refinement results of the effect of SO₄ on calcite, aragonite and vaterite lattice parameters

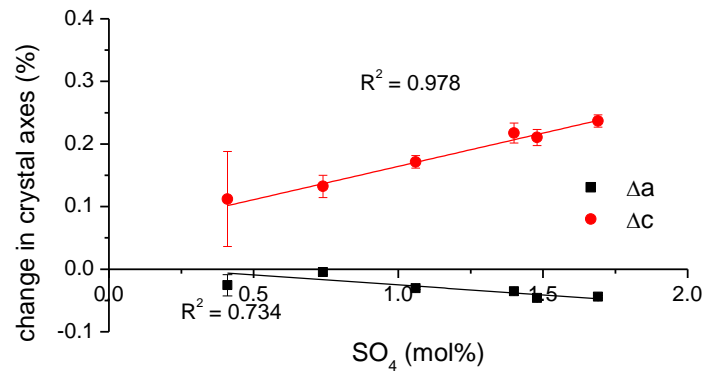


Figure A.11 changes in calcite lattice parameters as a function of the concentration of SO₄ in calcite

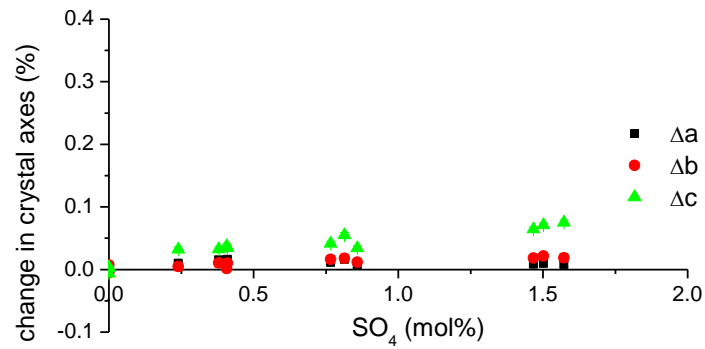


Figure A.12 changes in aragonite lattice parameters as a function of the concentration of calcite in aragonite

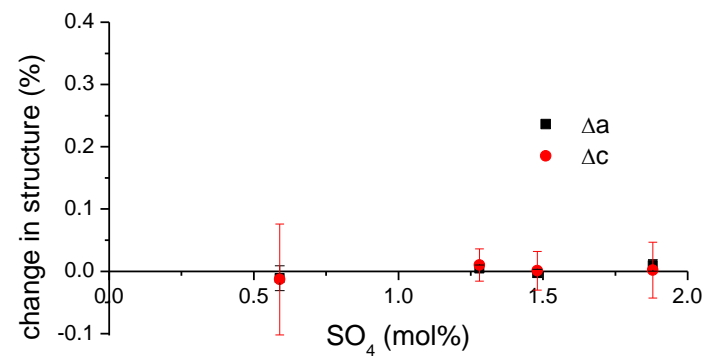


Figure A.13 changes in vaterite lattice parameters as a function of the concentration of SO₄ in vaterite

A.3 Constant addition experiments at 10 °C

This appendix briefly describes the results from a set of constant addition experiments performed at 10 °C. The experimental set-up was identical to the set-up used in chapter 4. The solution chemistry used and the resulting polymorph distribution are summarized in Table A.5 and the polymorph distribution is visualized in Figure A.14 and Figure A.15. Additionally, results from preliminary lattice parameter calculations from the Rietveld refinement on the samples are plotted in Figure A.16 (calcite), Figure A.17 (aragonite) and Figure A.18 (vaterite).

Similar to the experiments performed at 21 °C (chapter 4), aragonite was the dominant polymorph at high Mg/Ca. However, when the SO₄ concentration increased at Mg/Ca ratios ≥ 1 , calcite precipitation increased (Figure A.14 and C.2). Additionally, vaterite precipitated at low Mg/Ca in the presence of SO₄. The field of vaterite precipitation had increased significantly compared to the results at 21 °C (Figure A.14). During the experiments at 10 °C only three solid samples contained a single CaCO₃ polymorph (i.e. aragonite, Figure A.14). Hence, solid chemistry analyses would not supply information about the chemical composition on each polymorph as done for the constant addition experiments at 21 °C (chapter 4). However, the lattice parameters at 21 °C changed due to the incorporation of SO₄ into calcite (Figure A.11) and aragonite (Figure A.12). These changes could be used to estimate the SO₄ content of calcite (0.75-4 mol% SO₄) and aragonite (<0.3 mol% SO₄) from the lattice parameters in Figure A.16 and Figure A.17, respectively. These calculations indicate that the SO₄ incorporation into calcite was not significantly affected by a decrease in temperature. On the other hand, the decrease in temperature decreased the incorporation of SO₄ into aragonite dramatically from about 1.1 mol% to < 0.3 mol% in the presence of 50 mM SO₄.

Table A.5 Summary of the CaCO₃ mineralogy from the experiments at 10 °C

Solution chemistry as added		Solid composition		
SO ₄ (mM)	Mg/Ca (mM/mM)	Calcite (%)	Aragonite (%)	Vaterite (%)
0	0.5	84.6	15.4	0
0	1	2.3	97.7	0
0	1.5	1.4	98.6	0
0	3	0	100	0
0	3.5	0	100	0
0	5	0	100	0
10	0.5	3.1	75.5	21.4
10	1	4.6	85.1	10.3
10	1.5	6.7	93.3	0
10	4	13.6	86.4	0
20	0	39.3	0	60.7
20	0.5	8.1	77.3	14.7
20	1	24.3	75.7	0
50	0	3.1	6.1	90.9
50	0.2	12.5	72.0	15.5

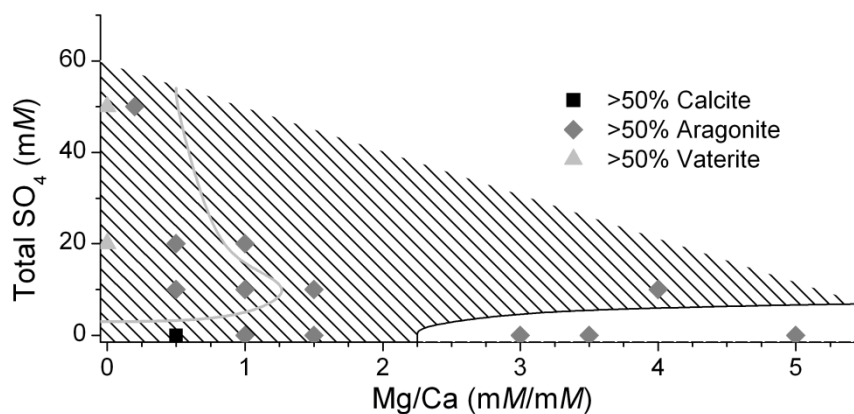


Figure A.14 Polymorph distribution as a function of the solution chemistry for the experiments at 10 °C; as in Figure 5.1, the closed symbols represent the dominant CaCO₃ polymorph, the shaded area represents the area where calcite was present in the solid phase after 48h as measured by quantitative XRD, the grey line indicates where vaterite was present after 48h

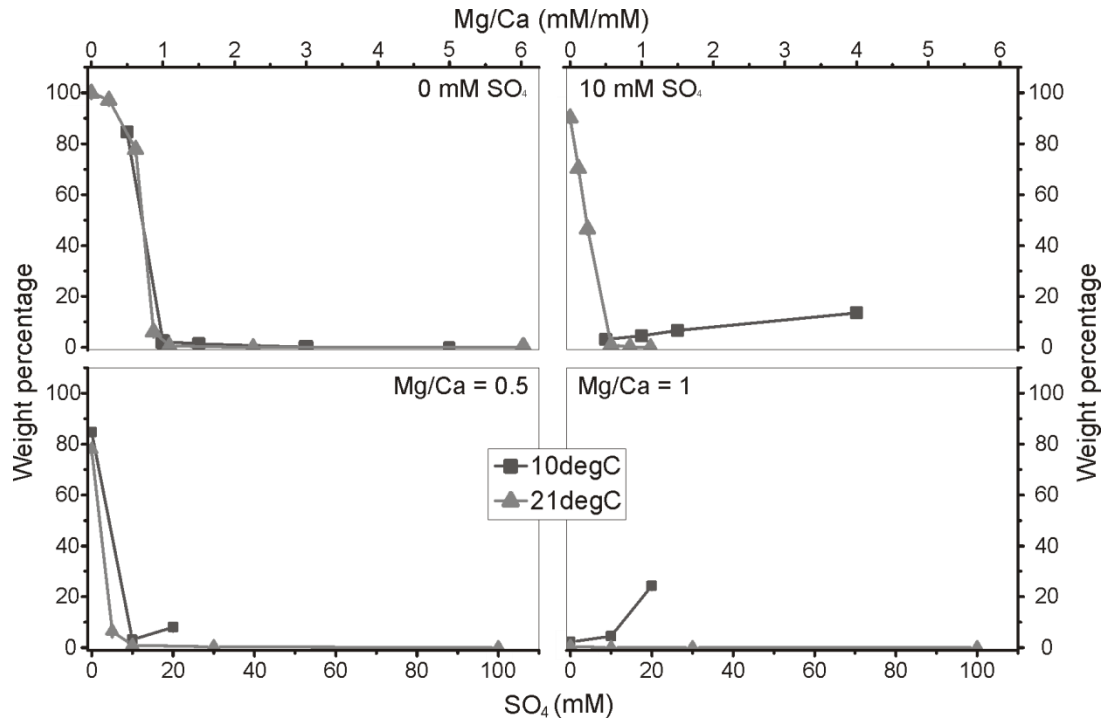


Figure A.15 Comparison of calcite weight percentage between the constant addition experiments at 10 °C and 21 °C with a constant SO_4 concentration or Mg/Ca ratio; the heading in the graphs represent the SO_4 concentration or Mg/Ca ratio in the comparison

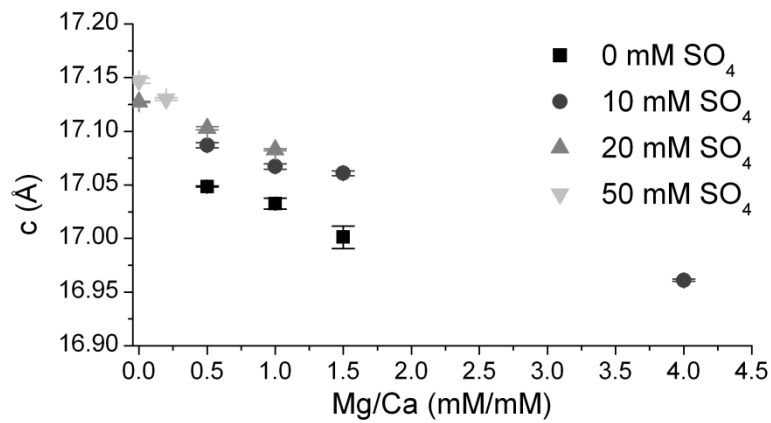


Figure A.16 Length of the calcite unit cell c-axis as a function of Mg/Ca in solution; the legend refers to the aqueous concentration of SO_4

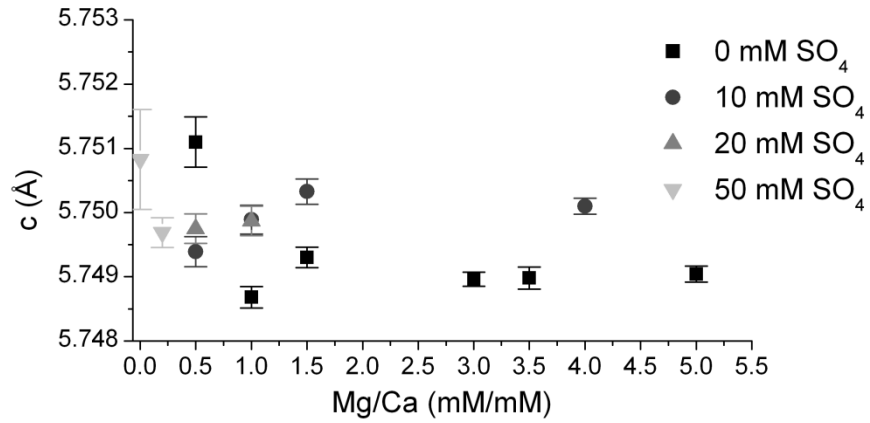


Figure A.17 Length of the aragonite unit cell c-axis as a function of Mg/Ca in solution; the legend refers to the aqueous concentration of SO₄

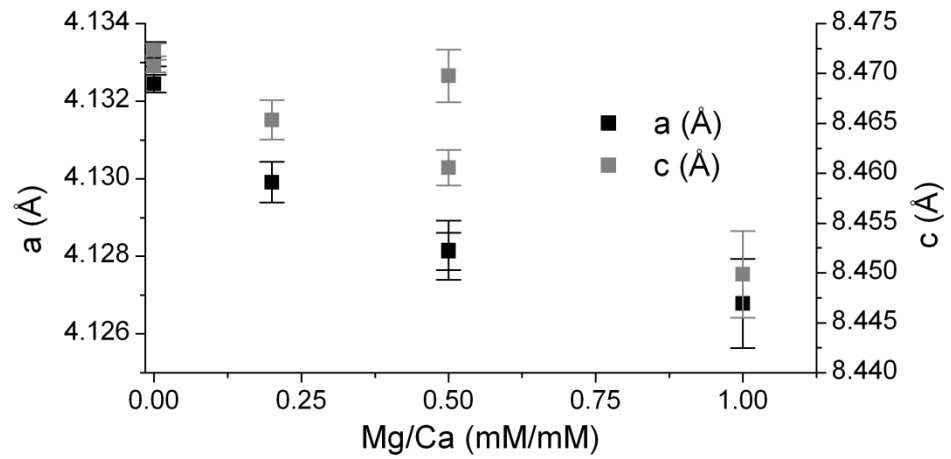


Figure A.18 Length of the vaterite unit cell axes as a function of the Mg/Ca ratio in solution; the legend refers to the unit cell axis

Appendix B

Supplementary information to chapter 5

Table B.1 Summary of the PHREEQC (PARKHURST and APPELO, 1999) modelling results, the measured pH, total calcium and total sulfate concentrations were used as input parameters to calculate the total inorganic carbonate (TIC), the aqueous speciation and the *SI* throughout the experiments

no additive time (min)	pH	Total concentrations (mM)			Aqueous speciation (mM)				SI (vaterite)
		Ca	TIC	SO ₄	Ca ²⁺	CO ₃ ²⁻	HCO ₃ ⁻	SO ₄ ²⁻	
1	9.5	26	30	0	20	4.0	7.3	0	2.3
2	8.5	11	18	0	9.9	0.71	12	0	1.2
5	8.2	9.2	17	0	8.7	0.36	12	0	0.89
8	8.2	8.9	16	0	8.4	0.35	12	0	0.86
10	8.2	9.0	16	0	8.5	0.35	12	0	0.87
20	8.2	8.7	16	0	8.2	0.34	12	0	0.84
30	8.2	8.5	16	0	8.0	0.32	11	0	0.81
replacement time (min)	pH	Total concentrations (mM)			Aqueous speciation (mM)				SI (vaterite)
		Ca	TIC	SO ₄	Ca ²⁺	CO ₃ ²⁻	HCO ₃ ⁻	SO ₄ ²⁻	
1	8.8	75	45	45	57	2.1	22	23	2.5
2	8.1	53	32	36	44	0.48	22	19	1.7
5	8.0	49	28	34	42	0.31	20	18	1.5
8	7.9	48	27	34	41	0.28	19	18	1.5
10	7.9	49	28	34	42	0.28	19	18	1.5
20	7.9	49	26	36	42	0.26	18	19	1.4
30	7.9	50	27	36	42	0.27	19	19	1.4
additive time (min)	pH	Total concentrations (mM)			Aqueous speciation (mM)				SI (vaterite)
		Ca	TIC	SO ₄	Ca ²⁺	CO ₃ ²⁻	HCO ₃ ⁻	SO ₄ ²⁻	
1	9.6	32	39	48	22	5.4	8.5	27	2.5
2	8.9	11	35	38	8.5	2.4	19	22	1.7
5	8.7	11	37	38	8.3	1.8	23	22	1.6
8	8.7	11	36	38	8.1	1.7	22	22	1.5
10	8.7	10	35	39	8.1	1.7	22	22	1.5
20	8.6	10	34	39	8.1	1.6	22	23	1.5
30	8.6	10	33	40	8.1	1.5	21	23	1.5